Gulf Petro Initiative
Final Report

Reporting Period Start Date: **August 06, 2008**
Reporting Period Ending Date: **February 05, 2011**

Principal Author: **Fathi Boukadi, Ph.D.**
Report Issue Date: **May 5, 2011**

DOE Award No.: **DE-NT0004651**

Submitted by:
University of Louisiana at Lafayette
Energy Institute
P.O. Box 44690
Lafayette, LA 70504

DISCLAIMER

ABSTRACT

In this report, technologies for petroleum production and exploration enhancement in deepwater and mature fields are developed through basic and applied research by:

1. Designing new fluids to efficiently drill deepwater wells that can not be cost-effectively drilled with current technologies. The new fluids will be heavy liquid foams that have low-density at shallow dept to avoid formation breakdown and high density at drilling depth to control formation pressure. The goal of this project is to provide industry with formulations of new fluids for reducing casing programs and thus well construction cost in deepwater development.

2. Studying the effects of flue gas/CO_2 huff n' puff on incremental oil recovery in Louisiana oilfields bearing light oil. An artificial neural network (ANN) model will be developed and used to map recovery efficiencies for candidate reservoirs in Louisiana.

3. Arriving at a quantitative understanding for the three-dimensional controlled-source electromagnetic (CSEM) geophysical response of typical Gulf of Mexico hydrocarbon reservoirs. We will seek to make available tools for the qualitative, rapid interpretation of marine CSEM signatures, and tools for efficient, three-dimensional subsurface conductivity modeling.

TABLE OF CONTENTS

EXECUTIVE SUMMARY

In this project, new fluids have been designed to efficiently drill deepwater wells that can be cost-effectively drilled. The new fluids are heavy-liquid foams with low density at shallow depths and high density at drilling depths.

Louisiana Immersive Technology Enterprise (LITE) visualization confirmed that significant end-effects existed at both ends of the sand packs. The end-affected length is about 3.5 cm in the 4.45 cm inner diameter tube. Visualization also indicated that gravity segregation effect in the horizontal flow experiments was not significant.

Flue gas was used for model building, fine tuning, and validation. Flue gas experiments indicated that MMP data generated using slim tube experiments do not portray reservoir conditions and ought to be replaced by MMP data generated using the actual reservoir under study. Besides, an augmented correlation has been developed to predict CO2 MMP. The correlation proved to be superior to standard correlations often adopted by the industry for quality control in CO2 enhanced oil recovery (EOR) programs. Additionally, an ANN model has also been generated to map recovery efficiencies for candidate reservoirs in Louisiana with API gravity ranging from 31 to 41^{o}, in-situ temperatures and pressures varying from 220 to 375 ^{O}F and 2000 to 3200 psia, respectively. Visualization was used to identify vaporization as the dominant enhanced oil recovery production mechanism. Besides, the potential for CO_2 EOR as a sequestration method is vividly demonstrated by simulation.

LITE visualization was also used to better understand dominant EOR mechanism under miscible conditions and monitor frontal advance rate movement for the candidate Louisiana oil reservoirs. The visualization part confirmed an active vaporization mechanism.

Visualization also confirmed the fact that the potential for CO_2 EOR as a sequestration method is vividly demonstrated.

A quantitative understanding for the three-dimensional controlled-source electromagnetic (CSEM) geophysical response of typical Gulf of Mexico hydrocarbon reservoirs has led to the development of a simplified, approximate model of marine controlled source electromagnetic responses. CSEM team has also developed a Standard and Bayesian inversion of MCSEM containing proven solutions to the common inversion problem of local minimum entrapment.

LITE visualization was also used to provide an immersive visualization that will allow Dr. Stalnaker to interact and to visualize in immersive 3-D the multiple reservoirs.

REPORT DETAILS

The following tasks represent the accomplishments gained for the three parts of the project, namely, Foam Task, CO2 Task, and the CSEM Task.

FOAM TASK

Experimental studies of heavy foams have been carried out in this project to identify the optimum formulations of heavy foams. Experimental setup is illustrated in **Figure 1**.

Totally 20 different formulations in three systems have been tested. The first system is the bentonite-barite system; the second one is bentonite-hametite system; and the third one is $CaBr_2$–Guar Gum system. Foams that were observed to be unstable were not further tested on other properties. Compositions and properties of the foams are summarized in **Table 1**.

Foam stability was evaluated with visual observation, half-life, and Fann Electrical Stability Tester. One foam was observed to be unstable and thus not tested by the Fann Electrical Stability Tester. Foam density was measured mud balance. Totally 3 foams in the $CaBr_2$–Guar Gum system were found heavy enough (>10.5 ppg) for deepwater drilling. These 3 foams were also stable. Their viscosities are in the range that is suitable for field application. Foam quality index (gas fraction) of these 3 foams are between 0.60 and 0.75, which are in the lower end for field applications.

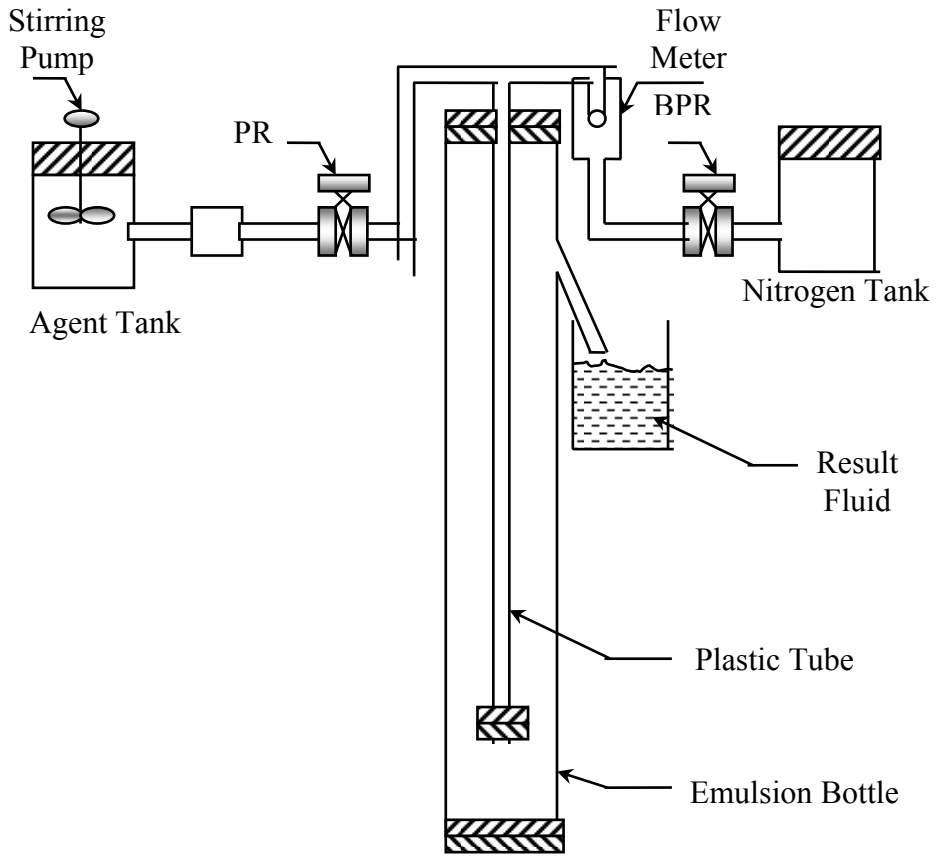

Figure 1: Experimental setup for foam studies

Table 1: Compositions and properties of foams

Foam Formulation	H_2O (ml)	Bentonite (g)	Barite (g)	HC-2 V%	QF V%	Density (ppg)	GAS V %	E-stability (volt)	Viscosity (cp)
1	350	20	200	8	0.03	-	-	1	-
2	350	20	300	8	0.03	-	-	1	-
3	350	15	100	10	0.03	8.00	100	1	75
4	350	15	120	10	0.03	8.55	100	1	59
5	350	15	150	10	0.03	-	-	1	40
6	350	10	150	5	0.03	8.85	84	1	61
7	350	10	150	0	0.03	-	100	1	-
Foam Formulation	**H_2O (ml)**	**Hematite (g)**	**Bentonite (g)**	**HC-2 V%**	**QF V%**	**Density (ppg)**	**GAS V %**	**E-stability (volt)**	**Viscosity (cp)**
8	350	10	20	9	0.03	6.9	98	1	40
9	350	15	20	9	0.03	7.2	97	1	148
10	350	30	20	9	0.03	7.49	99	1	79
11	350	90	40	9	0.03	-	-	-	-
12	350	35	20	37.8	0.03	7.6	99	1	55
13	350	40	20	34.2	0.03	8.28	99	1	58
14	350	45	20	37.8	0.03	8.28	99	1	64
15	350	50	25	37.8	0.03	8.2	98	1	68
16	350	50	20	37.8	0.03	8.4	98	1	53.5
17	350	55	20	38	0.03	8.42	98	1	50
Foam Formulation	**H_2O (ml)**	**$CaBr_2$ Solution (g)**	**Guar Gum (g)**	**HC-2 V%**	**AQF-2 V%**	**Density (ppg)**	**GAS V %**	**E-stability (volt)**	**Viscosity (cp)**
18	20	600	-	8.5	11	10.7	60	2	25
19	-	500	-	3.5	7.1	11.1	61.5	2	26
20	-	500	1	3.5	7.1	11.4	75	2	28

Further experimental studies of heavy foams have been carried out to investigate the rheological properties of heavy foams formulated. Compositions and properties of the tested foams are summarized in **Table 2**.

Two bentonite-barite foams were tested for rheology. Shear rate versus shear stress plots are shown in **Figure 2**. This figure indicates that bentonite-barite foams fall into the category of Bingham-Plastic fluids, although they behave like Newtonian fluids at low shear rates.

Three bentonite-hametite foams were tested for rheology. Their shear rate - shear stress relations are plotted in **Figure 3**, which indicates that bentonite-hametite foams fall into the category of Bingham-Plastic fluids.

Two $CaBr_2$–Guar Gum foams were tested for rheology. Shear rate versus shear stress plots are shown in **Figure 4**. This figure indicates that $CaBr_2$–Guar Gum foams fall into the category of Newtonian fluids, although they behave like Bingham-Plastic fluids at low shear rates.

Rheological parameters of these foam samples are summarized in **Table 3**, which indicates that all of these property values are in the practical range for well drilling operations.

Table 2: Composition and properties of the foams tested for rheology

Bentonite-Barite Foams								
Formulation No.	Water	Bentonite	Barite	HC-2	QF	Density	Gas V.	E-stability
	(ml)	(g)	(g)	V%	V%	(ppg)	%	(volt)
4	400	15	150	10	0.03	10.7	99	2
5	400	15	180	10	0.03	11.1	99	2
Bentonite-Hametite Foams								
Formulation No.	Water	Bentonite	Hematite	HC-2	QF	Density	GAS V	E-stability
	(ml)	(g)	(g)	V%	V%	(ppg)	%	(volt)
16	350	15	85	9	0.13	8.75	98	1
17	350	15	90	9	0.13	8.95	98	1
19	350	15	100	9	0.13	8.9	98	1
$CaBr_2$–Guar Gum Foams								
Formulation No.	Water	$CaBr_2$ Solution	Guar Gum	HC-2	AQF-2	Density	GAS V	E-stability
	(ml)	(g)	(g)	V%	V%	(ppg)	%	(volt)
22	-	500	-	3.5	7.1	11.1	62	2
23	-	500	1	3.5	7.1	11.4	75	2

Note: AQF-2 and QF are foaming agents and HC-2 is for foam quality control.

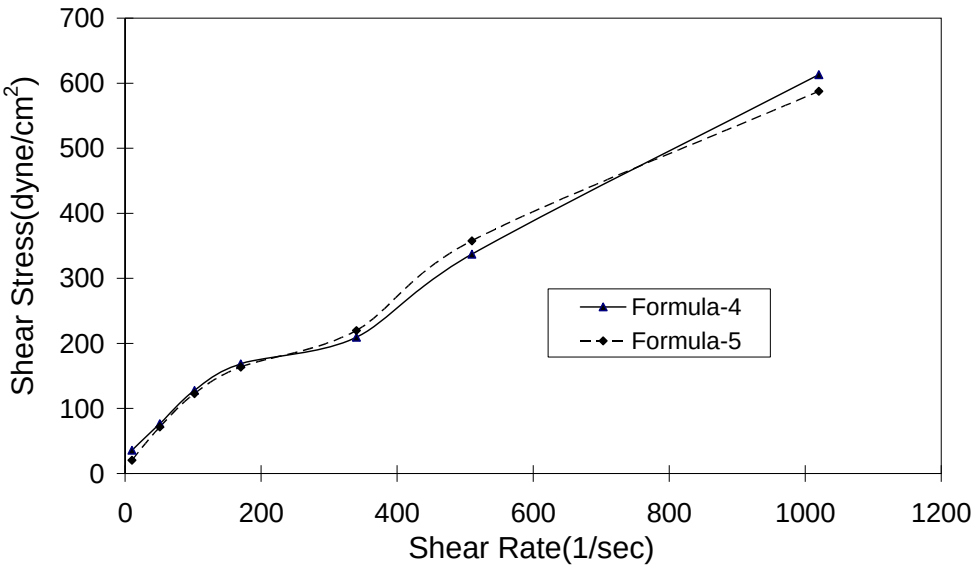

Figure 2: Shear rate versus shear stress plots for two bentonite-barite foams

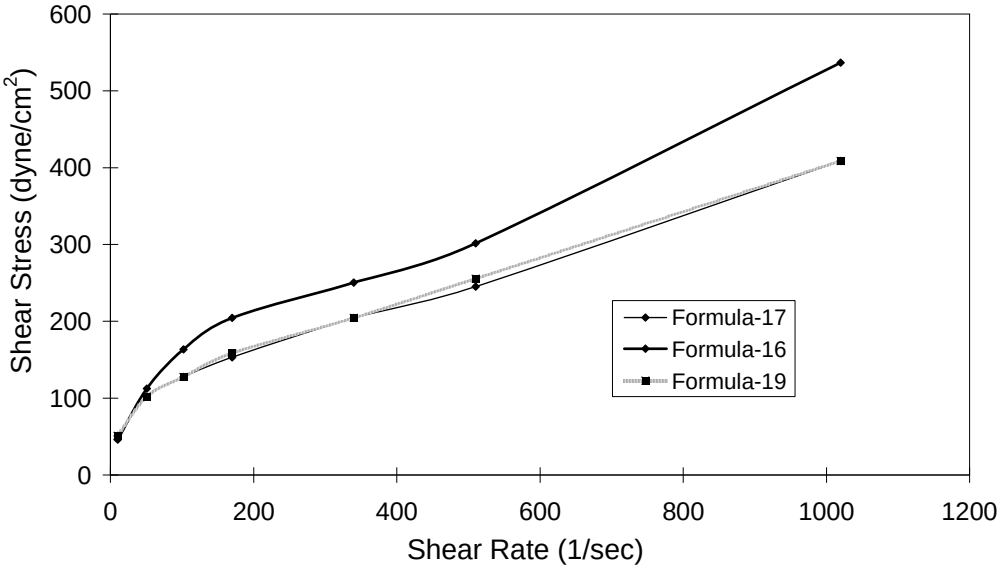

Figure 3: Shear rate versus shear stress plots for three bentonite-hametite foams

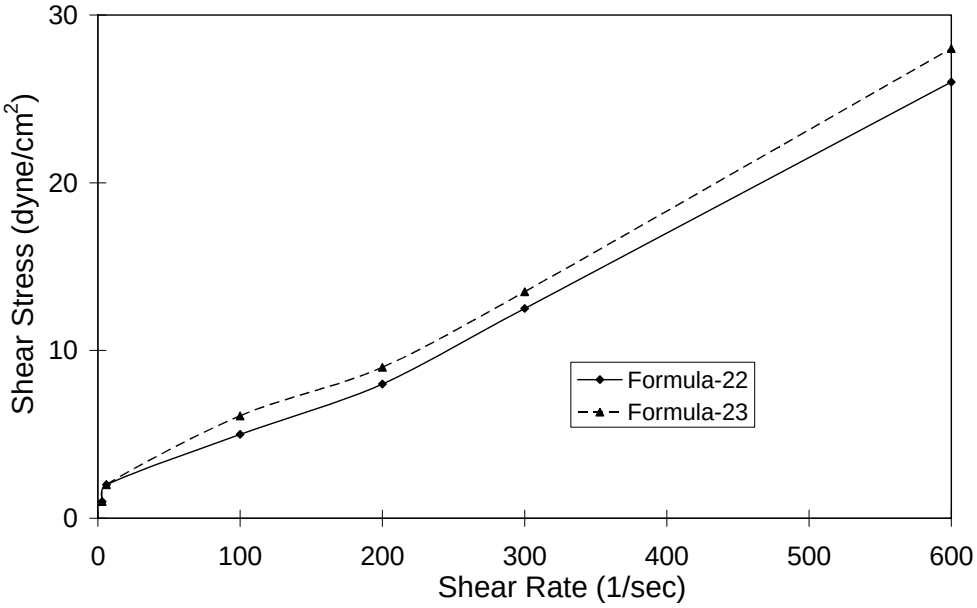

Figure 4: Shear rate versus shear stress plots for two $CaBr_2$–Guar Gum foams

Table 3: Rheological parameters of foam samples

Foam System	Formulation No.	PV (cp)	YP ($lb/100ft^2$)	Apparent Viscosity (cp)
Bentonite-Barite Foam	4	54	12	60
	5	45	25	57
Bentonite-Hametite Foam	16	46	13	52
	17	30	20	40
	19	32	16	39
CaBr2–Guar Gum Foam	22	---	---	26
	23	---	---	28

Furthermore the heavy foam research focused on simulation of heavy-foam flow in drilling conditions. A computer model was built to predict foam properties in the drilling system. The computed foam parameters and properties include:

- Foam pressures in drill string and annulus
- Foam velocities in drill string and annulus
- Foam densities in drill string and annulus
- Foam quality index in drill string and annulus
- Foam equivalent circulating density (ECD)

For the assumed data set given in **Table 4** and system dimension data in **Table 5**, the computed profiles of foam pressure, foam velocity, foam density, foam quality index, and foam ECD are shown in **Figures 5**, **6**, **7**, **8**, and **9**, respectively. The computer model is currently being validated with data from light-foam drilling operations.

Table 4: Input data to the computer model for heavy foam

Total Depth (H):	8000	ft
Liquid Injection Rate (Ql):	400	gpm
Depth of the Surface Choke:	0.00	ft
Surface Temperature:	540	^oR
Liquid Weight (W_m):	15	ppg
Foam Plastic Viscosity (PV):	50	cp
Foam Yield Point (YP):	60	$lb/100ft^2$
Gas Specific Gravity (S_g):	1	air=1
Formation Fluid Specific Gravity (S_f):	1	water=1
Geothermal Gradient (G):	0.01	$^oF/ft$
Formation Fluid (water and oil) Influx Rate (Q_f):	0	bbl/hr
Injection GLR:	1.3	scf/gal
Backpressure (Ps):	14.7	psia

Table 5: System data used for the computer modeling of heavy foam flow

Depth (ft)	Inclination (Deg)	Borehole Size (in.)	Pipe OD (in)	Pipe ID (in)
10.00	0.00	8.017	4.50	2.826
173.06	0.00	8.017	4.50	2.826
336.12	0.00	8.017	4.50	2.826
499.18	0.00	8.017	4.50	2.826
662.24	0.00	8.017	4.50	2.826
825.31	0.00	8.017	4.50	2.826
988.37	0.00	8.017	4.50	2.826
1151.43	0.00	8.017	4.50	2.826
1314.49	0.00	8.017	4.50	2.826
1477.55	0.00	8.017	4.50	2.826
1640.61	0.00	8.017	4.50	2.826
1803.67	0.00	8.017	4.50	2.826
1966.73	0.00	8.017	4.50	2.826
2129.80	0.00	8.017	4.50	2.826
2292.86	0.00	8.017	4.50	2.826
2455.92	0.00	8.017	4.50	2.826
2618.98	0.00	8.017	4.50	2.826
2782.04	0.00	8.017	4.50	2.826
2945.10	0.00	8.017	4.50	2.826
3108.16	0.00	8.017	4.50	2.826
3271.22	0.00	8.017	4.50	2.826
3434.29	0.00	8.017	4.50	2.826
3597.35	0.00	8.017	4.50	2.826
3760.41	0.00	8.017	4.50	2.826
3923.47	0.00	8.017	4.50	2.826
4086.53	0.00	8.017	4.50	2.826
4249.59	0.00	8.017	4.50	2.826
4412.65	0.00	8.017	4.50	2.826
4575.71	0.00	8.017	4.50	2.826
4738.78	0.00	8.017	4.50	2.826
4901.84	0.00	8.017	4.50	2.826
5064.90	0.00	8.017	4.50	2.826
5227.96	0.00	8.017	4.50	2.826
5391.02	0.00	8.017	4.50	2.826
5554.08	0.00	8.017	4.50	2.826
5717.14	0.00	8.017	4.50	2.826
5880.20	0.00	8.017	4.50	2.826
6043.27	0.00	8.017	4.50	2.826
6206.33	0.00	8.017	4.50	2.826
6369.39	0.00	8.017	4.50	2.826
6532.45	0.00	8.017	4.50	2.826
6695.51	10.00	8.017	4.50	2.826
6858.57	20.00	8.017	4.50	2.826
7021.63	30.00	8.017	4.50	2.826
7184.69	40.00	8.017	4.50	2.826
7347.76	50.00	8.017	4.50	2.826
7510.82	60.00	8.017	4.50	2.826
7673.88	70.00	7.875	6.75	2.826
7836.94	80.00	7.875	6.75	2.826
8000.00	90.00	7.875	6.75	2.826

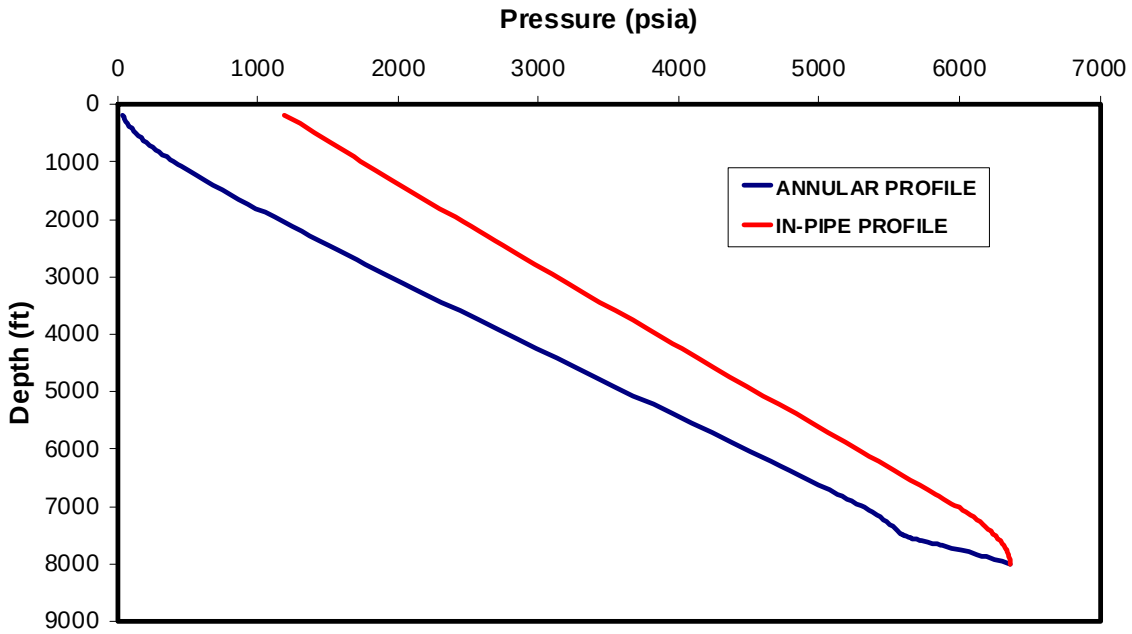

Figure 5: Computed foam pressure profile in a drill circulating system

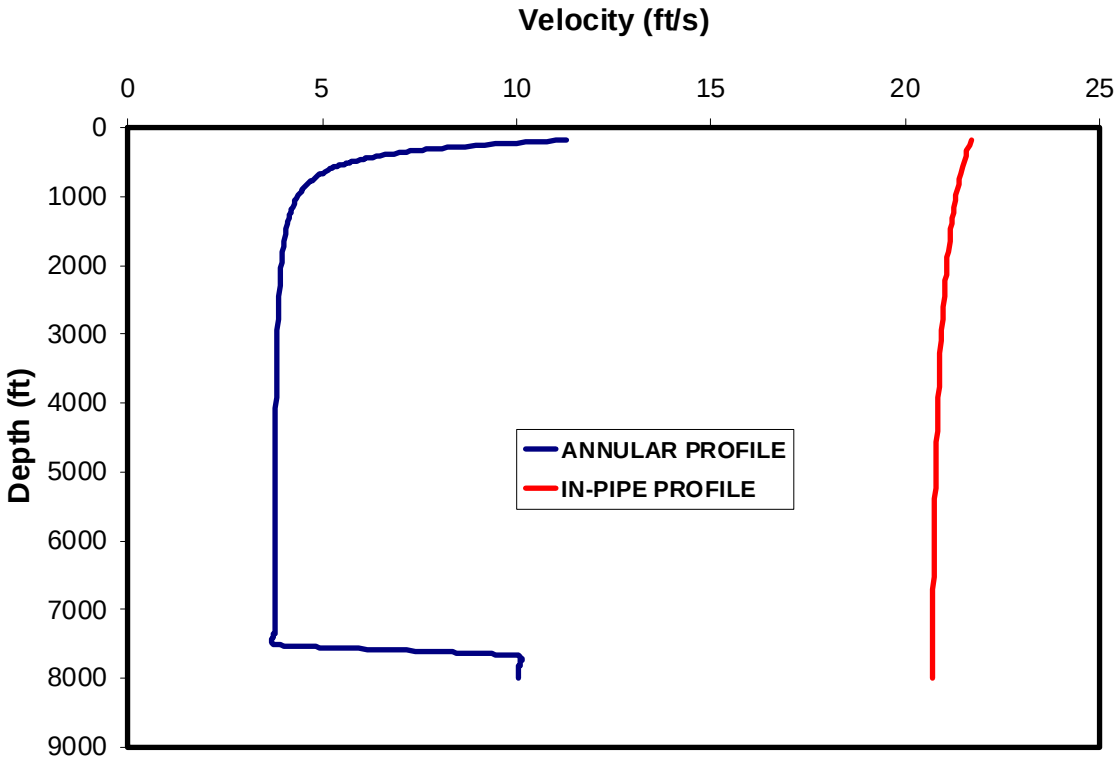

Figure 6: Computed foam velocities profile in a drill circulating system

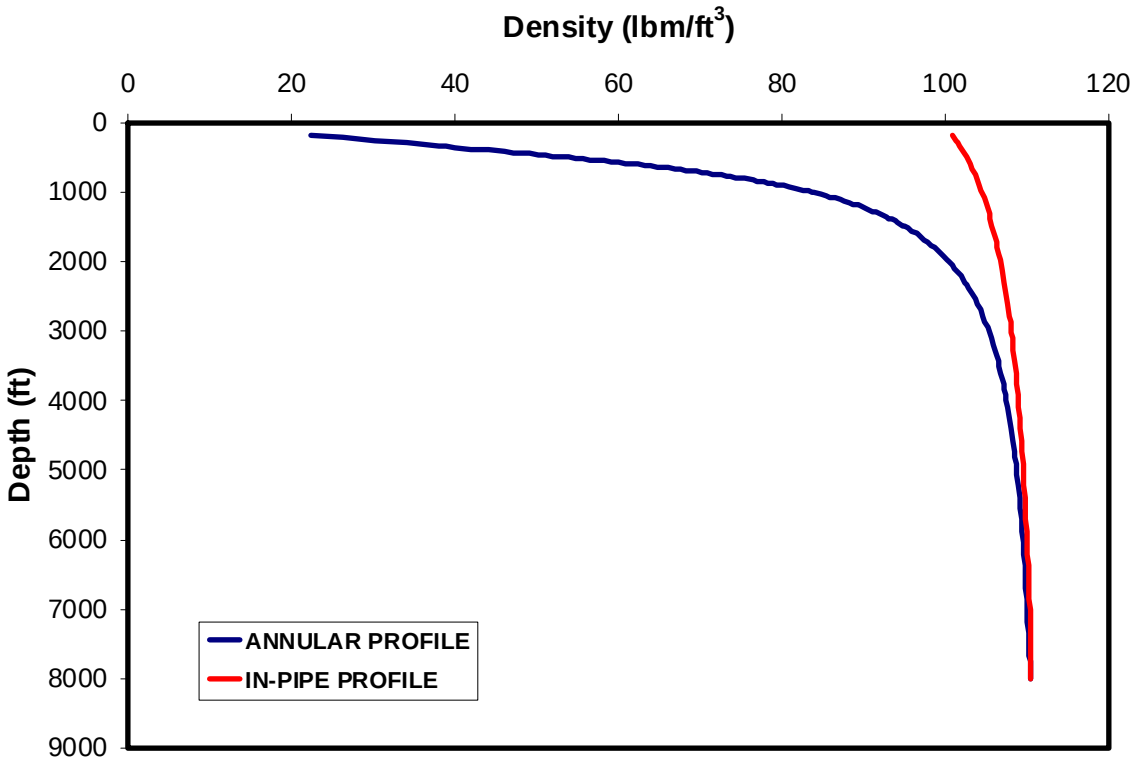

Figure 7: Computed foam densities profile in a drill circulating system

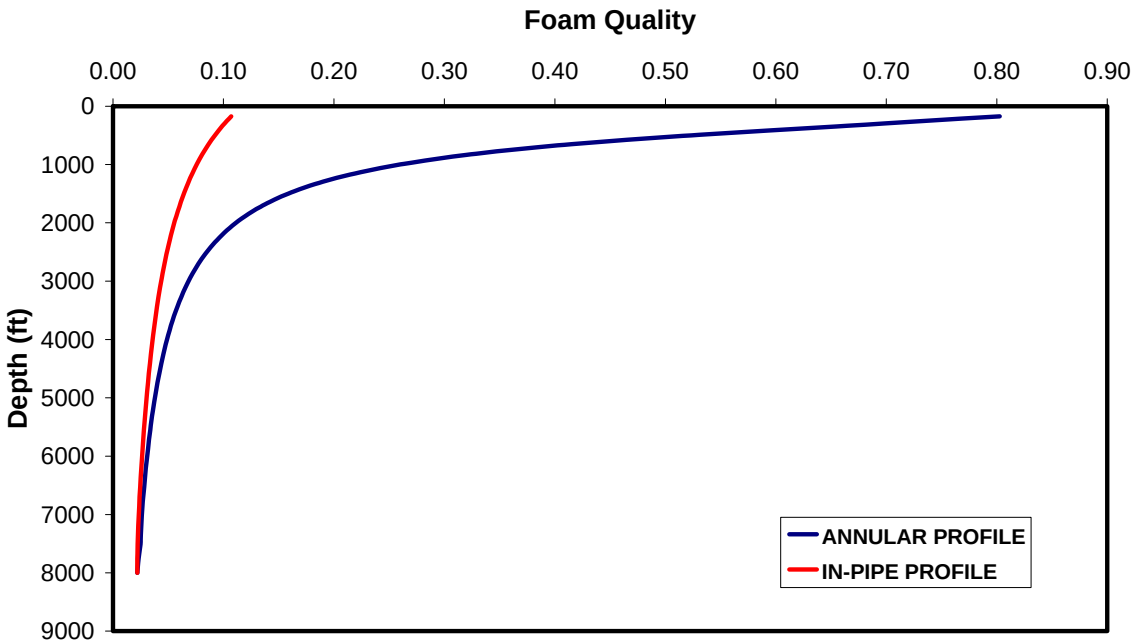

Figure 8: Computed foam quality index profile in drill circulating system

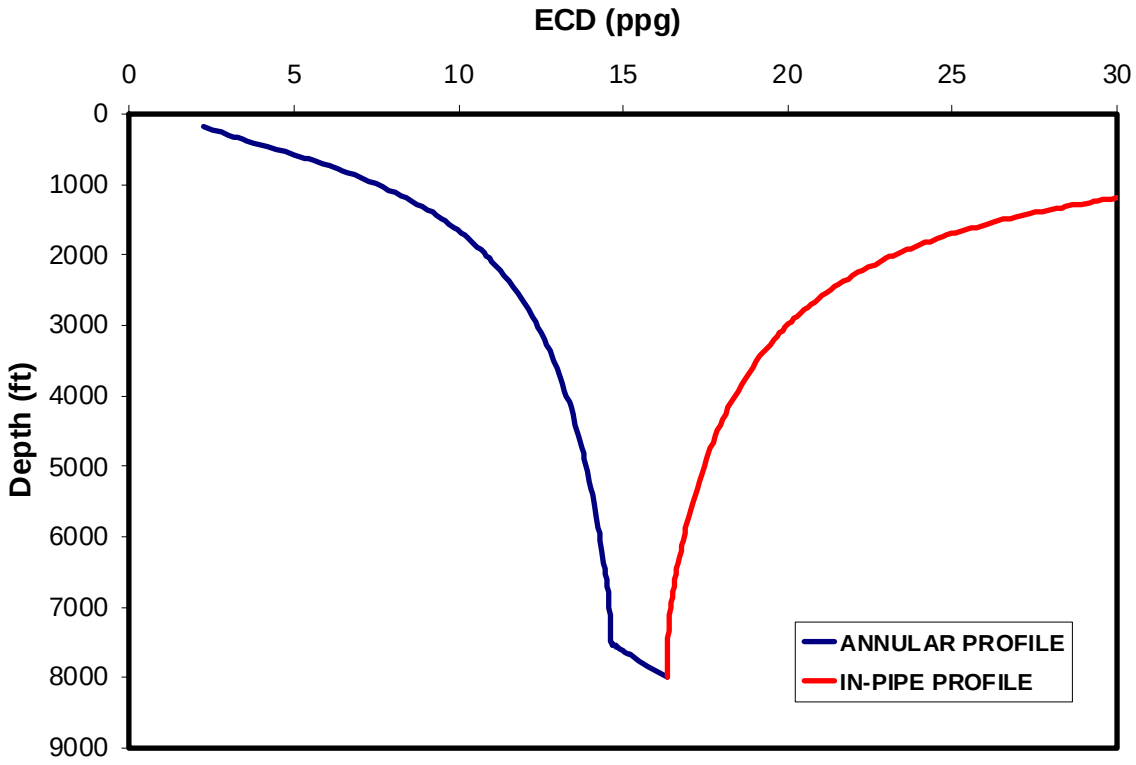

Figure 9: Computed foam ECD profile in drill circulating system

In addition, the heavy foam research focused on 3-dimensional visualization (3DV) of foam flow in porous media. Research work includes:

A. Generating images of liquid-gas two-phase flow in a sand pack (simulating oil reservoirs), and

B. Processing image data to create 3DV of two-phase flow in the sand pack.

Water and nitrogen were injected into a sand pack shown in **Figure 10**. Two-phase flow was tested vertically and horizontally to observe liquid and gas distribution in the sand pack. Water flow rate ranged from 8 to 150 cc/min. For the vertical tests, water was injected from the bottom to the top. Before nitrogen gas injection, 5 pore-volume of water was injected. X-Ray CT Scanning was then used to identify nitrogen gas distribution in the pack. **Figure 11** shows the color code for images from the X-Ray CT scanning.

In each vertical experiment, 85 images of cross sections were taken for each combination of water and nitrogen flow rates. **Figure 12** shows a set of images. In each horizontal experiment, 300 images of cross sections were taken for each combination of water and nitrogen flow rates. **Figure 13** demonstrates a set of images. The distance between each section is 0.05 cm in all the experiments. The range of CT Number in all images is between -500 and 3200. Examining the TC images allowed the following observations to be outlined:

1. Significant end-effect existed at both ends of the sand pack in Tube-C. The end-effected length is from 2 cm to 5 cm in the 4.45 cm inner diameter tube.
2. Gravity segregation effect in all the horizontal flow experiments was not significant.

In order to observe how gas and liquid phases flow in the sand pack, 3-dimentional visualization of simultaneous two-phase flow is necessary. Computation algorithms were developed to create 3DV of two-phase flow using the CT images.

Figure 10: Sand pack for testing liquid-gas two-phase in porous media: effective length 12.7 cm, inner diameter 4.45 cm

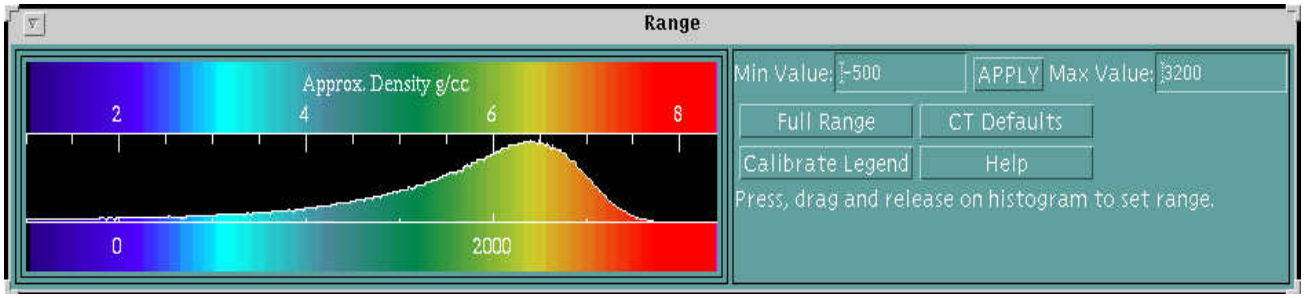

Figure 11: Color code for images from X-Ray CT scanning

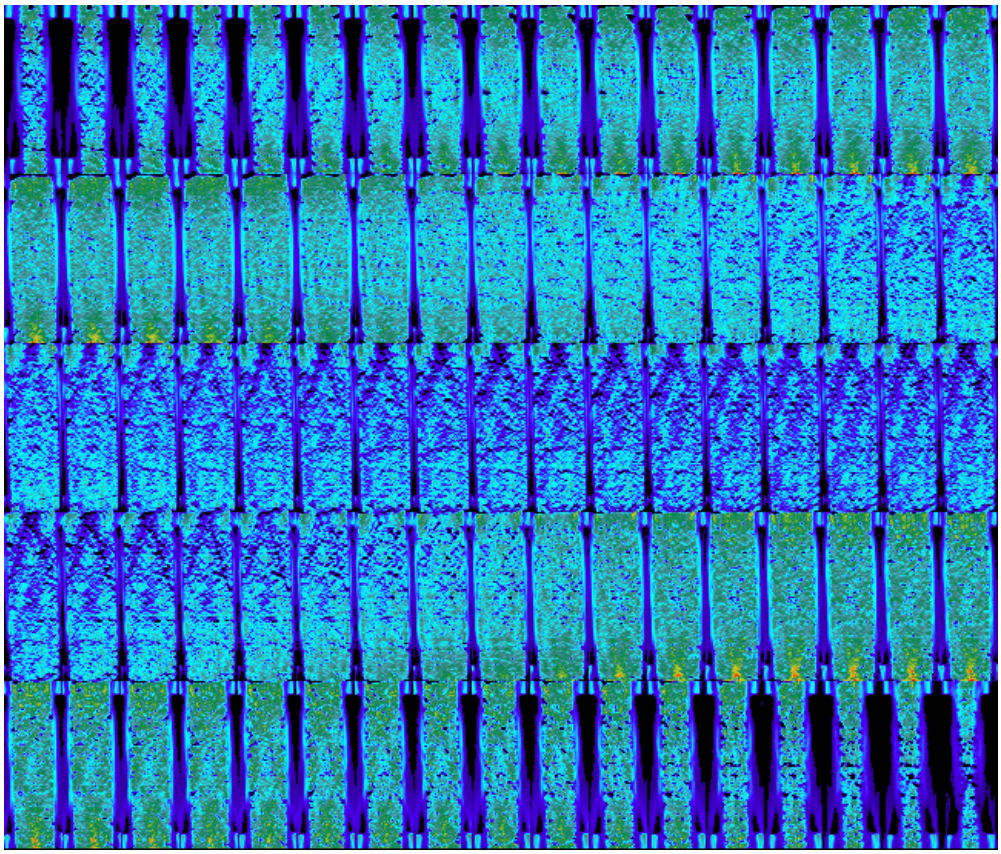

Figure 12: CT images of cross sections taken from vertical flow of water and nitrogen

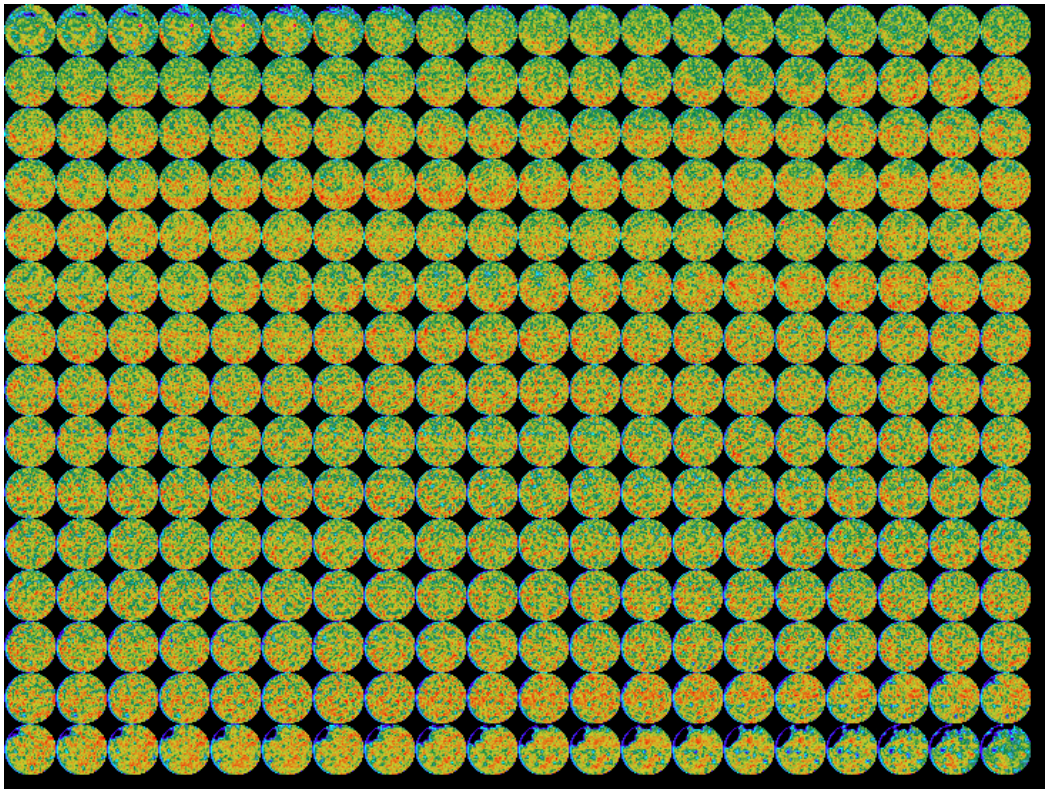

Figure 13: CT images of cross sections taken from horizontal flow of water and nitrogen

In addition, the heavy foam research focused on comparison of heavy foams with conventional light foams. The purpose is to identify their differences in critical properties that are essential to design hydraulics programs for foam drilling operations.

One light foam system and two heavy foam systems were developed in our experimental studies. Formulations of the light foams are presented in **Table 6**. In the first heavy foam system are water-barite-base foams. Their formulations are shown in **Table 7**. The second heavy foam system includes brine-barite-base foams. Their formulations are also shown in **Table 7**. These foams were studied using our newly acquired instrument FOAMSCAN®.

Table 6: Formulations of light foams

Components					
Water Foam No.	**Barite (g)**	**Water (ml)**	**Xanthun Solution (ml)**	**QF (ml)**	**HC2 (ml)**
1	0	100	5	3	10
2	0	150	5	3	10
3	0	200	5	3	10

Table 7: Formulations of heavy foams

Components in Water-Barite Foams					
Water-Barite Foam No.	**Barite (g)**	**Water (ml)**	**Xanthun Solution (ml)**	**QF (ml)**	**HC2 (ml)**
1	50	200	5	3	10
2	100	200	5	3	10
3	150	200	5	3	10
Brine-Barite Foam No.	**Barite (g)**	**CaBr2 (ml)**	**Xanthun Solution (ml)**	**QF (ml)**	**HC2 (ml)**
1	100	200	5	3	10
2	150	200	5	3	10
3	200	200	5	3	10

Figure 14 shows foam volume development and retention of light foams. Their final Bikerman Index ranges from 257 to 261, indicating good foamability. As evidenced by the flat shape of curves after foam generations, these foams are very stable.

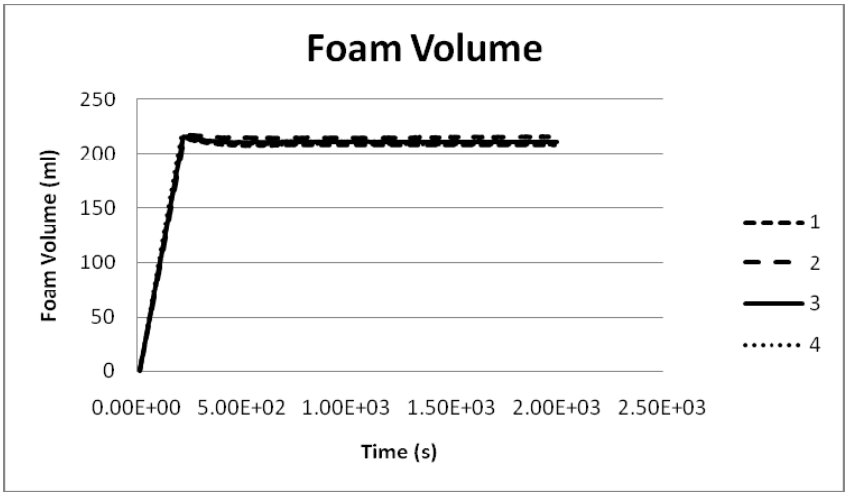

Figure 14: Volume development of light foams

Figure 15 shows foam volume development and retention of water-barite-base foams. Their final Bikerman Index ranges from 252 to 261, also indicating good foamability. Again, as evidenced by the flat shape of curves after foam generations, these foams are very stable.

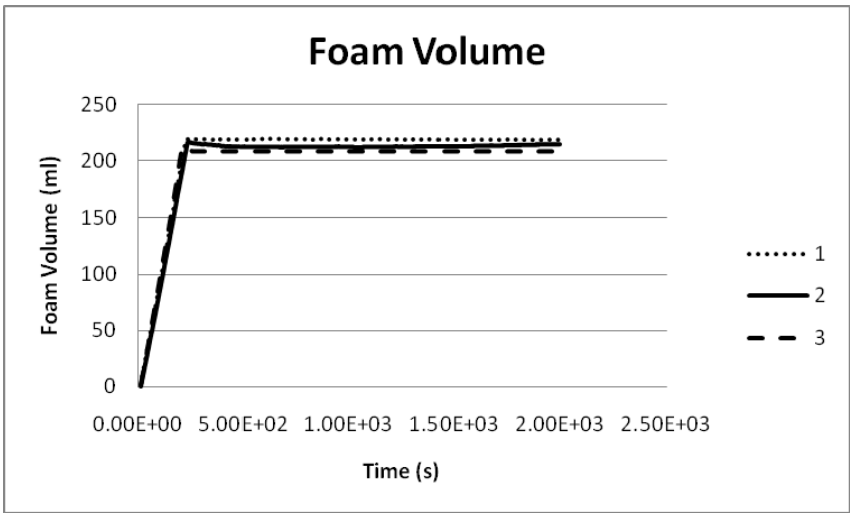

Figure 15: Volume development of water-barite-base foams

Figure 16 shows foam volume development and retention of brine-barite-base foams. Their final Bikerman Index ranges from 251 to 264, again indicating good foamability. However, as evidenced by the declining shape of curves after foam generations, these foams are less stable that the water-base and water-barite-base foams.

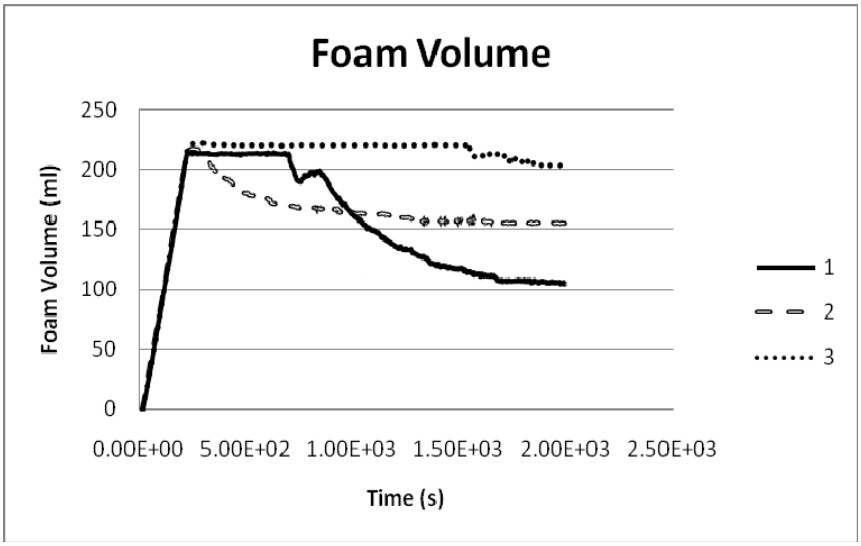

Figure 16: Volume development of brine-barite-base foams

Foam quality and stability were also analyzed using foam conductance data. **Figure 17** shows conductance of light foams. The peak conductance of these foams ranges from 400 to 1200. The collapse phase times for foam conductance to decrease by 50% are also marked in the graph. The collapse half-time ranges from 262 to 287 seconds. These values serve as a base for comparison with heavy foams.

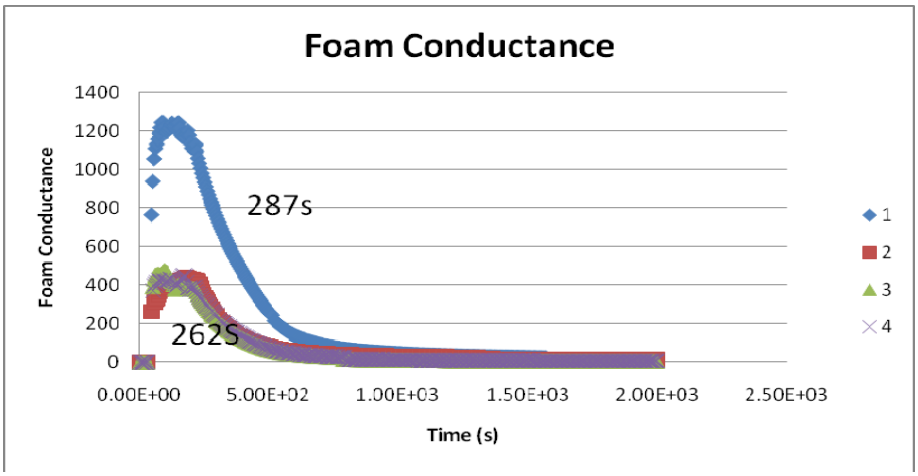

Figure 17: Conductance of light foams

Figure 18 presents conductance of water-barite-base foams. The peak conductance of these foams ranges from 2 to 18. The low conductance values mean high gas contents in the foams, or higher foam quality. The collapse half time ranges from 331 to 391 seconds, which are longer than the collapse half times of light foams, indicating that the water-barite foams have better stability than the light foams.

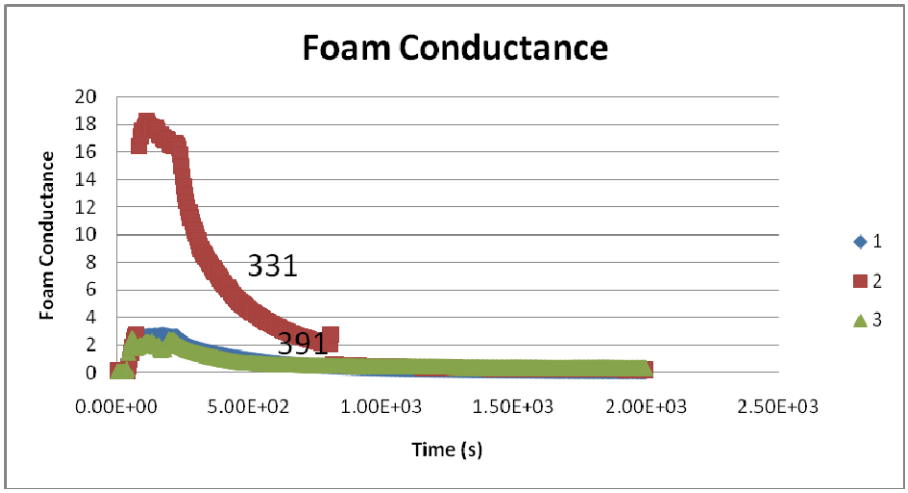

Figure 18: Conductance of water-barite-base foams

Figure 19 presents conductance of brine-barite-base foams. The conductance of these foams ranges from 7500 to 8500. The high conductance values are due to the high conductivities of brines. They do not mean low gas contents in the foams, or lower foam quality. The collapse half time ranges from 542 to 1339 seconds, which are much longer than the collapse half times of light foams and water-barite foams, indicating that the brine-barite foams have much better stability than the other two foam systems.

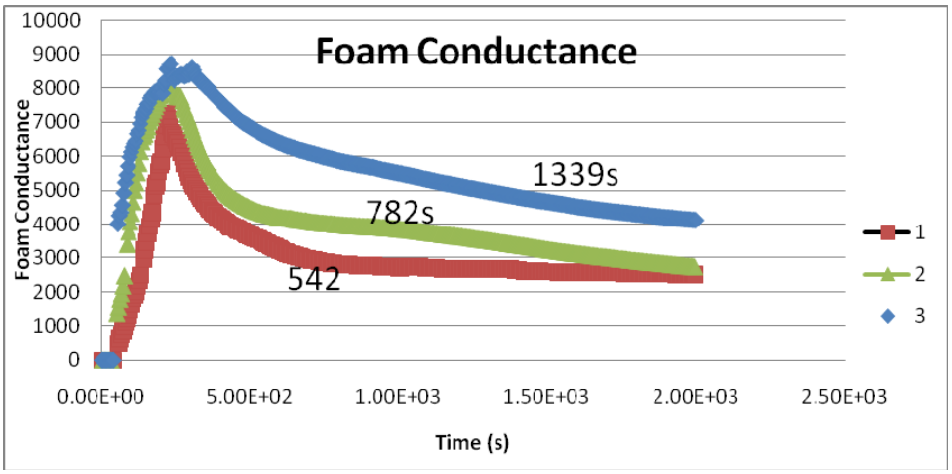

Figure 19: Conductance of brine-barite-base foams

Tables 8 and **9** summarize measured liquid density, foam density and foam quality of the three foam systems. A comparison of them shows that they have similar foam qualities about 80%, while the heavy foams did achieve higher foam densities up to 1 ppg.

Table 8: Density and quality of light foams

Water Foam No.	Liquid Density (ppg)	Foam Density (ppg)	Foam Quality (%)
1	8.23004	0.411502	81.52924919
2	8.2467	0.164934	79.94814175
3	8.33	0.2499	80.68902992
4	8.37998	0.418999	81.27376426

Table 9: Density and quality of heavy foams

Water-Barite Foam No.	Liquid Density (ppg)	Foam Density (ppg)	Foam Quality (%) (%)
1	9.7461	0.194922	79.84462667
2	10.81234	0.2162468	80.11744966
3	12.11182	0.2422364	79.38718663
Brine-Barite Foam No.	**Liquid Density (ppg)**	**Foam Density (ppg)**	**Foam Quality (%)**
1	15.51046	0.3102092	78.93589184
2	15.97694	0.6390776	81.48804252
3	17.20978	1.0325868	83.22324967

Furthermore, heavy foam research focused on 3-dimensional visualization (3DV) of foam flow in porous media. Research work includes processing image data to create 3DV of two-phase flow in the sand pack.

Water and nitrogen were injected into a sand pack. Two-phase flow was tested vertically and horizontally to observe liquid and gas distribution in the sand pack. X-Ray CT Scanning was used to identify nitrogen gas distribution in the pack. In each vertical experiment, 85 images of cross sections were taken for each combination of water and nitrogen flow rates. In each horizontal experiment, 300 images of cross sections were taken for each combination of water and nitrogen flow rates. Representative images were presented in the previous seasonal report. A typical 3DV of the images is shown in **Figure 20**. The following observations were made from the examining the 3DV of images:

1. Significant end-effect existed at both ends of the sand packs. The end-affected length is about 3.5 cm in the 4.45 cm inner diameter tube.
2. Gravity segregation effect in the horizontal flow experiments was not significant.

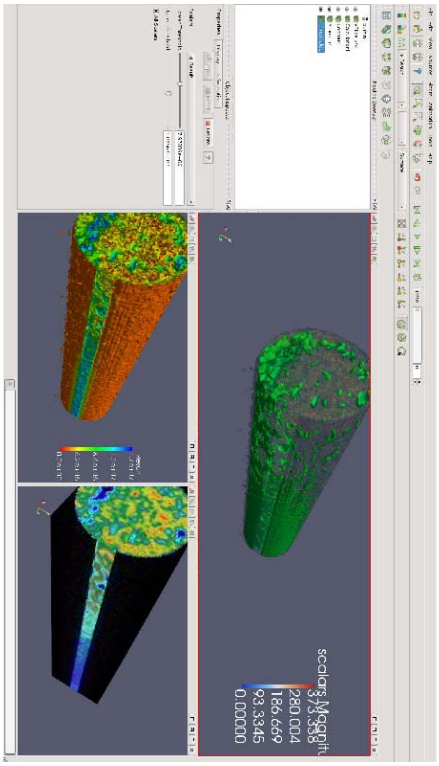

Figure 20: A 3DV of two-phase flow in porous media

Additionally, the heavy foam research focused on further investigations of heavy foam systems made from $CaBr_2$ solution and nitrogen. Research work includes formulae optimization of the heavy foams and comparison of $CaBr_2$-based foams and KCl-based foams. In total, 23 $CaBr_2$-based foam formulae and 3 KCl-based foam formulae were investigated. These foams were studied with instrument FoamScan. **Figure 21** shows conductance of four $CaBr_2$-based foams with low-concentration guar gum.

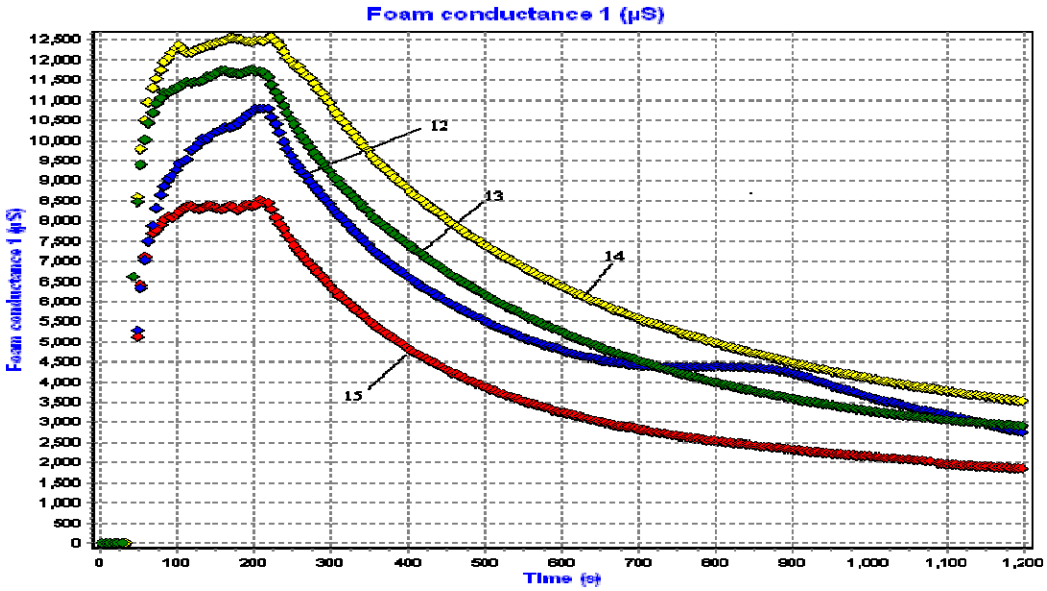

Figure 21: Conductance of four $CaBr_2$ -based foams (formulae 12, 13, 14, and 15)

The following conclusions were drawn from this study:

1. The best polymer used in the $CaBr_2$ -solution to generate heavy foam is guar gum. The optimum PV of guar gum is about 10 cp. It gives the optimum foam properties.
2. $CaBr_2$ -guar gum foams fall into the category of Bingham plastic fluid.
3. Heavy foams from $CaBr_2$ -solution and guar gum are better than the KCl-based foams in terms of stability, density, and rheological properties.

Besides, the heavy foam research focused on generating a guideline to design of drilling hydraulics with heavy foams for field applications. On the basis of feedback from the industry, we developed a special guideline for selecting flow-diverting joint (FDJ) in foam drilling operations using our foam hydraulics simulator.

System Design Procedure

Figure 22 illustrates a sketch of a Flow-Diverting Joint (FDJ). It is manufactured with multiple chambers for inserting nozzles of different sizes. These nozzles are exchangeable for obtaining desirable total area of flow.

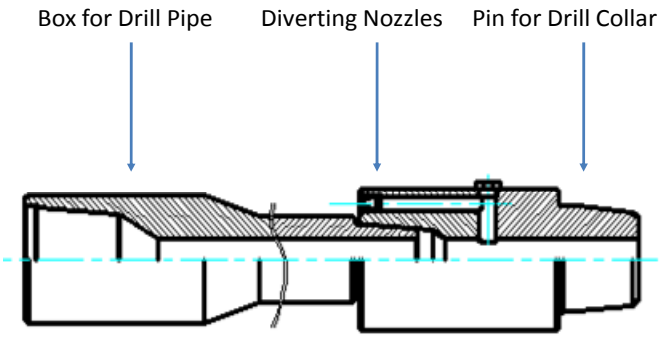

Figure 22: A sketch of Flow-Diverting Joint (FDJ)

Figure 23 shows a flow diagram in the foam drilling system with an FDJ installation at the drill collar shoulder. The total fluid injection rate in the drill pipe is divided into two streams, one toward the bottom hole through the drill bit and the other toward the drill pipe-openhole annulus through the nozzles of FDJ. The optimal area of FDJ nozzles can be designed so that the diverted flow of fluid through the FDJ nozzles will reduce the fluid KEI value in the drill collar-openhole annulus to a value similar to the value at the bottom of the drill pipe-openhole annulus.

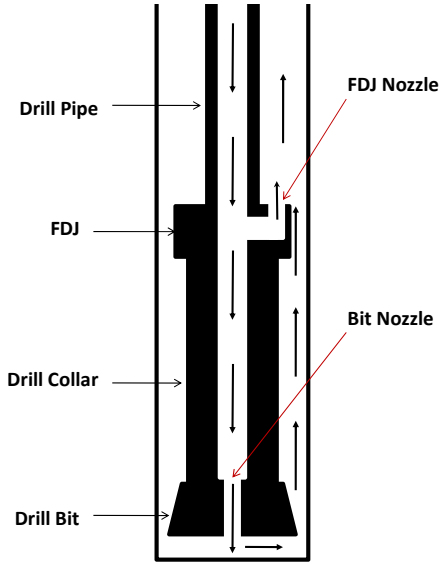

Figure 23: Flow diagram in the foam drilling system with FDJ installation

The FDJ nozzles should be selected using the following procedure:

1. For the given geological characteristics of the formations to be drilled with foam, planned borehole geometry, and drill pipe configurations, design the foam injection rate using the minimum kinetic energy criterion.
2. Calculate the annulus pressure at the bottom of the drill pipe-open hole annulus (downstream pressure of FDJ nozzles).
3. Predict the required gas flow rate at bottom hole based on the hole size and drill collar size using the minimum kinetic energy criterion.
4. Calculate the annulus pressure at the bottom hole.
5. Calculate the gas pressure above the bit nozzles based on the pre-selected bit nozzle sizes.
6. Calculate the pressure inside the drill collar at the FDJ depth (upstream pressure of FDJ nozzles).
7. Calculate the total area of the FDJ nozzles.

This procedure has been coded in our computer program for easy use to design foam drilling project. Use of the program is illustrated through the following example.

Illustrative Example

A well is to be drilled with nitrogen foam from 4000 ft to 8000 ft. Basic data are given in **Table 10**. The design task is to determine the required gas injection rate and the optimum FDJ nozzle area that will generate KEI value of 1.2 at the bottom of drill pipe-openhole annulus and bottom hole.

Figure 24 shows a calculated gas KEI profile at the drilling depth of 8000 ft without FDJ installation. This graph was generated by a computer program with gas injection rate of 1800 scfm. It indicates that the KEI values are 1.2 at the bottom of drill pipe-openhole annulus and 3.1 at bottom hole respectively. To reduce the gas KEI value at bottom hole from 3.1 to 1.2, the FDJ

module in the computer program was activated with a total nozzle area of 0.45 in^2. The resultant KEI profile is shown in **Figure 25**. The bypassed gas flow rate through the FDJ is 735 scfm.

It is desirable to know how the FDJ nozzle area is affected by the annular configuration. This knowledge can save field engineers' time in selecting FDJ nozzle size without running computer programs when annulus configuration changes. The effect of annulus configuration on the required FDJ nozzle area was investigated using annulus area ratio (AAR) and nozzle area ratio (NAR).

Using the same data given in the Application Example but different drill pipe/drill collar combinations, the NAR values for different AAR values were calculated using the computer program. The result is plotted in **Figure 26**, which indicates that the NAR is directly proportional to AAP for the 3 bit nozzles of No. 20. **Figure 27** presents the result obtained using 3 bit nozzles of No. 10. Again it shows that the NAR is directly proportional to AAP. This implies that, for a given set of drill collar and bit nozzles, the optimum FDJ nozzle area is proportional to the cross-sectional area of the drill pipe-openhole annulus.

Table 10: Base data for an application example

1) Well Geometry:		
Total measured depth:	8000	ft
Bit diameter:	7.875	in
9-5/8" casing inner diameter:	8.835	in
Casing depth:	4000	ft
4-1/2" drill pipe inner diameter:	3.643	in
or 5" drill pipe inner diameter:	4	in
5-3/4" drill collar inner diameter:	2.5	in
or 6-1/4" drill collar inner diameter:	3	in
Drill collar length:	250	ft
2) Material Properties:		
Specific gravity of rock:	2.7	water = 1
Specific gravity of gas:	1	air = 1
Gas specific heat ratio (k):	1.25	
Pipe roughness:	0.0018	in
Borehole roughness:	0.3	in
3) Operating condition:		
Surface choke/flow line pressure:	14.7	psia
Rate of penetration:	60	ft/hour
Rotary speed:	50	rpm
Bit orifices:	20	1/32nd in.
	20	1/32nd in.
	20	1/32nd in.
Maximum available gas injection rate:	2500	scfm
Kinetic energy index:	1.2	

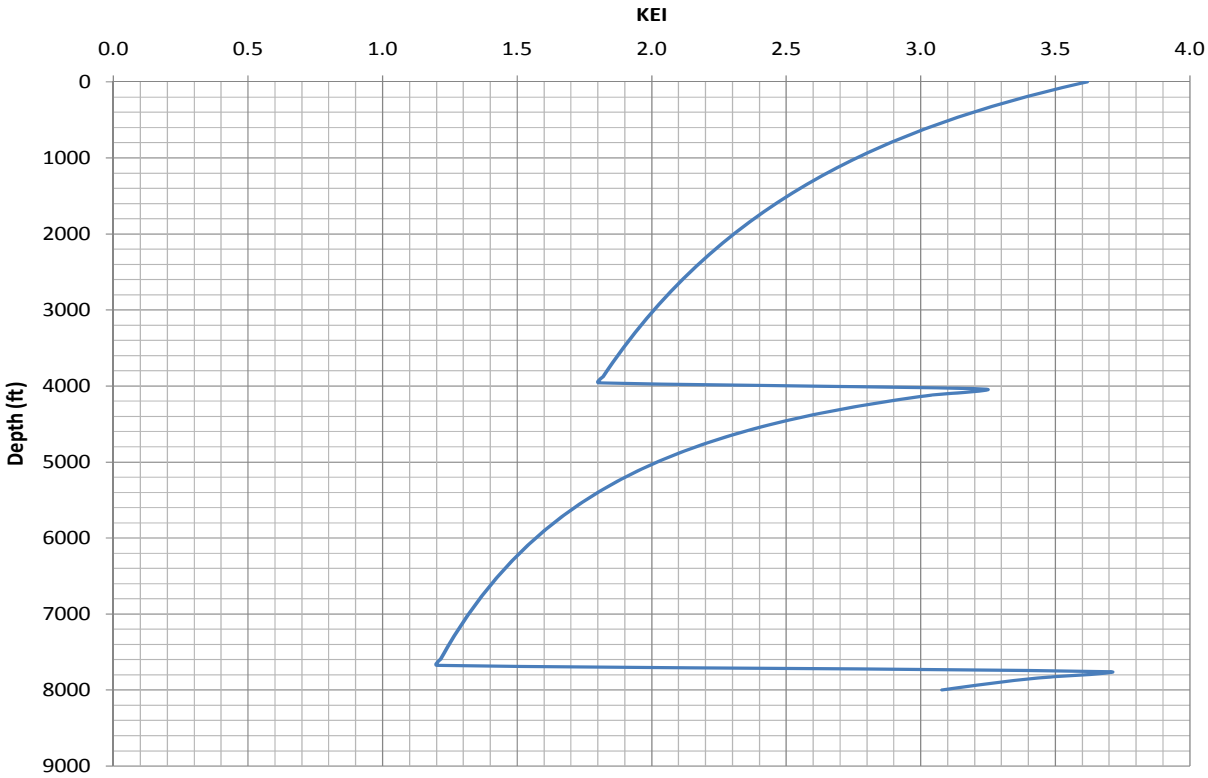

Figure 24: Kinetic energy index profile without FDJ (4-1/2” pipe and 6-1/4” collar)

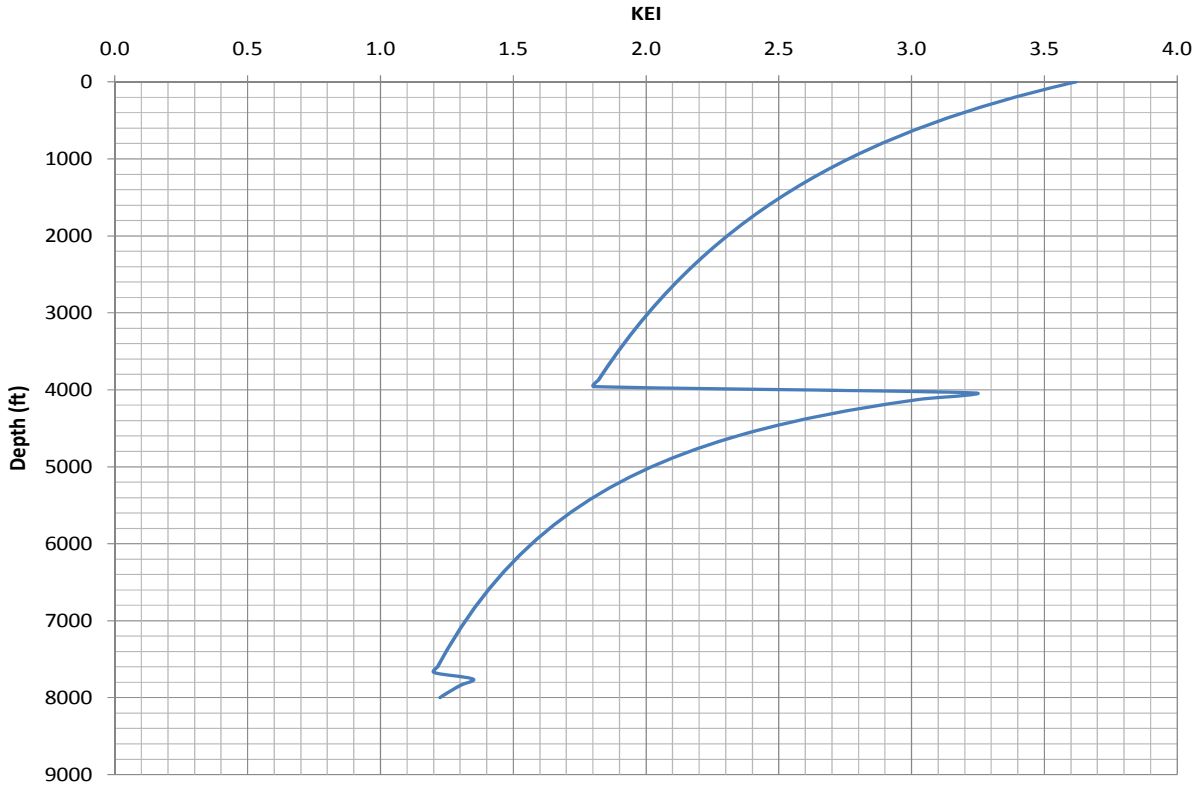

Figure 25: Kinetic energy index profile with FDJ nozzle area 0.45 in^2
(4-1/2” pipe, 6-1/4” collar, and 3x20 bit nozzles)

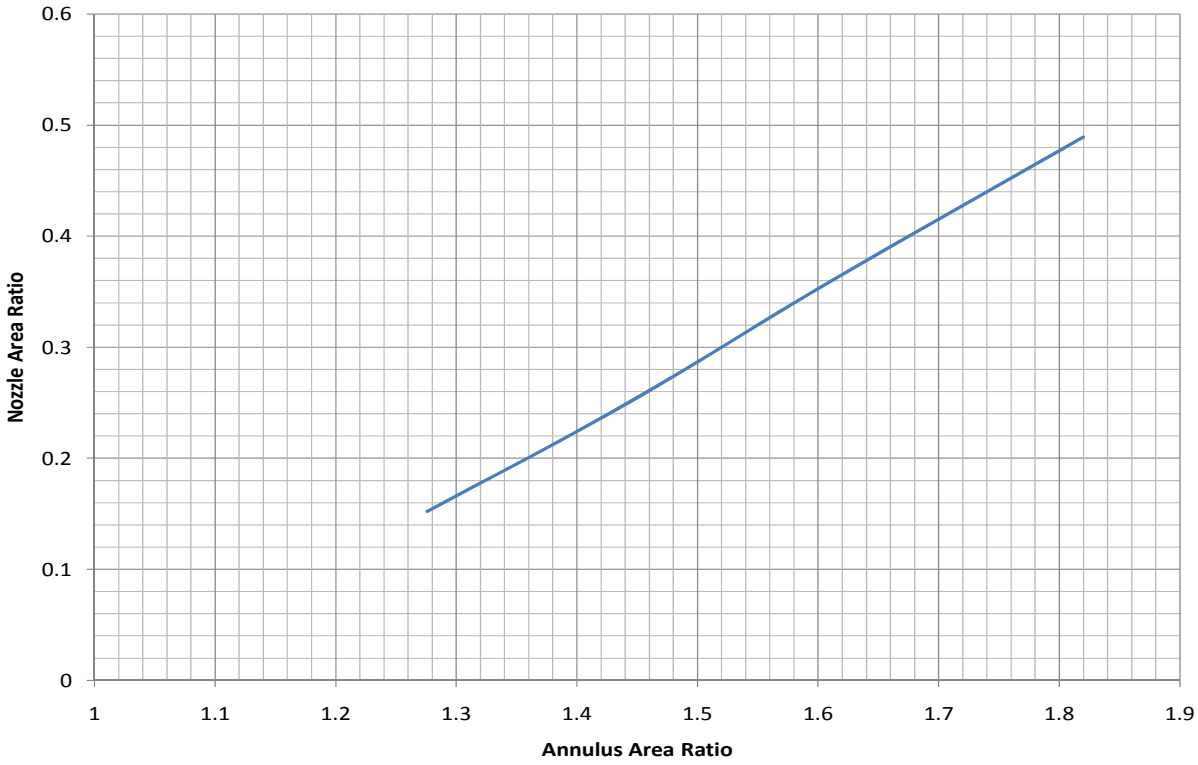

Figure 26: Relationship between nozzle area ratio and annulus area ratio (4.5" ~5" pipe, 5.75"~6.25" collar and 3x20 bit nozzles)

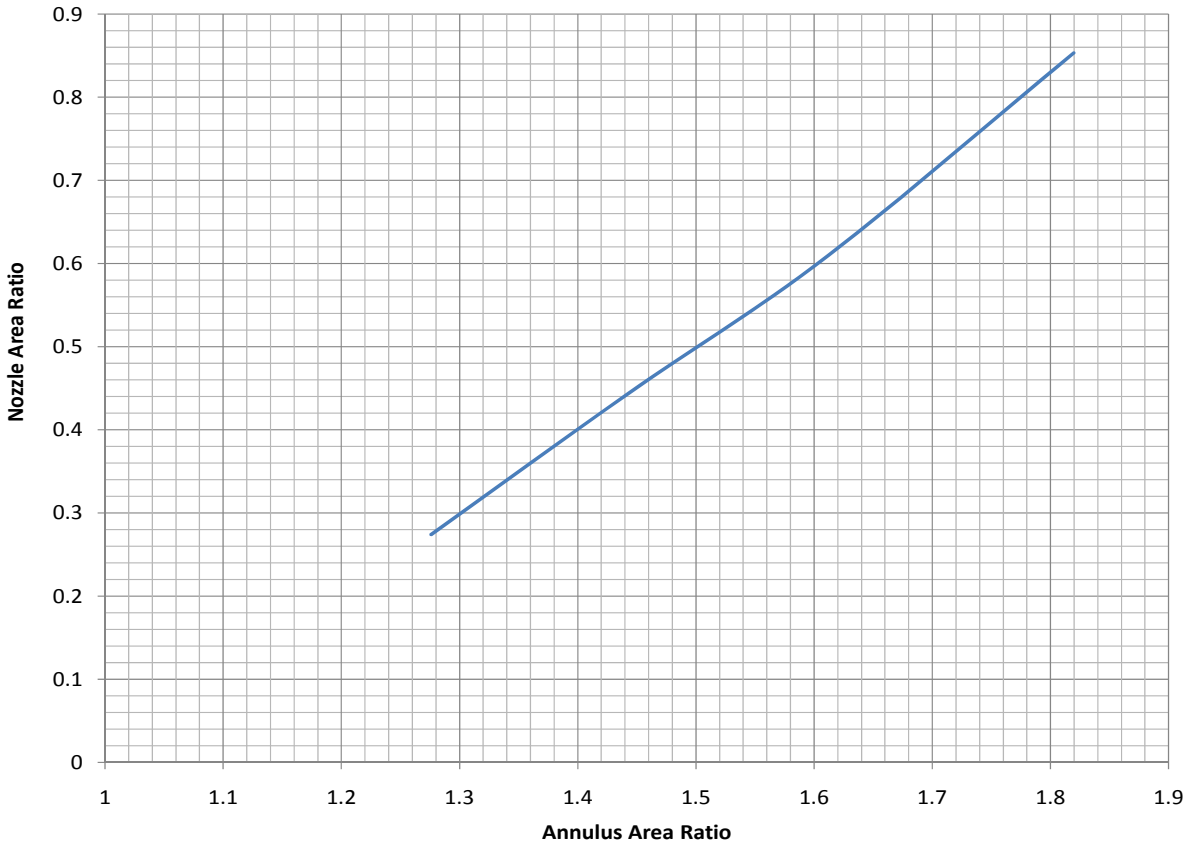

Figure 27: Relationship between nozzle area ratio and annulus area ratio (4.5" ~5" pipe, 5.75"~6.25" collar and 3x10 bit nozzles)

In addition, the heavy foam research focused on generating a guideline to design of drilling hydraulics with heavy foams for field applications. On the basis of feedback from the industry, we developed a special guideline for selecting flow-diverting joint (FDJ) in foam drilling operations using our foam hydraulics simulator.

The following procedure was developed for FDJ nozzles selection:

1. For the given geological characteristics of the formations to be drilled with foam, planned borehole geometry, and drill pipe configurations, design the foam injection rate using the minimum kinetic energy criterion.
2. Calculate the annulus pressure at the bottom of the drill pipe-openhole annulus (downstream pressure of FDJ nozzles).
3. Predict the required gas flow rate at bottom hole based on the well size and drill collar size using the minimum kinetic energy criterion.
4. Calculate the annulus pressure at the bottom hole.
5. Calculate the gas pressure above the bit nozzles based on the pre-selected bit nozzle sizes.
6. Calculate pressure inside drill collar at the FDJ depth (upstream pressure of FDJ nozzles).
7. Calculate the total area of the FDJ nozzles.

This procedure has been coded in our computer program for easy use to design foam drilling project.

Additionally, the heavy foam research focused on the effect of foam temperature on in-situ rock strength. We have developed a mathematical model to simulate the temperature profile in the rock in the near wellbore region. The developed mathematical model will be used for simulating thermal stress distribution in the formation rock to determine how rock strength changes during foam drilling. The final goal of this part of research is to gain insights of rock failure behavior so that engineers can design better foams and drill bits to improve drilling performance. The derived temperature model is summarized as follows.

The temperature profile in the rock can be analytically derived on the basis of heat conduction and the boundary condition at wellbore shown in **Figure 28**.

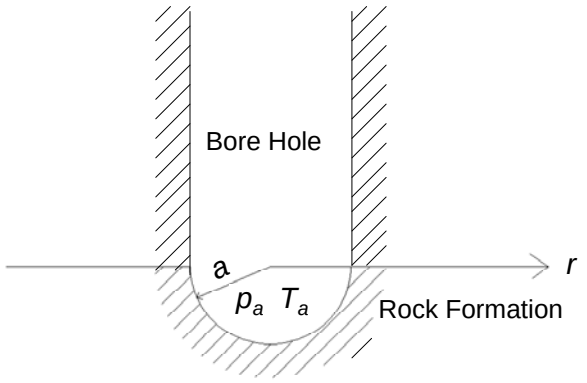

Figure 28: A sketch of borehole in formation rock

The resultant solution is expressed as:

$$T(r,t) = \frac{a}{r}(T_a - T_0)\,\mathrm{erfc}\left(\frac{r-a}{2\sqrt{\alpha t}}\right) + T_0$$

where,

T = temperature, °C
T_a = borehole temperature, °C
T_0 = in-situ rock temperature, °C
t = time, second
α = heat diffusivity coefficient, m^2/s

For $\alpha = 1.66 \times 10^{-6}\ m^2/s$, $T_0 = 110^\circ C$, $T_f = 48.15^\circ C$, and $a = 0.108\,m$, **Figure 29** shows the calculated transient temperature profiles given by the solution.

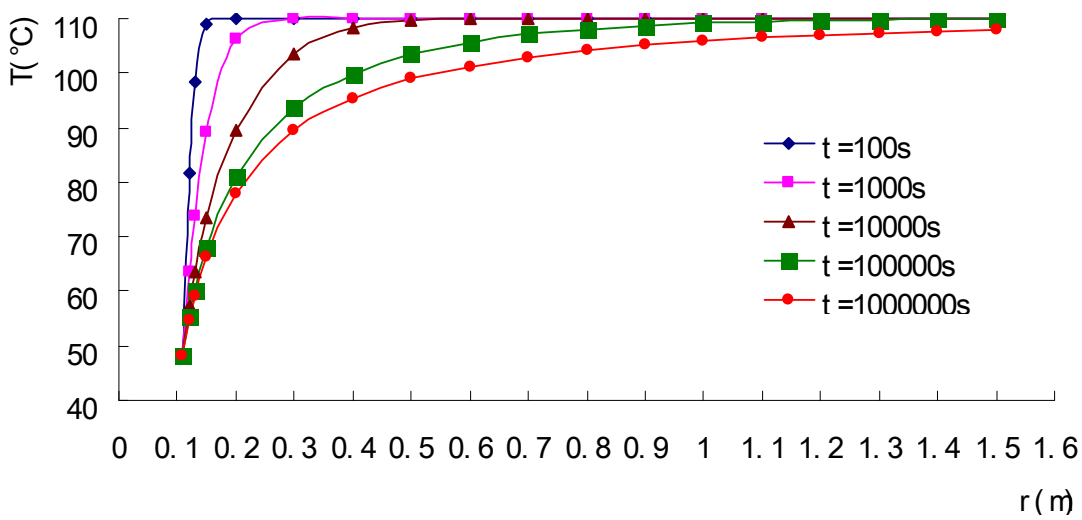

Figure 29: Calculated transient temperature profiles in the near borehole region

Furthermore, the heavy foam research focused on the effect of foam temperature on in-situ rock strength. We have applied the mathematical model developed in the last month to simulation thermal stress distribution in the formation rock to determine how rock strength changes during foam drilling. The final goal of this part of research is to gain insights of rock failure behavior so that engineers can design better foams and drill bits to improve drilling performance. The derived thermal stress model is summarized as follows:

$$\sigma_r^T = \frac{2\beta E}{1-\nu}\frac{1}{r^3}\int_a^r (T - T_0) r^2 dr$$

$$\sigma_t^T = \frac{2\beta E}{1-\nu}\left[\frac{1}{2r^3}\int_a^r (T - T_0) r^2 dr - \frac{1}{2}(T - T_0)\right]$$

where,

σ_r^T = temperature-induced radial stress, *MPa*
σ_t^T = temperature-induced tangential stress, *MPa*
β = thermal expansion factor, $1/^oC$
E = Young's modulus, *MPa*
ν = Poison's ratio.
T = temperature, °C
T_a = borehole temperature, °C

Application of the model requires numerical integration. Using E =35,000 MPa, ν=0.25, β=10^{-4} ^{o}C and the previous data presented in the last report, the thermal stresses were computed.

Figures 30 and **31** illustrate temperature-induced radial and tangential stresses, respectively.

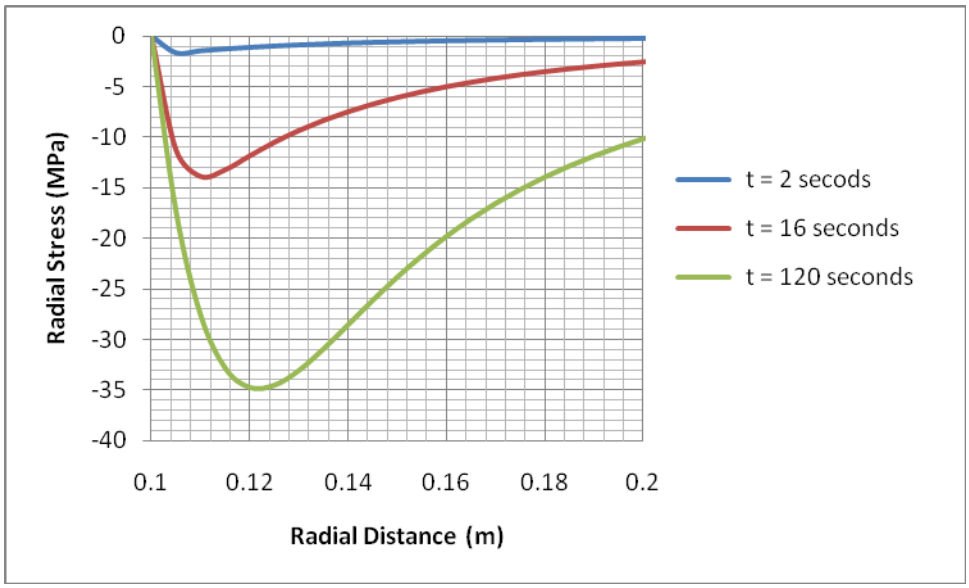

Figure 30: Calculated temperature-induced radial stress in the near bottomhole region

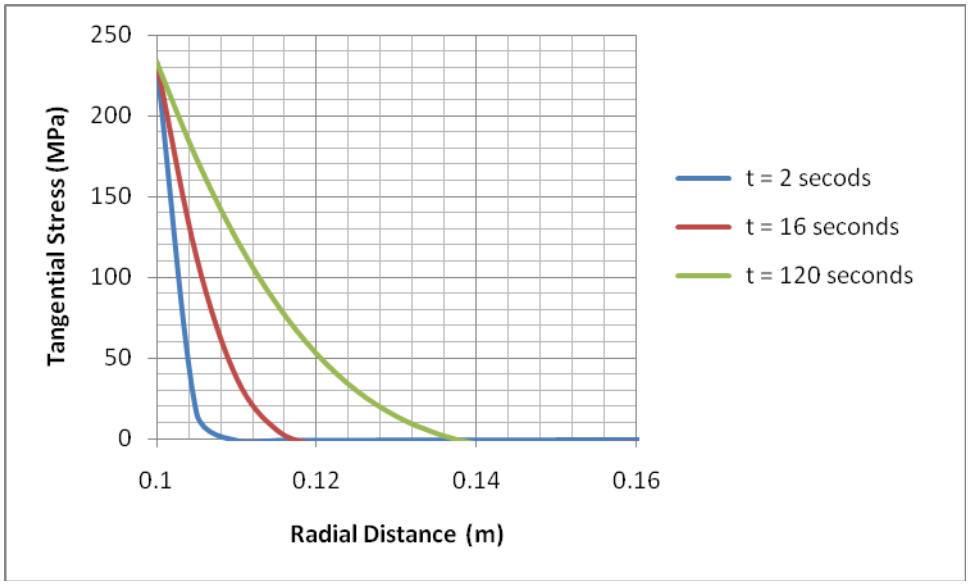

Figure 31: Calculated temperature-induced tangential stress in the near bottomhole region

Figure 30 implies that with a bottomhole temperature being less than the reservoir temperature, the thermal contraction will cause the compressive rock stress to decrease in the radial direction in the near bottomhole region. The figure also indicates an interesting behavior that the maximum reduction in radial stress occurs near the bottom hole, not at the bottom hole. This is due to the fact that the free surface at bottom hole allows the rock to deform without causing stress accumulation (boundary condition). The low stress region expands from the bottom hole with time and the rate of expansion slows down as the front propagates away from the bottom hole. The low stress region expands from 0.1m to 0.106m in the first 2 seconds, which gives the average speed of propagation of 0.003 m/s. The low stress region expands from 0.106m to 0.12m in the next 14 seconds, which gives the average speed of propagation of 0.0008 m/s.

Figure 31 indicates that with a bottomhole temperature being less than the average in-situ reservoir temperature, the rock stress is greatly increased in the tangential direction near the bottom hole.

CO2 TASK

Flue Gas Model Building, Testing, and Validation

A data bank of 15 different crude oil samples was provided by Southern Petroleum Laboratories. The samples are representative of Southern Louisiana reservoirs. Only 7 samples with high API gravities, mostly suited for flue gas studies, were retained. **Table 1**, below, summarizes sample composition, and API gravities. Heavy ends are lumped under C_{6+} fraction. In subsequent analysis, C_{6+} has to be defined in the component library as a pseudo-component with the molecular weight outlined in **Table 1**.

Table 1: Oil sample compositions (reported by Southern Petroleum Laboratories)

Component	A	B	C	D	E	F	G
CO_2	0.06	0.0	0.054	0.0	0.0	0.0	0.0
C_1	0.724	0.873	0.651	0.860	0.989	0.902	0.88
C_2	1.911	1.746	1.934	2.774	2.104	2.910	1.712
C_3	5.553	5.561	5.982	6.798	5.916	7.234	4.88
i-C_4	2.133	2.277	2.404	1.856	2.266	1.906	1.808
n-C_4	5.835	6.263	6.633	6.154	6.114	6.557	4.832
i-C_5	3.541	3.815	3.741	3.008	3.578	3.156	2.912
n-C_5	4.427	4.612	4.536	4.044	4.388	4.262	3.600
C_{6+}	75.816	74.853	74.065	74.506	74.645	73.073	79.376
C_{6+} Properties							
M.W.	247.53	234.56	224.38	243.80	222.17	260.61	187.30
API Gravity	37.3	39.7	40.9	36.0	41.3	37.0	40.9

Numerical simulation

A pressure-volume-temperature (PVTi) software, supporting the Schlumberger Eclipse 300 platform, was used to tune up the Peng-Robinson equation-of-state to a 10-component fluid system describing the laboratory measured oil properties and PVT data. Beside fluid composition, the input data for the flash experiment simulation were reservoir temperatures and pressures we chose for this study. The temperatures of 200, 288, and 375 ^{o}F and corresponding pressures of 2000, 2600, and 3200 psia are characteristic of reservoirs in South Louisiana. The percentage mole compositions of the oils (CO_2, C_1 to C_{6+}) were fed into the pure component library properties of the simulator. The molecular weight of the C_{6+} fraction had to be defined in the pure component library. The density, z-factor, and the critical properties were computed by the Lohrenz-Bray-Clark internal correlation.

Flash experiments

Flash experiments were done using the seven samples at in-situ reservoir conditions of temperature and pressure. The generated simulation results are measured using PVTi supporting software to Eclipse 300. Separator gas as a result of flash process has been considered as the injection gas. **Table 2** portrays the injection gas compositions.

Table 2: Injection gas composition

Component	Gas - FG1	Gas - FG2
N_2	0.85	0.70
CO_2	0.15	0.30

The flash experiments will be outlined in the next report along with other pertinent results.

Flash experiments have been executed. Among the 15 samples that have been previously selected for analysis, only 7 were used for flue gas testing. Pure component fingerprints indicated that only 7 samples differ in composition and that the remaining eight are duplicates (see **Figure 1**). Fingerprints indicated discrepancies in the composition of C1 (not obvious on **Figure 1**) and C6+ in most of the oil samples. These differences will surely affect the magnitude of the simulated minimum miscibility pressures. Variability in compositions of other components present in the oil samples like CO2, C2, C3, iC4, nC4, iC5, and nC5 was minimal. These will not affect the generated minimum miscibility pressure values.

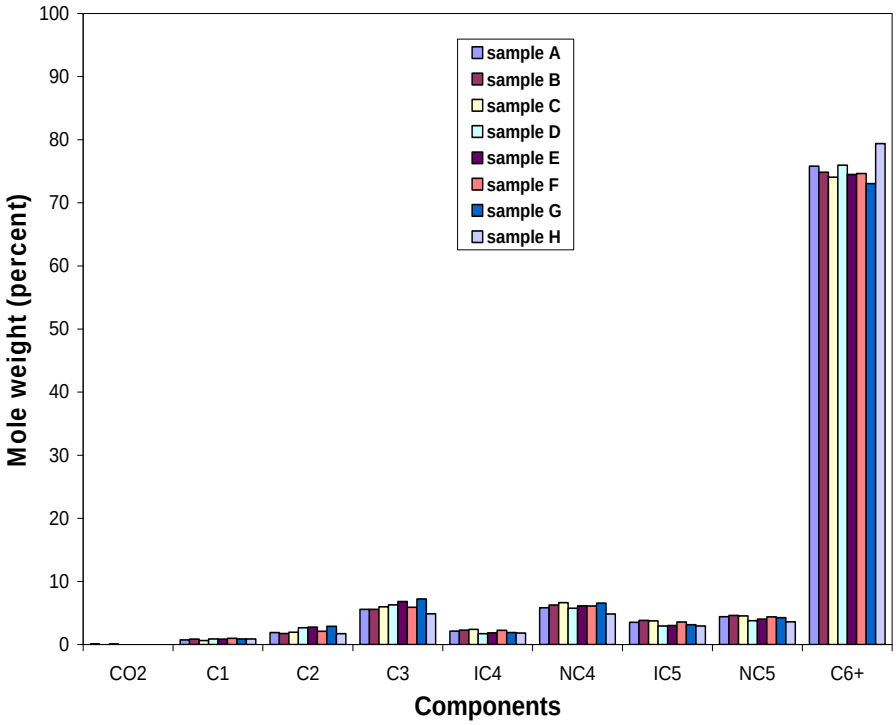

Figure 1: Samples' components and compositions

Table 3, below, depicts an example flash simulation calculation indicating that at reservoir conditions of temperature ranging between 200 and 375 ^{o}F and pressure ranging between 2000 and 3200 psia, composition of all pure components remain unchanged and that all pure components are in the liquid state.

Table 3: Example flash experiment composition (Sample A, API = 37.3°)

Components	200 °F & 2000 psia	288 °F & 2600 psia	375 °F & 3200 psia
CO2	0.06	0.06	0.06
C1	0.724	0.724	0.724
C2	1.911	1.911	1.911
C3	5.553	5.553	5.553
IC4	2.133	2.133	2.133
NC4	5.835	5.835	5.835
IC5	3.541	3.541	3.541
NC5	4.427	4.427	4.427
C6+	75.816	75.816	75.816
Sum	100	100	100

Table 4 shows some of the critical properties for sample A (API = 37.3°) obtained from a flash experiment at 200°F and 2000 psia using the ECLIPSE PVTi simulator. The critical properties of all components are well below reservoir pressure supporting the fact that oil sample is liquid in its entirety. Critical properties for the other six samples will be shown in the simulation data file that will be included in the final report.

Table 4: Critical properties obtained from flash calculation of Sample A

	CO_2	C1	C2	C3	IC4	NC4	IC5	NC5	C6+
P_c	72.9	45.44	48.2	41.9	36.0	37.47	33.45	33.26	14.31
T_c	304.7	190.6	305.4	369.8	408.1	425.2	460.4	469.6	769.3
M.W.	44.01	16.04	30.07	44.10	58.12	58.12	72.15	72.15	247.53

Simulation model description

The fluid samples' flash experiments were used as part of fluid PVT characterization in the generated slim tube data files. The data files were used in ECLIPSE 300, a fully-implicit compositional reservoir flow simulation package provided by Schlumberger, to simulate flue gas displacement experiments. The simulator accounts for interface mass transfer between all the phases present in the flue gas displacement process. The simulator model equations can track the movement of components constituting the oil-gas-water system as they move through the porous media. It is assumed that thermodynamic equilibrium exists at each grid block representing the model of the slim tube and the reservoir during simulation. The distribution of components between the gas and oil phases was obtained by performing flash calculation simulations at each reservoir condition; this allows the compositional model to account for the phase behavior effect in a multiphase system and the calculation of phase densities, viscosities and interfacial tension. The results of the flash calculation showed no distribution between the oil and gas phases and that there was no gas phase composition for any of the oil samples.

Slim tube experiment simulation

The slim tube was discretized with a 200-grid block system in order to accurately simulate multiphase flow and phase behavior taking into account temperature and pressure variation (see **Table 5**). This number of grid blocks was arrived at based on sensitivity analysis on cell dimensions and reflecting past slim tube simulation work in the literature. The selected size and number of grid blocks did not affect the quantitative displacement mechanism predictions. The porosity and absolute permeability values of the slim tube used were in accordance with the available data in the literature. It was assumed that the gas-oil capillary pressure was negligible (better describing

slim tube experiments' physics) and the only properties taken into consideration were the relative permeability data for the oil-water and gas-oil systems.

Table 5: Parameters for one-dimensional simulation of slim tube displacement

Type of grid block	Cartesian
# of grid blocks in x-direction:	200
# of grid blocks in y-direction:	1
# of grid blocks in z-direction:	1
Length of slim tube:	10m
Permeability:	2000md
Porosity:	10%
Water saturation:	0%
Flue gas injection:	Pressure controlled
Temperature:	200ºF, 288ºF, 375ºF
Pressure:	2000, 2600, 3200psi

Furthermore, slim tube simulation has been done. The water, gas, and oil relative permeability functional relationships used to mimic flue gas slim tube experiments and field simulation displacements are as depicted below:

For the oil-water system,

$$k_{rw} = k_{rwo}\left(\frac{S_w - S_{wcr}}{1 - S_{oirw} - S_{wcr}}\right)^{N_w}$$

$$k_{row} = k_{rocw}\left(1 - \frac{S_w - S_{wocn}}{1 - S_{wcon} - S_{orw}}\right)^{N_{ow}}$$

For the gas-oil system,

$$k_{rg} = k_{rgo}\left(\frac{S_g - S_{gcr}}{1 - S_{gcr} - S_{oirg} - S_{wcon}}\right)^{N_g}$$

$$k_{rog} = k_{rocg}\left(1 - \frac{S_g - S_{gocn}}{1 - S_{org} - S_{wcon} - S_{gcon}}\right)^{N_{og}}$$

Slim tube displacements using injection pressures ranging from 2000 psia to 3600 psia for oil samples A to G were conducted for each of flue gas; flue gas 1 (FG1; 15% CO_2/ 85 % N_2,) and flue gas 2 (FG2; 30% CO_2/70% N_2). These experiments were done under three conditions of temperature and pressure (Res.1, Res. 2, Res. 3). Res. 1 is for reservoir temperature of 200 ^oF and pressure of 2000 psia, Res. 2 is for reservoir temperature of 288 ^oF and pressure of 2600 psia, and Res. 3 is for reservoir temperature of 375 ^oF and pressure of 3200 psia. The oil samples were characterized as mentioned earlier by the Peng-Robinson equation of state and used in the flow simulator to mimic the slim tube displacement experiments. The simulated PVT data used to characterize the oil samples are limited to the data available and may not adequately capture the phase behavior of the flue gas-oil system. A key parameter in the design of a miscible

gas injection process is the minimum miscibility pressure (MMP). At that minimum pressure the local displacement efficiency is reported to approach 100%. Miscibility or complete mixing between the injected fluid and the displaced oil can be achieved at points of injection where oil is first contacted, at the gas-oil front, or somewhere in between.

To evaluate MMPs for all examined oil samples at aforementioned in-situ conditions characterizing candidate South Louisiana oil fields, lab-scale Eclipse data files are created in order to mimic slim tube experiments. Critical properties of the oil obtained from flash calculation as well as binary interaction coefficients, reservoir conditions of temperature and pressure, liquid and vapor fractions of the oil samples, rock properties, saturations, injection pressures and run time schedule were all input into the created data files. All factors were kept constant for each sample except for the injection pressure. Recovery factor sensitivity as a function of injection pressure was done in order to obtain MMPs for each tested sample.

The oil production totals at the beginning of the slim tube displacement test and at the end of the test are read from the summary data files created at the end of each soft experiment. The recovery is defined as the ratio between the oil volume produced and the oil volume fed to the slim tube, the sequence is repeated for several pressures and the recovery is recorded for each pressure. The recovery factor was then plotted against the each injection pressure to determine the minimum miscibility pressure. **Figures 2** to **8** below are illustrations of the recoveries for all the examined oil samples as a function of their injection pressures. The minimum miscibility pressure for each oil sample is read as the curve inflection point or the point at which there is no significant change in recovery as pressure increases.

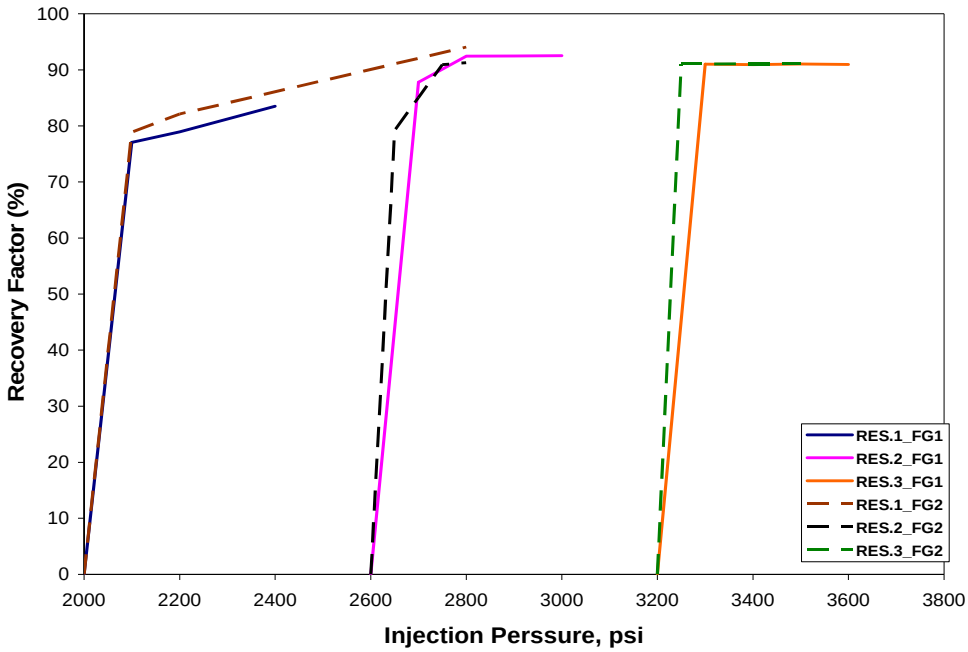

Figure 2: Slim tube recovery factor and injection pressure for sample A, 37.3ºAPI

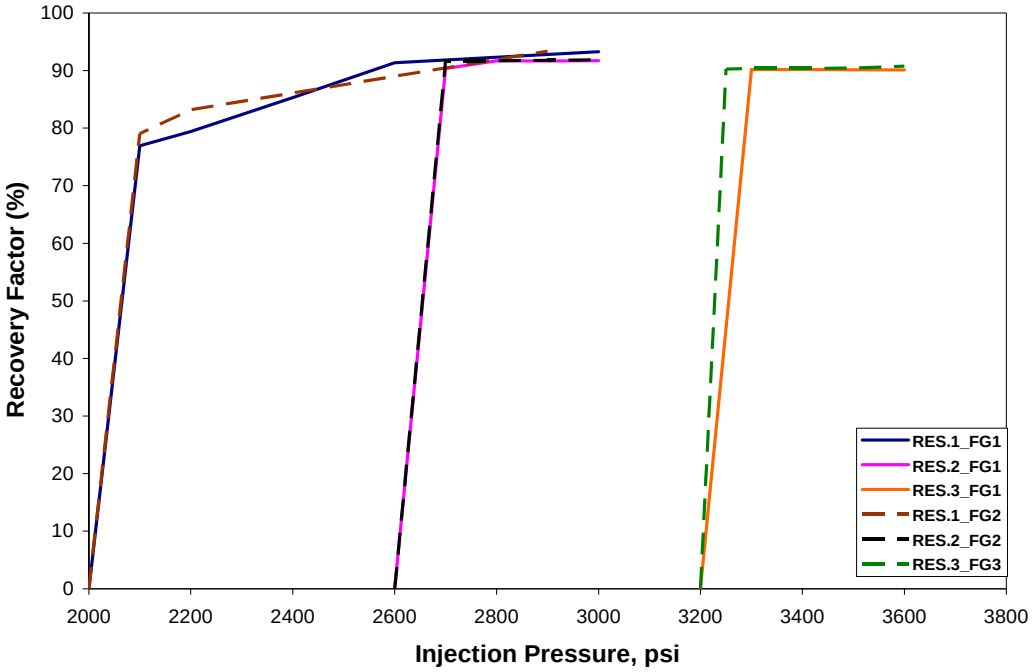

Figure 3: Slim tube recovery factor and injection pressure for sample B, 39.7ºAPI

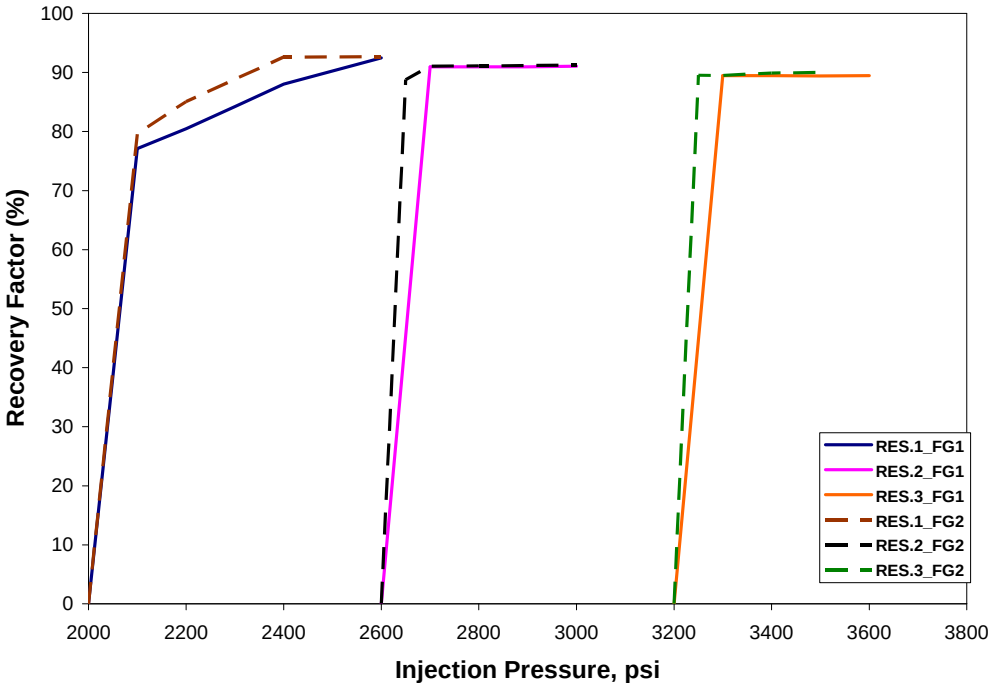

Figure 4: Slim tube recovery factor and injection pressure for sample C, 40.9ºAPI

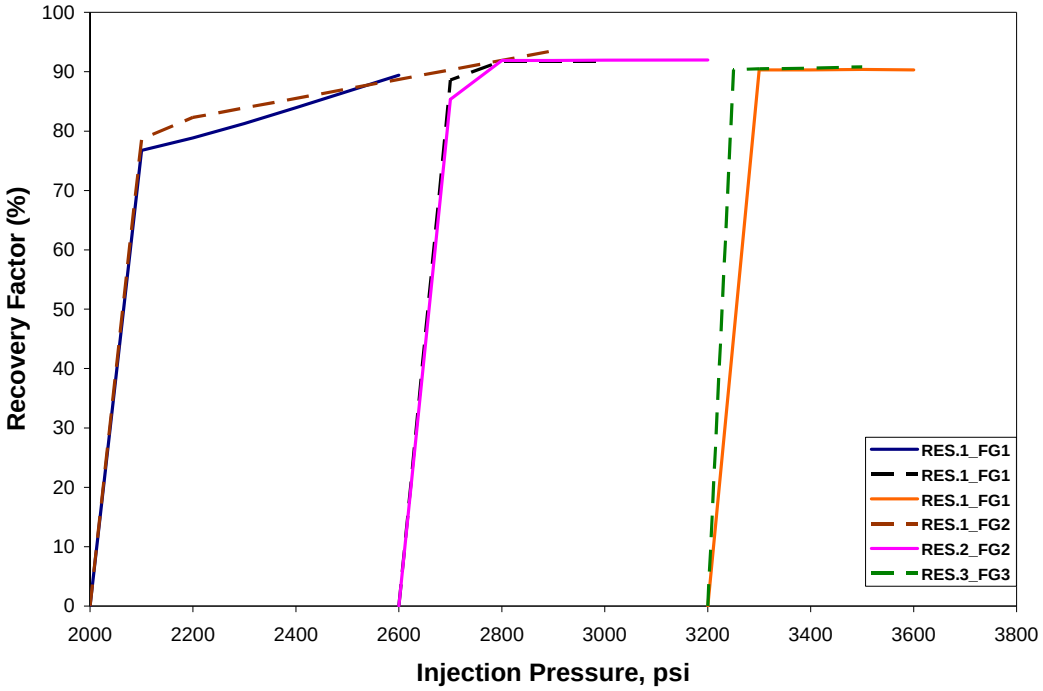

Figure 5: Slim tube recovery factor and injection pressure for sample D, 36.0ºAPI

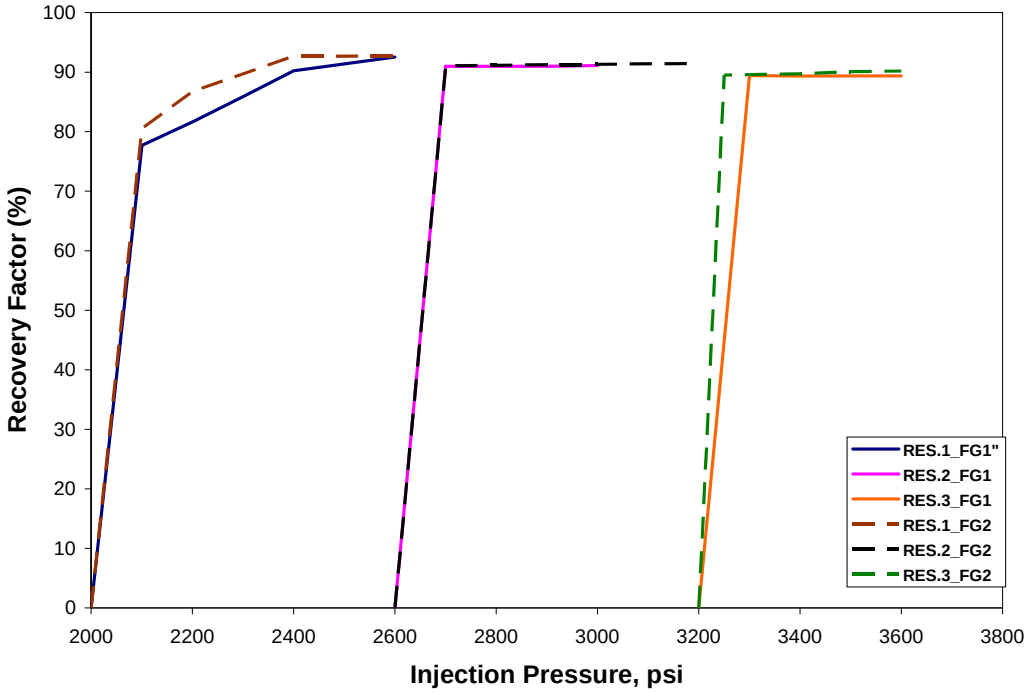

Figure 6: Slim tube recovery factor and injection pressure for sample E, 41.3ºAPI

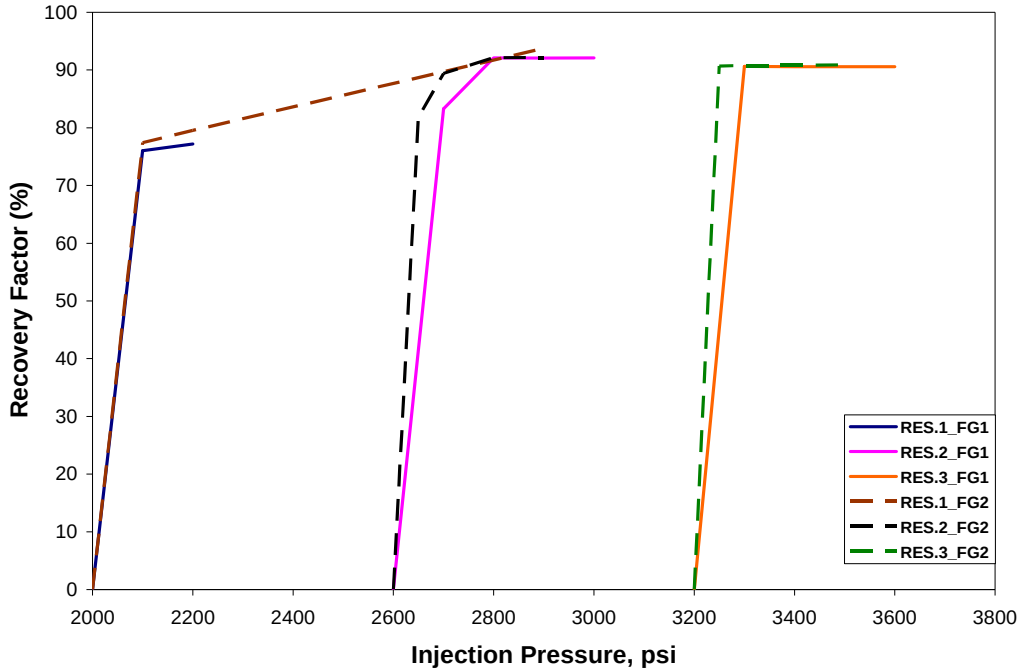

Figure 7: Slim tube recovery factor and injection pressure for sample F, 37.0ºAPI

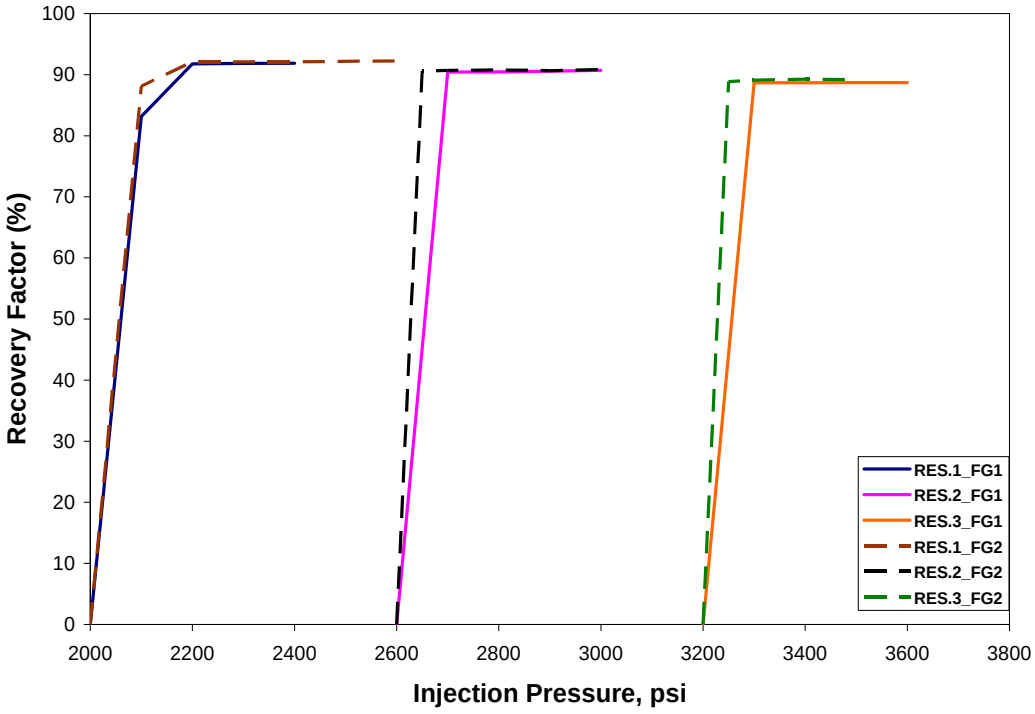

Figure 8: Slim tube recovery factor and injection pressure for sample G, 40.9ºAPI

Table 6 (below) summarizes MMPs for samples A-G under selected temperatures and pressures.

Table 6: MMP for flue slim tube simulations

	(200 °F, 2000 psi)		(288 °F, 2600 psi)		(375 °F, 3200 psi)	
	FG -1 MMP (psi)	FG – 2 MMP (psi)	FG -1 MMP (psi)	FG – 2 MMP (psi)	FG -1 MMP (psi)	FG – 2 MMP (psi)
A	2900	2200	2800	2740	3300	3250
B	2600	2200	2720	2700	3300	3240
C	2400	2400	2700	2700	3300	3250
D	2600	2250	2800	2700	3300	3250
E	2400	2400	2700	2700	3300	3250
F	2150	2100	2800	2700	3300	3250
G	2200	2200	2700	2650	3300	3270

Minimum miscibility pressure correlation results have produced. Most of the available MMP correlations are developed for lean gases, hydrocarbon gases, and CO_2 flooding. Firoozabadi *et al*. and Glasø correlations can be applied to flue gases. **Tables 7** and **8** portray the predicted minimum miscibility pressure using the Glasø and Firoozabadi correlations. Glasø correlation predicts that sample F will require the highest MMP for different in-situ temperatures of 200 °F, 288 °F, and 375 °F. That is attributed to the fact that of all samples, sample F has the highest molecular weight. Sample G required the lowest pressure due to the fact that it has the lowest molecular weight.

Table 7: Predicted MMP using Glasø correlation

T (°F)	A	B	C	D	E	F	*G*
200	2999	2872	2775	3009	2750	**3321**	*2464*
288	4349	4152	3999	4364	3958	**4846**	*3486*
375	5683	5416	5208	5704	5153	**6353**	*4496*

Table 8 represents the predicted results using Firoozabadi *et al*. correlation. Like Glasø, Firoozabadi *et al*. predicted sample F to have the highest MMP but calculated sample C to have the lowest minimum miscibility pressure.

Table 8: Predicted MMP using Firoozabadi *et al* correlation

T (°F)	A	B	C	D	E	F	G
200	5724	5508	5279	5591	5449	5660	5432
288	5981	5773	5551	5853	5716	5919	5700
375	6160	5958	5743	6036	5903	6101	5888

The only parameters used in Firoozabadi *et al*. correlation for a vaporizing-drive mechanism are the amount of intermediates, oil volatility, and reservoir temperature. The correlation doesn't account for varying injection gas compositions and was considered to overestimate MMP by a number of authors.

Comparison of slim tube simulation MMPs and correlations MMPs

This study's numerical simulation approach is based on the Peng-Robinson equation of state (EOS) model. The advantage of using EOS is that it is a self consistent method and can be easily tuned to available experimental data. The Glasø correlation was mostly developed from experimental slim tube MMP data of North Sea gas/oil systems, but the reservoir fluids and conditions used in this study are typical of South Louisiana. This could explain the source of discrepancy between the two methods; Glasø correlation which is only based on molecular weight and temperature and does not particularly consider mole percent of intermediates is not as accurate as the generated compositional simulator MMPs. The composition of the injection gas is said not to affect the pressure at which miscibility is achieved. That is not the case since MMP decreases when flue gas with a higher CO_2 concentration is injected.

The following bar graphs (**Figures 9** through **14**) are to illustrate comparison done between slim tube simulation MMPs and Glasø and Firoozabadi MMPs. Graphs show that Glasø underestimates MMPs for low temperatures and Firoozabadi MMPs is temperature insensitive and tends to always overestimates MMPs.

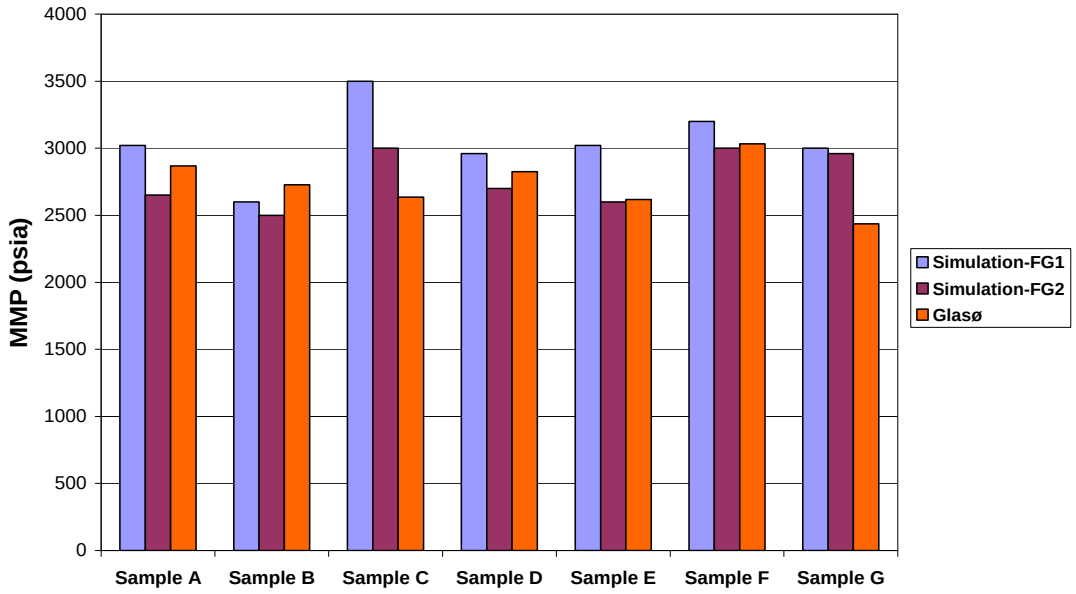

Figure 9: Glasø correlation comparison at 200ºF

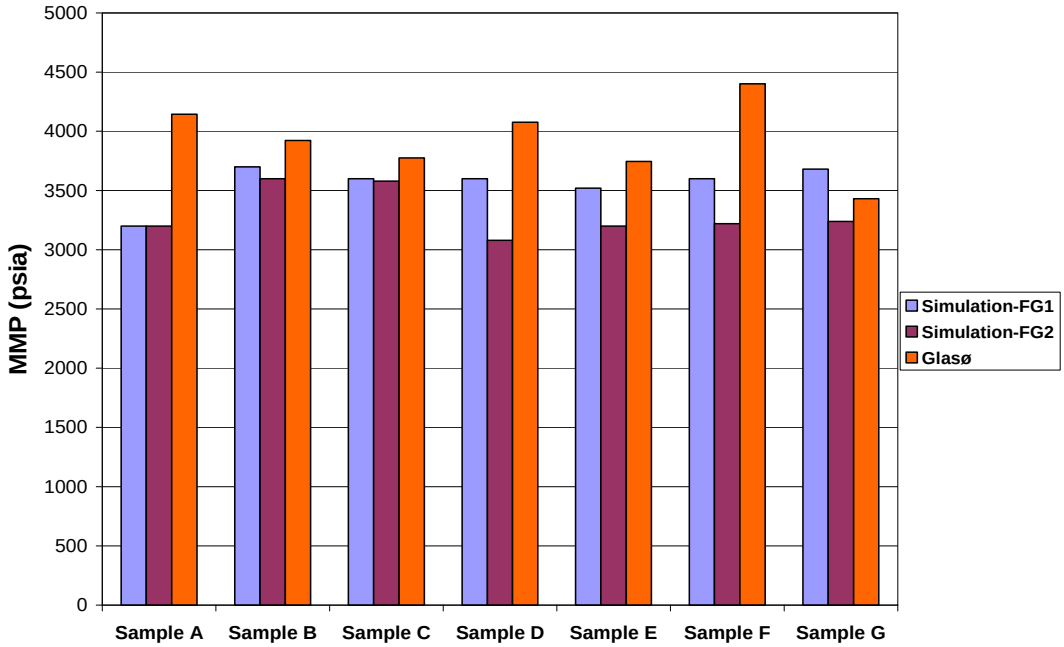

Figure 10: Glasø correlation comparison at 288ºF

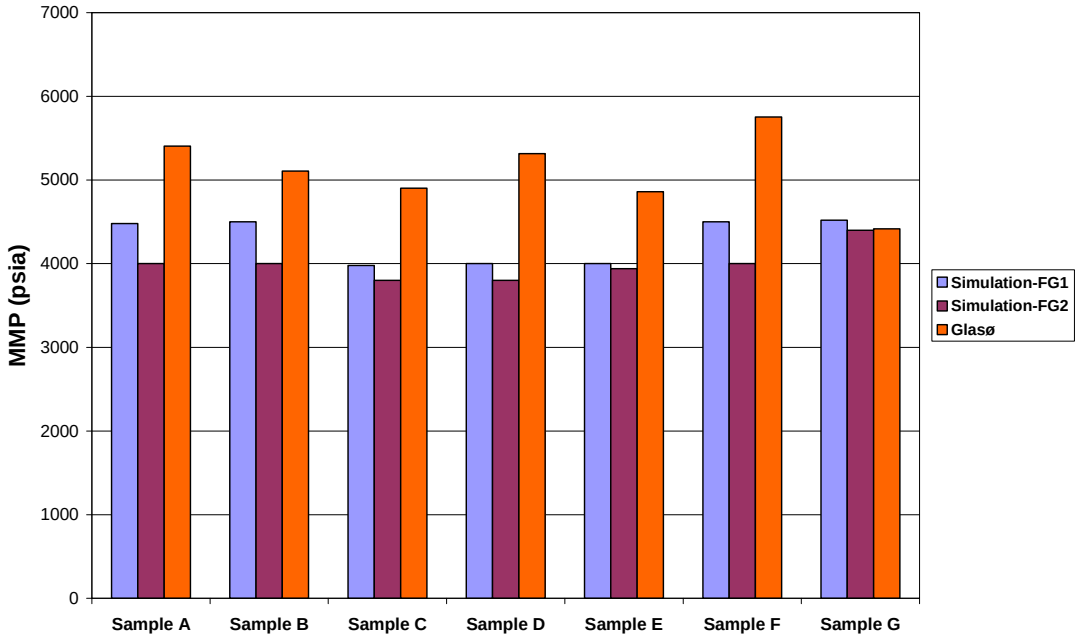

Figure 11: Glasø correlation comparison at 375ºF

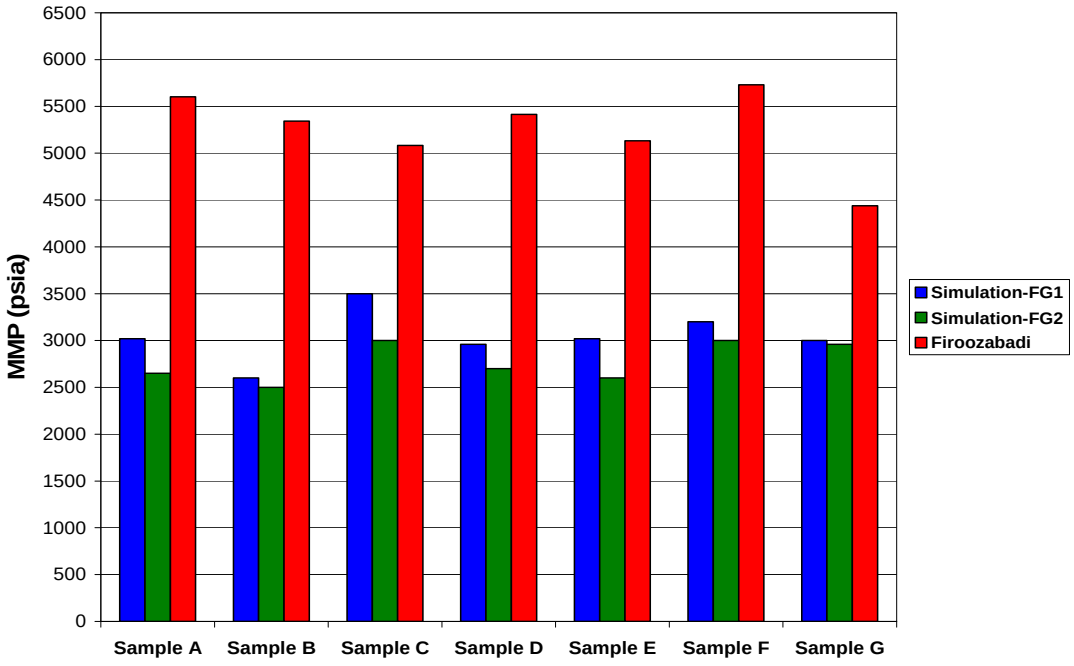

Figure 12: Firoozabadi correlation comparison at 200ºF

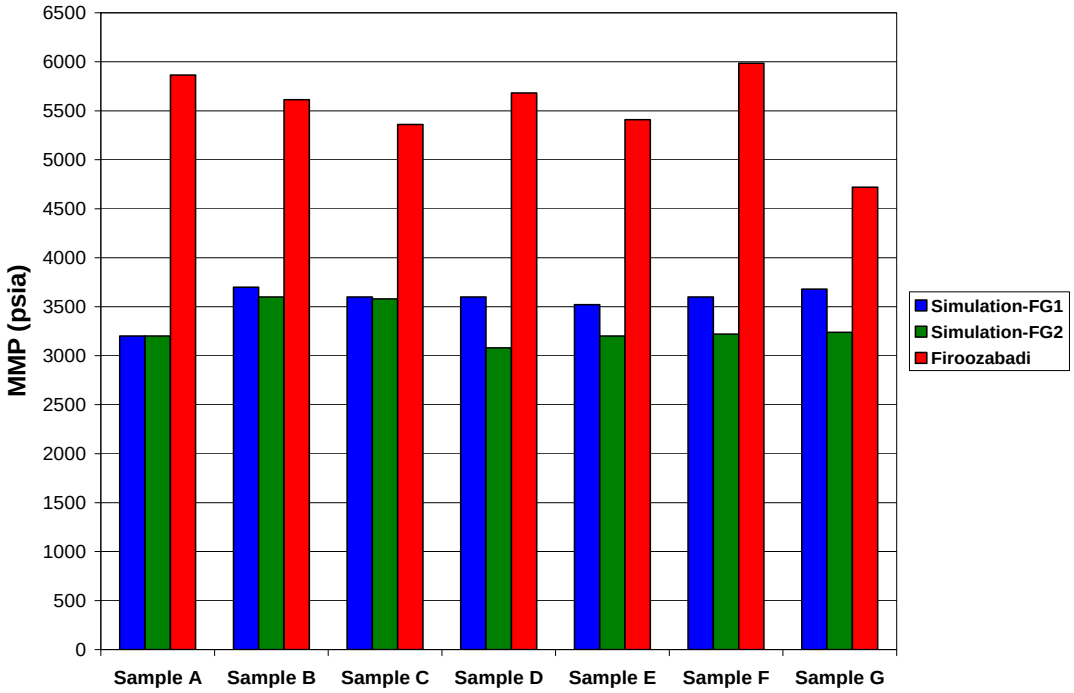

Figure 13: Firoozabadi correlation comparison at 288ºF

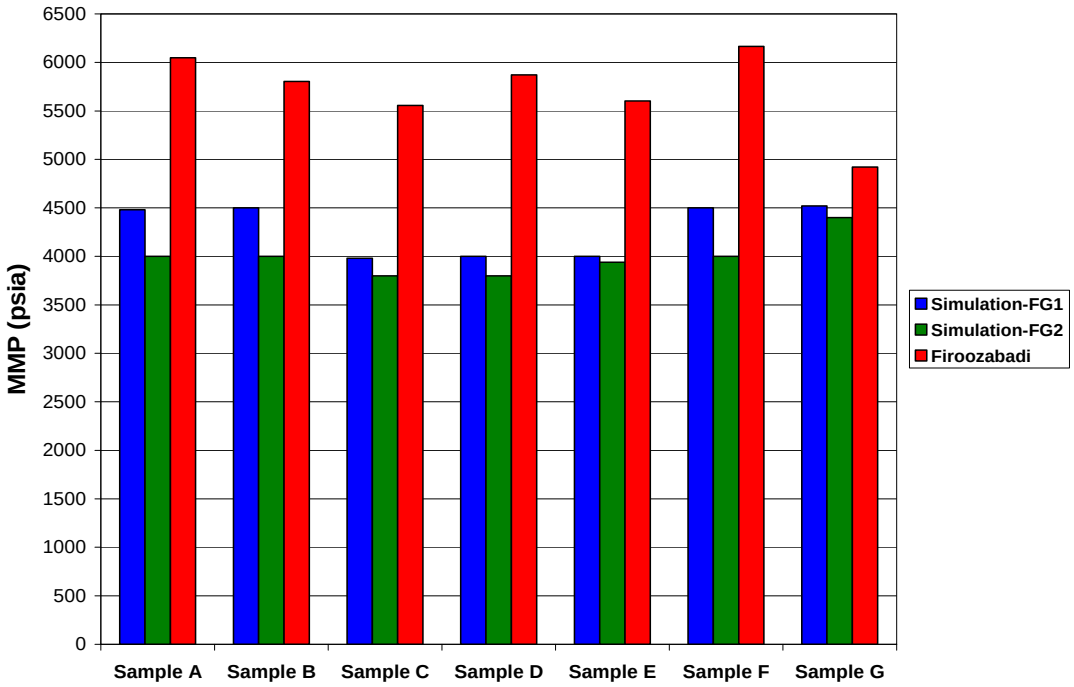

Figure 14: Firoozabadi correlation comparison at 375ºF

Table 3 illustrates the comparison of simulation MMP and Glasø and Firoozabadi MMPs for all the seven samples. Glasø MMP is strongly dependent on reservoir temperature and that is evident since MMP values increase as temperature increases. The Glasø MMPs are lower than those predicted Firoozabadi *et al.* correlation, but a little higher than simulations MMPs. Simulations MMPs and Glasø are closer at lower reservoir temperature of 200 ^{o}F but depart from each other at higher in-situ temperatures of 228 and 375 ^{o}F. Firoozabadi and simulation MMPs did not compare and are very far apart. It is suggested not to bank on MMP published correlations and to use compositional simulation generated MMPs in the absence of experimental measurements or for validation purposes.

Table 3: Comparison of slim tube simulation MMPs and correlations MMPs

SAMPLE A			
T (°F)	Simulation FG-1	Glasø	Firoozabadi
200	3020	2999	5604
288	3200	4349	5865
375	4480	5683	6047
SAMPLE B			
T (°F)	Simulation FG-1	Glasø	Firoozabadi
200	2600	2872	5342
288	3700	4152	5613
375	4500	5416	5803
SAMPLE C			
T (°F)	Simulation FG-1	Glasø	Firoozabadi
200	2500	2775	5084
288	2960	3999	5360
375	3980	5208	5557
SAMPLE D			
T (°F)	Simulation FG-1	Glasø	Firoozabadi
200	2960	3009	3539
288	3600	4364	3750
375	4520	5704	3923
SAMPLE E			
T (°F)	Simulation FG-1	Glasø	Firoozabadi
200	3000	2750	5133
288	3520	3958	5409
375	4000	5153	5604
SAMPLE F			
T (°F)	Simulation FG-1	Glasø	Firoozabadi
200	3000	3321	5730
288	3600	4846	5986
375	4500	6353	6165
SAMPLE G			
T (°F)	Simulation FG-1	Glasø	Firoozabadi
200	3000	2464	4439
288	3680	3486	4719
375	4520	4496	4923

Field-scale miscibility performance

The term miscible recovery is defined as any oil recovery displacement mechanism, where the phase boundary or interfacial tension between the displaced and displacing fluids is negligible. In this situation the capillary number becomes infinite and the residual oil saturation can be reduced to the lowest possible value because there is no interfacial tension (IFT) between the fluids. The miscibility option is imposed in the data file; it requests a miscible treatment of hydrocarbon relative permeabilities and capillary pressures by activating dependence of relative permeability and capillary pressure on surface tensions according to the PARACHOR values. The adopted arbitrary reference surface tension is 90 dyne/cm. Eclipse assigns this value for grid blocks containing a single phase. Therefore, the immiscibility factor equals to unity. The immiscibility factor approaches to zero for grid blocks containing two phases. It becomes zero when two phases form a single phase and become fully miscible. Injection of cost-effective flue gases could be employed in reservoirs where a favorable combination of pressure, reservoir characteristics and

fluid properties make the gas injection project a competitive process compared to other secondary oil recovery methods. However, for a gas injection project, to be competitive several conditions should be satisfied. The incremental oil recovery is largely dependent on injection pressure, reservoir characteristics and fluid properties such as homogeneity, capillarity, gravity segregation. A parametric study is done, using a compositional simulator to analyze the effect of such important parameters in miscible performance recovery from the reservoir.

Field simulation description

A brief description of the reservoir model is given in the **Table 4** below. Adaptive implicit solution avoids the time step restrictions imposed by small blocks and minimizes the computational expense of a fully implicit solution. The layers are homogenous and of constant porosity, permeability, and thickness. Saturation and PVT data of the reservoir fluid are provided in **Table 4** and in PROPS section of the developed simulation data file. The reservoir conditions of temperature and pressure considered in the field study are the same as those used in the slim tube displacement experiments. The same reservoir fluids are used; however, the flash experiments are re-run using field units. The reservoir oil gravities are presented in previous reports. The water viscosity is 0.56 cp at initial reservoir conditions. Initial oil and water saturations are 0.85 and 0.15, respectively. The flue gases, having the same compositions as stated in previous reports, are injected continuously into the reservoir.

Table 4: Reservoir grid data

NX =100, **NY** = 1, **NZ** =5 **DX** = 40 ft, **DY** = 1000 ft, **DZ** = 41 ft **Porosity** 0.18 **Datum (subsurface), ft** 8073 **Water - Oil Contact, ft** 10000 **Gas – Oil Contact, ft** 8000 **Capillary pressure at contact, psi** 0 **Oil Saturation** 85%					
P (psi)	**T (°F)**	**Perm. (mD)**		**Thickness (ft)**	**Depth to top (ft)**
2000	200	0.5	30	41	8268
2600	288	60	150	41	8268
3200	375	90		41	8268
Water Properties					
Compressibility (psi^{-1})			3.2792×10^{-6}		
Density (lb/ft^3)			62.4280		
Viscosity (cp)			0.56		
Rock Compressibility (psi^{-1})			4.0×10^{-6}		

Constant injection pressure is the only constraint applied to the injection well.

Figures 7 through **13** portray oil recovery factor as a function of flue gas injection under different reservoir conditions of temperature and pressure for flue gases 1 and 2. The results of the soft MMP experiments are summarized in **Table 5**.

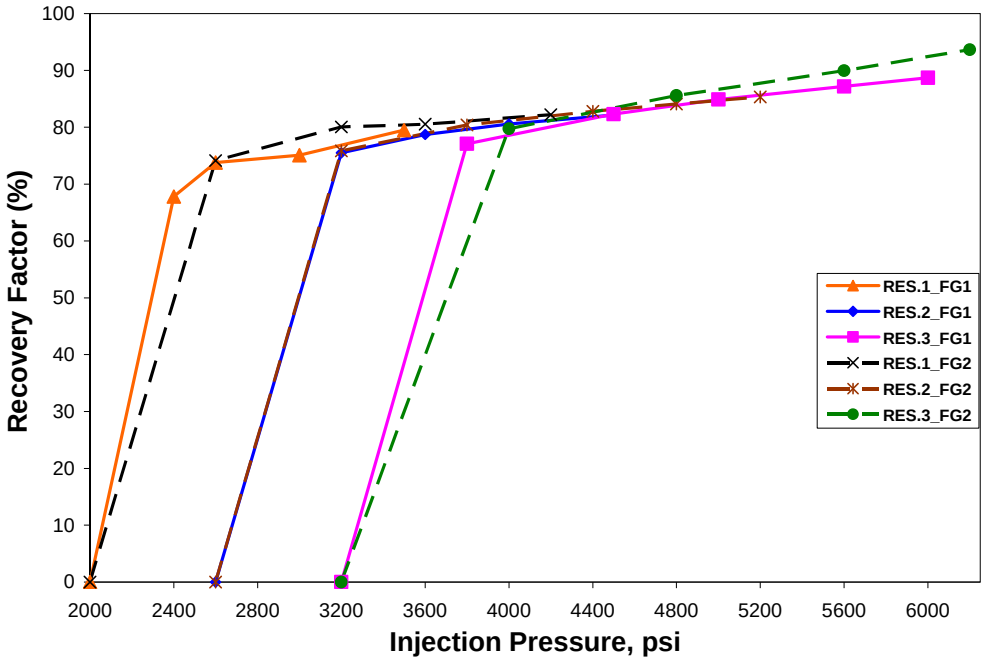

Figure 7: Field-scale recovery factor and injection pressure for sample A, 37.3ºAPI

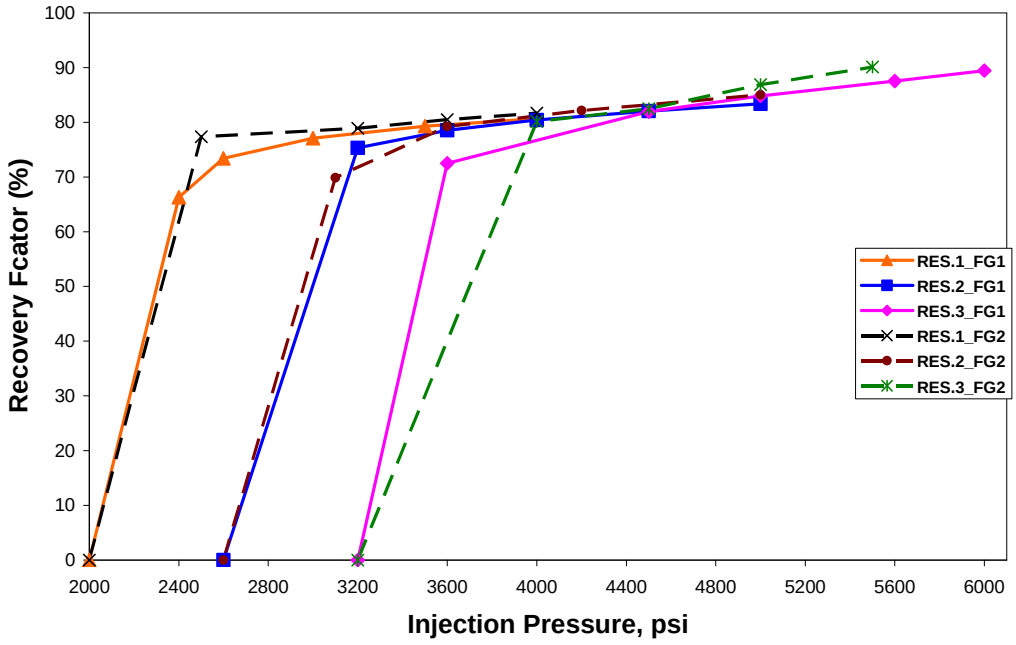

Figure 8: Field-scale recovery factor and injection pressure for sample B, 39.7ºAPI

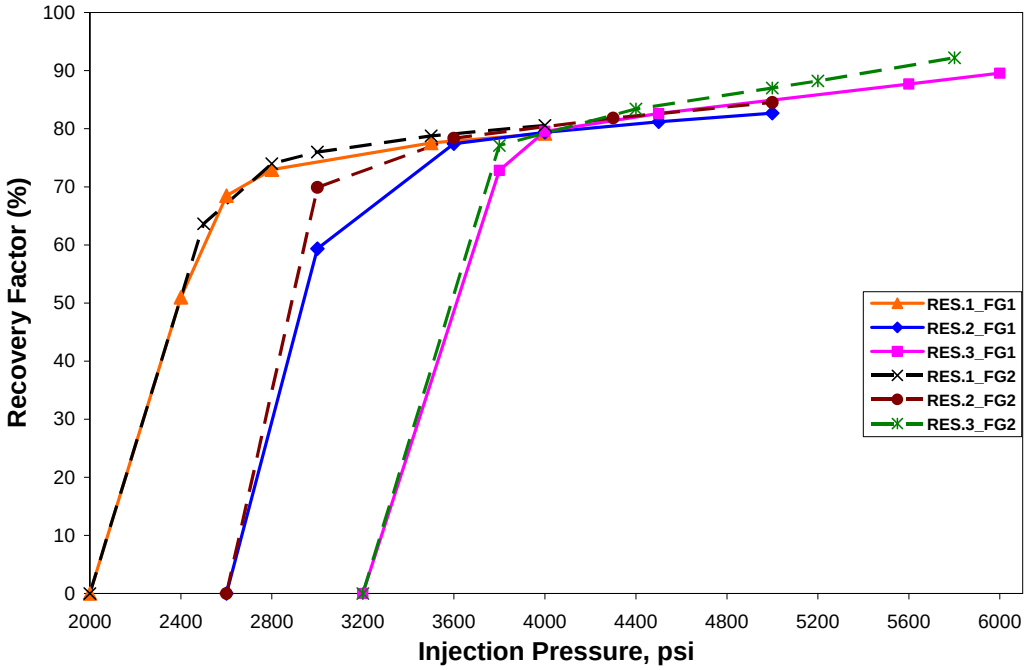

Figure 9: Field-scale recovery factor and injection pressure for sample C, 40.9ºAPI

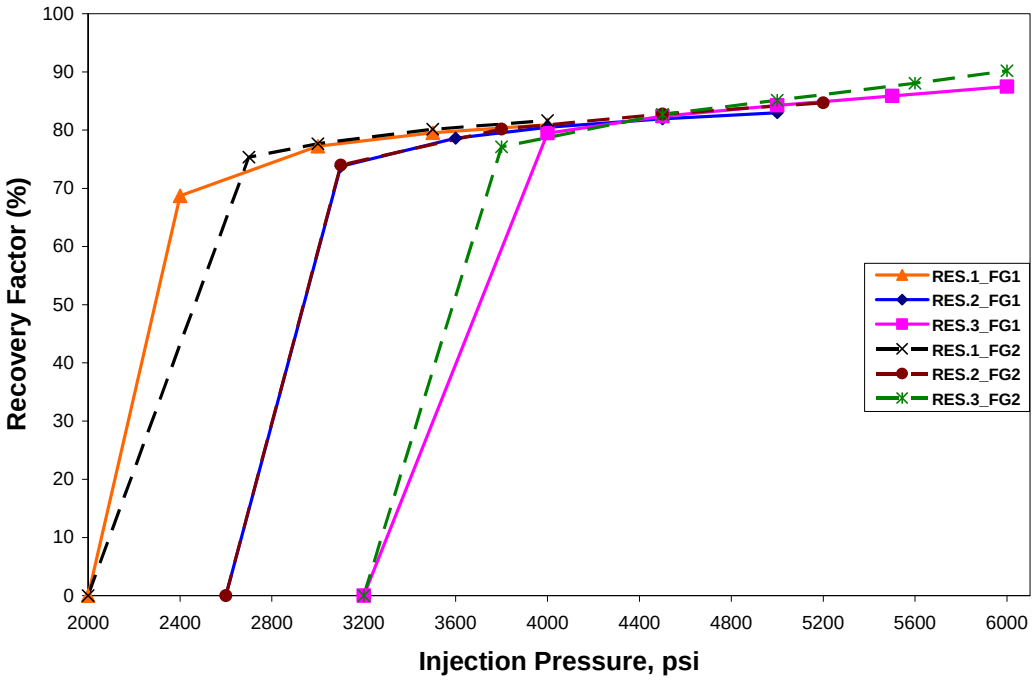

Figure 10: Field-scale recovery factor and injection pressure for sample D, 36.0ºAPI

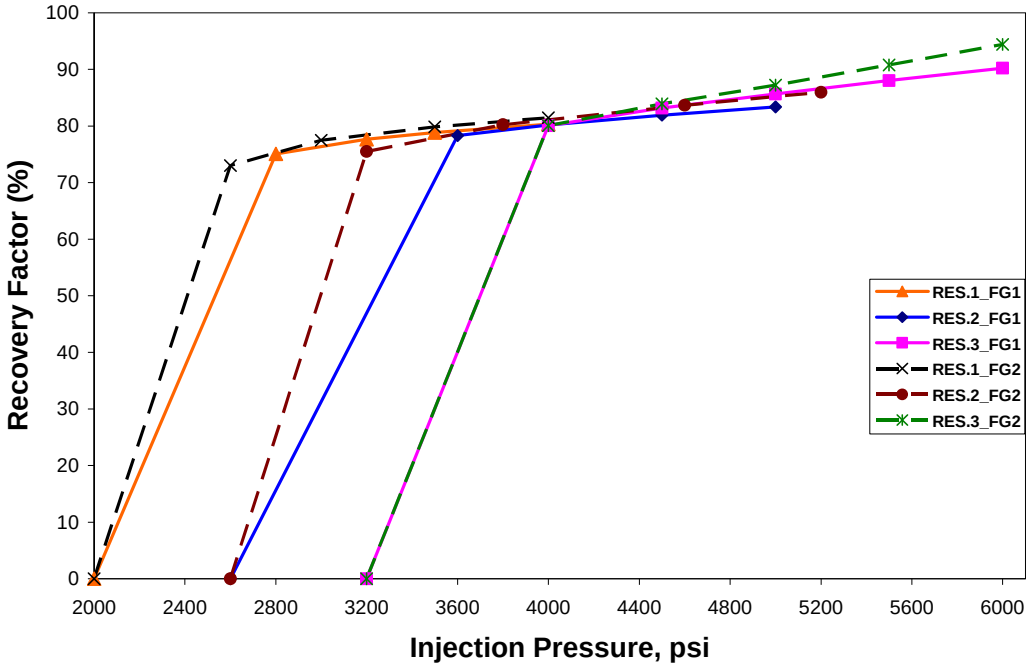

Figure 11: Field-scale recovery factor and injection pressure for sample E, 41.3ºAPI

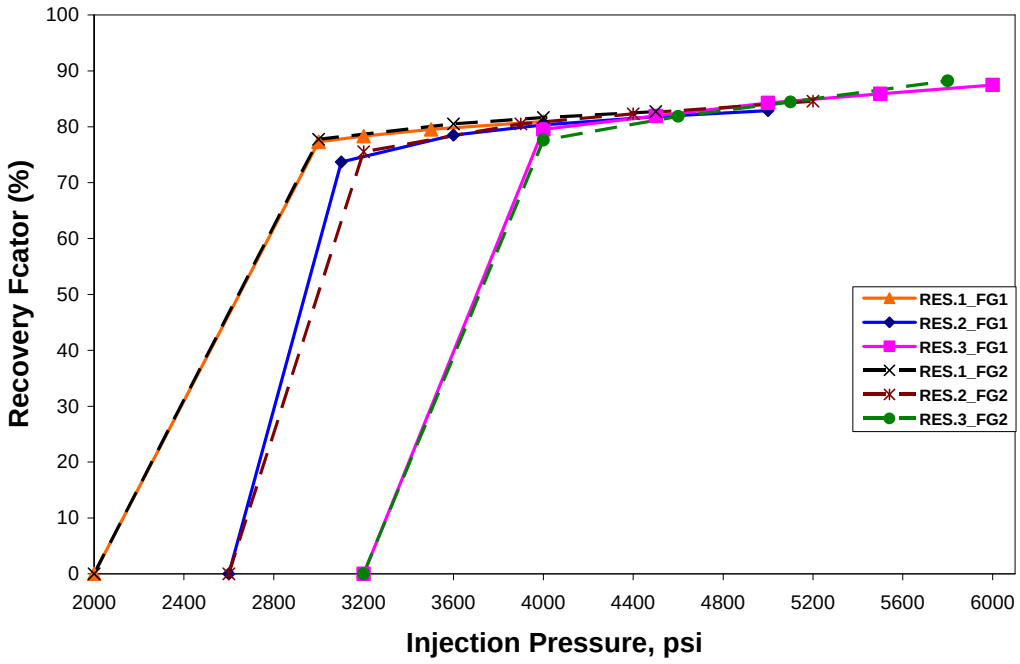

Figure 12: Field-scale recovery factor and injection pressure for sample F, 37.0ºAPI

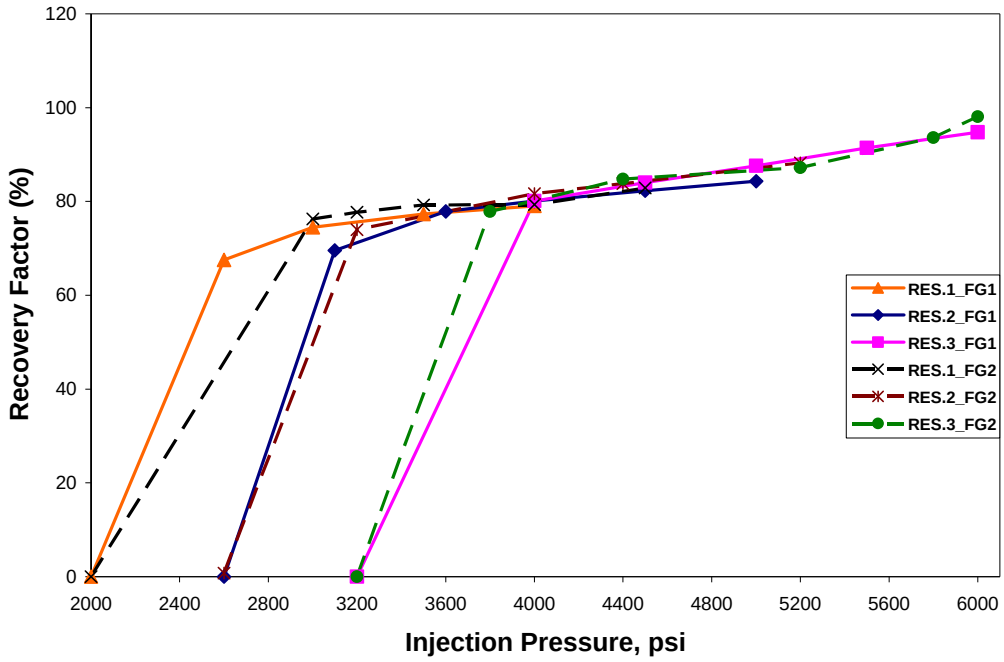

Figure 13: Field-scale recovery factor and injection pressure for sample F, 40.9ºAPI

Table 5 below summarizes minimum miscibility pressures under different reservoir conditions for all the examined seven samples. The minimum miscibility pressures for flue gas 2 (30 % CO_2 content), exhibit lower MMPs as compared to flue gas 1 (15% CO_2 content).

Table 5: Minimum miscibility pressure of field-scale simulations

	RES. 1		**RES. 2**		**RES. 3**	
	MMP FG-1 (psia)	MMP FG-2 (psia)	MMP FG-1 (psia)	MMP FG-2 (psia)	MMP FG-1 (psia)	MMP FG-2 (psia)
A	3020	2600	3200	3200	4480	4000
B	2600	2500	3700	3600	4500	4000
C	3500	3000	3600	3580	3980	3800
D	2960	2700	3600	3080	4000	3800
E	3020	2600	3520	3200	4000	3940
F	3200	3000	3600	3220	4500	4000
G	3000	2960	3680	3240	4520	4400

Comparison of slim tube MMPs and field-scale MMPs

The results of the slim tube displacement experiments and field-scale simulation for the tested oil samples at in-situ temperatures of 200, 288, and 375°F and 2000, 2600, and 3200psia are depicted in **Figures 14** to **19**. All figures indicate that field-scale simulation MMPs are higher than the slim tube displacement MMPs for all seven oil samples. The departure between slim tube-measured MMPs and field-scale measured MMPs depart further with increasing temperature for both flue gas 1 and flue gas 2. The contrast is not as pronounced for low API high molecular weight oils but is considerable for high API low molecular weight oils.

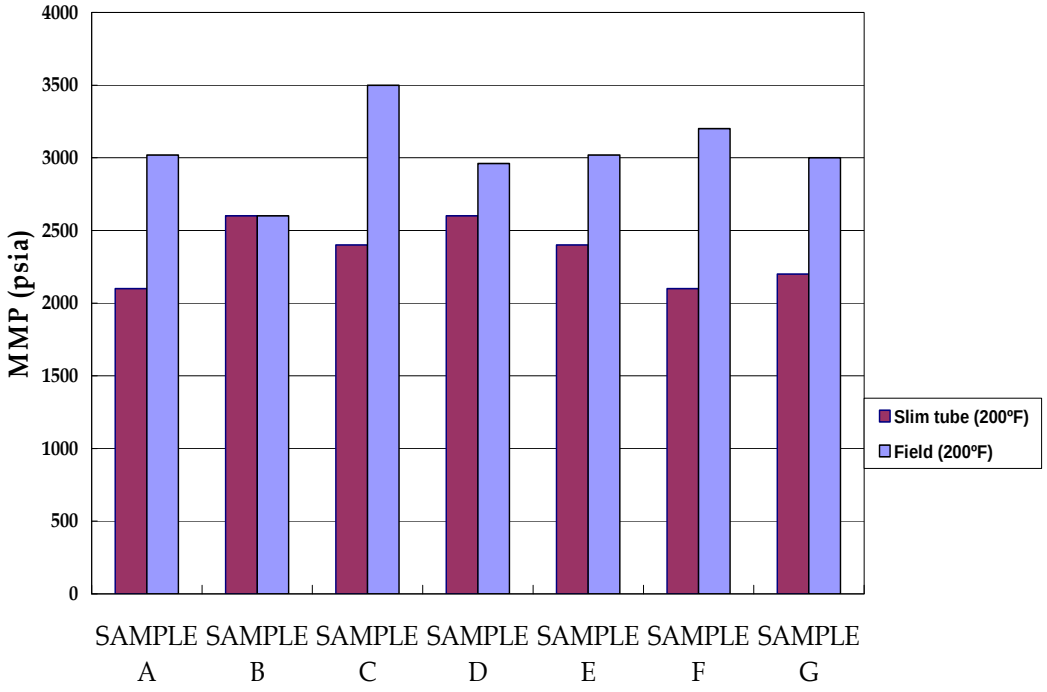

Figure 14: Slim tube and field-scale MMPs (FG – 1 at 200ºF)

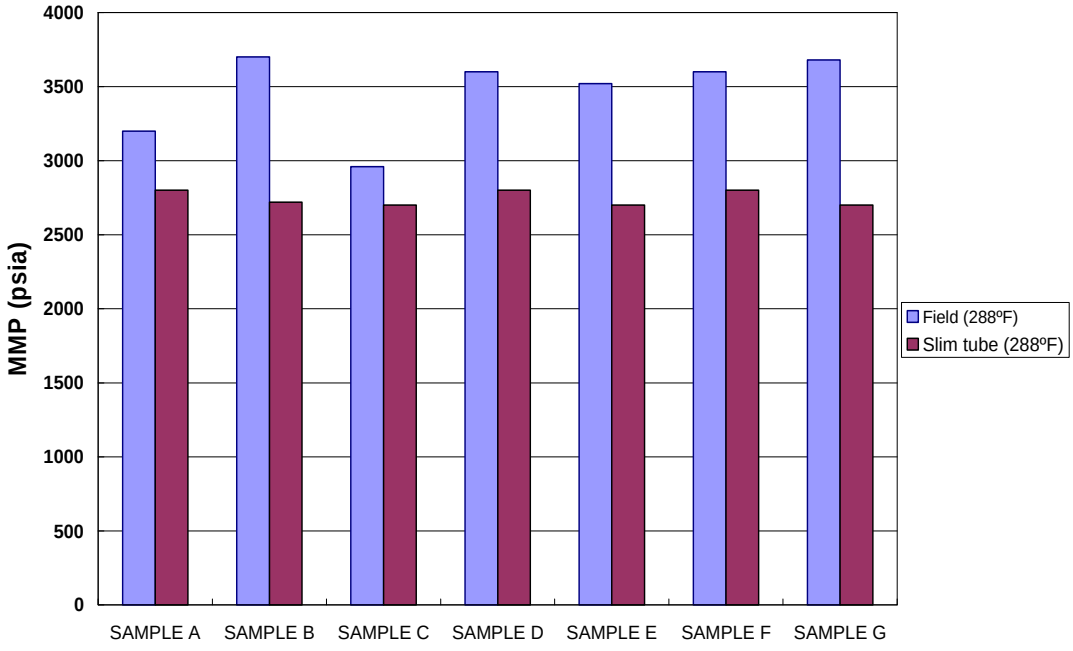

Figure 15: Slim tube and field-scale MMPs (FG – 1 at 288ºF)

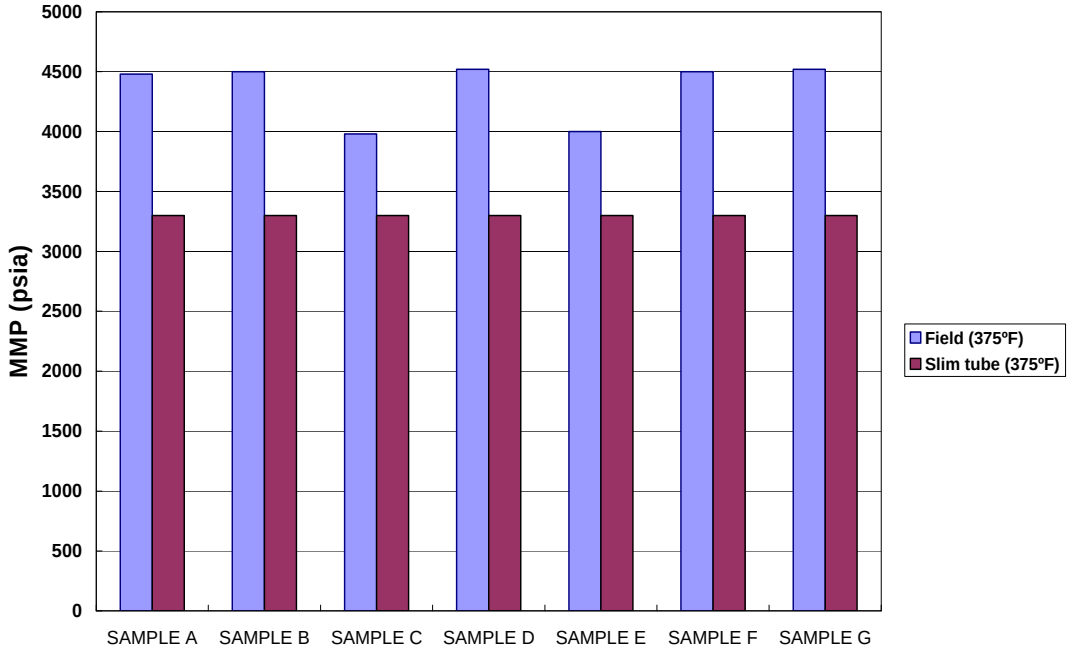

Figure 16: Slim tube and field-scale MMPs (FG – 1 at 375ºF)

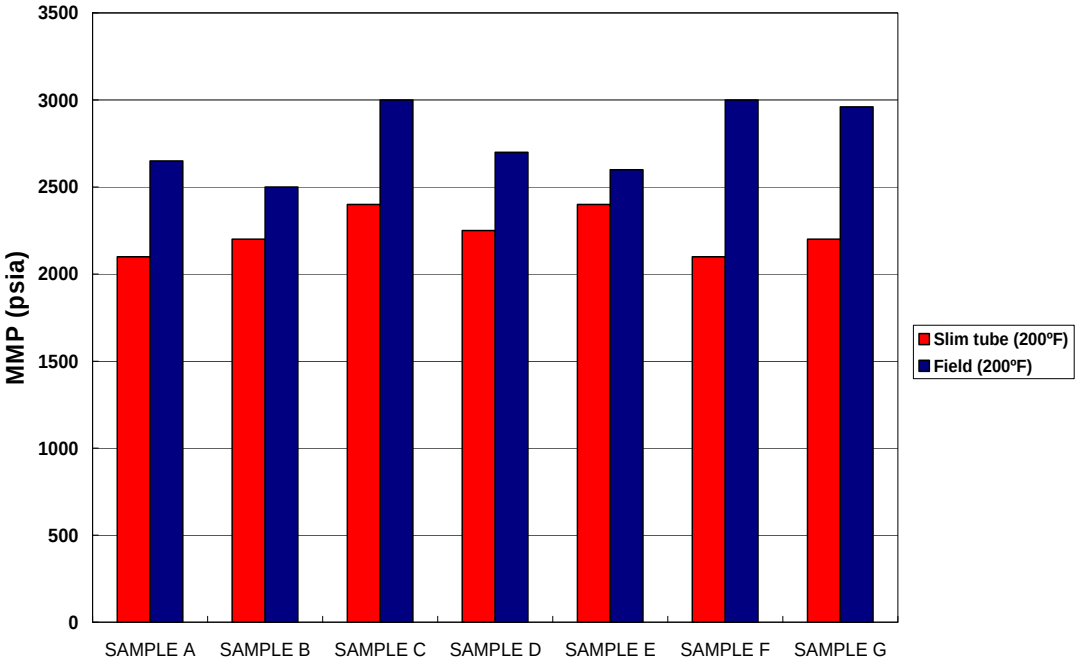

Figure 17: Slim tube and field-scale MMPs (FG - 2 at 200ºF)

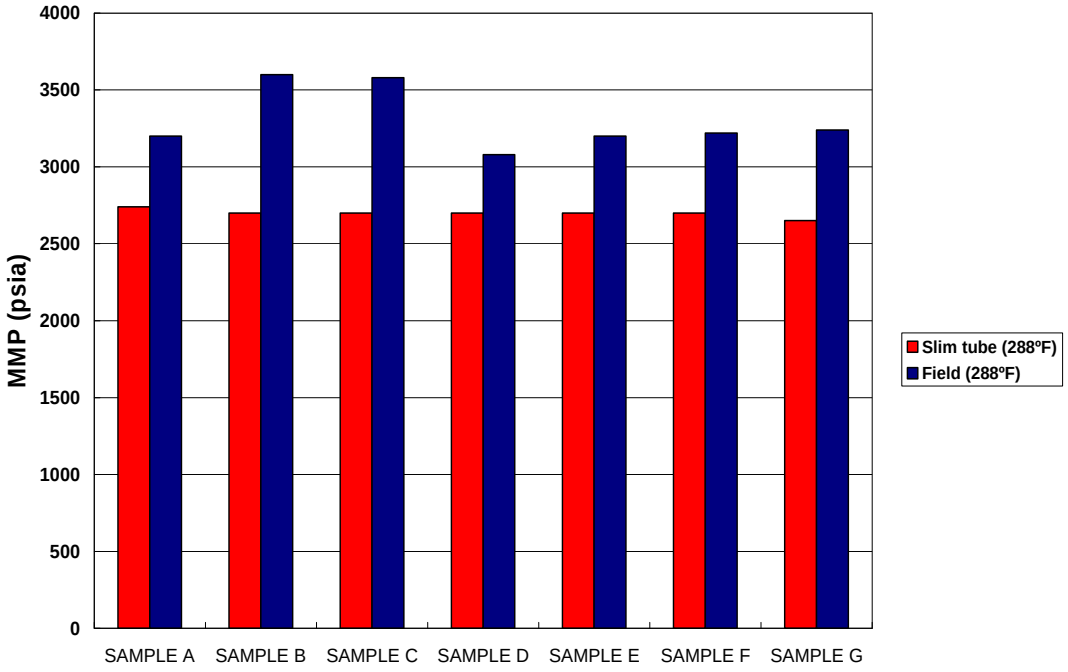

Figure 18: Slim tube and field-scale MMPs (FG - 2 at 288°F)

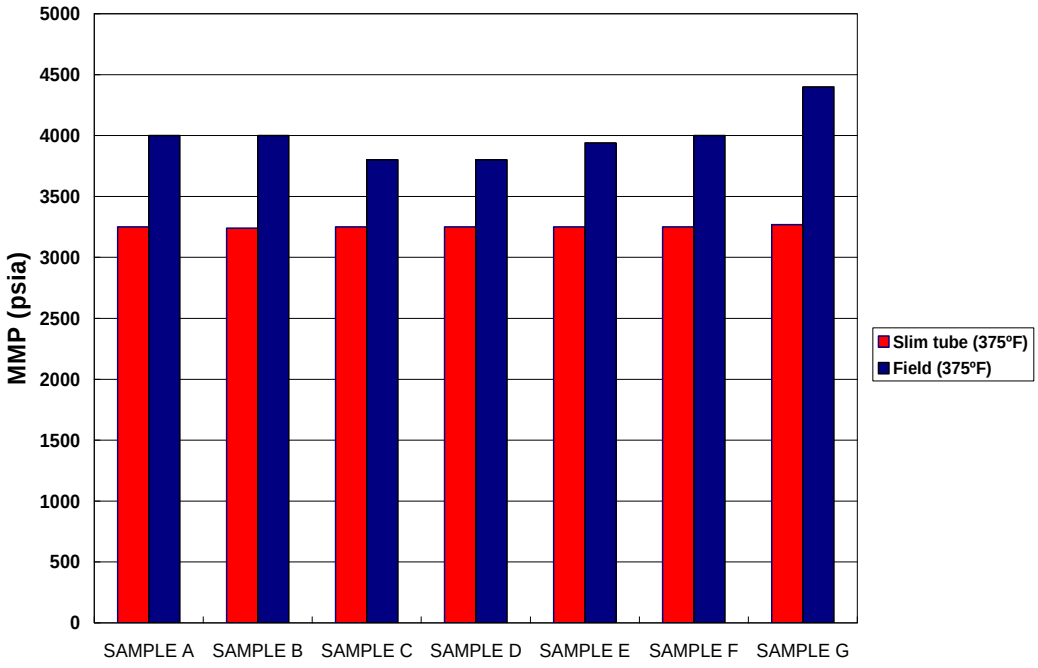

Figure 19: Slim tube and field-scale MMPs (FG - 2 at 375°F)

Tables 6 and **7** illustrate the comparison between slim tube MMPs and field-scale MMPs. The field-scale MMPs are higher and use of slim tube MMPs as a basis in the design of a field miscible gas injection can be misleading. Conditions under which first contact miscibility applies can be underestimated and field performance can be hampered if one opts for slim tube experiment results in the design of a miscible gas injection project.

Table 6: Comparison of slim tube MMPs and field-scale MMPs for flue gas – 1

	(200 °F, 2000 psi)		(288 °F, 2600 psi)		(375 °F, 3200 psi)	
	Slim Tube	Field	Slim Tube	Field	Slim Tube	Field
SAMPLE A	2100	3020	2800	3200	3300	4480
SAMPLE B	2600	2600	2720	3700	3300	4500
SAMPLE C	2400	2500	2700	3600	3300	3980
SAMPLE D	2600	2960	2800	3600	3300	4000
SAMPLE E	2400	3020	2700	3520	3300	4000
SAMPLE F	2100	3200	2800	3600	3300	4500
SAMPLE G	2200	3000	2700	3680	3300	4520

Table 7: Comparison of slim tube MMPs and field MMPs for flue gas – 2

	(200 °F, 2000 psi)		(288 °F, 2600 psi)		(375 °F, 3200 psi)	
	Slim Tube	Field	Slim Tube	Field	Slim Tube	Field
SAMPLE A	2100	2650	2740	3200	3250	4000
SAMPLE B	2200	2500	2700	3600	3240	4000
SAMPLE C	2400	3000	2700	3580	3250	3800
SAMPLE D	2250	2700	2700	3080	3250	3800
SAMPLE E	2400	2600	2700	3200	3250	3940
SAMPLE F	2100	3000	2700	3220	3250	4000
SAMPLE G	2200	2960	2650	3240	3270	4400

Oil recovery performance

The oil recoveries obtained from slim tube and field-scale displacement simulations are shown in **Tables 8** and **9**. The tables summarize the results of several simulation runs carried out at various injection pressures and stated reservoir in-situ conditions of temperature and pressure. In view of the fact that oil samples used in this work have been well represented by the equation of state calculations and the flow compositional simulator, the results show that the increased CO_2 content of the flue gas increases oil recovery. The trend is the same across the board for all seven samples used in this study.

Figure 8 (above) depicts oil recovery performance of sample B as a function of injection pressure and captures the effect of CO_2 content in the flue gas. The simulated results show that FG – 1 gives lower recovery compared to FG – 2 at same injection pressures and the same conditions of temperature and pressure. This increased oil recovery is a direct result of the dissolution of the CO_2 content of flue gas in the residual oil left behind after gas breakthrough. The dissolution results in swelling and reduction of oil viscosity, which in turn assists in the displacement of additional oil. This behavior is observed for all tested oil samples.

This reveals that recovery efficiency in miscible displacement mechanism and at injection pressures above the MMP is considerably dependent on injection-gas composition. The effect of injection gas composition on oil recovery for all seven oil samples is more significant in the field-case model than in the slim tube displacement simulation. A comparison of calculated recovery factors for the oil samples illustrates that miscibility develops efficiently with increasing pressure and temperature. This behavior accounts for the importance of considering the heavy hydrocarbons' molecular weight in compositional oil recovery estimation as well as the CO_2 content of both the sample oil and the injection gas. It can also be seen from **Table 9** that the highest recovery pertains to sample E (lowest molecular weight) under the highest reservoir in-situ temperature of 375°F. **Table 8** and **9** also indicate that recovery from slim tube simula-

tions tends to be more optimistic and that care should be taken when relying on slim tube experiments to predict reservoir performance. Field-scale simulation results are more conservative and better describe miscible gas injection at in-situ conditions since rock and rock-fluid properties are all considered, unlike slim tube experiments where no water is considered and only oil is modeled.

Table 8: Recovery factor for slim tube simulations

	RES. 1		RES. 2		RES. 3	
Samples	**RF (FG-1)**	**RF (FG-2)**	**RF (FG-1)**	**RF (FG -2)**	**RF (FG –1)**	**RF (FG2)**
A	94.14	94.35	92.56	92.58	90.95	91.16
B	93.25	93.45	91.72	91.86	90.10	90.75
C	92.48	92.68	91.06	91.66	89.47	90.02
D	89.40	93.53	91.65	91.95	90.28	90.83
E	92.53	92.76	91.11	92.46	89.36	90.19
F	91.07	93.87	92.12	92.17	90.60	90.89
G	91.88	92.24	90.73	90.86	88.70	89.20

Table 9: Recovery factor for field-scale simulations

	RES. 1		RES. 2		RES. 3	
Samples	**RF (FG-1)**	**RF (FG-2)**	**RF (FG-1)**	**RF (FG -2)**	**RF (FG –1)**	**RF (FG2)**
A	80.88	82.22	83.31	85.33	88.72	92.84
B	80.69	81.69	83.39	85.71	89.44	93.61
C	79.19	80.58	82.70	85.29	89.55	93.60
D	80.93	81.63	82.10	84.69	87.46	90.19
E	80.31	81.46	83.40	85.97	90.23	94.01
F	80.94	82.71	82.88	84.59	87.47	89.40
G	79.05	82.89	84.33	88.24	94.93	98.08

It is observed that vaporizing gas drive is the dominant fluid flow mechanism when first contact miscibility prevails. In addition, the marginal increase in oil recovery as a result of injection at pressures higher than the MMP may not compensate for additional equipment and operating costs. Oil recoveries are maximized when operating at injection pressures equal or higher than field-scale MMP. When flue gas is injected to enhance the recovery of reservoir fluids and this has been verified for crude oils of low density (API gravity > 35^{o}), it is important to evaluate the criteria for economic termination of the process. If it is cost effective, the process can be terminated when the flue gas breaks through. This also ensures that CO_2 (a greenhouse gas) in the flue gas remains sequestered in the reservoir.

Development of an Augmented Correlation that Estimates CO2 MMP

Development of an MMP correlation for CO2 has been initiated. The residual hydrocarbons (C_{7+}) contain millions of components that cannot be analyzed in the laboratory (Eclipse PVTi Manual 1998). Thus, to adequately define these components in a way that will be suitable for use in EOS simulation, they have to be split and regrouped. Whitson splitting technique was used for splitting the heavy fractions in the 15 oil samples to sub-fractions. This process relates mole fractions to molecular weight by a three parameter Probability Density Function (PDF). PDF was used to separate the fractions into several Single Carbon Numbers (SCN). **Figure 20** shows fingerprint plot of Whitson Split fractions. Each SCN was re-grouped into Multiple Car-

bon Number (MCN) groups by dividing molecular weight range of components into intervals. Components in each interval are then lumped together. This process of re-grouping is known as Pseudo-ization. **Table 10** presents the 12 components EOS properties for sample 1.

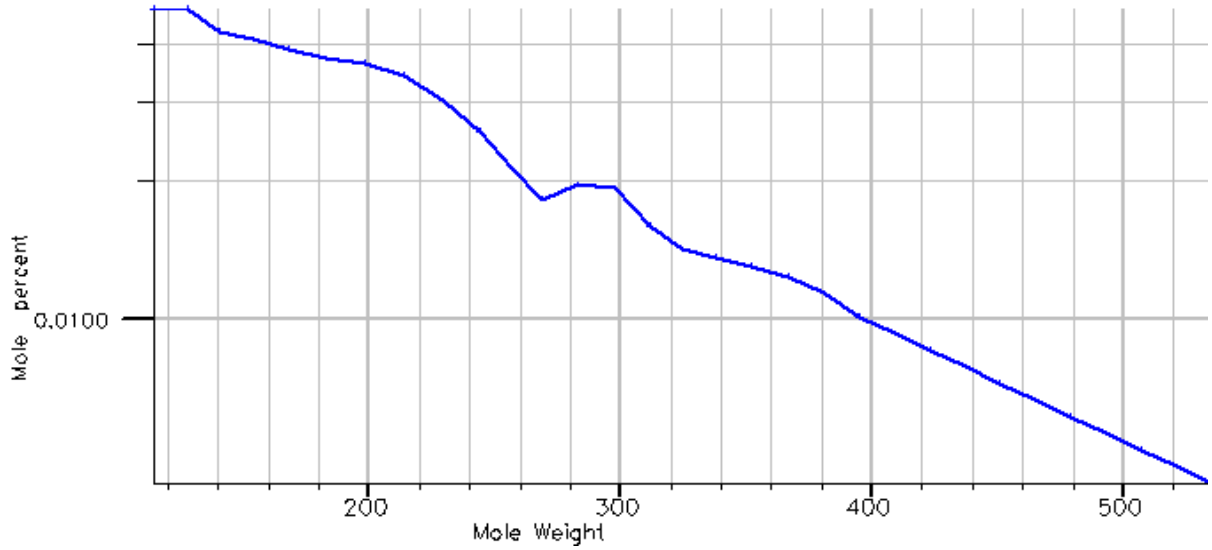

Figure 20: Fingerprint plot of Whitson split fractions for sample 1

For hydrocarbons, components with similar molecular weights were grouped together since they exhibit similar properties. However, CO_2 ($M_w = 44$), a non hydrocarbon, was grouped with C_2 ($M_w = 20$) rather than C_3 ($M_w = 44$) because K-values of each component was considered. A plot of log of the K-values as a function of pressure for both components shows similar trends.

Table 10: EOS parameters for 12-component system of oil sample 1

Components	Mol Weight	Crit. Pres (psia)	Crit. Temp (F)	Acentric Factor	Parachors	V Crit (ft3 /lb-mole)	Z Crit
CO2	44.01	1071.3	88.79	0.225	78	1.5057	0.27408
C1	16.043	667.78	-116.59	0.013	77	1.5698	0.28473
C2	30.07	708.34	90.104	0.0986	108	2.3707	0.28463
C3	44.097	615.76	205.97	0.1524	150.3	3.2037	0.27616
IC4	58.124	529.05	274.91	0.1848	181.5	4.2129	0.28274
NC4	58.124	550.66	305.69	0.201	189.9	4.0847	0.27386
IC5	72.151	491.58	369.05	0.227	225	4.9337	0.27271
NC5	72.151	488.79	385.61	0.251	231.5	4.9817	0.26844
C6	84	436.62	453.83	0.299	271	5.6225	0.25042
C7+	133.13	379.91	646.81	0.4284	383.26	8.3908	0.26847
C14+	245.38	226.15	937.76	0.78705	631.94	15.286	0.23053
C25+	529.8	102.8	1392.6	1.4108	1333.5	32.495	0.16805

To verify if the re-grouping of the 12 components to 9-components is successful, simulation runs for both groups were done. The results of the two groups matched. **Table 11** shows the 9-component system for sample 1 (EOS properties for all 15 samples is presented in Appendix C).

Table 11: EOS parameters for 9-component system of oil sample 1

Components	Mol. Weight	Crit. Pres. (psia)	Crit. Temp. (^oF)	Acentric Factor	Parachors	V Crit. (ft^3 /lb-mole)	Z Crit.
C1	16.043	667.78	-116.59	0.013	77	1.5698	0.28473
C2	30.07	708.34	90.104	0.0986	108	2.3707	0.28463
C3	44.097	615.76	205.97	0.1524	150.3	3.2037	0.27616
C4	58.124	544.81	297.37	0.19662	187.63	4.1194	0.27625
C5	72.151	490.04	378.17	0.24022	228.58	4.9602	0.27034
C6	84	436.62	453.83	0.299	271	5.6225	0.25042
C7	131.79	367.86	624.81	0.42614	380.55	8.4358	0.26665
C8	242.18	217.87	907.19	0.78601	624.04	15.324	0.22761
C9	470.65	108.6	1285.3	1.3352	1187.6	29.388	0.17044

Binary interaction coefficients (BIC)

BIC is a function of a weighted average of the proximity within which two unequal species can come into contact. Thus, binaries are assumed to be zero except for interactions between non hydrocarbons (in this case, CO_2) and hydrocarbons and between light and heavy hydrocarbons. For the 3-Parameter Peng and Robinson EOS, Katz and Firoozabadi correlations determined experimentally between hydrocarbons and non-hydrocarbons, was used to predict BIC. The BIC for sample 1 is shown in **Table 12**.

Table 12: Binary interaction coefficients (BIC) for sample 1

Components	C1	C2	C3	C4	C5	C6	C7	C8	C9
C1	0								
C2	0.002063	0							
C3	0	0.002063	0						
C4	0	0.002063	0	0					
C5	0	0.002063	0	0	0				
C6	0.0279	0.011857	0.01	0	0	0			
C7	0.06157	0.011857	0.01	0	0	0	0		
C8	0.06157	0.011857	0.01	0	0	0	0	0	
C9	0.06157	0.011857	0.01	0	0	0	0	0	0

Parameter PR EOS

For hydrocarbon liquids, $Z_c \leq 0.29$. SRK predicted Z_c for liquids = 0.333, Peng and Robinson predicted $Z_c = 0.307$. 3-parameter Peng and Robinson EOS addresses this shortcoming by introducing a correction factor for critical volume. The $Z_c s$ predicted by 3-parameter PR EOS for hydrocarbons in the work are shown in **Table 11** for sample 1. An examination of the Z_c column confirms that all the components Z_c are less than 0.29. Thus, appropriate EOS was selected.

Viscosity correlation

Three viscosity correlations are available in *PVT*$_i$ suite: Lohrenz, Bray and Clark (LBC), Pedersen, and Aadsberg and Pedersen correlations. Pedersen correlation was adopted to predict the viscosities of hydrocarbon fluids. This correlation predicts viscosity of fluids up to 90% of measured viscosity when experimental data are lacking (as is the case in this study). Pedersen calculates viscosities from a modified form of the Corresponding States Method (CSM). In the LBC correlation, viscosity is a function of the fourth power of density making it sensitive to small differences in density estimation.

Flash calculations

Table 13 shows results of flash calculation for sample 1. Phase plot of sample 1 is presented in **Figure 21**.

Table 13: Flash calculation for sample 1

Peng-Robinson (3-Parm) on ZI with PR corr.		
Pedersen Viscosity Correlation		
Single phase liquid state		
Specified temperature	°F	199.9400
Specified pressure	PSIA	1998.6424
Calculated	Fluid properties	
Mole Weight		184.8287
Z-factor		1.0442
Viscosity		2.4413
Density LB/FT3		49.9792
Molar Distributions	Total, Z	Liquid, X
Components	Measured	Calculated
CO2	16.0468	16.0468
X2+	5.3799	5.3799
C2	6.6557	6.6557
C4+	5.9898	5.9898
C5+	5.1950	5.1950
NC4	4.3641	4.3641
C10+	20.3424	20.3424
C18+	17.9868	17.9868
C40+	18.0395	18.0395
Composition	100.0000	100.0000

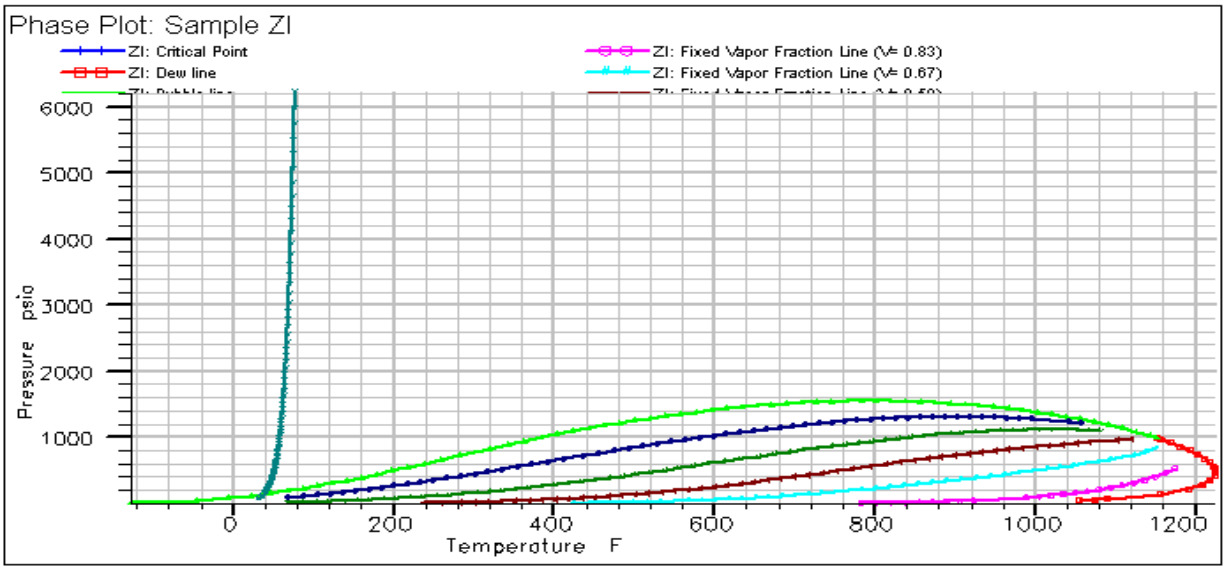

Figure 21: Phase plot for sample 1

Slim tube simulation experiments

The second part of this study involved performing slim tube simulation experiments for 15 oil samples. The simulation was performed based on the following assumptions:

a. Effect of viscous fingering was ignored and complete mixing of fluids within a grid block assumed.
b. Numerical dispersion adequately modeled physical dispersion through grid refinement and solution method of flow equations.

Slim tube experiments were performed at three different temperatures (200, 288 and 375°F) on all sample fluids. For each oil sample, 3 MMP values were determined. In total, about 315 slim tube simulations were performed. For each slim tube simulation, MMP value was determined as the pressure at which 95% of oil is recovered at 1.2PV of injected CO_2 or 90% at injected CO_2 breakthrough in the plot between % recovery and injection pressure.

The slim tube displacements were simulated with 3-parameter PR EOS. 100 mole % CO_2 displaces 9-components reservoir fluids at reservoir pressures of 2000, 2600 and 3200 psia. Simulation was performed at 1.2 Pore Volume of injected CO_2. Percentage oil recovery was determined for each simulation runs using the following equation:

$$\%\ \text{oil recovery} = \frac{(FOIP)_i - (FOIP)_{1.2PV}}{(FOIP)_i} \times 100$$

$(FOIP)_i$ is the initial Field Oil in Place, and $(FOIP)_{1.2PV}$ is the Field Oil in Place at injection of 1.2PV of CO_2.

Slim tube model

The model slim tube is 10m long, inside diameter is 0.44cm, porosity is 0.15 and absolute permeability is 2000mD. Grid block dimensions are 400 X 1 due to the fact that 1-D simulation model for slim tube experiments is a common practice. Sensitivity of grid block was investigated by varying the grid block sizes. Simulation runs were performed for cases of 50, 100, 200 and 400 grid block sizes. The results for the 400 grid block shows improvement on that of 200 and 100 grid blocks. Hence, 400 blocks option was selected because it is more refined and therefore less dispersive.

In order to mimic the physical dispersion in actual reservoirs, Adaptive Implicit (AIM) solution method was selected for solving the set flow equations. Implicit Pressure and Explicit Saturation (IMPES) method is less dispersive but very unstable while Fully Implicit (FULLIMP) method is highly dispersive but more stable. In addition, a specific combination of grid length, velocity, and time-step size was used.

The gas and oil relative permeability and saturation functions for the slim tube model are shown in **Table 14** and **Figures 22** and **23**.

Table 14: Saturation and permeability functions of slim tube experiment

Sw	krw	Pcow	Sg	krg	Pcog	So	krow	krog
0.1500	0.0000	5.0000	0.0000	0.0000	0.0000	0.0000	0.0000	0.0000
0.2000	0.0000	3.5000	0.0500	0.0000	0.0000	0.0889	0.0000	0.0000
0.2899	0.0022	1.9030	0.0889	0.0010	0.0000	0.1500	0.0000	0.0000
0.3778	0.0180	1.0070	0.1778	0.0100	0.0000	0.2000	0.0000	0.0110
0.4667	0.0607	0.4900	0.2667	0.0300	0.0000	0.2667	0.0080	0.0370
0.5556	0.1438	0.1800	0.3556	0.0500	0.0000	0.3000	0.0150	0.0560
0.6444	0.2809	0.0500	0.4444	0.1000	0.0000	0.3556	0.0340	0.0878
0.7000	0.4089	0.0050	0.5333	0.2000	0.0000	0.4444	0.0950	0.1715
0.7333	0.4855	0.0010	0.6222	0.3500	0.0000	0.5333	0.2178	0.2963
0.8222	0.7709	0.0000	0.6500	0.3900	0.0000	0.6222	0.4153	0.4705
0.9111	1.0000	0.0000	0.7111	0.5600	0.0000	0.7111	0.5950	0.6305
1.0000	1.0000	0.0000	0.8500	1.0000	0.0000	0.8500	0.8000	0.8000

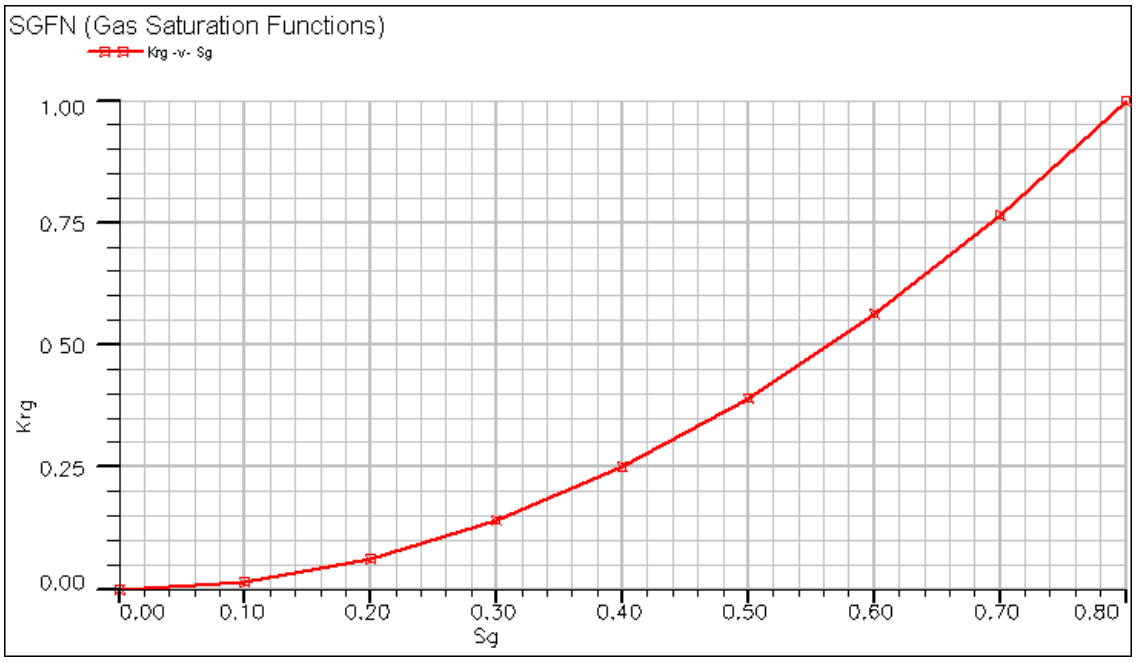

Figure 22: Gas saturation function for slim tube experiment

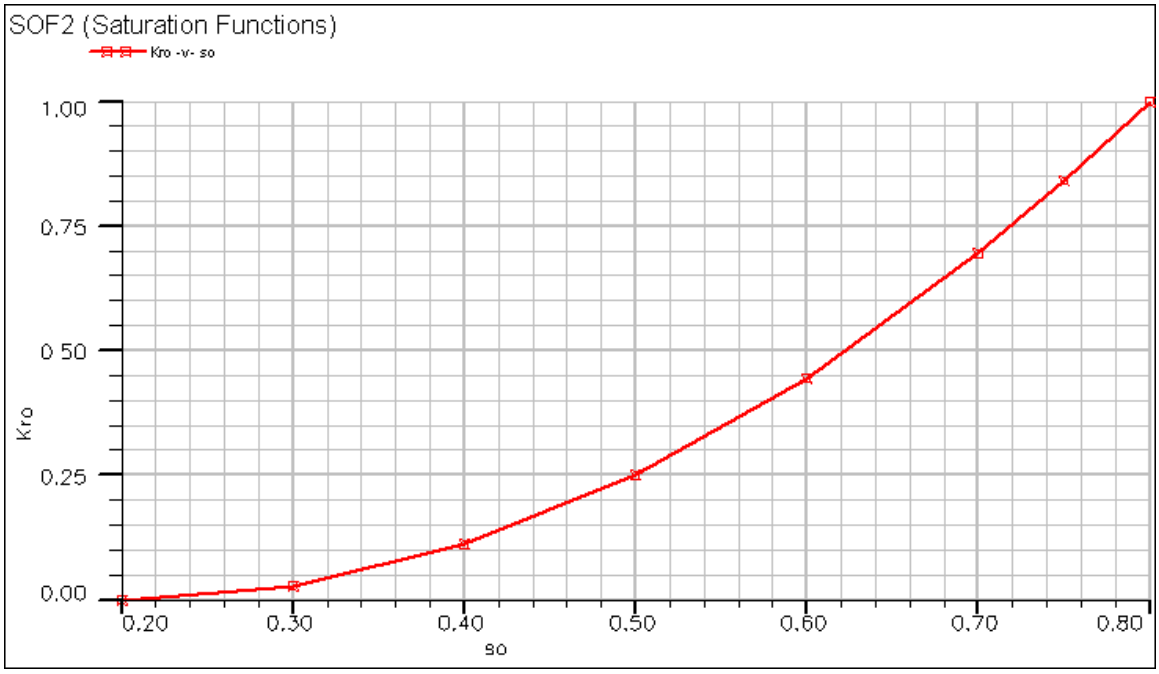

Figure 23: Oil saturation function for slim tube experiment

Development of CO2 MMP correlation

To develop MMP that will encompass all the important thermodynamic properties, a scaling method was used as the starting point. This approach is based on dimensionless scaling groups of EOS properties including reservoir temperature, critical properties of oil, acentric factors. In addition, API gravity was introduced as a dimensionless group. Overall, five dimensionless group were developed and a multiple regression analysis was performed on the five predictors to develop a new MMP correlation for light oils.

The first four dimensionless groups were determined based on weight based grouping method to calculate pseudo properties of hydrocarbon fluids. Basically, oil components were divided into light and heavy components. Light components comprise of C_1-C_6 hydrocarbon components while heavy components are the C_{7+} plus fractions.

The dimensionless groups are determined as follows using weight based grouping:

$$T_{cl} = \frac{\sum_{i=1}^{6} z_i M_{wi} T_{ci}}{\sum_{i=1}^{6} z_i M_{wi}}$$

$$T_1 = \frac{T_R}{T_{cl}}$$

In the above equations, z_i is the mole fraction of component i, M_{wi} is the molecular weight of component I, T_{ci} is critical temperature of component i, T_{cl} is the pseudo critical temperature of light hydrocarbon components (C_1-C_6). T_R is the reservoir temperature and T_i is the dimensionless pseudo reduced temperature for light hydrocarbon components.

$$T_{ch} = \frac{\sum_{i=7}^{\infty} z_i M_{wi} T_{ci}}{\sum_{i=7}^{\infty} z_i M_{wi}}$$

$$T_2 = \frac{T_R}{T_{ch}}$$

For group 2, T_{ch} (see above equations) is the pseudo critical temperature of heavy hydrocarbon components (C_{7+}). T_R is the reservoir temperature and T_2 is the dimensionless pseudo reduced temperature for heavy hydrocarbon components. Other parameters are as defined above.

$$\omega_{cl} = \frac{\sum_{i=1}^{6} z_i M_{wi} \omega_{ci}}{\sum_{i=1}^{6} z_i M_{wi}}$$

$$W_1 = \omega_{cl}$$

In group 3, ω_{cl} (see above equations) is the weighted acentric factor for light pseudo components and $W_1 = \omega_{cl}$ is the acentric factor dimensionless group pseudo reduced temperature for light hydrocarbon components, ω_{ch} is the acentric factor for component i.

$$\omega_{ch} = \frac{\sum_{i=7}^{\infty} z_i M_{wi} \omega_{ci}}{\sum_{i=7}^{\infty} z_i M_{wi}}$$

$$W_2 = \omega_{ch}$$

In group 4, ω_{ci} is the weighted acentric factor for C_{7+} pseudo components and $W_2 = \omega_{ch}$ is the acentric factor dimensionless group pseudo reduced temperature for heavy hydrocarbon components (see above equations).

The fifth dimensionless group is the oil samples API gravity defined in terms of specific gravity (γ) as in the following equations:

$$API = \frac{141.5}{\gamma} - 131.5$$

$$P = API$$

The five dimensionless groups comprised of variables affecting MMP value including reservoir temperature, molecular weight, critical temperature, acentric factor, API gravity and mole fractions.

Furthermore, model training and validation were executed. The five dimensionless groups served as input into the model building process in R (an open source statistical computing package). The dependent variable is MMP while independent variables (predictors) are T_1, T_2, W_1, W_2 and P.

The general form of the model is given by the following equation;

$$MMP = f(T_1, T_2, W_1, W_2, P, \varepsilon)$$

where, ε is a random error term with mean $E(\varepsilon) = 0$ and variance $\sigma^2\{\varepsilon\} = \sigma^2$.

The error term makes the relationship a statistical relationship, and efforts will be made to ensure this term is as closed to zero as possible.

Data splitting

Data sets are often split into model-building and model validation sets. The first set, called the model-building set is used to develop the model. The second data set, called the validation set, is used to evaluate the equanimity and predictive ability of the chosen model. However, it is important that the model building data set be large enough so that a reliable model can be developed. If the data set is not large enough for making an equal split, validation data set will be smaller than the model-building data set.

One way of splitting of data sets, is to split at random which was adopted in this work.

Model building

In model training, a linear regression is assumed, however, if this does not give a good fit, non linear regression will be explored. For any set of p-1 predictors, 2^{p-1} alternative models can be constructed. Thus, for 5 predictors, $2^5 = 32$ different possible models can be formed from the pool of 5 predictor variables. The question arises whether to fit each of the 32 possible models one by one and select the best option or to use an algorithm that can automatically search for some of the best models.

Forward Stepwise Regression procedure is probably the most widely used of the automatic search methods. This method was employed to search for the best model. However, Kutner suggested that the subset model identified by this procedure should serve as a starting point for searching for other 'good' models.

The procedure is described below:

1. The stepwise regression routine first fit a regression model for each of the P-1 potential subset models. For each model, the t* statistic for testing whether the slope is zero or not is determined using the following equation.

$$t_k^* = \frac{b_k}{s\{b_k\}}$$

2. If the corresponding P-value is less than a pre-determined α, the X variable is added.
3. Assume X7 is the variable added in step 1, the stepwise regression routine now fits next regression model with two X variables, where X7 is one of the pair.

These steps continued until the best set of variables are selected. It is to be noted that this algorithm allows an X variable, brought into the model at an earlier stage, to be dropped later if is no longer helpful in conjunction with variables added at later stages.

A program was written in R codes using the algorithm, and the subset selected was used as a starting point for identifying the best model.

Model validation

After the 'best' model has been selected, the model has to be validated with similar data sets not used in the model building process. This step is necessary to determine the robustness and predictive ability of the model. The validation was done by regressing the model with the new data sets. Then, the correlation was compared with existing correlations from the literature.

Simulation results

This part of the report presents the results of simulation runs and regression analysis for development of a new MMP correlation for light oils. The results of model building and validation will be highlighted in the next report.

Two recoveries were reported from the plot of oil recovery vs. injection pressure of CO_2; 90% at breakthrough of CO_2 and at 95% after injection of 1.2 PV of CO_2 as the MMP values. These definitions were based on the fact that some simulation runs show early CO_2 breakthrough at less than 1.2 PV.

For sample 1, the oil recovery (%) at 200°F is 82%, at 288°F is 84%, and at 375°F is 88%. In all three cases, recovery is less than 90%, an indication that miscibility is not achieved as evident in **Table 15**. **Table 15** shows the final MMP values for all the fluids at three different reservoir temperatures. Overall, 42 MMP values were determined for all fluid samples.

Table 15: MMP values for each fluid sample at different temperatures

Fluid Sample #	T = 200 °F	T = 288 °F	T = 375 °F
1	-	-	-
2	2100	3160	3300
3	2300	2745	3220
4	2440	2870	3265
5	2550	3010	3310
6	2160	2700	3220
7	2530	2930	3290
8	2025	2840	3220
9	2100	2680	3220
10	2050	2620	3220
11	2285	2795	3280
12	2020	2620	3220
13	2490	3080	3305
14	2030	2625	3220
15	2540	3120	3310

Constructing CO2 MMP correlation

For each MMP value in **Table 15** (see above), there are unique critical temperatures (T_c), critical pressure (P_c) and acentric factors (ω) for all components. However, P_c is less reliable than T_c and is[*] not included in the correlation. These thermodynamic properties are lumped into light and heavy pseudo-components dimensionless groups as discussed in the previous report.

In the build up to model development, the five dimensionless groups, serve as the independent variables (predictors) while MMP is the dependent (response) variable. 27 MMPs selected at random for 9 samples at temperatures of 200°F, 288°F and 375°F were used as response variables for training the models. Also, dimensionless groups for the 27 MMPs were used as the model training independent variables. **Table 16** presents calculated slim tube MMP and the five dimensionless groups input to R*. The dimensionless groups are regressed against MMP values to generate a regression model in R.

Table 16: Regression parameters - MMP values and dimensionless groups

MMP (Psia)	W2	W4	T1	T2	API (P)
2200	0.22334115	0.986412	0.594469	0.192865	37.3
2440	0.21113925	1.071458	0.63679	0.177331	31.7
2030	0.22825842	0.953331	0.580283	0.197935	39.7
2300	0.21812263	1.032612	0.614312	0.183418	34.4
2540	0.19193796	1.11239	0.741185	0.172085	31.9
2550	0.19208606	1.114466	0.739734	0.171586	31.3
2025	0.22993754	0.932174	0.576584	0.199673	40.9
2100	0.22515752	0.982128	0.592603	0.189726	36
2490	0.19652994	1.152139	0.720142	0.182374	33.4
3150	0.22334115	0.986412	0.856035	0.277725	37.3
2870	0.21113925	1.071458	0.916977	0.255356	31.7
2625	0.22825842	0.953331	0.835608	0.285027	39.7
2745	0.21812263	1.032612	0.884609	0.264123	34.4
3120	0.19193796	1.11239	1.067307	0.247803	31.9
3010	0.19208606	1.114466	1.065217	0.247084	31.3
2840	0.22993754	0.932174	0.830281	0.287529	40.9
2680	0.22515752	0.982128	0.853348	0.273205	36
3080	0.19652994	1.152139	1.037004	0.262619	33.4
3300	0.22334115	0.986412	1.04032	0.337513	37.3
3265	0.21113925	1.071458	1.114382	0.310329	31.7
3220	0.22825842	0.953331	1.015496	0.346387	39.7
3220	0.21812263	1.032612	1.075046	0.320982	34.4
3310	0.19193796	1.11239	1.297074	0.301149	31.9
3310	0.19208606	1.114466	1.294534	0.300275	31.3
3220	0.22993754	0.932174	1.009022	0.349427	40.9
3230	0.22515752	0.982128	1.037055	0.33202	36
3305	0.19652994	1.152139	1.260248	0.319155	33.4

[*] R is an open source system for statistical computation and graphics

More work has been done on model development. The number of possible models for 5 predictors is 32. Manually searching for the 'best' model is a tedious and time consuming task and equally prone to human error. Hence, a time savings algorithm for model selection, based on Akaike's Information Criterion (AIC) was employed to determine the 'best' subsets. AIC penalizes modes having large numbers of independent variables (a better model selection criterion than R^2 which increases with increasing number of predictors). The goal is to search for models that have small values of AIC.

At the start of the stepwise search, different combinations of the predictors were predefined (including polynomials and interactions). In the base model, MMP was regressed against T2, then t* statistics and corresponding P-values were calculated. The predictor having the smallest P-value (largest t* value) was chosen to enter the equation. The search continued until the lowest possible value of AIC was reached, AIC = 249.6.

The algorithm identified (T_2, W_1P, T_2P and T_1T_2) as the best subsets of independent variables (**Table 17**). The coefficient of determination, $R^2 = 0.962$ and $R^2_{adj} = 0.955$, appeared to have been an excellent fit (Table 3). Predictor variables T_2 and T_1T_2 (with regression coefficients of 2612.7 and -1708.2, respectively) have t* values of 0.85 and 1.47 (very low) and corresponding P-values of 0.4037 and 0.1560, respectively. The t* values are very low and P-values are greater than significant code ($\alpha = 0.001$). These variables have insignificant contributions to the regression model and were removed.

Table 17: Regression coefficients

Model		Unstandardized coefficients		t value	Pr(>|t|)
		B	Std. Error		
1	(Intercept)	3444.3	380.7	9.05	7.20E-09
	T2	2612.7	3068.6	0.85	0.4037
	W1P	-371.8	60.1	-6.18	3.20E-06
	T2P	209.4	65.9	3.18	0.0044
	T1T2	-1708.2	1162.7	-1.47	0.156
2	(Intercept)	3382.15	115.99	29.2	< 2e-16
	W1P	-316.65	18.11	-17.5	3.70E-15
	T2P	199.3	8.81	22.6	< 2e-16
Signif. Codes		'***' 0.001	'**' 0.01	'*' 0.05	'.' 0.1

Then, variables W_1P and T_2P were regressed with MMP. Results are also shown in **Table 17**. t*-values for intercept and variables are quite high and the corresponding P-values are small compared to α. This indicates an excellent fit. In addition, R^2 was 0.958 and R^2_{adj} equals 0.955 (**Table 18**). This also confirms that the variables removed from model 1 are insignificant as R^2_{adj} remains unchanged.

Table 18: Model summary

Model	R	R square	Adjusted R Square	Residual Std. Error	F- statistic	P-Value
1	0.962	0.955	0.955	93.6	139	2.83E-15
2	0.979	0.958	0.955	93.9	275	<2e-16

Analysis of Variance (ANOVA), **Table 19** reveals the results of the F test. The high value of F* (37.9 and 511.6 for W_1P and T_2P, respectively) also replicate the significance or high level of correlation between regressed variables and MMP.

Table 19: Analysis of variance (ANOVA) for model 2

	Df	Sum Sq	Mean Sq	F value	Pr(>F)
W1P	1	334655	334655	37.9	2.30E-06
T2P	1	4512757	4512757	511.6	< 2e-16
Residuals	24	211704	8821		

The final model is given in the following simplified form:

$$MMP_{\Pr edicted} = a_o + (a_1 W_2 + a_2 T_2)P$$

with, $a_o = 3382.15$

$a_1 = -316.65$

$a_2 = 199.3$

Substituting for W_1 and T_2 and coupling in the above equation gives the following empirical model:

$$MMP_{\Pr edicted} = 3382.15 + \left(3382.15 T_R \left\{ \frac{\sum_{i=7}^{\infty} z_i M_{wi}}{\sum_{i=7}^{\infty} z_i M_{wi} T_{ci}} \right\} - 316.65 \left\{ \frac{\sum_{i=1}^{6} z_i M_{wi} \omega_{ci}}{\sum_{i=1}^{6} z_i M_{wi}} \right\} \right) API$$

All parameters have already been defined in the 7th quarterly report.

Validation of correlation

The final step in the model-building process is the validation of selected regression correlation. It involves checking the correlation with the original data used for building the model, then checking with independent data to test its predictive performance.

Obviously, the first stage of validating the correlation is to compare the predicted MMP with the calculated MMP (slim tube) of data set used for the model building (**Table 20**).

Table 20: Slim tube MMP vs. MMP predicted from new correlation

MMP slim tube (psia)	2160	2050	2285	2020	2490	2620	2795	2620	3080	3290	3220	3210	3280	3220	3305
MMP pred. (psia)	2241	2042	2093	2172	2518	2774	2694	2964	3052	3336	3162	3290	3117	3522	3428

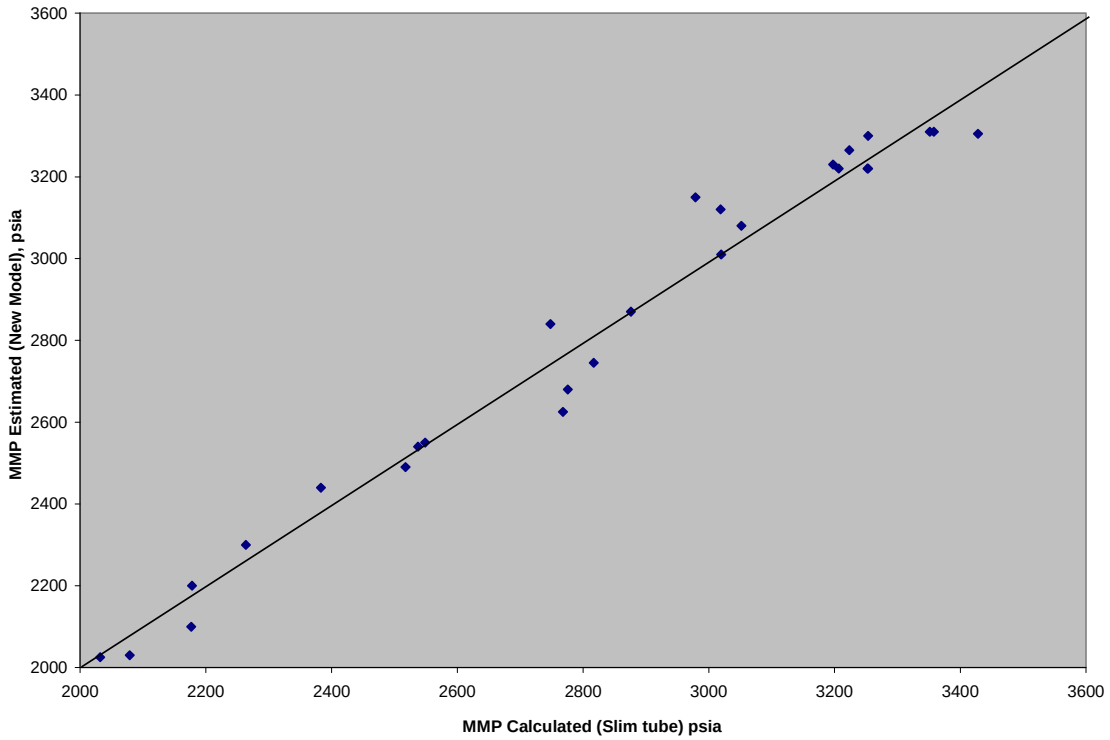

Figure 24: Comparison of slim tube and estimated MMP values from new regression correlation

Also, **Figure 24** depicts the excellent agreement between the calculated and the predicted MMP values.

We validated the new empirical model with independent data and the correlation was used to predict the MMP values of data that were not used in the development of the model. **Table 21** and **Figure 25** show a good fit between calculated MMP and predicted MMP from the new correlation.

Table 21: Comparison of MMPs estimated from correlations to slim tube MMPs and this study predicted MMPs for oil displacement by CO2

API (°)	Temp. (°F)	MMP Calc. (Psia)	C_1 (mol %)	C_2-C_6 (mol %)	Mwt (C_{7+})	MMP Pred. (Psia)	Yelling–Metcalfe (Psia)	Glasϕ (Psia)	Yuan *et* al. (Psia)
37.3	200	2200	0.724	28.1	258	2178	2385	2499	2185
31.7	200	2440	1.281	31.2	289	2383	2385	2573	1578
39.7	200	2030	0.873	30.5	248	2079	2385	2273	2131
34.4	200	2300	1.055	32.1	275	2264	2385	2439	1749
31.9	200	2540	12.472	26.3	304	2537	2385	2555	1591
31.3	200	2550	12.060	26.0	305	2549	2385	2675	1585
40.9	200	2025	0.880	26.5	197	20321	2385	2164	2376
36	200	2100	0.860	31.1	258	2177	2385	2349	2009
33.4	200	2490	12.751	29.0	326	2518	2385	2726	2359
37.3	288	3150	0.724	28.1	258	2809	3465	3049	2374
31.7	288	2870	1.281	31.2	289	2877	3465	3178	2537
39.7	288	2625	0.873	30.5	248	2768	3465	3052	3023
34.4	288	2745	1.055	32.1	275	2817	3465	3020	2795
31.9	288	3120	12.472	26.3	304	3019	3465	3527	2888
31.3	288	3010	12.06	26.0	305	3020	3465	3537	3045
40.9	288	2840	0.880	26.5	197	2748	3465	2886	2764
36	288	2680	0.860	31.1	258	2776	3465	2949	2908
33.4	288	3080	12.751	29.0	326	3052	3465	3418	2830
37.3	375	3300	0.724	28.1	258	3253	4133	3683	2967
31.7	375	3265	1.281	31.2	289	3223	4133	3565	3014
39.7	375	3220	0.873	30.5	248	3253	4133	3417	3008
34.4	375	3220	1.055	32.1	275	3207	4133	3433	3463
31.9	375	3310	12.472	26.3	304	3358	4133	3439	3609
31.3	375	3310	12.06	26.0	305	3352	4133	3679	3916
40.9	375	3220	0.880	26.5	197	3253	4133	3397	3626
36	375	3230	0.860	31.1	258	3198	4133	3584	3570
33.4	375	3305	12.751	29.0	326	3428	4133	3687	3864

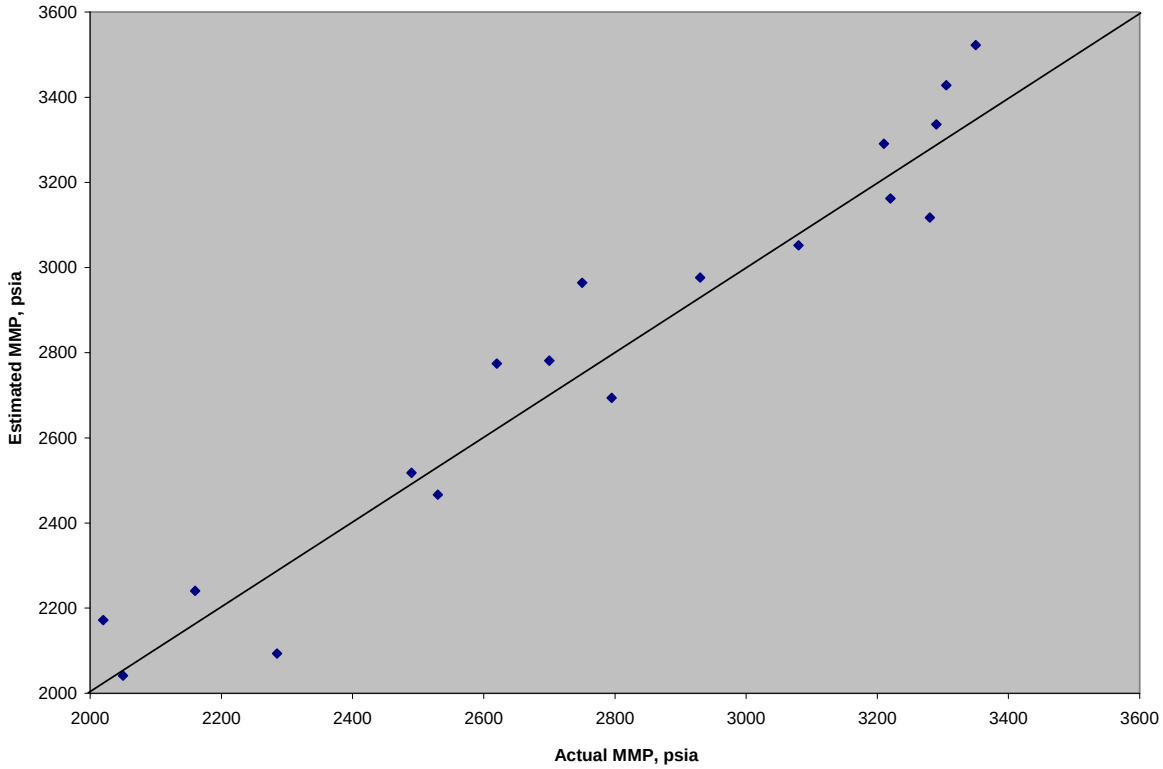

Figure 25: Results of MMP predictions to validate developed correlation

The correlation was then compared with existing correlations MMP values. The results presented in **Table 21** and **Figure 26** (below) indicate that the new developed model produces more deterministic predictions than those estimated by Yelling and Matchafe, Glasϕ, and Yuan *et* al. correlations.

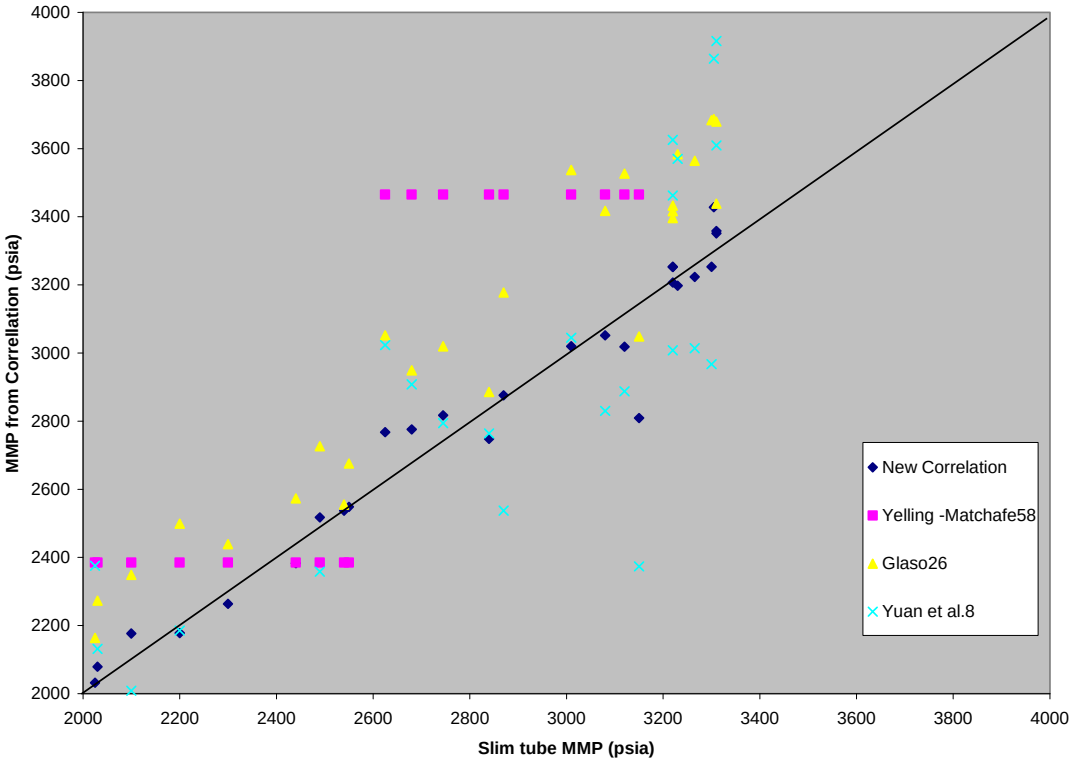

Figure 26: Comparison of the new correlation with published correlations

The development of an artificial neural network (ANN) model that ought to predict CO2 MMP values has been finalized. The modeling routines are all included in the CO2 appendix. The parameters used for model development are defined as follows:

T_1 = reduced temperature for light hydrocarbons (C_1-C_6)
T_2 = reduced temperature for heavy hydrocarbons (C_{7+})
W_1 = acentric factor for light hydrocarbons (C_1-C_6)
W_2 = acentric factor for heavy hydrocarbons (C_{7+})
P = API gravity.

The parameters used are functionally independent and won't affect the reliability of the ANN model. In model development, some of the simulation-generated data have been used to train the ANN model (75% of the data) and the remaining data (25%) have been used for validation purposes. The CO2 MMP values used in the model development reflect minimum pressures needed for complete miscibility between CO2 and the tested oils. Theoretically, operating under these pressures guarantees a 90% oil recovery.

The generated soft data from numerical simulation minimum miscibility pressures (MMPs) study have been divided into a training data set and a validating data set. The training and validating data sets involve input neurons of reduced temperature for light hydrocarbons (C_1-C_6), T_1, reduced temperature for heavy hydrocarbons (C_{7+}), T_2, acentric factor for light hydrocarbons (C_1-C_6), W_1, acentric factor for heavy hydrocarbons (C_{7+}), W_2, and API gravity, P.

Different ANN predictor models have been tested with different input parameters. Functional links involving complex functions have been tested to generate the most accurate model. Once a model is generated validation was done using a set of observations that was not used to

train the model. **Figure 27** depicts a schematic of a simplistic model with three input neurons (input layer).

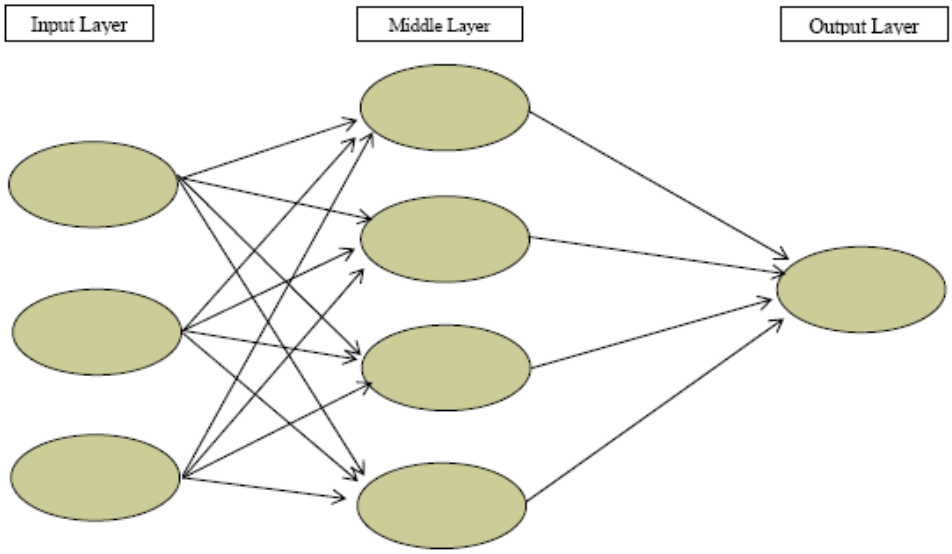

Figure 27: A schematic of an ANN model with 3 input layers

Table 22 groups all data used in the determination of the ANN model. Model results will be compared to the regression analysis results that have already been performed.

Table 22: Data used to develop the CO2 ANN model

MMP (Psia)	W2	W4	T1	T2	API (°)
2200	0.22334115	0.986412	0.594469	0.192865	37.3
2440	0.21113925	1.071458	0.63679	0.177331	31.7
2030	0.22825842	0.953331	0.580283	0.197935	39.7
2300	0.21812263	1.032612	0.614312	0.183418	34.4
2540	0.19193796	1.11239	0.741185	0.172085	31.9
2550	0.19208606	1.114466	0.739734	0.171586	31.3
2025	0.22993754	0.932174	0.576584	0.199673	40.9
2100	0.22515752	0.982128	0.592603	0.189726	36.0
2490	0.19652994	1.152139	0.720142	0.182374	33.4
3150	0.22334115	0.986412	0.856035	0.277725	37.3
2870	0.21113925	1.071458	0.916977	0.255356	31.7
2625	0.22825842	0.953331	0.835608	0.285027	39.7
2745	0.21812263	1.032612	0.884609	0.264123	34.4
3120	0.19193796	1.11239	1.067307	0.247803	31.9
3010	0.19208606	1.114466	1.065217	0.247084	31.3
2840	0.22993754	0.932174	0.830281	0.287529	40.9
2680	0.22515752	0.982128	0.853348	0.273205	36.0
3080	0.19652994	1.152139	1.037004	0.262619	33.4
3300	0.22334115	0.986412	1.04032	0.337513	37.3
3265	0.21113925	1.071458	1.114382	0.310329	31.7
3220	0.22825842	0.953331	1.015496	0.346387	39.7
3220	0.21812263	1.032612	1.075046	0.320982	34.4
3310	0.19193796	1.11239	1.297074	0.301149	31.9
3310	0.19208606	1.114466	1.294534	0.300275	31.3
3220	0.22993754	0.932174	1.009022	0.349427	40.9
3230	0.22515752	0.982128	1.037055	0.33202	36.0
3305	0.19652994	1.152139	1.260248	0.319155	33.4

To generate the ANN model, a first trial with 5 neurons was done and results were promising. A function that can generate MMP from any set of input data has been written. To build the ANN model, we have built a 5 hidden tan-sigmoidal neuron model. The resulting function is as follows:

$$y = w_1 \times x + b_1$$
$$MPP = w_2 \times f(y) + b_2$$

where,

- x is the input vector defined by: $x = \begin{bmatrix} W_2 \\ W_4 \\ T_1 \\ T_2 \end{bmatrix}$
- y is the output of the 5 linear neurons (y has the same dimension as x.
- w_1 is the input layer weight vector (5x4).
- b_1 is the input layer bias vector (5x1).
- w_2 is the output layer weight vector (1x5).
- b_2 is the output layer bias vector (1x1).
- The tan sigmoidal function is defined by: $f(y) = \frac{2}{1 - \exp(-2y)} - 1$

Note that the input vector data should be first normalized (set [-1 1]) before using the above equations. The obtained result value of MMP should be multiplied by its normalization factor.

The values of the weight and bias vectors which were obtained after training the ANN model for 4000 iterations (epochs) are as follows:

```
w1 =
   2.0497    4.8516  -11.0687   -1.4318
   3.5586    3.5268  -17.4037   17.6296
  21.0985    9.3383   34.4231  -33.2755
  11.1258    8.2332   -5.5919   -5.9995
  19.4837    1.0782    1.8764   -5.2538

>> b1

b1 =
   3.4288
  -8.8754
 -25.5683
  -8.6753
 -13.0183

>> w2

w2 =
   2.1088   -0.6294   -0.2574   -2.2839    1.1130

>> b2

b2 =
  -0.5527

>>
```

The back-propagation ANN training algorithm was used. Below are the results of the training:

Number of Hidden Nodes = 5
Total Number of Epochs = 4000

Normalization rate: W2 = 2.29938e-001
Normalization rate: W4 = 1.15214e+000
Normalization rate: T1 = 1.29707e+000
Normalization rate: T2 = 3.49427e-001
Normalization rate: MMP = 3.31000e+003
Contribution of W3 = 26.26 [p.c.]
Contribution of W4 = 12.38 [p.c.]
Contribution of T1 = 32.23 [p.c.]
Contribution of T2 = 29.13 [p.c.]

The maximum values of the variables used during the normalization and de-normalization processes are:

W2	W4	T1	T2	MMP
0.22993754	1.152139	1.297074	0.349427	3310

The developed model can now be used to map recovery under miscible conditions using CO2 as the miscible gas for candidate reservoirs, in Louisiana and elsewhere, bearing oil with API gravity ranging between 31° and 41°. The developed model is only valid for reservoir temperatures ranging between 200 to 375 ^{o}F and reservoir pressures varying between 2000 to 3200 psia. Extrapolation outside the API, temperature, and pressure ranges is not recommended.

CSEM TASK

Introduction

As known oil reserves dwindle and the worldwide demand for petroleum rises, exploration efforts move to riskier arenas with less tolerance for failure. Deepwater exploration in particular continues to increase despite the high exploration and production costs involved. With such a high price of failure, the risk inherent in a new venture must be reduced as much as possible. Further complicating matters, risk assessment has to be done remotely to decrease the time and cost incurred.

The exploration industry has enjoyed widespread, undeniably successful application of seismic techniques to the discovery of oil. It stands to reason, then, that the amassed remotely collected; high fidelity data and expertise should be used, if possible, in the de-risking of hydrocarbon prospects. Due to the low sensitivity of compressional wave velocity to changes in reservoir quality, however, seismic methods prove to be poor risk analysis tools. As few as one third of exploration wells assessed through traditional means lead to commercial quality discoveries (MacGregor, et al., 2006).

It has long been known (and relied upon) that the presence of hydrocarbons—particularly gas—in the pore spaces of a formation significantly alters acoustic impedance. Ostrander (1984) showed, using Gassman's equations, compressive and shear wave velocities are insensitive to gas saturation. A 10% gas saturation can have the same p-wave to s-wave velocity ratio (VP/VS) as a commercial accumulation of gas, rendering approaches such as amplitude versus offset (AVO) ineffective as a quality analysis tool (Hou et al., 2006). Reflection amplitude anomalies alone are no longer compelling enough to justify the expense of an exploratory well.

Since the 1940s, it has been well known to anyone even passingly familiar with exploration well-logging that electrical resistivity longs are invaluable in reservoir potential assessment. Brine saturated sediments have a resistivity around 1-5 ohm-m, which increases to roughly 10-100 ohm-m when oil or gas replaces the brine (Constable, 2006). Thus, any technique that relatively inexpensively yields the same information about the subsurface, but in a wholesale sense over a large subsurface volume would be likewise invaluable. Furthermore, imaging subsurface resistivity can provide structural information in rock types that are challenging to image seismically, such as low porosity (and thus highly resistive) basalt or salt (Constable, 2006). The hydrocarbon exploration industry has a historical familiarity with terrestrial magnetotelluric surveying (MT) as a means of remotely detecting subsurface electrical properties. In the deep submarine environment, however, controlled source electromagnetic surveying (CSEM) proves to be more practical, given the rapid attenuation of MT source fields in sea water and the low sensitivity of the method to thin, resistive bodies like hydrocarbon filled reservoirs. CSEM demonstrates much higher sensitivity to hydrocarbon potential than seismic velocity, and is a promising remote de-risking approach (**Figure 28**).

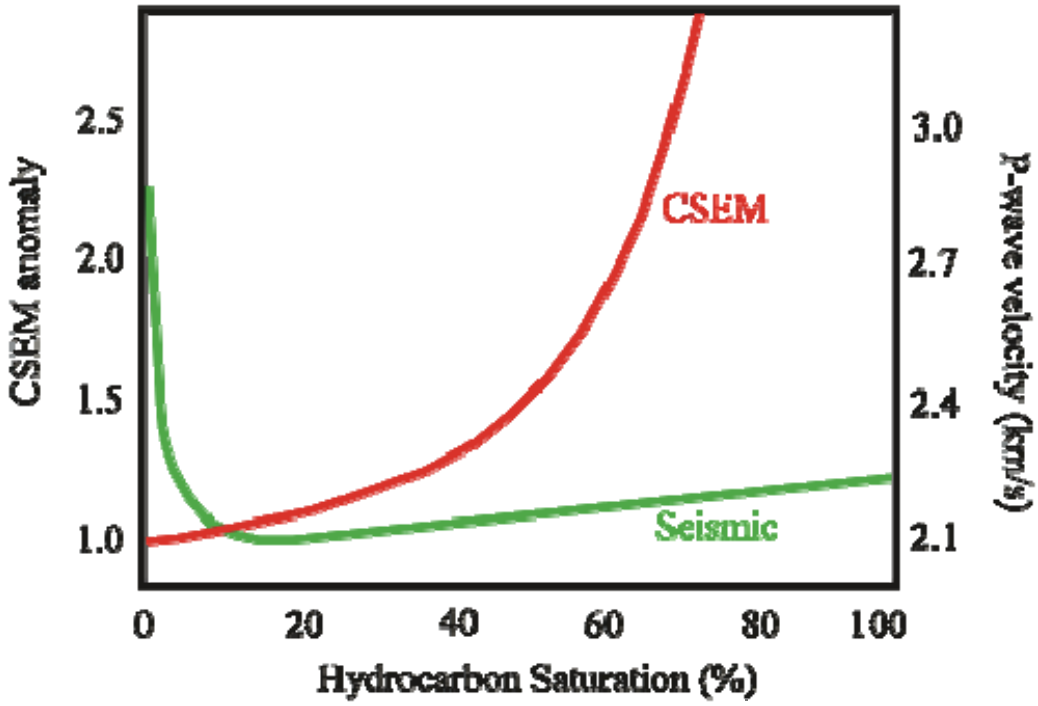

Figure 28: The effect of hydrocarbon saturation percentage on compressional wave velocity versus controlled source electromagnetic (CSEM) response. As saturation increases, p-wave velocity is relatively unchanged beyond 10%, while CSEM response rapidly increases (after MacGregor (2005)

Though CSEM has garnered significant industry attention as of late, the large-scale adoption of CSEM as a hydrocarbon de-risking modality is hindered by many difficulties, largely because the application to hydrocarbon exploration is in its infancy. Robust data processing, interpretation, and visualization software is mostly inviable for commercial application (Constable, 2006). Current, first-order interpretation of CSEM relies on the detection of characteristic, non-unique amplitude anomalies within raw data. Any higher order interpretation generally requires modeling and data inversion. In the literature, the application of one and two dimensional modeling is widespread (e.g Chave and Cox (1982), Li and Key (2007)). Three-dimensional modeling is extant but rarer (e.g. Badea, (2001)). The widespread adoption of fully three-dimensional CSEM modeling and interpretation is hampered by the computational expense incurred when imaging the arbitrary, complex resistor shapes characteristic of potential hydrocarbon reservoirs.

The expense can be greatly reduced by applying a simply solved model that very generally approximates the physics of CSEM in an arbitrary reservoir. This approach is justified by the well known low resolution of the CSEM method—particularly at the frequencies used in a marine survey. If the ultimate goal is the automated statistical classification of an unknown subsurface conductivity anomaly as a reservoir or non-reservoir, a less that accurate model will produce good results, as shown in Aliamiri, et al. (2007).

Simplified modeling and first order amplitude anomaly extraction reduce interpretation costs demonstrably. At least two major problems are immediately evident, however. First, we have little knowledge of how effective the first order amplitude anomaly detections is in realistic marine CSEM exploration. Second, while an approximate model is justifiable, what is the best

possible model? We address both questions with a statistical investigation of the general nature of submarine hydrocarbon reservoirs and the associate CSEM response. Reservoir geometry and electrical properties are probably regionally specific, being controlled by formative geological processes. Within a given region, there exists a good deal of variability, and we characterized the properties of a reservoir and the related CSEM responses probabilistically. From the publicly available descriptions of approximately 100 known, producing Gulf of Mexico (GOM) reservoirs, we compiled a statistical database which was used to generate nonparametric probability density functions (pdfs) of a common set of reservoir parameters. All identified reservoirs could be (with some justifiable approximations) expressed as a section of a hemi-ellipsoid. A three dimensional finite element CSEM modeling code, previously developed for near surface investigations, was redesigned to model the unique physics of deepwater marine CSEM surveying. From the model and the probabilistic descriptions of reservoir parameters, we computed a Monte Carlo simulation of the responses of 1000 hypothetical GOM reservoirs, simplified to crude boxlike approximations (due to limitations in the modeling software). The collection of responses was used to quantitatively gauge the effectiveness of the aforementioned response anomaly detection as an interpretation tool, and to determine the probability distribution of GOM reservoir CSEM responses.

To address the second problem, we drew inspiration from prior work in unexploded ordnance (UXO) detection and discrimination (Stalnaker et al., (2006), Aliamiri et al., (2007)). UXO is approximately modeled as a collection of wire loops, the electrical and geometric characteristics of which are directly related to the nature of the UXO itself. The model is justified because UXO differ electrically from the host medium and sufficiently distant from the sensor. By a similar argument, a hydrocarbon reservoir is a relatively compact, electrically different target. We modeled hydrocarbon reservoirs as a collection of lengths of wire, reusing much of the machinery from the UXO detection, discrimination and classification literature. A simple model led to rapid inversion. With prior information about reservoir parameters and reservoir response, we made use of statistical estimation techniques like maximum likelihood estimation (MLE) and Bayesian inversion to improve the realism of our inverse modeling.

Marine Controlled Source Electromagnetometry

In a typical marine CSEM geophysical survey, an electromagnetic transmitter is towed by ship some distance above the seafloor (**Figure 29**) at a speed of 1.5 − 2 knots. Various transmitter styles have been used, but the horizontal electric dipole (HED) transmitter has become the standard. The HED transmitter is a current carrying, horizontal length of wire. Most terrestrial CSEM surveys utilize a vertical magnetic dipole (VMD), which is a loop of wire oriented such that the normal to the loop area is vertical, and transmitting a purely transverse electric (TE) mode. The TE mode is relatively insensitive to thin horizontal resistors such as hydrocarbon reservoirs. By contrast, the HED transmits both in the TE mode and the transverse magnetic (TM) mode, which is sensitive to horizontal resistors (**Figure 30**). The electric field generated by the transmitter is purely vertical at all points in the line of the HED, and purely horizontal for all points on any line perpendicular to the transmitter. Most surveys are conducted in the frequency domain (though time domain surveys are becoming increasingly common), with the HED oscillating in a square wave with frequencies between 0.01 and 3 Hz. Typical detectors are dropped to the seafloor, and measure the horizontal electric field magnitude and phase parallel (inline) and perpendicular (broadside) to the transmitter axis.

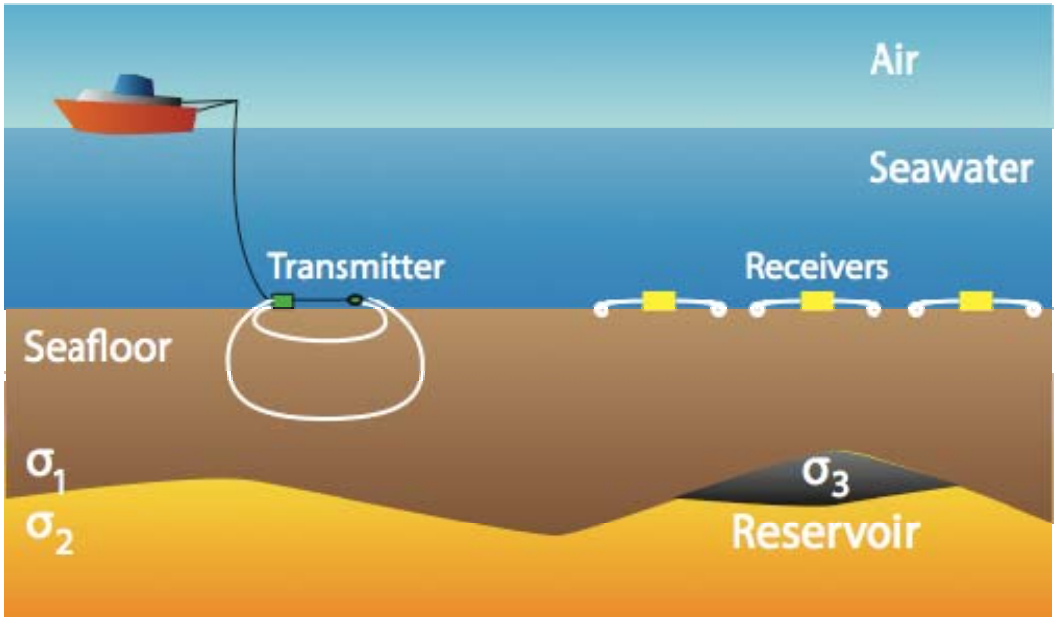

Figure 29: Typical marine CSEM survey

The collection of orthogonal data allows one to quickly distinguish horizontal resistors. The vertical inline fields (and currents) are interrupted by the presence of a horizontal resistivity change, while the broadside component is largely unaffected. In fact, the measured electric field is the combination of several effects. The transmitter field amplitude drops off geometrically as distance from the source increases, while phase remains unchanged. Fields arising from in any conductive bodies fall off in magnitude and phase according to the skin depth. Finally, fields experience a magnitude (though not phase) discontinuity at material interfaces due to surface charge buildup—the so-called galvanic effect (Constable, 2010). Because this galvanic effect only occurs when electric fields cross resistor boundaries, it is used as an indicator of horizontal resistors when the fields are vertical.

The galvanic effect manifests as an increase in electric field magnitude with increased offset from the transmitter, which appears when magnitude is plotted versus offset (MVO) (Eidesmo et al., 2002). MVO curves are typically compared to background responses, and any deviation from background is attributed to a resistive layer. The MVO curve (**Figure 31**) is often normalized against the half-space response. While MVO assessment is a good first order reconnaissance technique, no information is provided about resistor lateral extent or resistivity. Less commonly phase versus offset (PVO) is also observed.

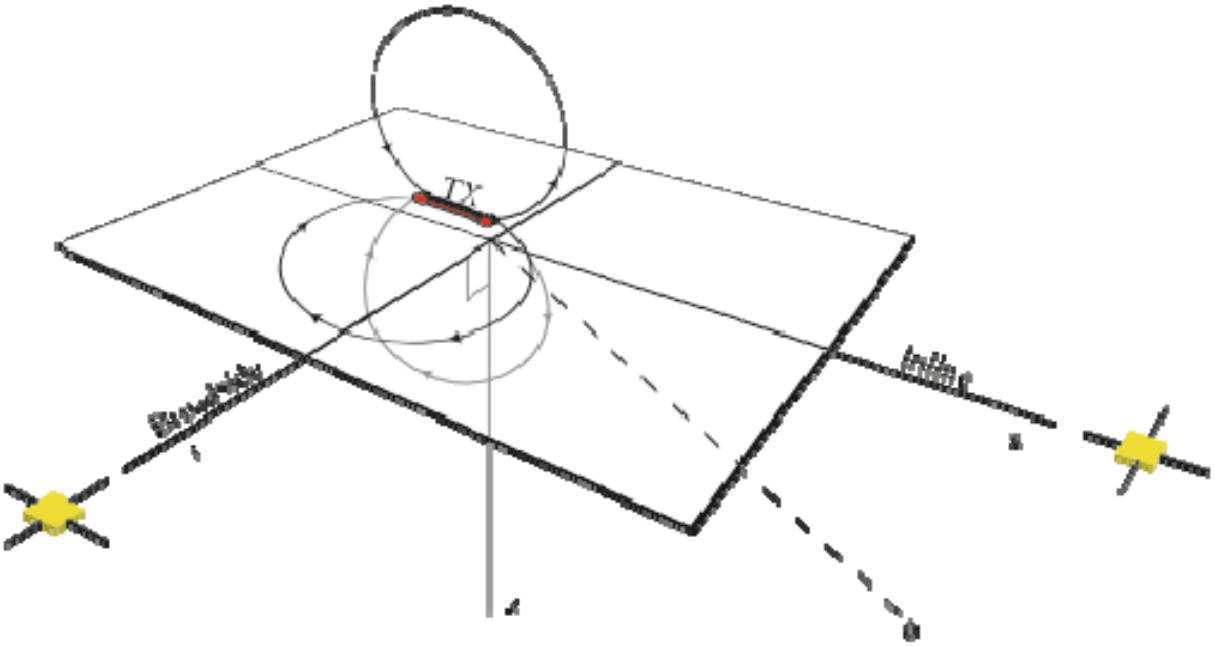

Figure 30: Horizontal electric dipole transmitter (HED). Note that the electric field (arrows) is purely vertical for inline receivers (yellow) and purely horizontal for broadside receivers (from Tinley (2010)

More in-depth interpretation of MCSEM responses must be done by inverse modeling. One-dimensional and two-dimensional modeling and inversion approaches abound in the literature, including the now-famous 1-D model by Chave and Cox (1982), and more recent models by Flosadottir and Constable (1996) and Key (2009). Eidesmo (2002), Metha (2005), and Li and Constable (2007), among many others, have used two-dimensional modeling and inversion to interpret and understand MCSEM responses. Three-dimensional modeling is far less widespread, but approaches include Commer et al. (2008) and Constable and Weiss (2005). Three-dimensional modeling offers the highest resolution results, but at the greatest computational expense.

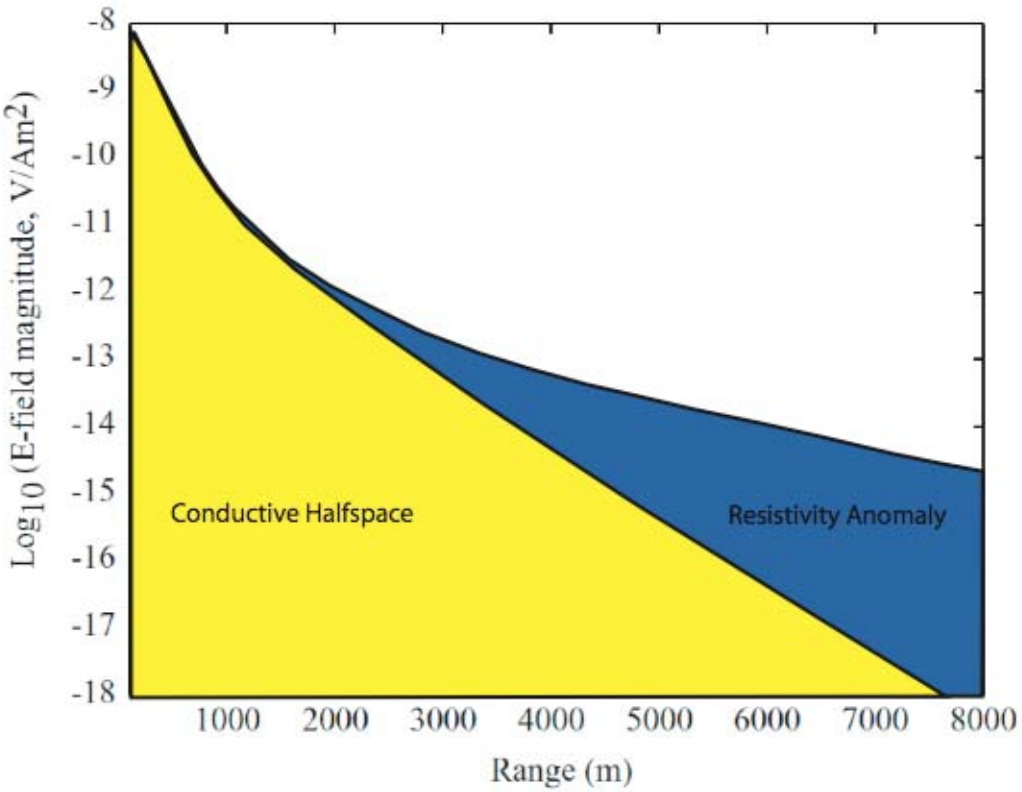

Figure 31: Additional electric field magnitude anomaly attributed to the presence of a resistive later (blue) versus a uniform halfspace. The magnitude is displayed versus offset from the transmitter (MVO) (from Tinley (2010)

Geology of Reservoirs under Study

Location of study

The study area (**Figure 32**) is part of the central Gulf of Mexico continental shelf. In particular, it is the first set of protractions off the coast of Louisiana, and consists of the West Cameron, East Cameron, Vermillion, South Marsh Island, Eugene Island, Ship Shoal, South Pelto, South Timbalier, Grand Island, West Delta, South Pass, Main Pass, Breton Sound, and Chandeleur Sound areas. The study region is located in federal and state waters, and covers approximately 16,344 square miles, following the Louisiana coast from 93.83°W to 88.76°W longitude.

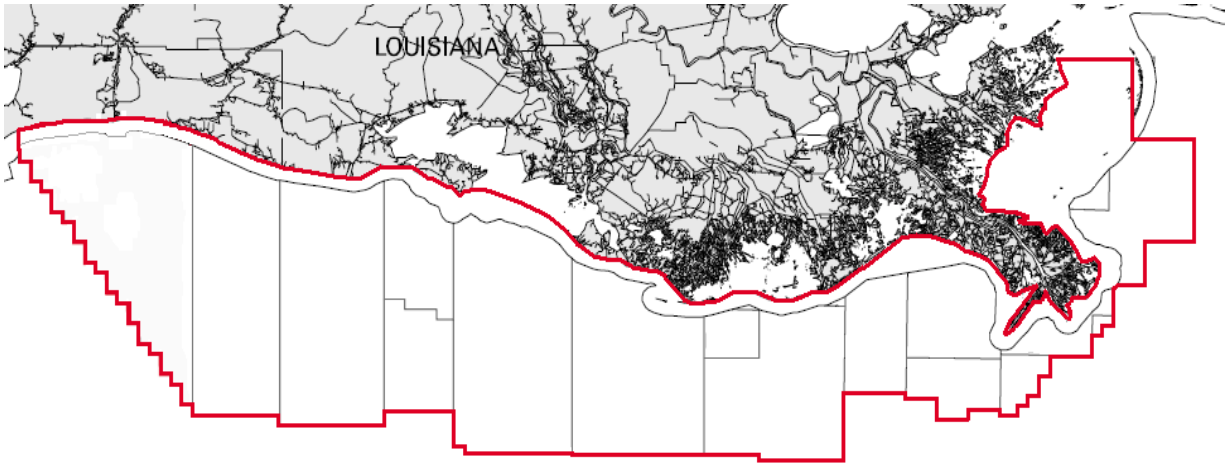

Figure 32: Map of study area (modified from US Department of the Interior, 2000)

Geology

Offshore Louisiana, as defined for this study, is part of the continental shelf, which is a submerged continental margin, and extends to the shelf break or continental slope, where a drastic increase in slope occurs (Sivakumar, 1998). The reservoirs of this area are Early Miocene to Pleistocene in age. The following geological description of the reservoirs used in this study is excerpted from Gueho (2009), and the reader is referred to this thesis for more expansive discussion.

The study area contains sands with good primary porosity and permeability and that are in the proximity of organic-rich source rocks, making offshore Louisiana an excellent target for hydrocarbon exploration. Hydrocarbon production usually occurs in the outer-neritic and slope environments due to extensive deposition and structural activity. The most productive areas within these environments are those associated with alluvial channel fills, delta front sheets and submarine basin floor fans (Sivakumar, 1998). Most traps of the area are due to structure or a combination of structure and stratigraphy, and the typical structural features are diapiric structures, domal structures, roll-over from growth faulting or faulted anticlines. Seals are formed from shelf or prodelta shales (Sivakumar, 1998).

The origin of Gulf of Mexico hydrocarbons is the subject of great debate. Salvador (1991) posits that the source rocks associated with most Tertiary reservoirs are not in direct contact with them. Instead, they are believed to be black, calcareous, thermally mature, marine shales that contain a high amount of total organic content from varying depositional ages with the prominent source coming from Upper Jurassic (Tithonian) sediments. Other sources suggest that these source rocks could have been drained to the Tertiary traps by deep-seated faults and piercement of salt structures (Sivakumar, 1998).

The depositional facies associated with these reserves can be broken into four basic categories: transgressive, aggradational, progradational and submarine fan. Transgressive facies are upward-fining retrogradational packages of thin sandstones that are separated by thicker shales. Aggradational facies are upward-fining thick, blocky stacked sandstone bodies that are separated by thinner shales. Progradational facies are typically upward-coarsening and thickening sandstone bodies that are separated by subequally thick shales. Submarine fan facies contain extremely variable grain sizes and thicknesses, and can occur as singular or stacked packages that are overlain by thick shales (Hunt, 1995). Total hydrocarbon dispersal of the area is not equally divided amongst these facies: progradational 65%, aggradational 31%, submarine fan 4% and transgressive 1% (John et al., 1996).

The determination of depositional facies allows for a better understanding of the depositional environments. Using this information, a general external form of the facies can be determined and related to reservoir geometry. Since the location of depositional facies has been previously defined by Hunt (1995), reservoir geometries can also be estimated for these areas. The basic depositional environments of the area are channels, levees, overbank deposits, lobes, mass transport complexes and debris aprons, therefore only four basic external forms/geometries are present: sheets, wedges, lens and mounds (Weimer, 1996).

The oldest reservoirs penetrated in the study area are in Early Miocene sediments, which are restricted to the Texas-Louisiana border near the present day shoreline. They are composed of progradational and submarine fan facies. The earliest sediments of this time are the result of the basinward edge deposits of the ancestral Mississippi delta. The major deltaic depocenter was located landward of the present day shoreline and was gradually moving basinward. Hydrocarbons are present throughout this unit (Hunt, 1995), but appear to be more abundant landward.

The Middle Miocene contains the earliest productive aggradational and transgressive depositional facies of the area. The paleoshoreline had prograded to the location of the present day western Louisiana shoreline. All four depositional facies were being deposited during this time. Progradational sediments were being deposited east of the present day Mississippi River, while submarine fan sediments were being deposited to the South Pass and Viosca Knoll areas. As time progressed, productive aggradational facies became more concentrated at the location of current shoreline, while progradational and transgressive facies become more extensive. By the end of the Middle Miocene, the productive sediments extended from western Louisiana to east of the current Mississippi delta. However, no transgressive sediments deposited during this time are responsible for hydrocarbon production (Hunt, 1995).

The Late Miocene represents a time in which the Mississippi River's depocenter migrated westward and had deposition significantly more basinward than in previous times. The shoreline originated near the present day central Louisiana area and prograded basinward. The lower portion of this unit contains minor amounts of hydrocarbons in progradational facies. By the end of the Neogene, extensive hydrocarbons were present in progradational, aggradational facies and especially submarine fan facies (Hunt, 1995).

Similar to the Miocene, the major depocenter of the Pliocene remained in the same general area, and the productive units include all four depositional facies. However, they extend farther basinward than the Miocene facies. Two major hydrocarbon trends containing progradational and submarine fan facies are prominent from this time period. The progradational trend is located along the current day Louisiana shoreline, and the submarine fan trend is located outside the study area in the Garden Banks and Green Canyon areas (Hunt, 1995). Pliocene reservoirs are numerous and laterally extensive, and are associated with the largest percentage of salt domes in comparison to other stratigraphic units of the area. Sedimentation during this time was voluminous, and was the last episode of major deposition in the Gulf Coast Basin (Sivakumar, 1998).

The final productive stratigraphic unit is the Pleistocene, which is Early Quaternary in age. Early Pleistocene sediments are responsible for the majority of production from this unit, and these reservoirs occur in the southern most portions the study area. Similar to previous times, all four depositional facies are present and responsible for hydrocarbon production. Sedimentation rates were approximately 94 in/yr, which allowed the clastic wedge of the Louisiana shelf to increase from 1,000 ft to almost 5,000 ft in thickness.

The geologic conditions present during the Plio-Pleistocene were very similar to current conditions, because the Mississippi River flowed into the Gulf of Mexico and deposited sediments, however during low sea-level; it eroded submarine canyons into the outer shelf and continental slope. This process allowed for coarser sediments to be carried beyond the shelf to the continental rise, submarine fans and abyssal plains. Over this period, the main depocenter of the Mississippi delta shifted 186 miles southwestward of the present mouth of the Mississippi to the shelf edge south of the Louisiana-Texas border. The result of this shift was 50 miles of progradation of the continental shelf edge to its current location near the 655 ft isobath (Sivakumar, 1998).

Probabilistic Characterization of Off-shore Louisiana Gulf of Mexico Reservoirs

Central to the concepts of simplified modeling is a maximally descriptive, yet minimally parameterized account of that which is to be modeled, which in this case is the "typical" off-shore Louisiana Gulf of Mexico hydrocarbon reservoir. Furthermore, successful Bayesian inversion requires a probabilistic description—usually a probability density function (pdf)—of each parame-

ter. Here, we establish a coordinate system with which we describe encountered, known, producing reservoirs, and provide statistically derived probabilistic descriptions of those reservoirs. Though these pdfs are applicable only to the off-shore Louisiana region, the method itself is region-agnostic, and can easily be applied to other areas given sufficient statistical information. New, relevant pdfs can be generated for different regions.

Reservoir data source

Reservoir information was taken from publicly available data, with the exception of the reference map from which the likelihood of reservoir occurrence was computed. The electrical properties and reservoir depths were determined from 194 well logs (291 reservoirs) that were obtained through Louisiana Department of Natural Resource's online data base, SONRIS (Strategic Online Natural Resource Information System). These logs were chosen because they contained both resistivity measurements and scout report information that included depths of successful perforations. The geometry data was obtained from 23 major oil and gas fields that contained 74 reservoirs in *Offshore Louisiana Oil and Gas Fields: Volumes 1 and 2*, which contained structure maps, type logs, seismic lines, and cross-sections of the reservoirs. The likelihood of reservoir occurrence was determined from maps of offshore Louisiana reservoirs supplied by Plains Exploration and Production. This was the only proprietary source used.

Nonparametric probability density estimation

Because we cannot make any *a priori* assumptions about the distribution of reservoir geometric and electrical properties, we describe the distributions instead nonparametrically. Kernel density estimation (KDE) is selected to construct the pdfs. As the name implies, KDE builds a pdf out of a summation of kernel functions φ centered at observed data values. Overlapping kernels from adjacent or coincident observations increase the contribution of that observed value to the pdf. To maintain an area of 1, the summation is scaled by the inverse number of observations. The formula for estimated pdf is defined as:

$$\hat{f}(x) = \frac{1}{Nh^d}\sum_{i=1}^{N}\phi\left(\frac{1}{h}(x - x_i)\right)$$

where, N is the number of observations, x_i is observation i, d is the number of dimensions, h is the bandwidth of the kernel functions (Hwang, 1994). Kernel function choice is arbitrary, but Gaussian kernels are commonplace. Bandwidth choice is critical: if the width is too narrow, an unrealistic number of modes will appear in the pdf. If the width is too broad, the pdf becomes overly generic (see **Figure 6**). Empirically (Hwang, 1994), a good bandwidth choice is:

$$h = AN^{\frac{1}{d+4}} \qquad where \qquad A = \left[\frac{4}{2d+1}\right]^{\frac{1}{d+4}}$$

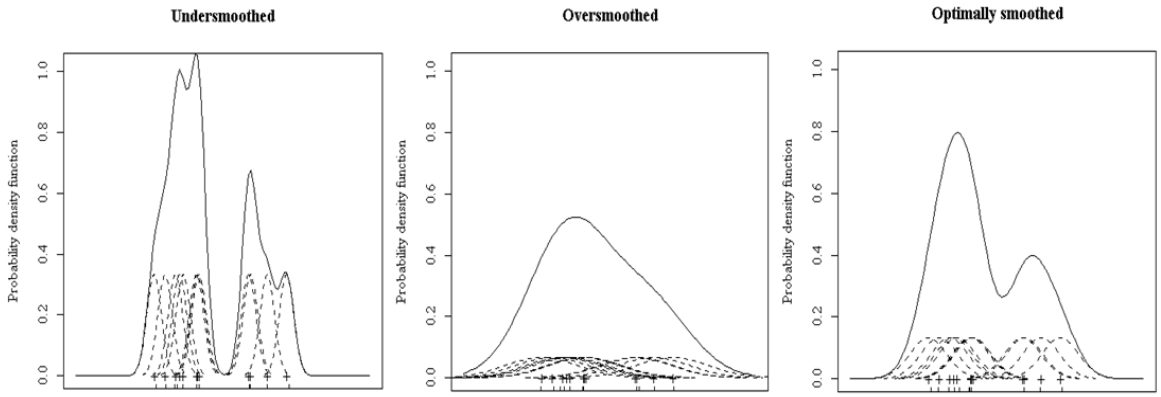

Figure 33: Kernel density estimation (KDE) and the effect of bandwidth variation (modified from Duong, 2001)

Reservoir and host electrical properties

Electrical parameters were gathered from available resistivity well log data. Though, massive amounts of resistivity logs exist, only logs with associated scout reports detailing successful perforations (with or without associated resistivity anomalies) could be used. Because of this requirement, our study was limited to wells drilled after 1990, due to the lack of scout reports before this time. In total, 194 resistivity logs, containing 291 reservoirs, were surveyed.

Raster images of well logs were downloaded from SONRIS and imported into NeuraLog for digitization. The digitized logs were exported as log ASCII standard (LAS) files and imported into Microsoft Excel. The LAS files contained the resistivity measurements in 0.5 foot intervals. The approximate depth and thickness of each encountered reservoir were determined from accompanying scout report information. This allowed us to separate host and reservoir resistivity properties as well, compiling those values into separate databases for later KDE pdf computations.

Reservoir geometry

One of the most challenging aspects of this project was determining a common coordinate system or prototype onto which all GoM reservoirs could be projected and measured. Obviously, real reservoirs are complexly shaped, but the low resolution of MCSEM warrants the assumptions that most of the detailed nuances of reservoir shape are negligible.

After observing data and some reflection, our so-called prototype hemi-ellipsoid model was designed. We assume that all reservoirs encountered could be described as a section of an hemi-ellipsoid, where all pinch-outs fall on ellipsoid edges, and fault closures are described by a subtended angle or chord across the elliptical plan view (see **Figure 34**). Therefore, the reservoir geometry is described by two principal axes, two angles describing the starting and ending of the subtended angle, and a radius that define the radial extent of the reservoir. **Figure 34** illustrates four radii, but in practice, only a single radius was necessary.

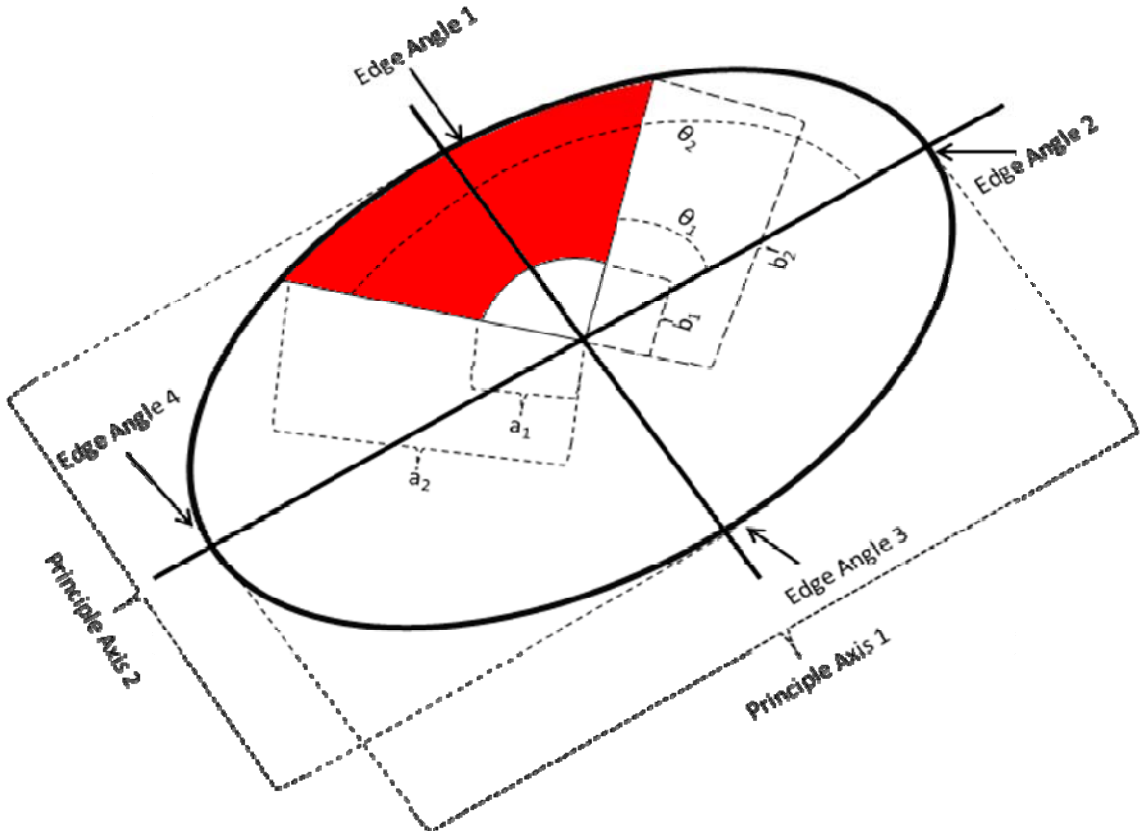

Figure 34: Plan view of a prototype hemi-ellipsoid reservoir geometry model. The model defines geometry using principle axis lengths, radii, angular extent, and edge angles

In section view, initially four edge angles were used to define reservoir geometry. Faults were assumed to dip at 45° for simplicity. Later revisions of the model were simpler, defining the vertical axis of the ellipse instead. The revised model allows the means to define a vertical radius, so that the final reservoir body no longer has an unrealistic flat bottom (**Figure 35**), and can be made to conform to strata. The statistics and derived pdfs in this report were, however, computed before the new ellipsoid model was developed.

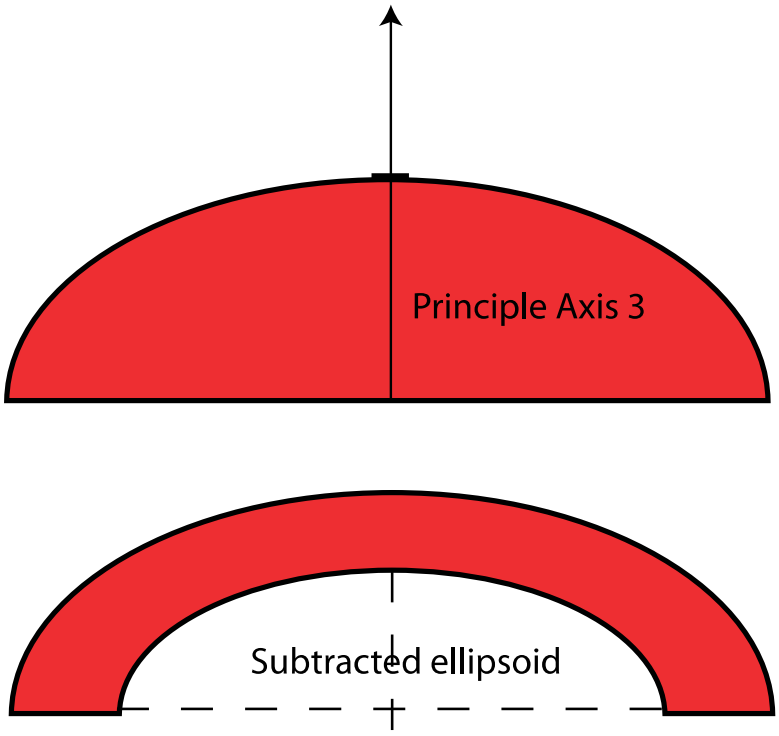

Figure 35: For the new prototype hemi-ellipsoid model, the plan view remains unchanged, but the cross-sectional view is now defined only in terms of a third principal axis, rather than edge angles (top). This allows the specification of subtracted ellipsoid (bottom), allowing the reservoir to follow local stratigraphy

Geometric parameters were measured on structural maps, seismic lines, and cross-sections of 23 major oil and gas fields containing 74 reservoirs, as reported in *Offshore Louisiana Oil and Gas Fields: Volumes 1 and 2.* Assuming, as discussed above, flat reservoir bottoms, cross-sections were produced for each reservoir, and simple trigonometry was used to determine edge angles, as in **Figure 36**. In plan view, an ellipse was fit by eye, and the remaining parameters determined. Examples are given in **Figures 37** and **38**. More accurate parameter determination could be done by least squares fitting in the future. Not coincidentally, the prototype ellipsoid model corresponds well with Weimer's (1990) four basic reservoir geometries expected in our study area (see **Figure 39**).

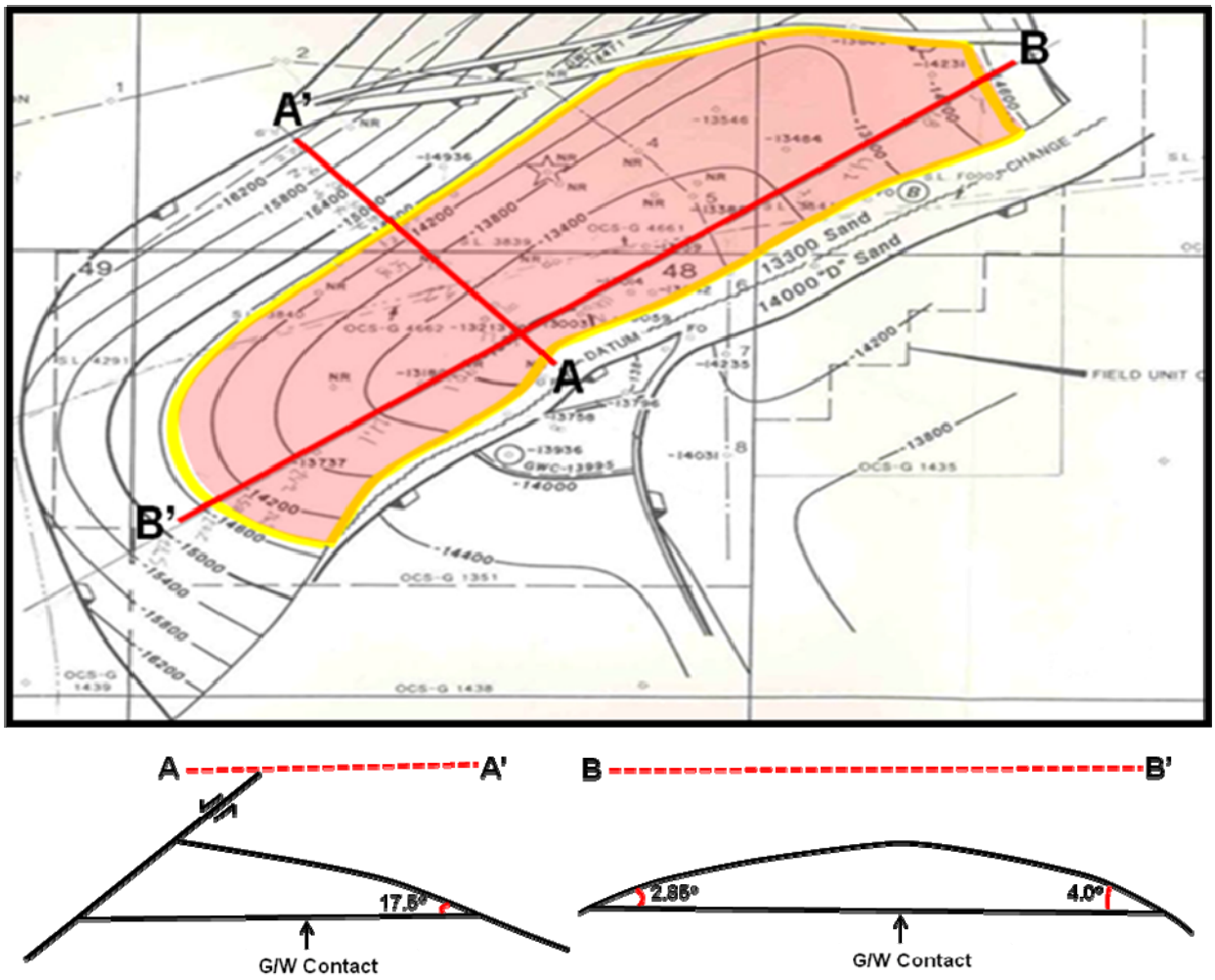

Figure 36: Determination of edge angles from structure maps (modified from New Orleans Geological Society, 1988)

Reservoir occurrence

Finally, we determined the probability that a reservoir will be found at any given location within the study area. To determine this probability, maps detailing the size and shape of all known offshore Louisiana reservoirs were digitized using Plan Plus 2002 and a Cal Comp Drawing Board III. Once digitized, the software calculated the total area of each protraction and reservoirs in each. The total area of each was tabulated, and the fractional area occupied by reservoirs was computed as a probability.

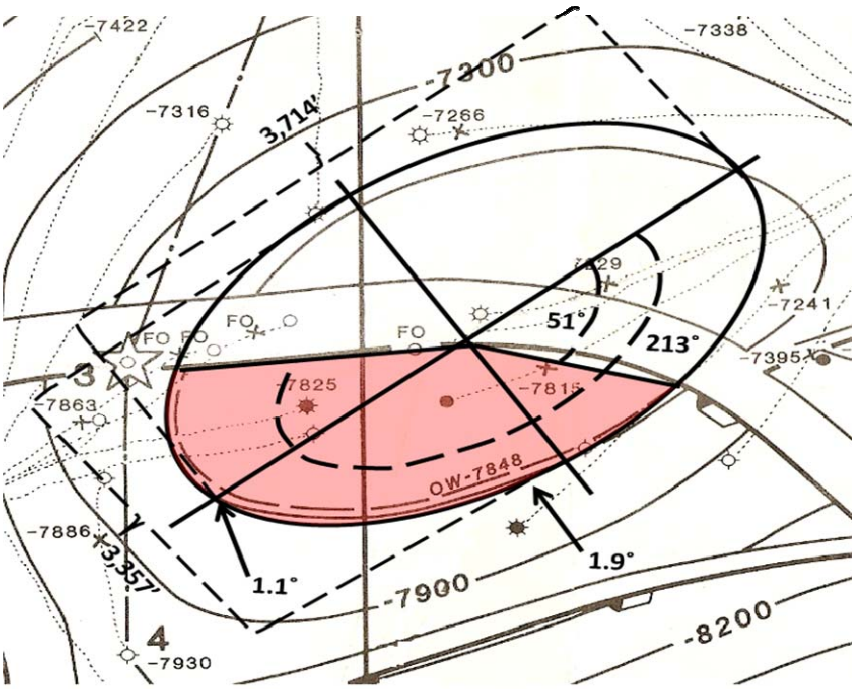

Figure 37: Example reservoir defined using the prototype ellipsoid model (modified from New Orleans Geological Society, 1988)

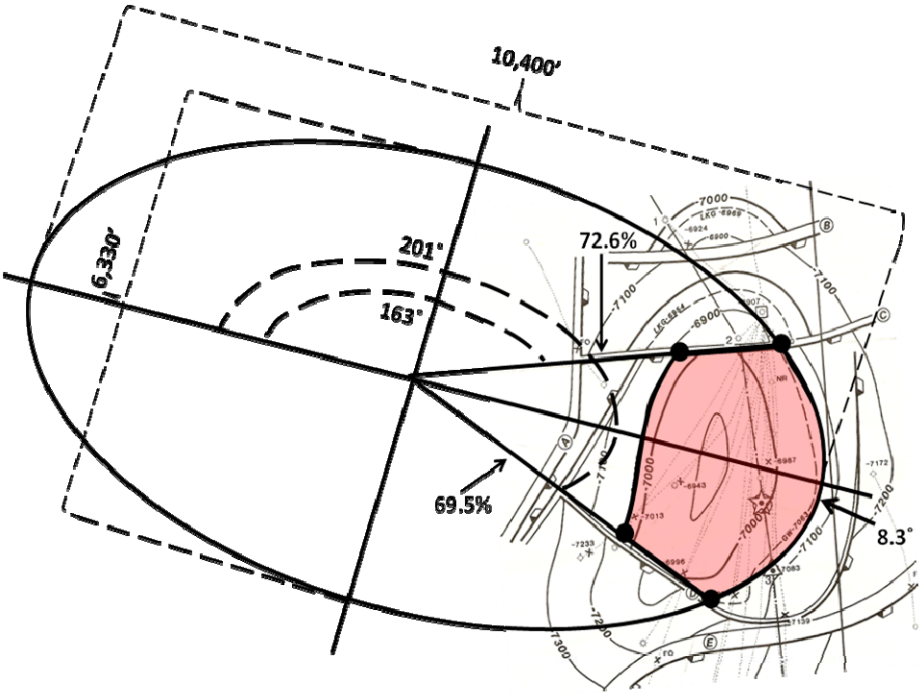

Figure 38: Example reservoir defined using the prototype ellipsoid model (modified from New Orleans Geological Society, 1988)

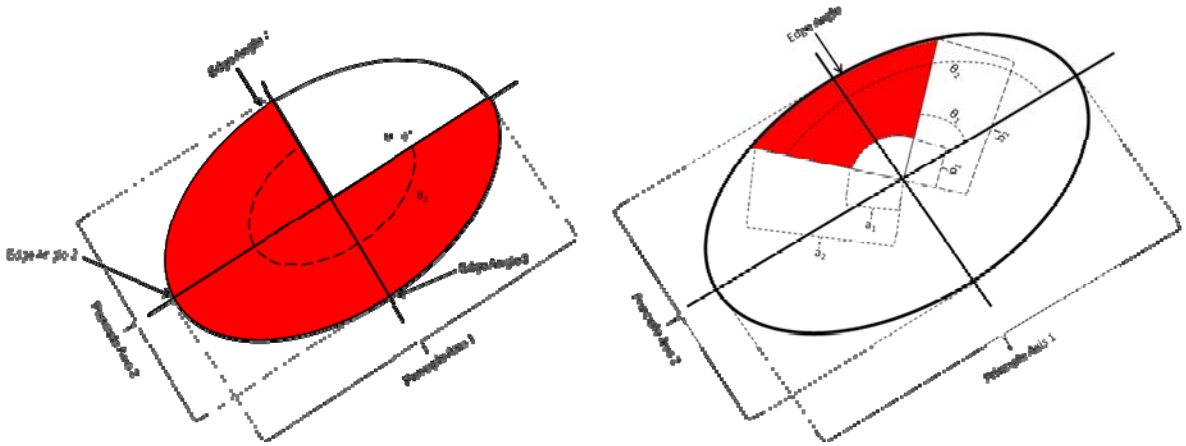

Figure 39: Example reservoir defined using the prototype ellipsoid model (modified from New Orleans Geological Society, 1988)

Probability density functions

The observed values of all parameters, geometric and electrical, were used to derive pdfs using KDE. A multidimensional KDE algorithm was written in Matlab after Hwang (1994). Though the algorithm was fully capable of generating multidimensional, joint pdfs, each parameter was treated as independent. In particular, there is no compelling reason to believe that the geometric and electrical parameters are correlated. It could be argued that the geometric parameters could be correlated through geological origin. However, the independence of the pdfs was tested as described later. Histograms and pdfs for each property are illustrated below, with histogram bin width defined by Scott (1979);

$$W = 3.49\sigma N^{-\frac{1}{3}}$$

where, σ is standard deviation and N is sample size.

Electrical properties

The pdfs for host and reservoir resistivity are well-defined. The observation set consisted of 295,680 feet of host resistivity measurements and 15,493 feet of reservoir measurements.

- The **host resistivity** pdf (**Figure 40**) is normal-like with a maximum at 0.7 ohm-m.
- The **reservoir resistivity** is a bit more complex (**Figure 41**), appearing trimodal with maxima at 1.17, 11.4, and 21.8 ohm-m. The lower resistivity measurements are the result of low resistivity pay reservoirs, which are defined as having deep-resistivity log values from 0.5 to 5.0 ohm-m. The main factor for these low values is the presences of clay, which causes an increase in fluid conductivity (Boyd et al. 1995). It appears that low resistivity pay reservoirs are 7 times more likely to occur than the 10-15 ohm reservoirs.

Reservoir depth

The distribution of reservoir depth is irregular, suggesting that the distribution is in fact uniform. The multimodal appearance may be attributed to a dearth of data (**Figure 42**).

Reservoir geometry

The most common cause of variation among reservoir geometry attributes appears to be faulting. In particular, this is because growth faulting plays a role during deposition and acts as a trapping mechanism.

- The **edge angle** pdf is a bimodal, normal-like distribution with maxima at 1.72° and 10.8° (**Figure 43**).
- The **angular coordinates** (labeled θ in **Figure 34**) are bimodal and normal-like. The first angle has maxima at 10° and 162°. The second angle has maxima at 161° and 360° (**Figures 44** and **45**).
- The **principal axis** pdfs are normal like with a major axis maximum at 9400 feet, and a minor axis maximum a 5225 feet (**Figures 46** and **47**).
- The **radial coordinate** pdf is normal like with a maximum at 0 (**Figure 48**).

Reservoir occurrence

The probability of a reservoir occurring at any given location in the study area is 0.0972. The results for each protraction are in **Table 1**.

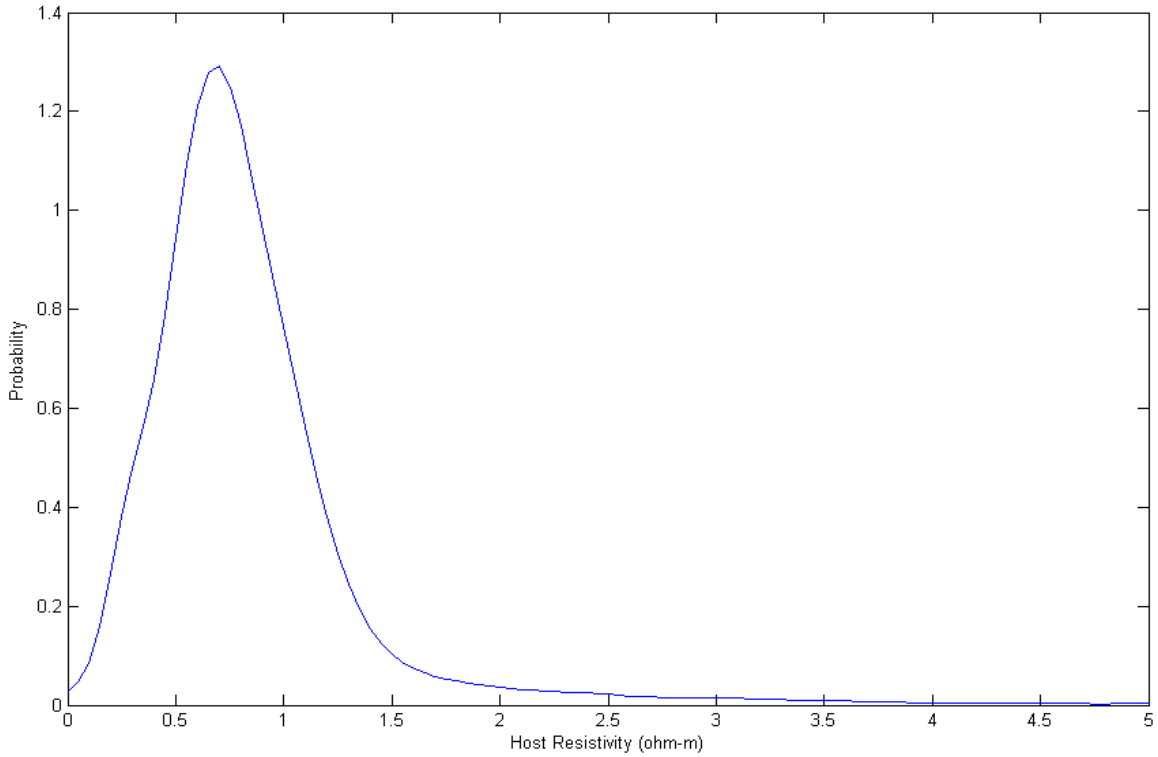

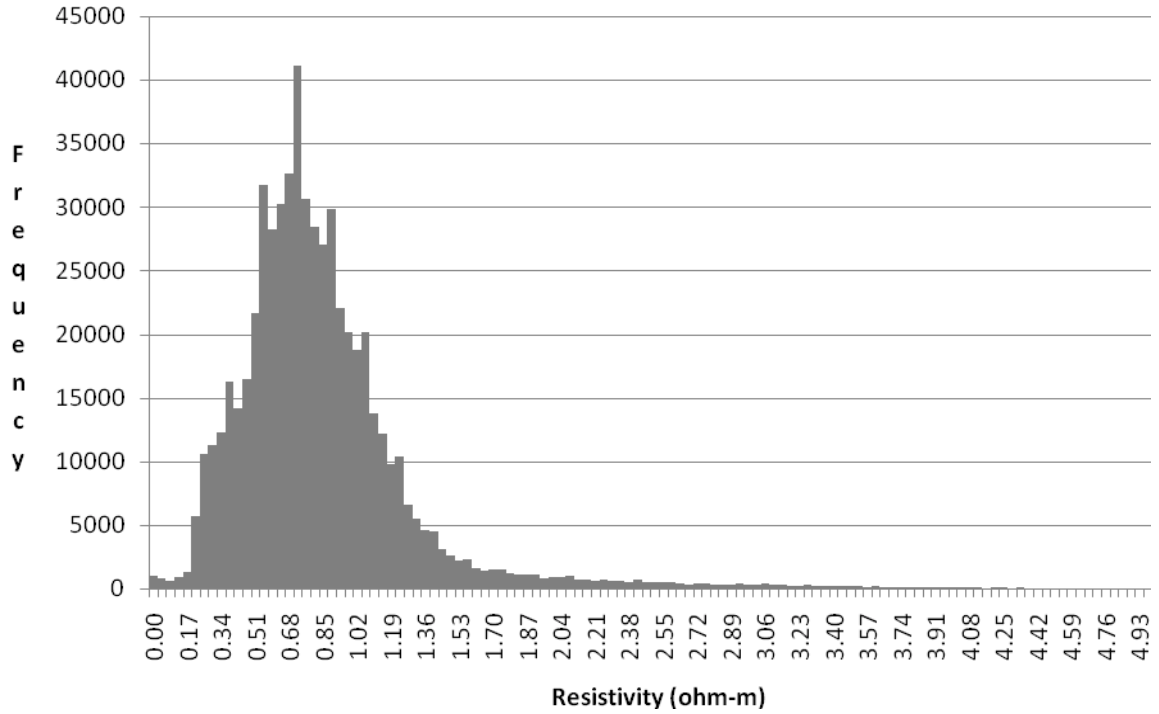

Figure 40: Host resistivity pdf (top) and histogram (bottom)

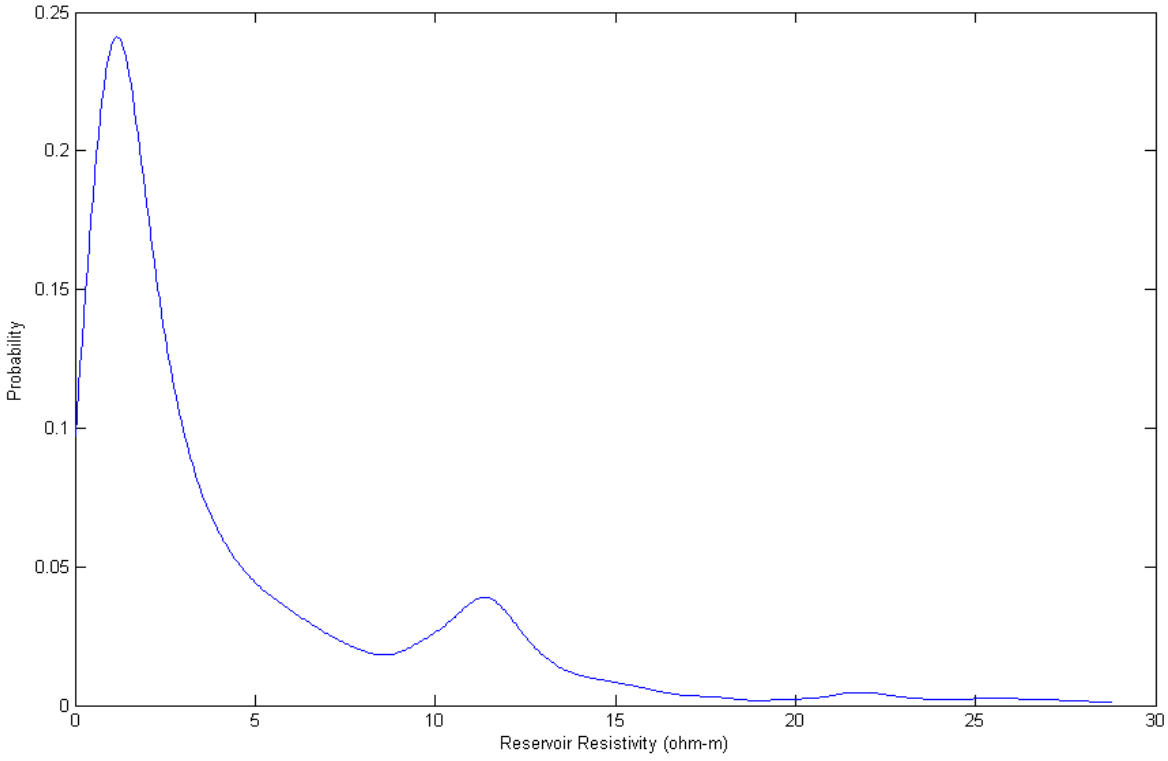

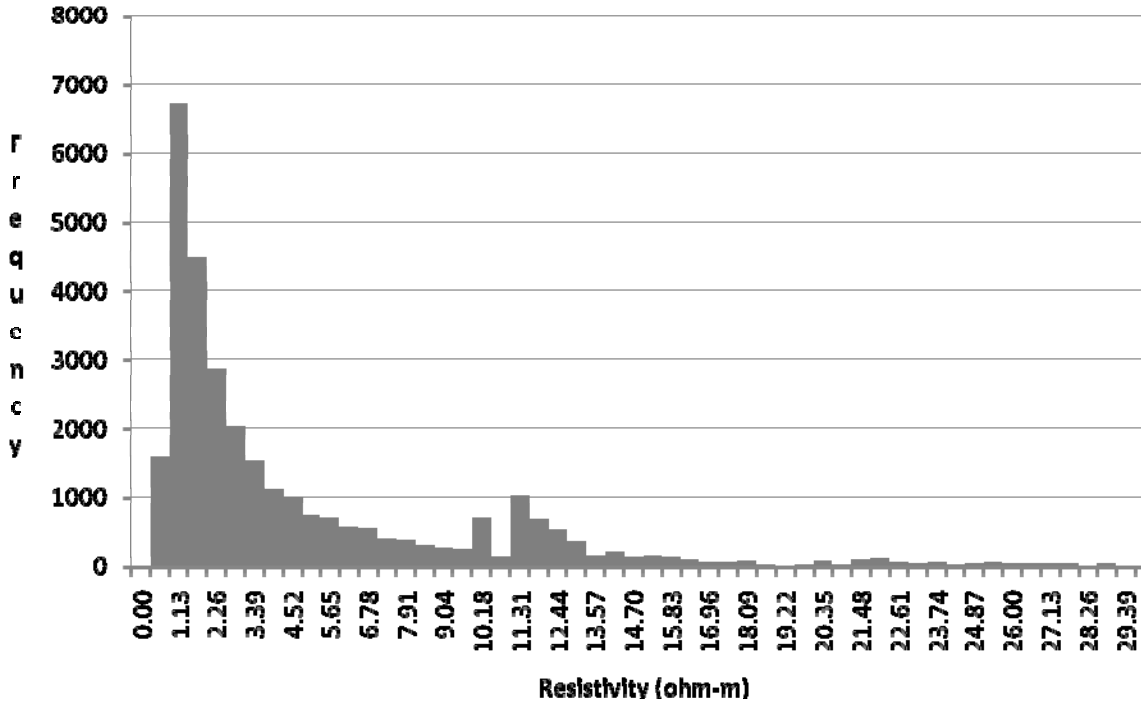

Figure 41: Reservoir resistivity pdf (top) and histogram (bottom)

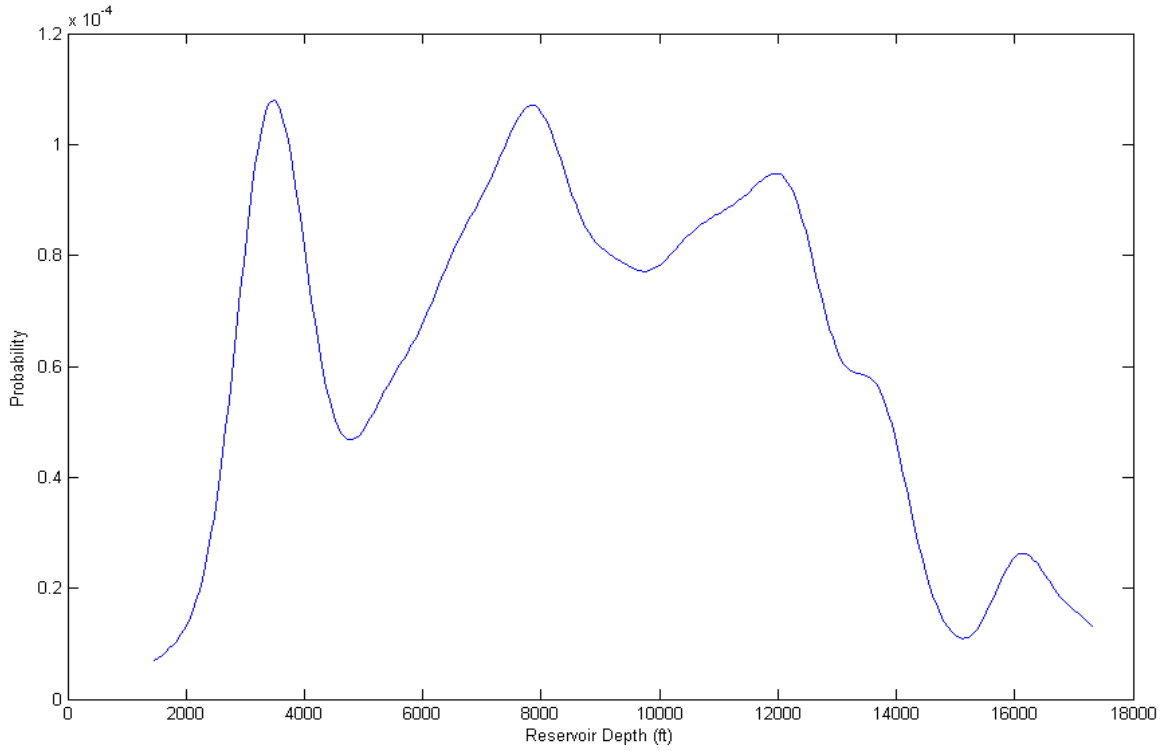

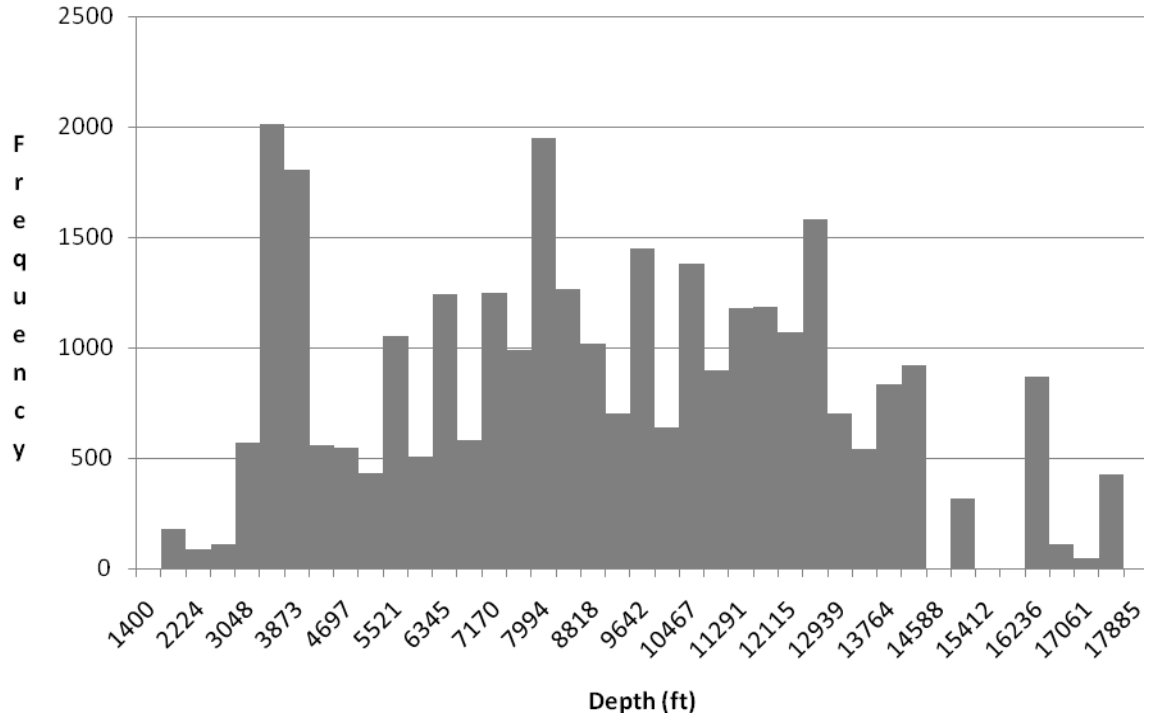

Figure 42: Reservoir depth pdf (top) and histogram (bottom)

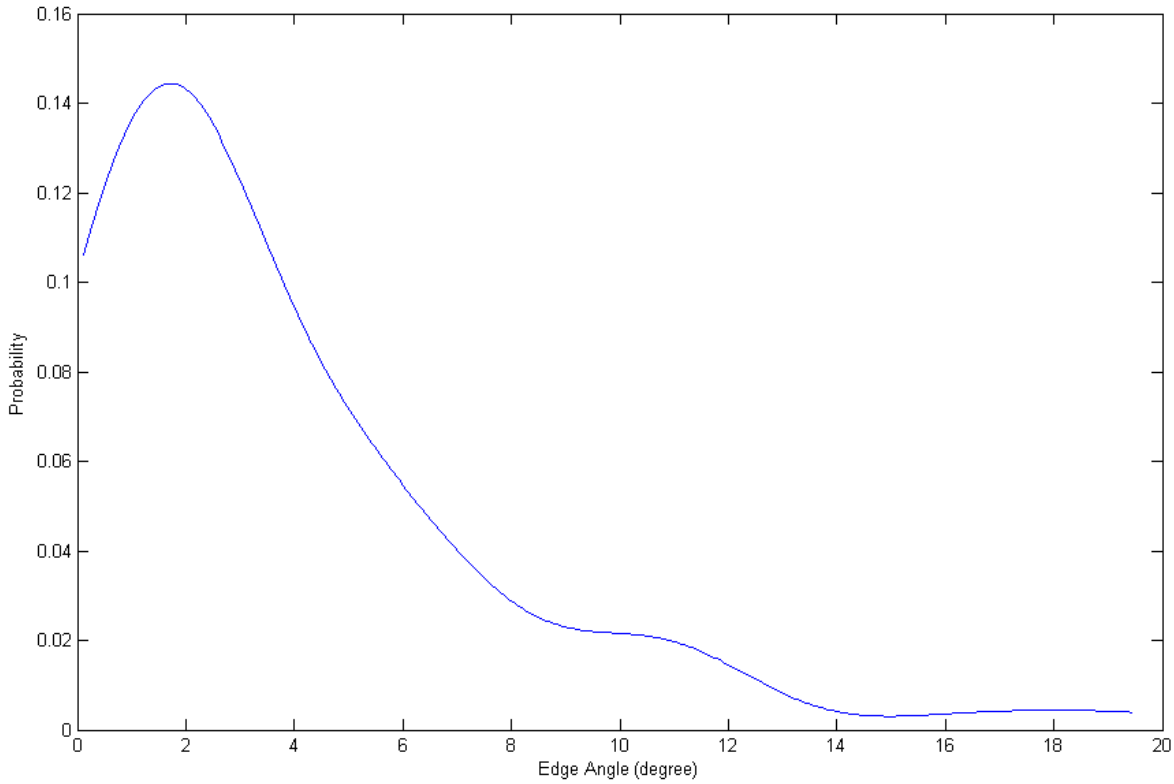

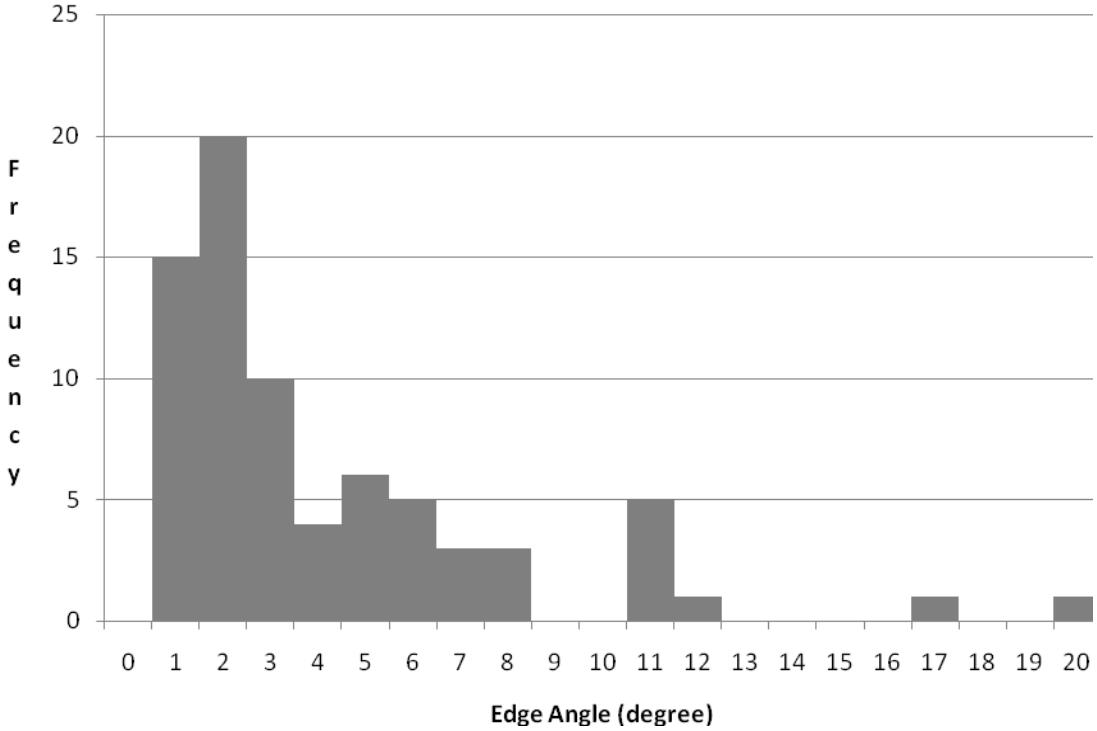

Figure 43: Reservoir edge angle pdf (top) and histogram (bottom)

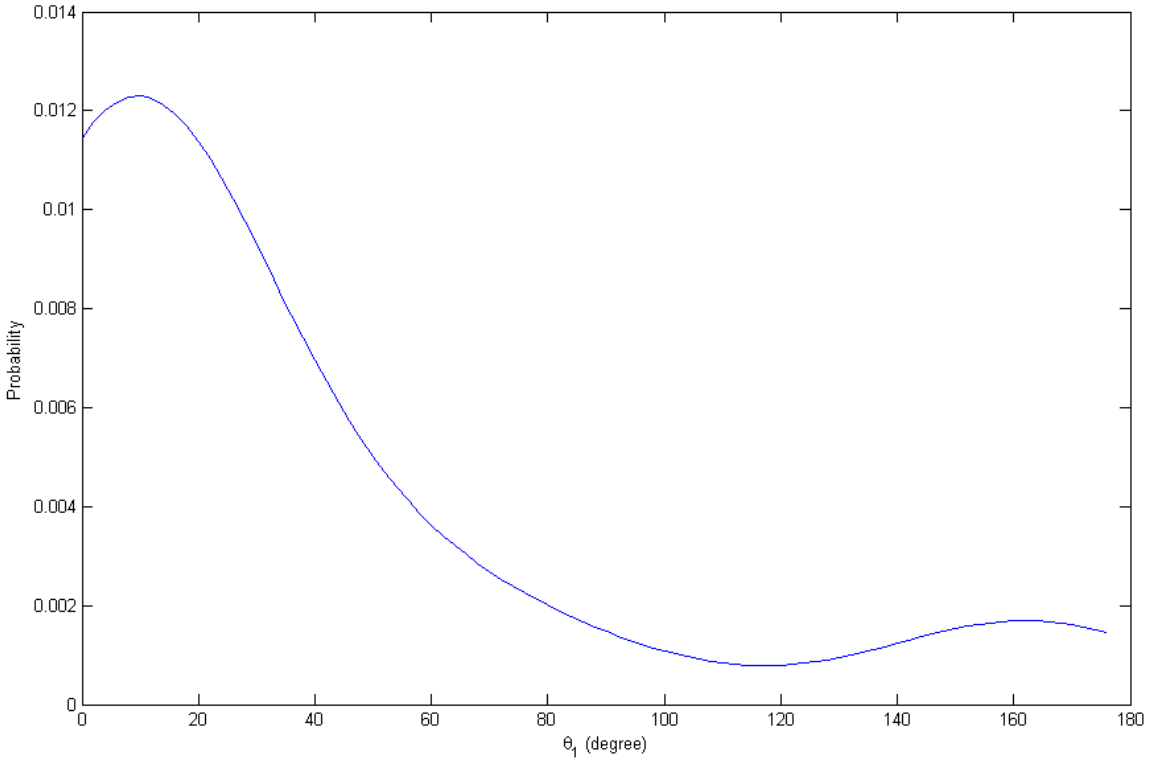

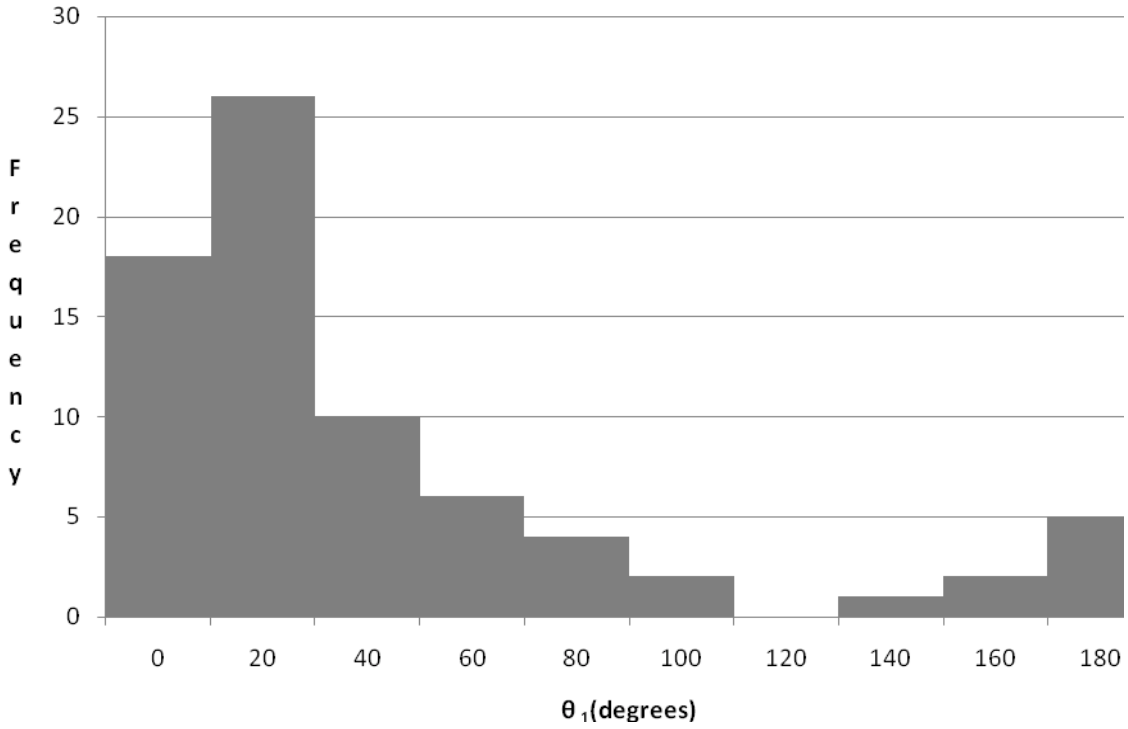

Figure 44: Reservoir angular coordinate θ_1 (see figure 7) pdf (top) and histogram (bottom)

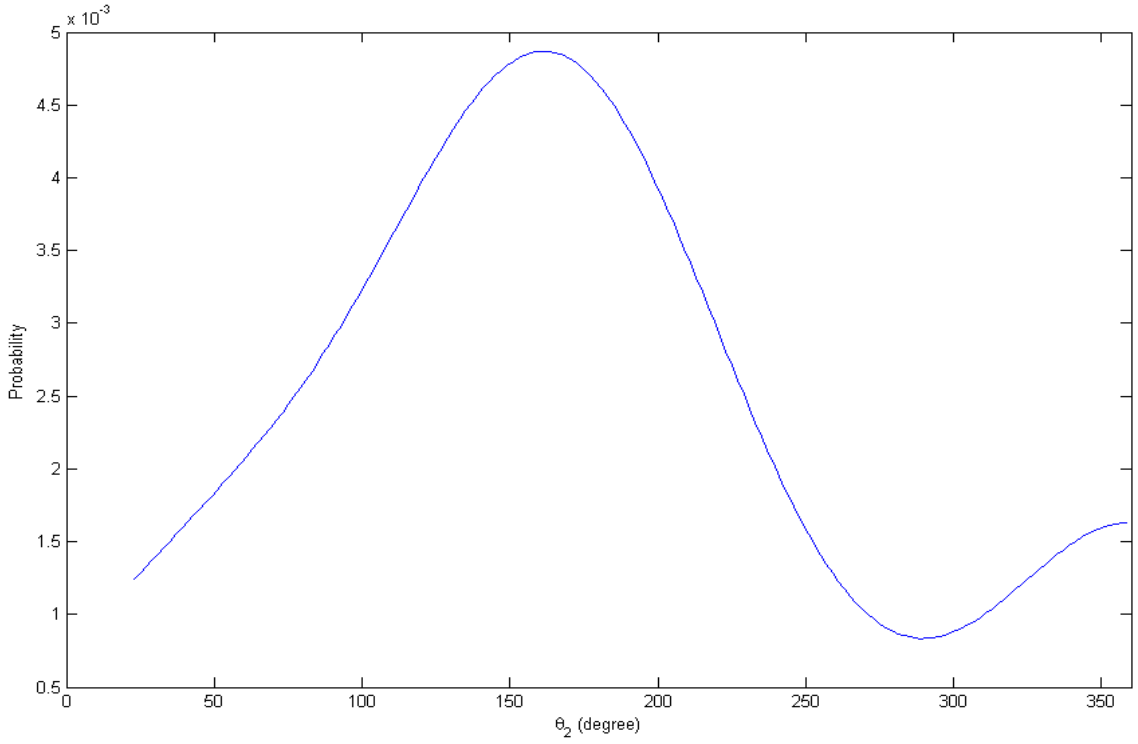

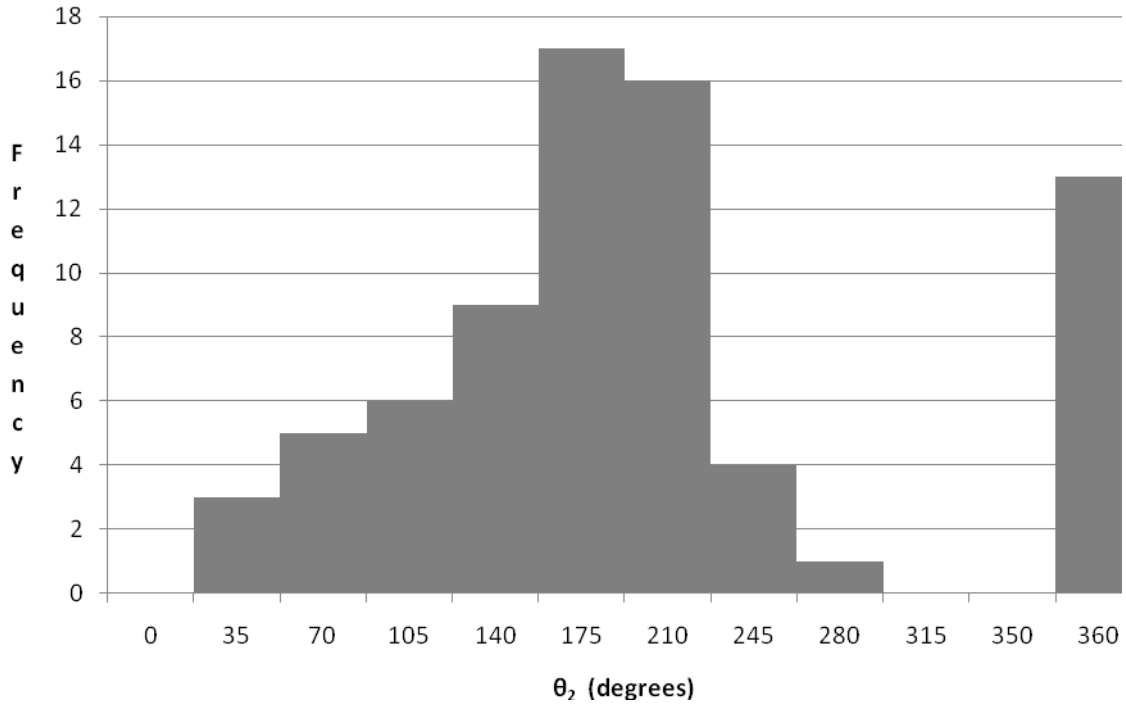

Figure 45: Reservoir angular coordinate θ_2 (see figure 7) pdf (top) and histogram (bottom)

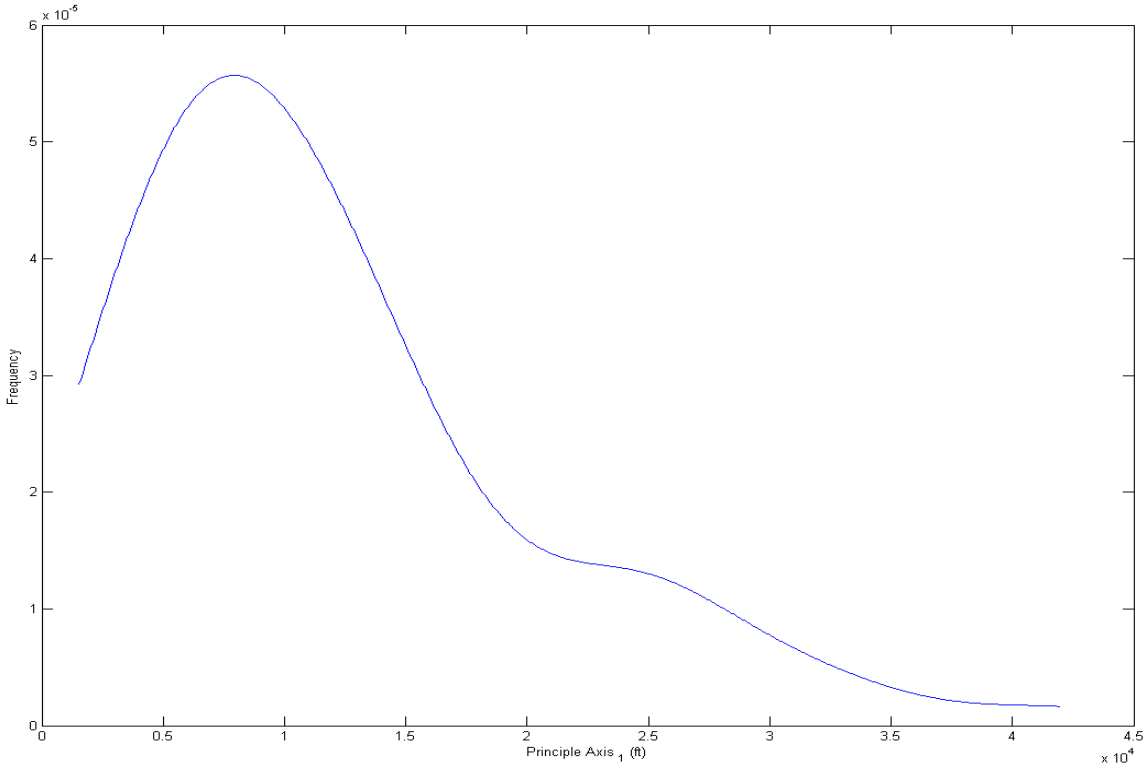

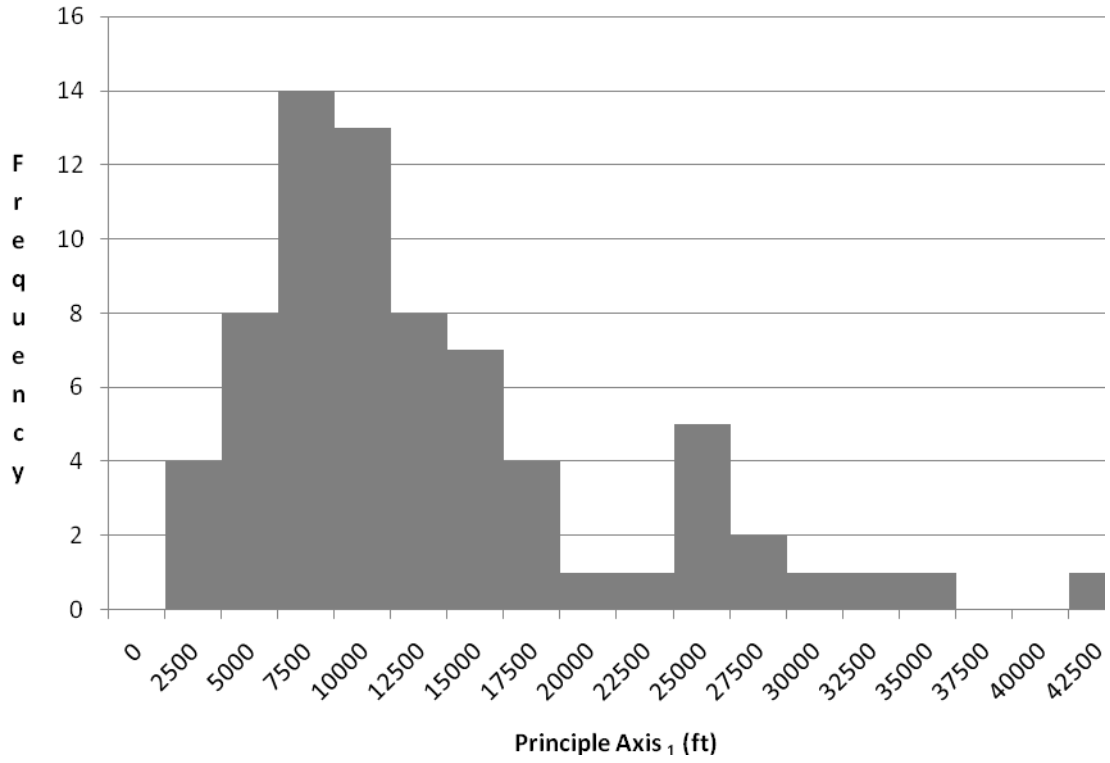

Figure 46: Reservoir major principal axis pdf (top) and histogram (bottom)

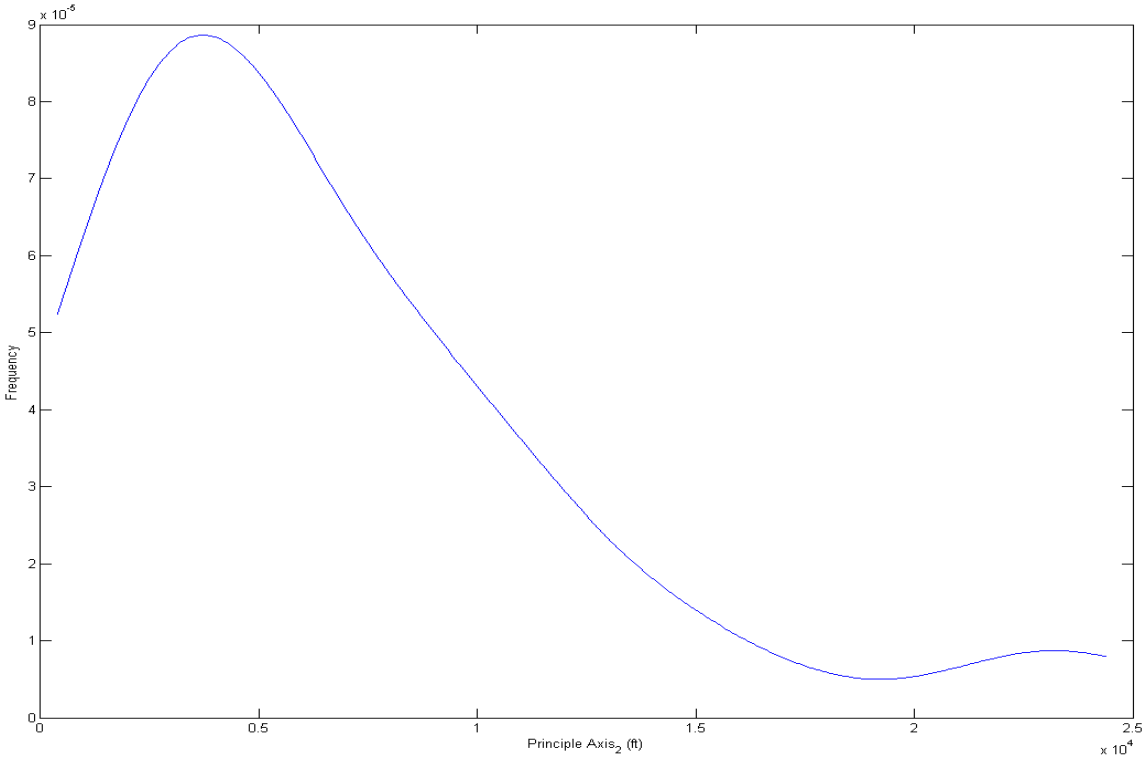

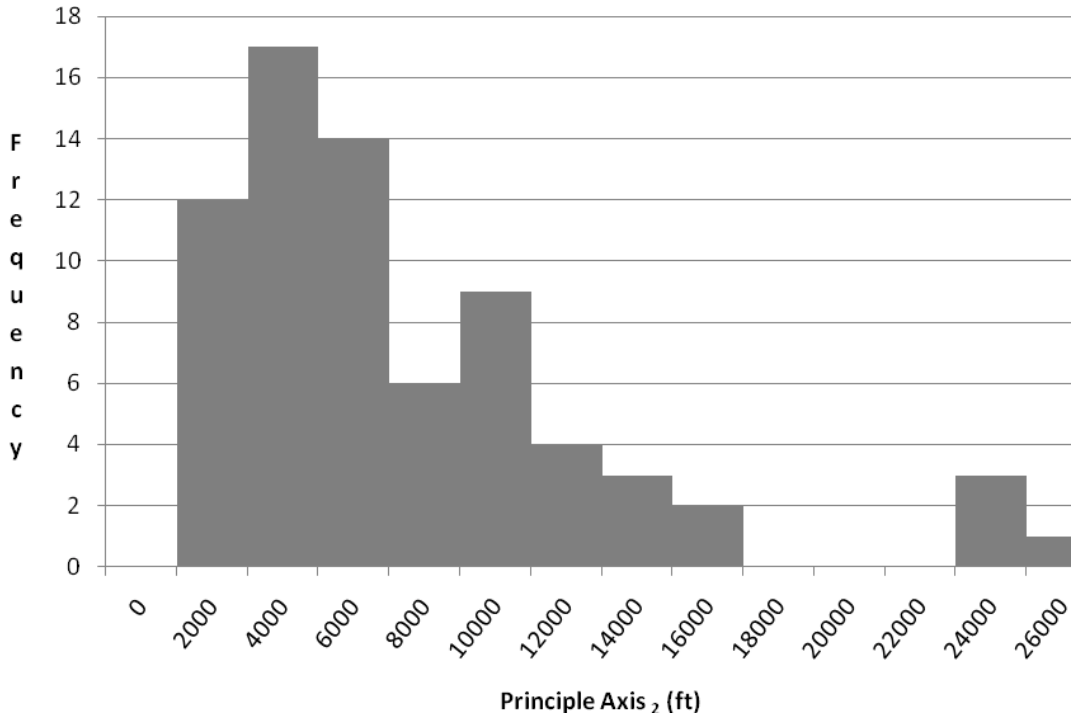

Figure 47: Reservoir minor principal axis pdf (top) and histogram (bottom)

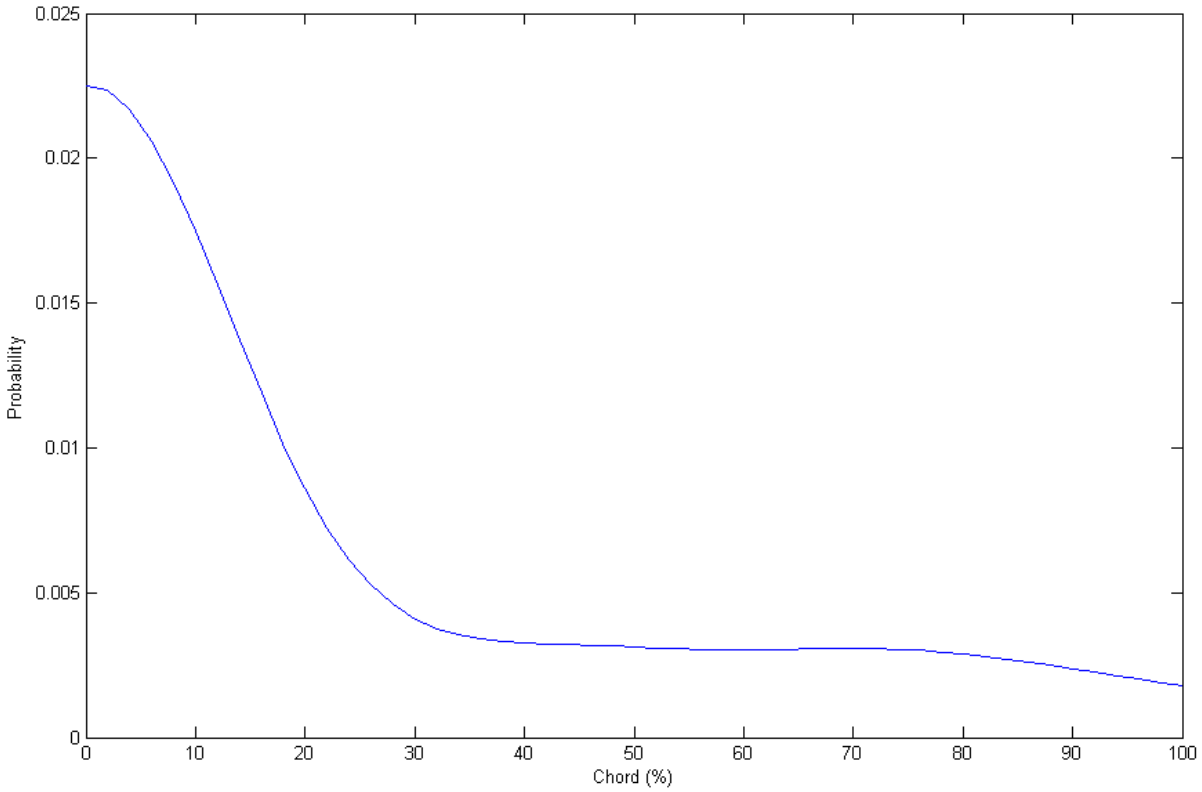

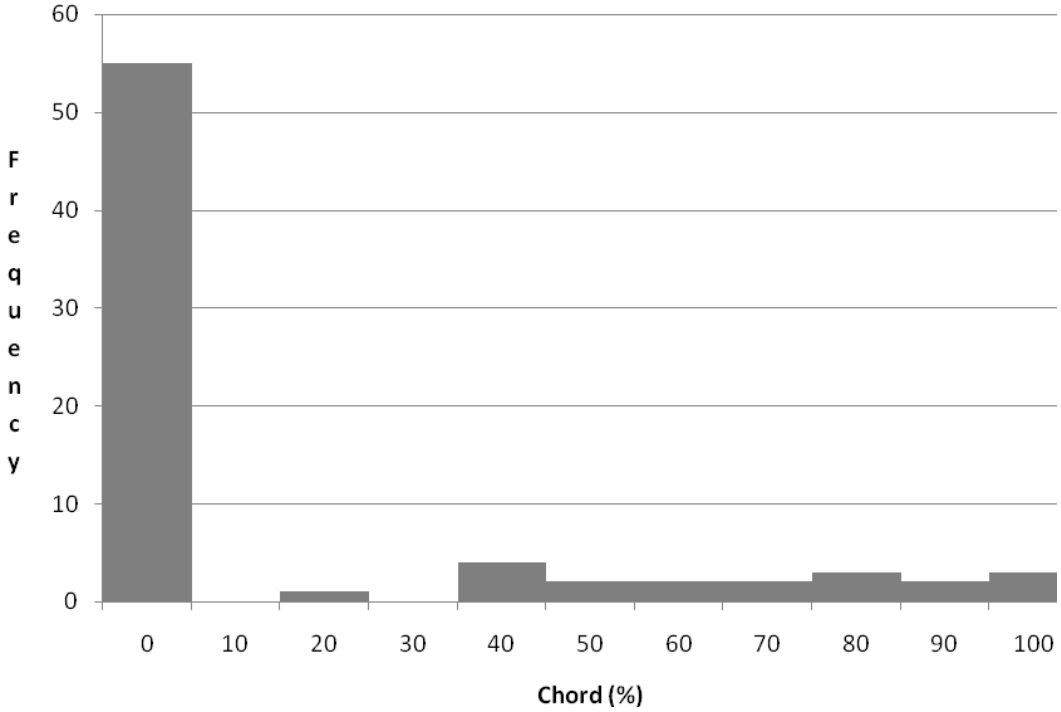

Figure 48: Reservoir radial coordinate pdf (top) and histogram (bottom)

Table 23: Probability of reservoir occurrence by study area protraction

Protraction	Total Area (acres)	Reservoir Area (acres)	Percent
West Cameron	1271652	126907	9.98%
East Cameron	1093363	73648	6.74%
Vermillion	1205408	96695	8.02%
South Marsh Island	766706	81906	10.68%
Eugene Island	1367503	120000	8.78%
Ship Shoal	1146112	93223	8.13%
South Pelto	125508	13442	10.71%
South Timbalier	969980	109530	11.29%
Grand Isle	398080	42671	10.72%
Chandeleur Sound	334112	13729	4.11%
West Delta	501689	84447	16.83%
South Pass	265593	43628	16.43%
Breton Sound	278100	28678	10.31%
Main Pass	736258	87756	11.92%
Totals	10460064	1016260	9.72%

Statistical Testing of Parameter pdfs

Independence testing

Intuitively, the electrical parameters characterizing off-shore Louisiana GoM hydrocarbon reservoirs should be independent of geometric parameters. However, we cannot assume that the geometric parameters are independent from one another. Data support for a multidimensional, joint geometry probability is insufficient, so that independent pdfs are desirable. By definition, two parameters are independent if the joint pdf is equal to the multiplication of each individual pdf:

$$f(x_1, x_2, \ldots, x_N) = f(x_1)f(x_2)\ldots f(x_N)$$

where, f represents a pdf, x is a geometric parameter identified by subscript. Full independence testing requires ensuring that all possible combinations of parameters are independence. With 9 geometric parameters (2 angular coordinates, 2 principal axis lengths, 4 edge angles, and 1 radial coordinate), $2^9 = 512$ individual independence tests are required. The difference between the full joint pdf and all 9 multiplied individual pdf is 3.4890e-18, which indicates to first order that the pdfs are strongly independent. A selection of pairwise independence tests are displayed in **Table**

24. There is evidence of correlation between edge angles, but we proceeded as if all pdfs are independent for simplicity.

Normality testing

According to the Central Limit Theorem, the average of any random phenomenon tends to be normally distributed, and in the presence of uncorrelated random errors, many observations tend to be normally distributed as well. It makes sense, therefore, to test the parameter pdfs for normality. Additionally, a normally distributed pdf is simpler to draw samples from (as required in later Monte Carlo modeling), and supports a number of statistical tests and inferences. Though it seems clear from simple observations that the distributions are not Gaussian, quantitative testing for normality was undertaken.

The Komologrov-Smirnov (K-S) test statistic allows one to test whether a set of observations are from a specified, continuous distribution. Typically, a chi-squared test is used for this purpose, but it has been shown that the K-S test works better for small sample sizes, and often appears to be a more powerful test than the chi-squared test for any sample size (Lilliefors, 1967). The K-S test compares the cumulative distribution function (CDF) of a known distribution to the empirical distribution function (EDF) of the observations, where the EDF is defined as:

$$F_n(x) = \frac{1}{n}\sum_{i=1}^{n} I_{x_i \le x}$$

and the CDF of a pdf f(x) is:

$$F(x) = \int_{-\infty}^{x} f(u)du.$$

The test statistic is the maximum difference between the CDF and the EDF. If the observations come from the hypothetical distribution, the statistic follows a known distribution. A Komologrov-Smirnov test was performed on all ten data parameters. As suspected, each parameter failed the test, and therefore cannot be treated as normal.

To confirm the K-S test results, an Anderson-Darling (A-D) test was also performed. The A-D test is a modification of the K-S test. The A-D test uses a critical value that depends on the specific distribution being tested. The test is therefore more sensitive than the distribution-agnostic K-S test, but critical values must be calculated for each distribution of interest (Anderson, 1952). The A-D test statistic A is defined as:

$$A^2 = -n - S,$$

where,

$$\frac{2i-1}{n\left[\ln F(Y_i) + \ln\left(1 - F(Y_{n+1-i})\right)\right]}$$

and n is the sample size, F is the CDF of interest, and Y is the standardized data in order from least to greatest. Testing again indicated that all distributions should be treated as non-normal.

Table 24: Pairwise independence test matrix

	θ1	θ2	PA1	PA2	EA1	EA2	EA3	EA4	Radial
θ1		7.87e-7	6.3e-7	8.8e-7	0.0029	0.0028	0.0029	0.0029	0.0015
θ2			4.9e-7	6.09e-7	0.0031	0.0032	0.0031	0.0030	8.0e-4
PA1				2.5e-8	3.9e-6	3.7e-6	3.91e-6	4.0e-6	8.1e-7
PA2					3.7e-6	3.71e-6	3.7e-6	3.8e-6	9.8e-7
EA1						0.3690	0.5968	0.4415	0.0026
EA2							0.3436	0.4325	0.0027
EA3								0.3545	0.0026
EA4									0.0026
Radial									

Finite Element Modeling of CSEM Responses

One of the primary objectives of this study is a statistical understanding of the variation in the MCSEM responses of off-shore Louisiana GoM reservoirs. In order to gain this understanding, a high fidelity three-dimensional model of the MCSEM response of an arbitrary subsurface conductivity distribution must be used. Our model is a finite element (FEM) solution of the coupled potential formulation of Maxwell's equations based on work presented in Badea (2001) and Stalnaker et al. (2006). In this model, the magnetic and electric fields are represented by a vector potential **A**, and a scalar potential φ, such that,

$$\mathbf{B} = \nabla \times \mathbf{A}$$
$$\mathbf{E} = -i\omega(\mathbf{A} + \nabla\psi)$$

where, ω is angular frequency. The potentials are divided into a source or primary field component, and a secondary, or scattered component:

$$\mathbf{A} = \mathbf{A}_P + \mathbf{A}_S$$
$$\psi = \psi_P + \psi_S$$
$$\sigma = \sigma_P + \sigma_S$$

The equation (three vector component equations solved separately, actually) to be solved numerically is therefore,

$$\nabla \times \nabla \times \mathbf{A} + i\omega\mu_0\sigma(\mathbf{A} + \nabla\psi) = \mu_0 J_P.$$

where, $\mathbf{J}_P$ is source current density and μ_0 is the magnetic permeability of free space. The Coulomb gauge $\nabla \cdot \mathbf{A} = 0$ is applied, and a fourth, constitutive equation—the conservation of charge—is added:

$$\nabla^2\mathbf{A} - i\omega\mu_0\sigma(\mathbf{A} + \nabla\psi) = \mu_0 J_P$$
$$\nabla \cdot [i\omega\mu_0\sigma(\mathbf{A} + \nabla\psi)] = 0.$$

The differential equation range is projected onto a set of basis functions, and following Galerkin, the solution is projected onto the same basis:

$$A_j(x,y,z) - \sum_{i=1}^{N} A_{ji}\alpha_i(x,y,z)$$

where, N is the number of basis functions, and j is the component of A of interest.

The "nodes" at which the basis functions above are defined are split into known boundary nodes and unknown free interior nodes. The solution domain is split into a set of elements over which the conductivity is constant. In our model, the elements are simple tetrahedra (**Figure 49**). Given the four Maxwell's equations and N interior nodes, the result is an NxN system of equations which must be solved. The matrix is sparse, asymmetric, and complex. Therefore, we solve the system using the quasi-minimum residual (QMR) iterative solution method.

The finite element approach is attractive because it allows increased resolution only where necessary, and arbitrary subdivision (meshing) of the model domain. The trade-off is increased computation time compared to alternative numerical solution approaches like the finite difference method. The potential formulation avoids issues with spurious solution modes manifesting due to discontinuities in the electric field at material interfaces. However, the actual magnetic and electric fields must be recovered from the potentials by numerical differentiation (we use moving least squares interpolation).

The model as presented in Stalnaker et al. (2006) was translated from Fortran 77 to C++ to take advantage of the code optimization and memory management of the freely available Gnu C++ compiler and the C++ language. The object-oriented nature of C++ makes the code more extensible—a feature that was used to great effect when code modeling the marine HED source was added. The new C++ code was verified against published modeling results and the existing Fortran 77 codebase. The model execution speed was dramatically improved, and dynamic memory management allowed the specification of higher resolution meshes, as memory consumption rises with resolution.

As presented in Badea (2001) and Stalnaker et al. (2006), the finite element model only simulates a vertical magnetic dipole (VMD) source. Any source is simulated by providing the relevant primary potential solution. The VMD primary magnetic vector potential is based on an electric field solution described in West and Macnae (1991). The VMD primary potential is that of a wire loop in free space or above a homogeneous halfspace. Thus, the secondary potential computed by the finite element model is attributed to any additional conductivity structure added to the primary model.

Considerable effort was devoted, therefore, to adapting the FEM model to the marine HED source. A primary magnetic vector potential solution was constructed after the one-dimensional HED electric field model designed by Chave and Cox (1982). HED modeling results were verified against one dimensional model results abundant in the recent MCSEM hydrocarbon literature. Though the Chave and Cox (1982) model provided for an N layered subsea conductivity structure, the derived primary potential model treats the primary seafloor as a homogeneous half-space.

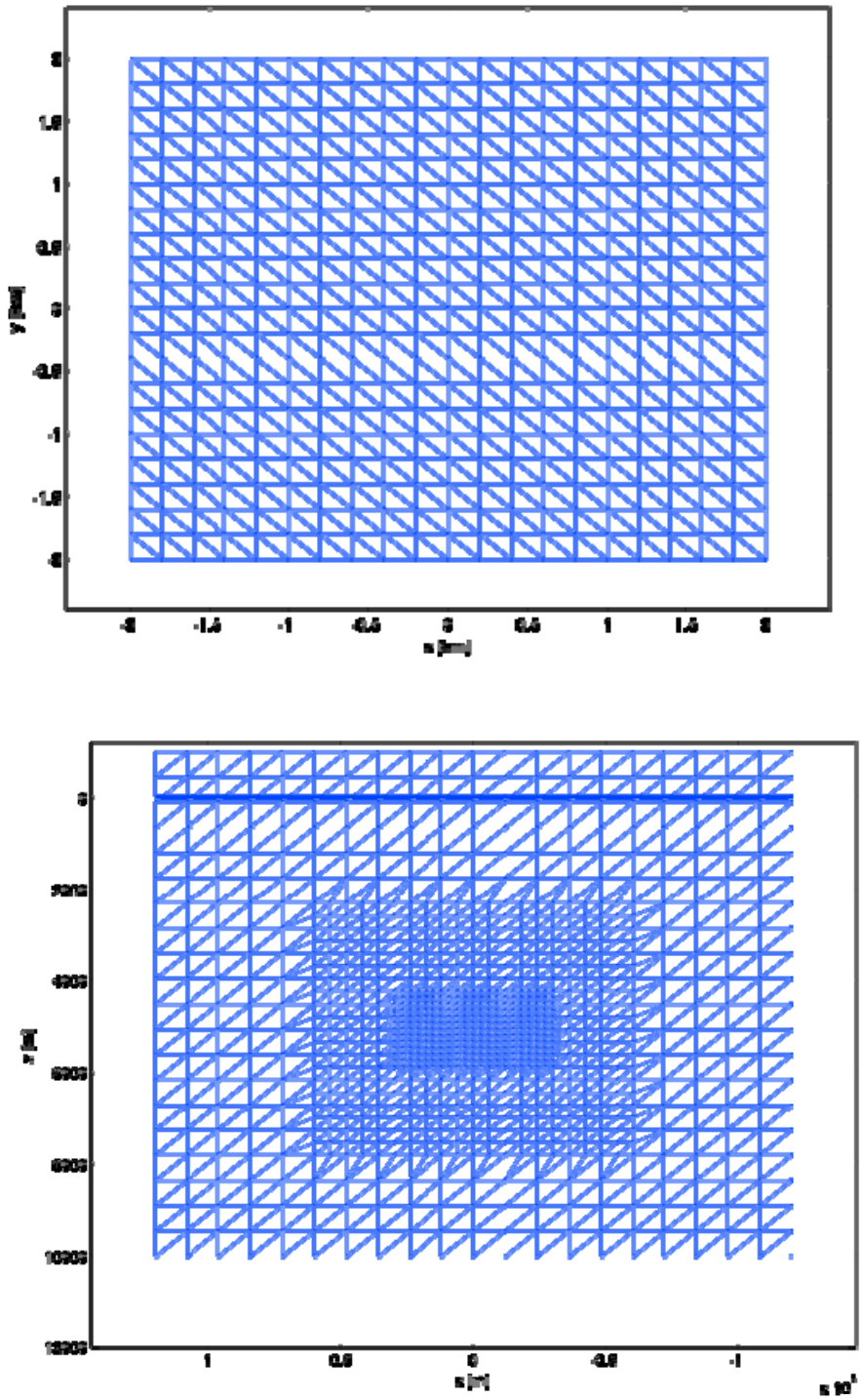

Figure 49: Unrefined finite element mesh (a), and a mesh containing two nested local refinements (b)

Monte Carlo Modeling

To understand the variation in off-shore Louisiana GoM reservoir MCSEM responses, we must observe a statistically significant number of measurements. Unfortunately, MCSEM data is expensive, proprietary, and scarce. We can, however, generate any number of synthetic GoM reservoirs from the statistically derived *a priori* probabilistic descriptions of reservoir geometric and electrical properties. The MCSEM response can be calculated using the high resolution three-dimensional FEM model. From these Monte Carlo modeled MCSEM responses, *a posteriori* probability distributions can be computed by kernel density estimation.

Drawing random samples from the reservoir parameter pdfs is not a trivial matter. Most computer programming languages or calculator packages, like Matlab or C++, can produce psuedo-random samples from uniform or standardized normal distributions, but not arbitrary distributions like those generate by KDE. Rejection sampling can be used to convert samples from a distribution h(x) that can be sampled to another distribution f(x) which cannot by, as the name implies, rejecting a selection of the samples that are unlikely to have come from the distribution of interest. We create an envelope function everywhere greater than f(x) by scaling h(x), so that g(x) = M h(x). A random sample x is drawn from g(x), and a second U from a uniform distribution between [0,1]. If U >= f(x)/g(x), the sample is rejected (Gilks, 1995).

1000 synthetic GoM reservoirs were drawn from the statistically derived KDE computed parameter pdfs. Though the appeal of the FEM method lies in its ability to use a completely unstructured mesh, doing so requires a suitable meshing algorithm. Our rather limited meshing software is best suited for rectangular structures. It should be noted, however, that due to the modular nature of the C++ FEM code, a superior meshing algorithm can be "dropped in" at any time. The rectangular mesh generator was used in the interest of simplicity and time. Thus, each reservoir was replaced by the best fitting box. The best fitting box was found simply, through a series of conditional statements that replaced the hemi-ellipsoid with a box. The best quadrant or quadrants containing the reservoir were assigned the reservoir resistivity (**Figure 50**).

The FEM model is controlled by a group of ASCII text files. A PERL language script was developed to draw a sample from a file containing row-sorted random GoM reservoirs generated using rejection sampling, and to create the requisite FEM model parameter files. The script then executed the model and automatically stored, labeled, and sorted the modeled MCSEM responses.

A posteriori probability and examining the utility of MVO as an interpretation technique
From the Monte Carlo modeled data set, it is possible to compute the posterior probability of offshore GoM MCSEM responses. The probability could be expressed in various ways, many of which are dependent on survey geometry. We chose to assess the variation of inline MVO power, which should be invariant under receiver spacing, and which should also serve as an assessment of the utility of the MVO approach.

Energy of a signal is only meaningful if a signal has a finite square integral. That is, the signal must converge to zero. The normalized MVO (nMVO) response, which is taken to indicate the presence of a horizontal resistor, does converge to zero, and the energy of normalized MVO therefore exists. The energy of MVO is,

$$M = \int_{-\infty}^{\infty} \left(\frac{|E_r(x)|}{|E_{bg}(x)|} \right)^2 dx$$

where, x is offset and E_r is the inline electric field with the reservoir present and E_{bg} is the so-called "barren ground", or reservoir-free response. Our MVO is discrete, defined only at receiver locations. Therefore, the integral must be computed numerically. We compute nMVO energy using the built-in trapz function in Matlab. The 1000 resulting nMVO energies are displayed in figure 24. We are most interested in the a posteriori pdf of nMVO energy, and as before, we convert our observed values to a nonparametric pdf using KDE. The pdf is displayed in figure 25. The implications of this pdf are enormous, because even when full, three-dimensional inversion is used to interpret MCSEM data, the go-ahead for interpretation is often based upon the initial detection of a resistor using MVO. Thus, if the MVO signature of a paying reservoir is

small (i.e. its energy is low), it is possible that the reservoir will be missed entirely if MCSEM is used as the reconnaissance tool.

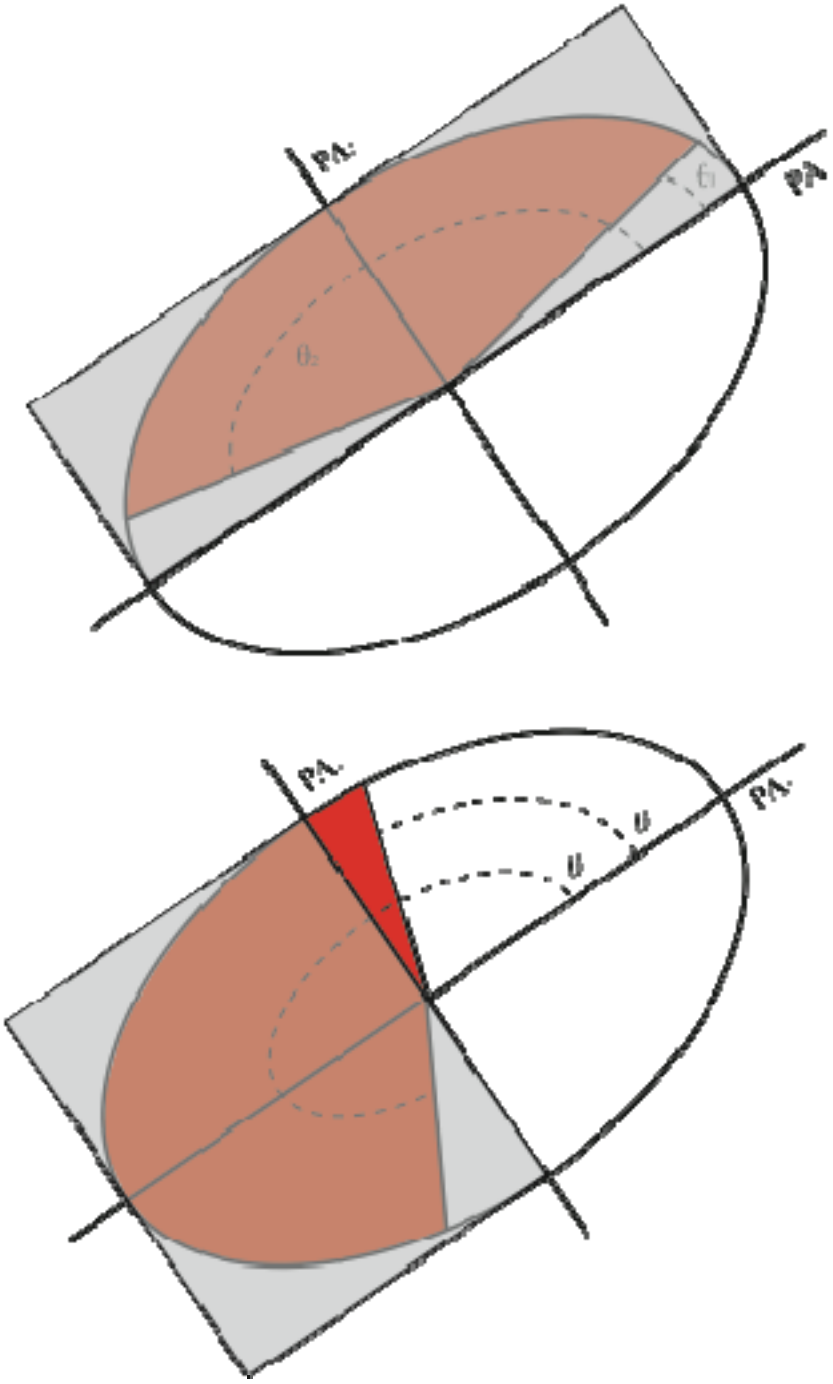

Figure 50: The best-fitting "box" model (in gray) for several reservoir ellipsoid sections (in red)

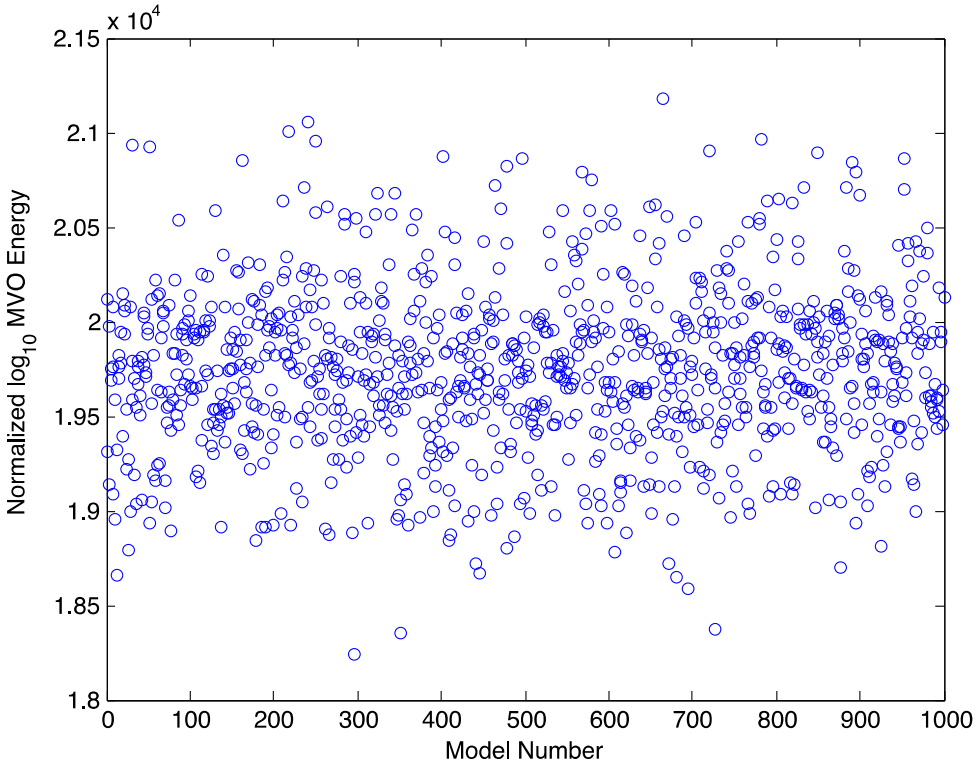

Figure 51: Energy (size) of normalized magnitude versus offset signatures associated with 1000 synthetic reservoirs drawn from the parameter pdfs defined above

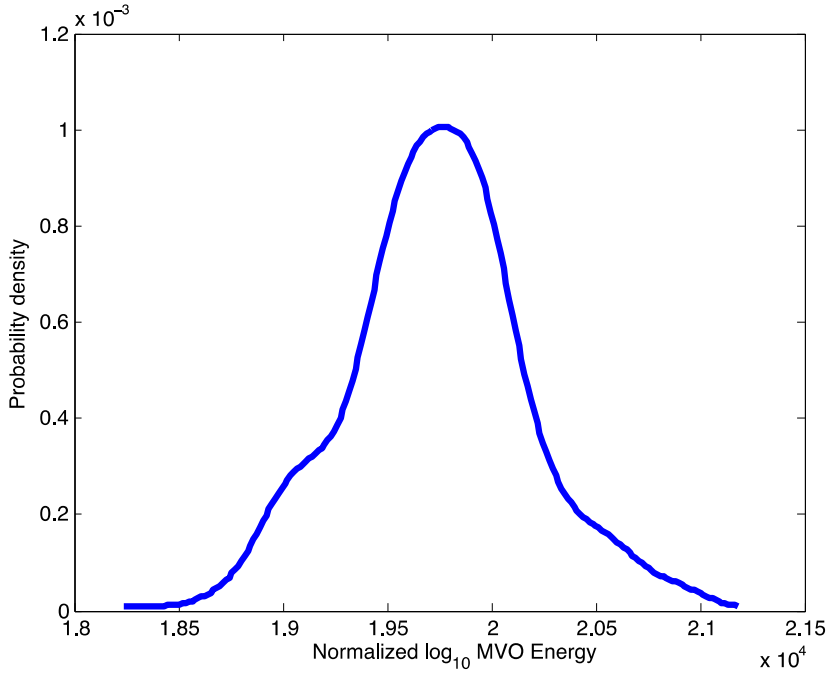

Figure 52: Posterior pdf of normalized magnitude versus offset energies in figure 24

Simplified Modeling of MCSEM Responses

Before the development of a simplified model could proceed, we needed an understanding of the range of variation in off-shore Louisiana GoM MCSEM responses in order to determine empirically the best model. Based on work in unexploded ordnance (UXO) detection and discrimina-

tion, we propose a similar dipole model here, albeit altered to suit the different physics and source type employed in a marine environment.

In UXO modeling, an arbitrary bomb is replaced with a wire loop which is broken down onto the three principal axes of the spheroidal bomb. This approximation is warranted as long as the bomb is sufficiently far away from the transmitter—A VMD—to be uniformly illuminated by the primary magnetic field, and sufficiently far from the receiver to appear as a point source of secondary magnetic field. When both conditions are satisfied, the CSEM response of a metallic ordnance-like target can be modeled by the simple expression,

$$\varepsilon_{RX,T} = \frac{i\omega\mu_0}{I_{RX}} \mathbf{H}_{RX} \cdot R^T \Lambda R \cdot \mathbf{H}_{TX}$$

where, $\varepsilon_{RX,T}$ is the emf measured by by the receiver RX due to target T, $\mathbf{H}_{TX}$ is the transmitter magnetic field at the target loop, R is the rotation matrix constructed from Euler angles and describing the orientation of the target, Λ is the diagonalized polarizability tensor, and $\mathbf{H}_{RX}$ is the hypothetical field of the receiver at the target location, justified by the principle of reciprocity (dipole model papers). The polarizability tensor describes the moment induced in the three orthogonal wire loops representing the target. In the frequency domain, the tensor entries are:

$$\lambda_j = d_j + a_j \frac{i\omega}{p_j + i\omega}$$

where, a is an expansion coefficient dependent on loop area, d is a DC offset due to magnetic permeability, and the loops, and thus the target, are specified by the so-called "pole" values p. These pole values are target type specific, and are found through inversion. Comparing these pole values to a library provides a means of classifying unknown targets (Aliamiri et al., 2007). We have demonstrated that this type of classification works well even when the model assumptions (e.g. distance from transmitter) are violated (Aliamiri et al., 2007).

The UXO model works well because the target—an unexploded ordnance—is compact and electrically different from the surrounding host medium. By analogy, a hydrocarbon reservoir is a relatively compact (at least vertically) target that is electrically different than the host medium. In contrast, however, the reservoir represents a more resistive body than the surrounding host, and the transmitter is an HED rather than a VMD. Furthermore, the host, being closer in resistivity to the reservoir than to an UXO, cannot be ignored as is often the case in UXO modeling.

The overwhelming source of secondary, or target, response in the UXO case is the induction of currents (vortex currents) by time varying primary magnetic fields. The induced currents are similar in shape to the transmitter and receiver currents, and the entire system appears as a set of three coupled current loops. In a similar fashion, the source of target response from a horizontal resistor is the galvanic effect resulting from charge buildup at the interface between host and resistor. The charge buildup forms an electric dipole similar to the source and receiver (**Figure 53**). This response is in phase with the transmitter. A weaker induced vortex current is also created in both the host and the resistor. The induced current magnitude is relatively low, however, because by Ohm's law, it is proportional to the conductivity of the resistor. Nevertheless, the vortex current response is measurable and shifts the phase of the measured secondary electric field (**Figure 54**).

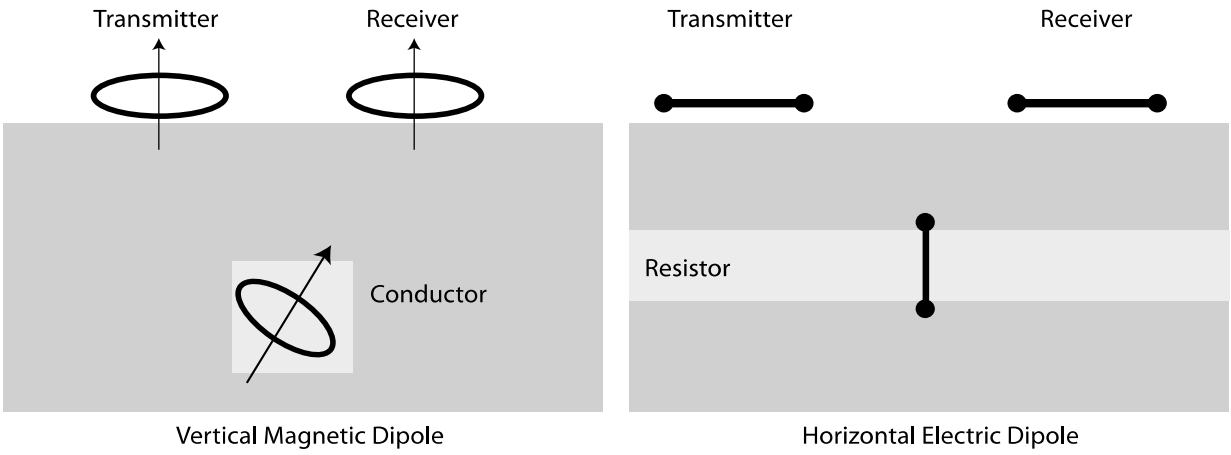

Figure 53: Currents induced in a conductor by a vertical magnetic dipole source mirror the source and receiver (left), as does charge buildup on a resistive layer

It is clear, then, that the simplified model must at least contain provisions for 1) the host response, 2) the induction response of the reservoir, and 3) the dipole-like galvanic response of the reservoir (which is what we detect in an MVO survey):

$$E = E_{host} + E_{vortex} + E_{galvanic}$$

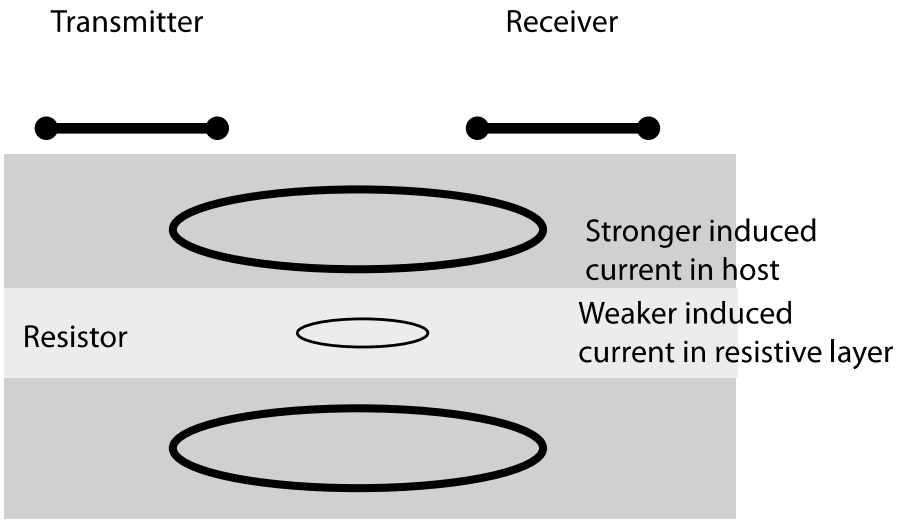

Figure 54: Vortex currents are induced in the reservoir and host. The reservoir currents are relatively weak, however

Because the galvanic response has a flat transfer function, the electric "polarizability" tensor has a simple frequency independent form. The induction response remains unchanged from the UXO case, and the semianalytic response of the ocean/background halfspace model, taken from Chave and Cox (1982) is added without consideration of mutual interaction with ei-

ther of the reservoir effects. The vortex electric field can be found by differentiation of the dipole magnetic field, according to Faraday's law.

It is possible that the inductive response of the reservoir is negligible. At the time of this writing, the model has been designed, but testing and revision are underway. It is clear from testing thus far that the large lateral extent of typical reservoirs violates the assumption that the response originates from a single point source. To address this issue, the reservoir is represented by a spread of non-interacting electric dipoles, the extent of which is determined by the size of the reservoir:

$$E_{restator} = \sum_{i=1}^{N} E_{\substack{electric \\ dipole\ i}} + E_{\substack{magnetic \\ dipole\ i}}$$

where, the electric dipoles arise from galvanic interactions, and the magnetic dipoles arise from inductive interactions.

We are also currently deciding how best to map dipole model parameters to the geometry defined by the prototype hemi-ellipsoid.

Inversion and Bayesian Inversion

Inversion

The low dimensionality of the simplified model lends itself well to simple, least-squares inversion. We are adapting inversion approaches initially developed for UXO detection and discrimination (Aliamiri, et al., 2007). Inversion seeks to solve the problem:

$$\hat{\theta} = \arg\min_{\theta} \|d - s(\theta)\|$$

where, d is a measured MCSEM response, and s is a response modeled using the simplified model and the parameter vector θ. Minimization is achieved using the standard Levenberg-Marquardt algorithm.

The Levenberg-Marquardt algorithm, like all local optimizers, is prone to local minimum entrapment leading to erroneous inversion results that nonetheless achieve a minimum cost. We have previously shown (Stalnaker and Miller, 2007) that initializing a local optimizer using a coarse briefly applied global optimizer yields results that while less efficient than a local optimizer in terms of computation time, are more efficient than a full global optimizer, and yield lower error inversion results on average. We use that approach here, implementing particle swarm optimization (PSO) as our global optimizer of choice due to its simplicity and extensibility. PSO operates by "flying" a set of trial solutions, dubbed "particles", randomly through parameter space. Though each step is random, the particles are simultaneously accelerated toward the optimum each particle has encountered thus far and toward the global best solution encountered. This way, each particle explores parameter space broadly while concentrating the search around any optima encountered already, maintaining a particle "memory" (PSO source).

Estimation

If *a priori* or *a posteriori* probability information is available, it can be used to drive inversion. Statistically steered inversion is often called "estimation" by contrast. Given *a posteriori* information about the data distribution, such as the distribution of MCSEM responses for each possible set of model parameters, the model parameter vector most likely to have produced the observed data can be found. The parameters for which the observed data set is most likely to have

occurred is selected, and the process is called maximum likelihood estimation (MLE). If the parameters are also random and the distributions are known, Bayes's theorem may be used, and we maximize the conditional *a posteriori* likelihood of the observation occurring given the set of parameters in question. This approach accounts for variability in the parameters themselves, penalizing unlikely parameter estimates, and is called maximum *a posteriori* (MAP) estimation, or simply Bayesian inversion. Curiously, both approaches modify the basic least squares inversion technique only slightly, and we continue to use the same Levenberg-Marquardt/PSO hybrid optimization approach.

If we assume the data distribution is normal with covariance matrix C, the MLE approach seeks to solve the problem:

$$\hat{\theta} = \arg\min_{\theta} \left\| C^{-\frac{1}{2}} d - s(\theta) \right\|_2^2$$

and MAP estimation seeks to solve the problem:

$$\hat{\theta} = \arg\min_{\theta} \left\| C^{-\frac{1}{2}} d - s(\theta) \right\|_2^2 + \left(\sqrt{-\ln f_{\theta}(\theta)} \right)^2$$

where, the likelihood f of parameter vector θ functions simply as a penalty term. Bayesian inversion also opens the path to sophisticated classification (i.e. reservoir vs. non-reservoir) that could aid on-ship, layman interpretation of MCSEM data—something that is severely lacking in current MCSEM technology.

As with the simplified modeling, the inversion and Bayesian inversion approaches and algorithms have been designed and developed as computer software at the time of this writing, but testing is currently underway.

VISUALIZATION

A 3D visualization task has been initiated. The visualization team has hired a Research Scientist, Christian Odom, to focus on start the research on advanced immersive 3D visualization for several of the components of this project.

The first visualization task we are addressing is the visualization of the volumetric foam data in collaboration with Dr. Boyun Guo. Dr. Guo has a series of slice that show the foam distribution inside a pipe as an intensity map.

Our first step was to register the series of slices to a unified coordinate system so we could create a continuous volume representing the entire pipe and the foam distribution. Since the slices came into a single image (see **Figure 55**), for registration we had to first separate each individual slice into an image and then apply a registration algorithm to align them correctly into a single coordinate system to properly integrate the data.

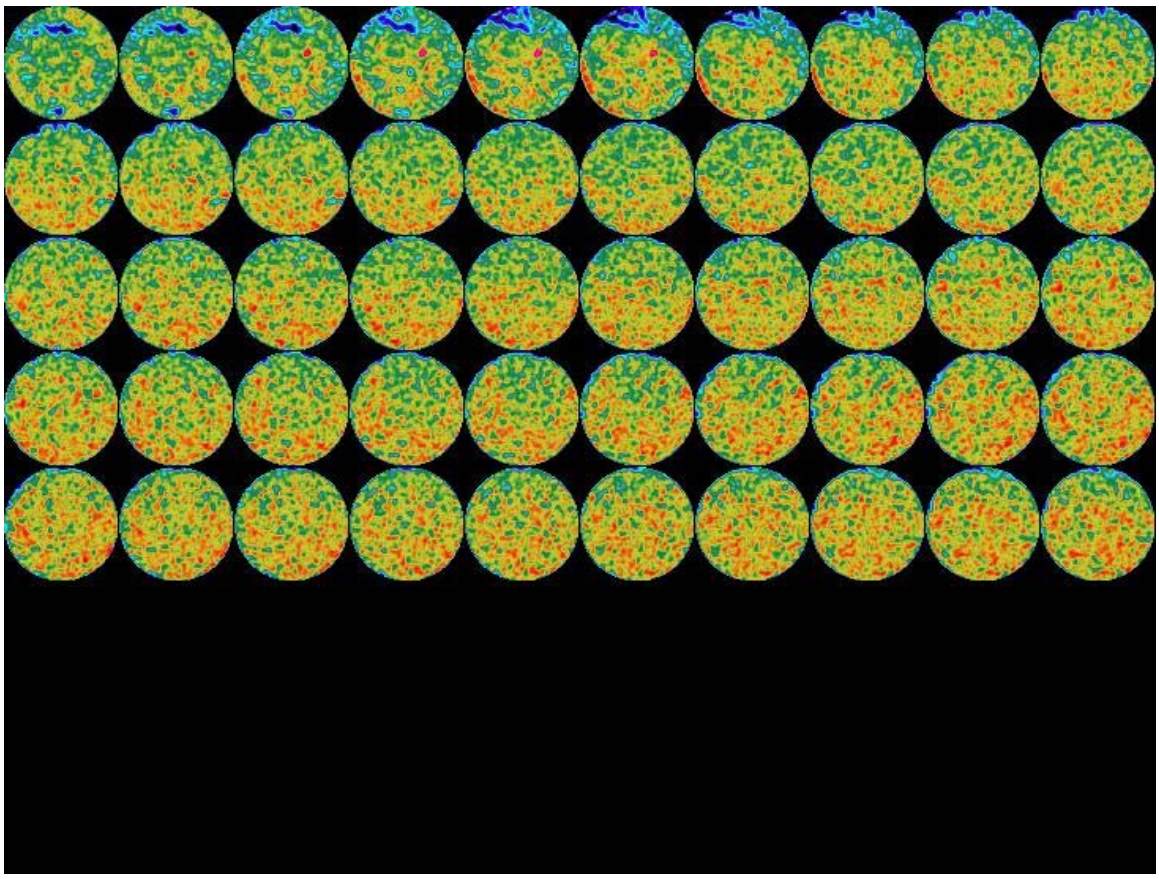

Figure 55: Original slices

The registration algorithm was a spatial method matching intensity patterns in the images. We utilized the Open Source tool ITK[1] to perform the registration.

After the images were properly registered, we performed a first-pass visualization to have a preliminary visualization of the foam structure within the pipe. The three images (**Figures 56 to 58**) below show this preliminary visualization.

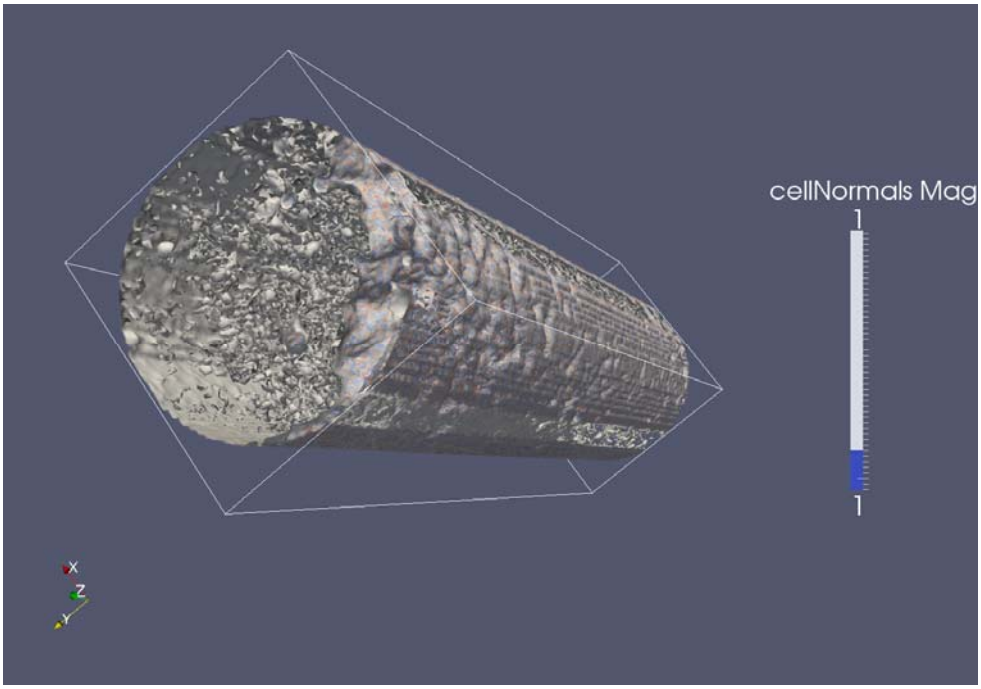

Figure 56: Full contour

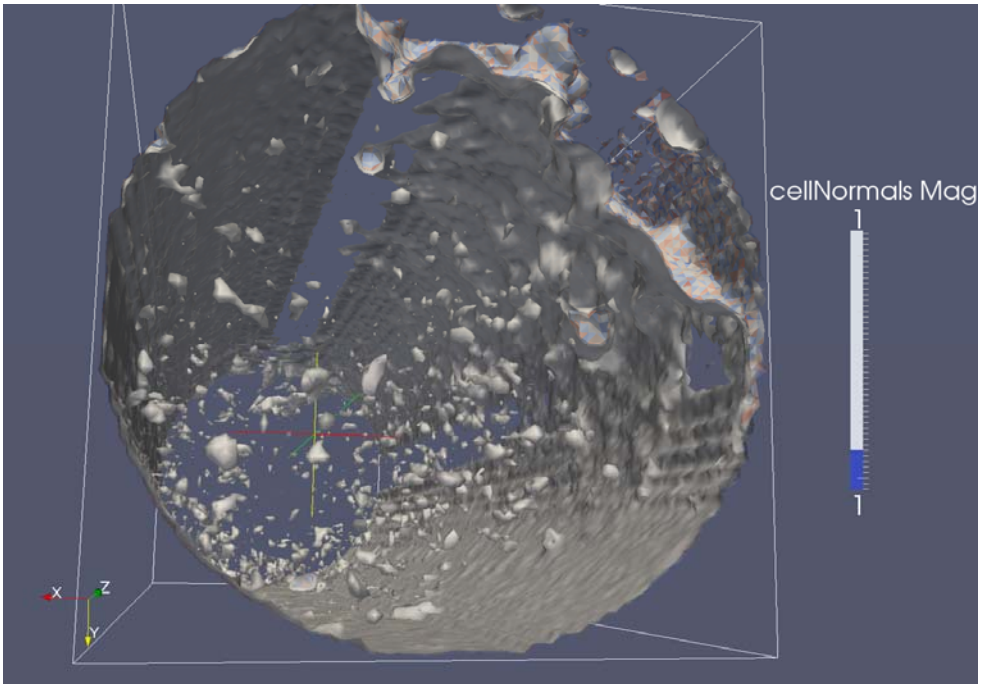

Figure 57: Low contour values

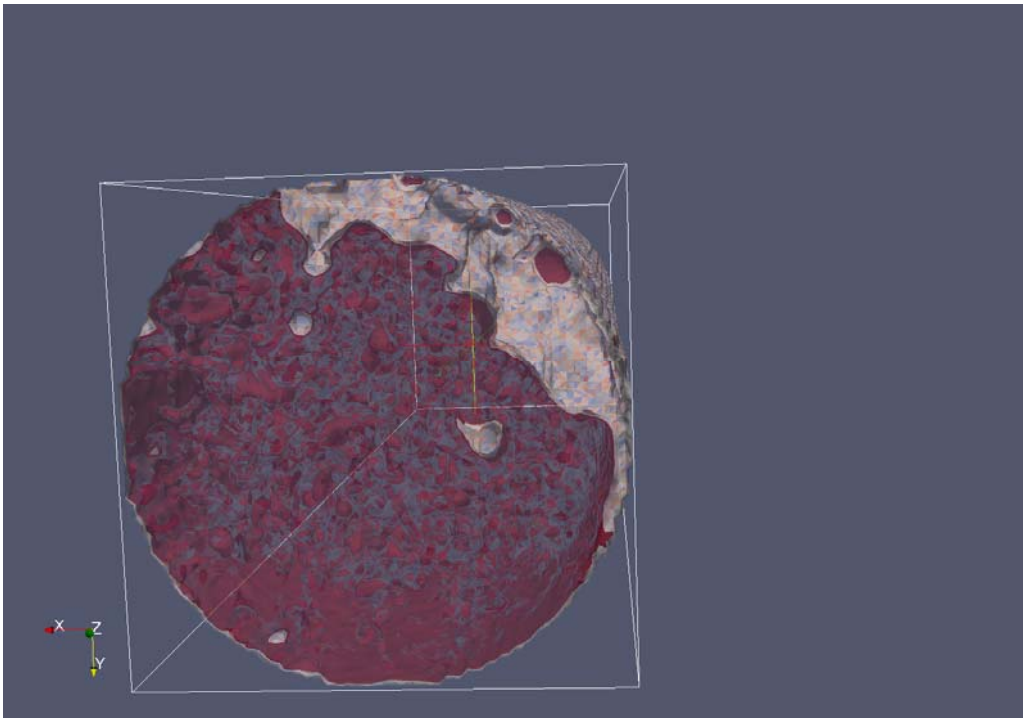

Figure 58: Mid contour values

Our initial visualization pass was successful in creating a volume, but in doing so we lost some information from our data set. After correcting the issue of hashing our data, we are able to produce more information rich volumes (**Figure 59**).

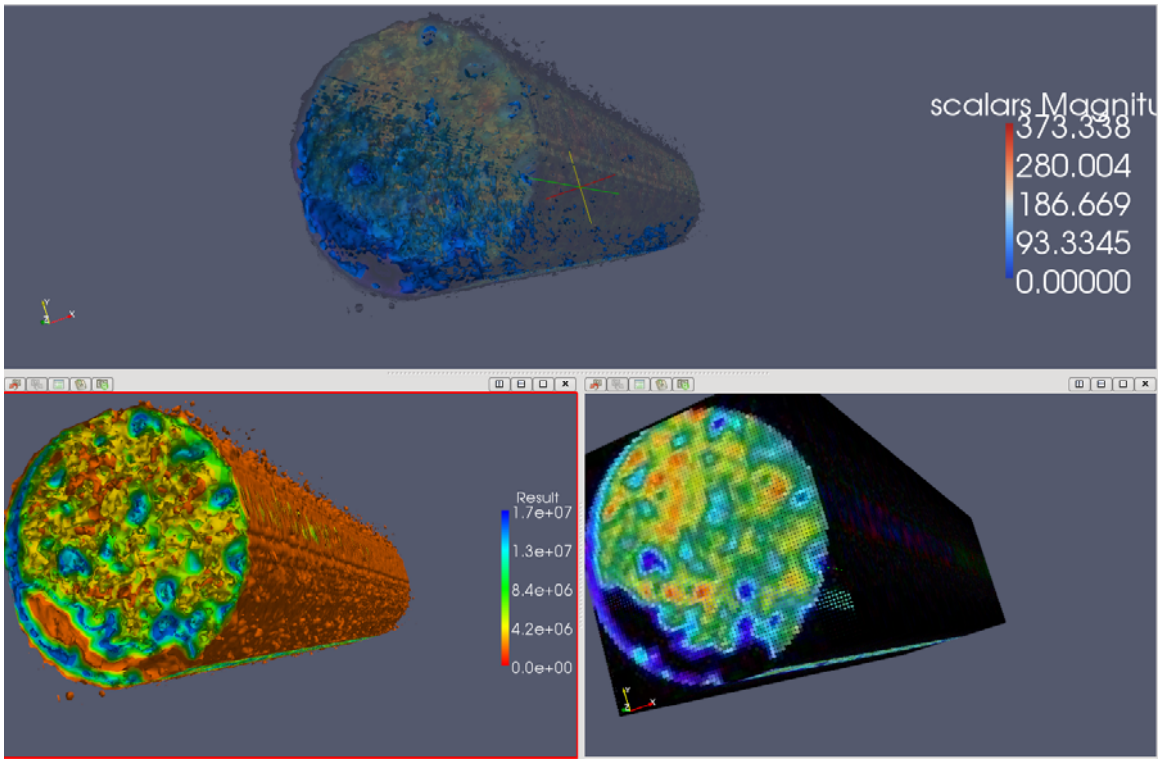

Figure 59: Visualization stages
(starting at the bottom right and proceeding in counter clockwise order)

Our contouring algorithm allows us to select a range of values to be rendered. This allows us to see a selected value range, normally only visible on the surface, throughout the vol-

ume. We are able to add contextual information to the selected value range by performing multiple passes on the data and rendering the subsequent passes with a reduced alpha channel. **Figures 60** and **61** show the registered slices arranged into a volume, volume produced from contour algorithm after value conversion and volume produced from isolating a particular value in the original data space.

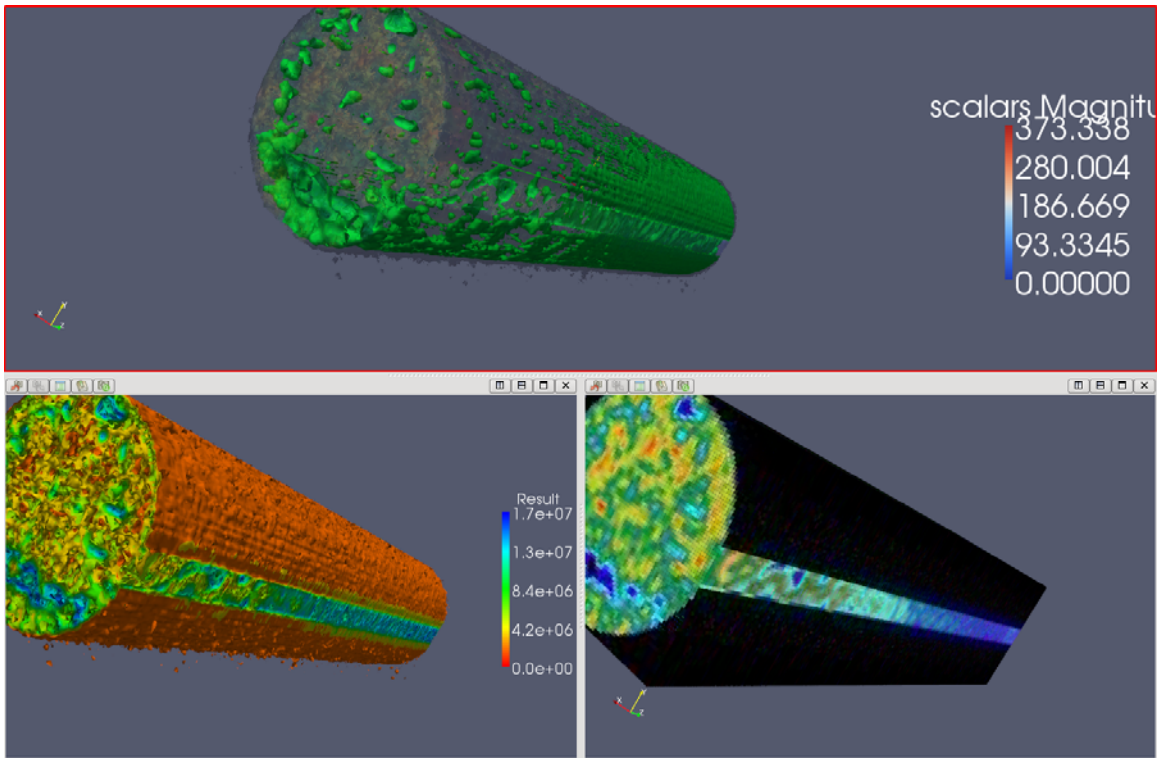

Figure 60: Isolation of different values with contextual information

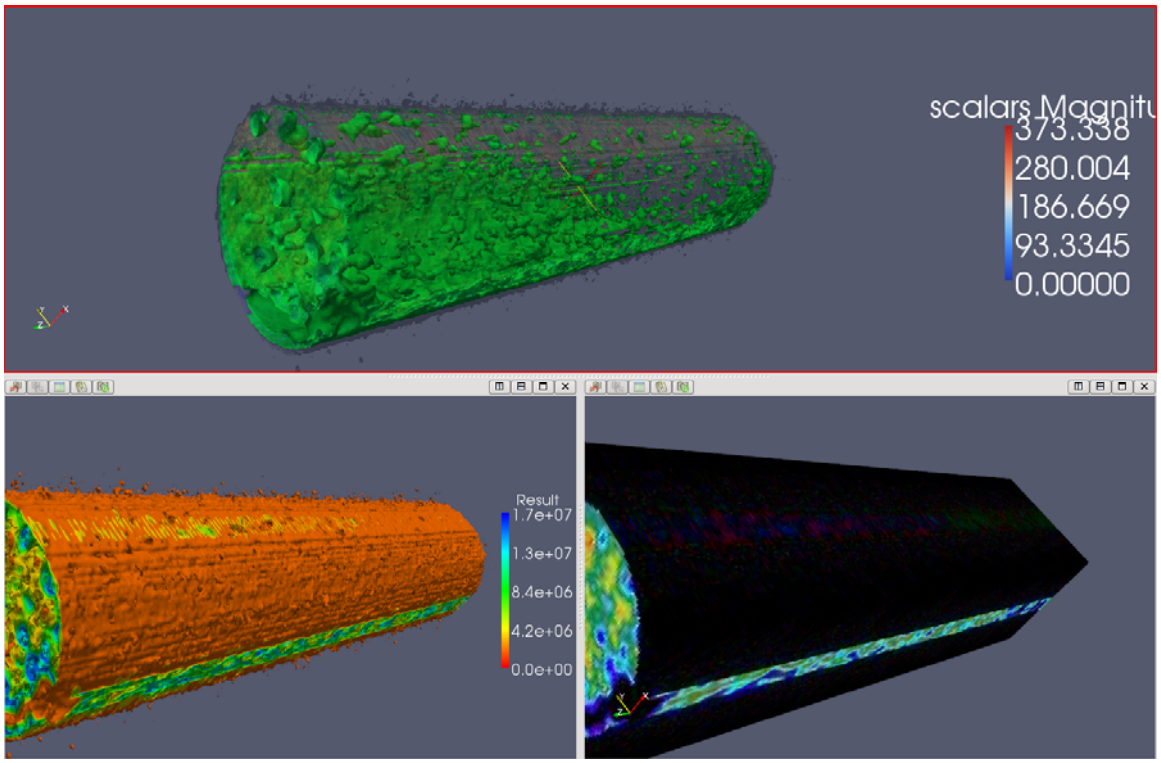

Figure 61: Linked views

From here, our next step is to incorporate interactive exploration of the volume in the immersive space.

Furthermore, we were able to visualize oil and CO2 saturation distribution and the CO2 flood front advance rate during CO2 flooding. The data is obtained from the Schlumberger Eclipse 300 compositional simulation model. We looked at the static model, analyzed the output from Eclipse, and came to the conclusion that the output is being written as a corner-point geometry grid (**Figures 62** and **63**). We wanted to leverage the scientific visualization tool VTK's functionality, so we needed to find a way to make the datasets compatible between Eclipse and VTK. To that end, we identified an Open Source package, OPM, that could do the work, but even with the Open Source denomination, we were unable to get access to the software. The group that manages it is considering other options for distribution and has for now restricted access to the software.

Because of this and on interest of time, we designed and implemented our own format conversion algorithm to reproduce xyz coordinates for all corners from the corner-point grid information. This method works well, but it requires us to parse fairly large and complex Eclipse files to find the necessary input parameters to our method. This introduces extra performance penalties as well as one more step in a process we would like to be as automated as possible.

Recently, the OPM software group has agreed to granted access to their package. We have been successful on installing it and integrating it into our environment and we can now very efficiently convert eclipse input files into VTK-compatible files using the OPM libraries. Using a scientific visualization front end to VTK, the package Paraview, integrated with VR Juggler we are able to display Dr. Boukadi's data, specifically the Johansen formation, in our immersive visualization systems. In a similar manner than for the work we are doing with Dr. Stalnaker, the use of VR Juggler provides us with the ability of using head and hand tracking and 3D navigation techniques to explore the datasets.

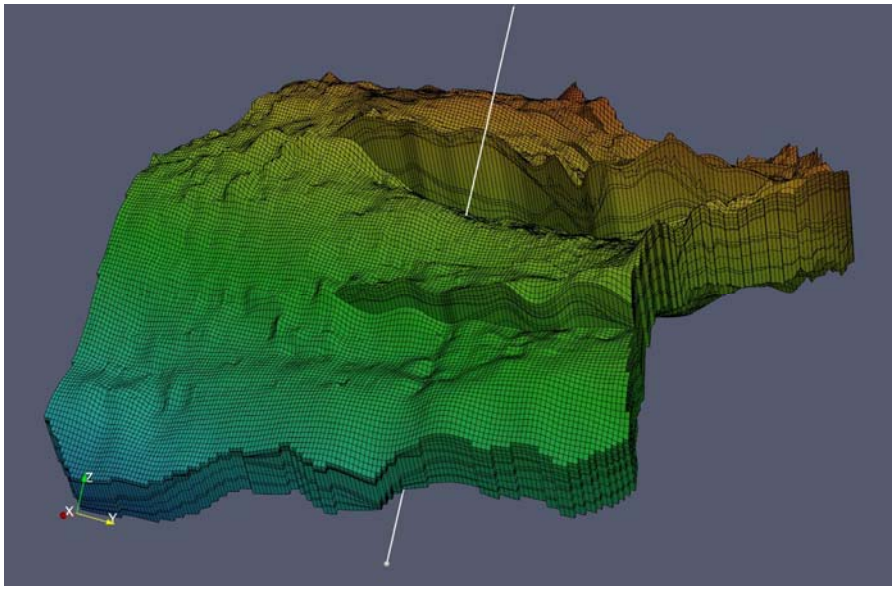

Figure 62: Static model 3-D view

In the case of Dr. Boukadi's data, because it is so large and complex, we also had to investigate the right combination of viewing and data selection parameters in order to provide real-time navigation through the datasets. Paraview and VTK provide a wide gamma of filters that allowed us to select the right segments of the data needed to render each frame. We can now re-

duce the dataset to desired subsets using a threshold filter. We can also take 2-D slices (**Figure 64**) or use a plane to remove sections of the dataset from view.

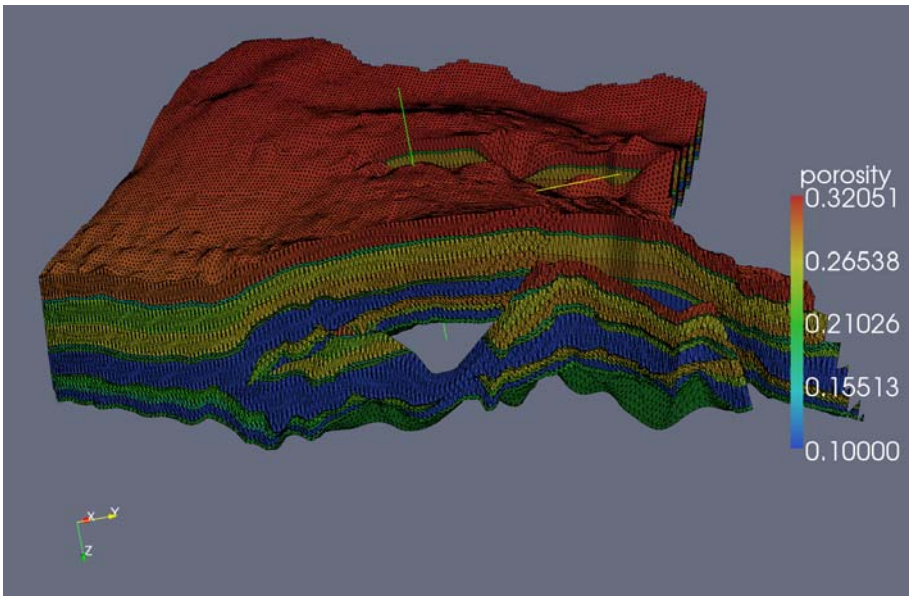

Figure 63: A perspective view of porosity distribution

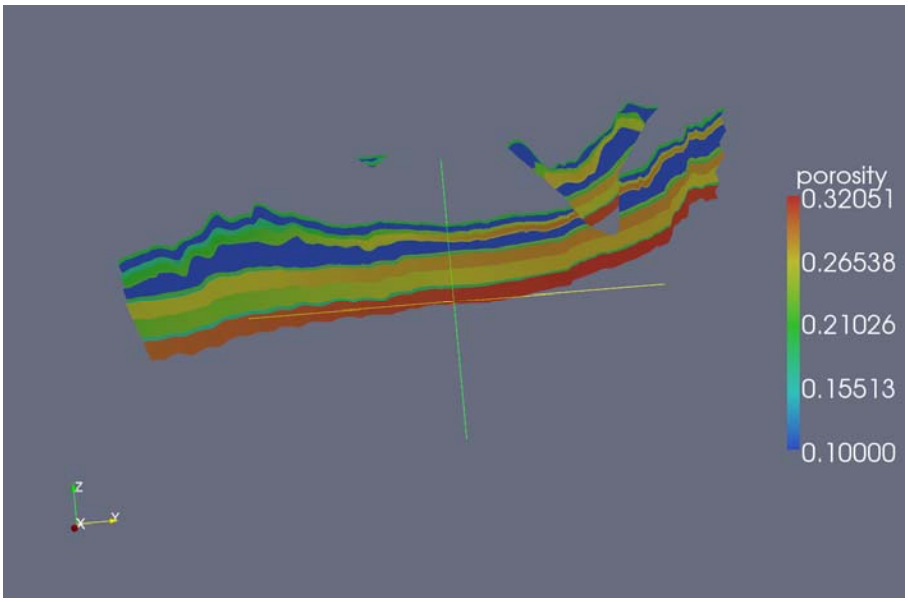

Figure 64: A cross-sectional view of porosity distribution

Furthermore, we designed and implemented our own format conversion algorithm to reproduce xyz coordinates for all corners from the corner-point grid information. Our algorithm had a couple of problems with index ordering that could cause incorrect visual representations of the simulation results. By working with Dr. Boukadi to acquire a larger sample of data files, we were able to correct these problems with our algorithm. The data files were obtained from simulation of CO2 front advance profile in a two-dimensional model (**Figure 67**).

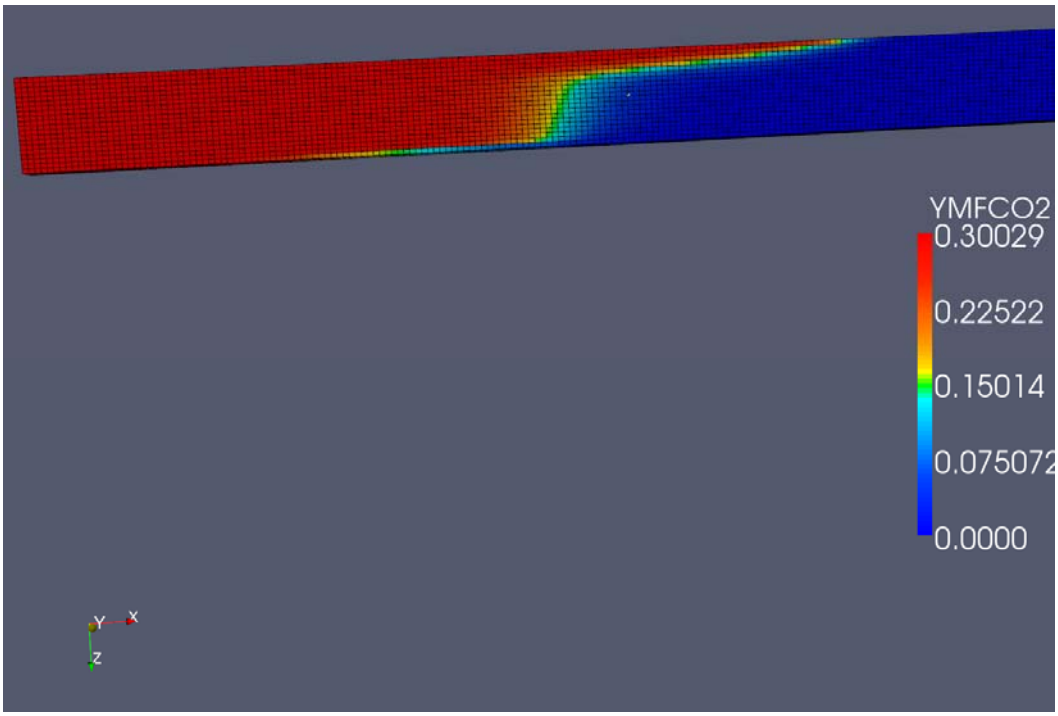

Figure 67: CO2 front advance profile

In addition, the compositional reservoir simulation software ECLIPSE 300 (Schlumberger TM) was extensively utilized. A candidate reservoir was injected with CO_2 gas at constant flow rate under miscible conditions and compositional grading of the gas front column investigated along the i-j planes at different depths and times. The extraction mechanism of the lighter hydrocarbons by the CO_2 gas phase was examined. Visualization of the extraction process, as well as data analysis of the simulation results was conducted to understand the process of CO_2 vaporizing, condensing and sequestration mechanisms.

The simulation conducted study gave a visual depiction of the gas flow through the reservoir and the corresponding oil depletion with time. CO_2 was injected continuously at a constant rate of 1000Mscf/day for 1800 days. The gas saturation at the beginning of the simulation was 0 (zero) while the oil saturation was 1, meaning the entire hydrocarbon pore volume was occupied by oil at initial conditions. With the different time steps, the gas front shape was clearly visible as flow progressed through the reservoir.

The initial injection pressure was 1992 psia and after 1800 days it had dropped to 1772 psia. The production well bottomhole pressure remained constant at 1500 psia throughout the simulation. **Figure 68** shows the bottomhole pressure at the injection and production wells.

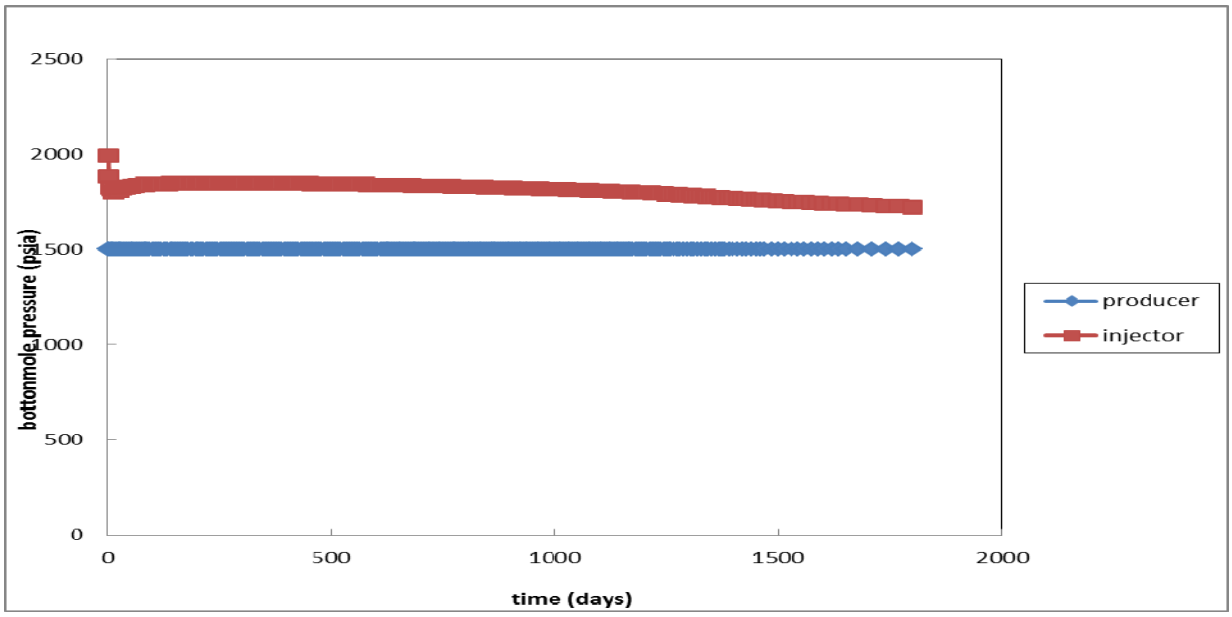

Figure 68: Bottomhole pressure with time for injection and production wells

The gas saturation profiles for initial and final conditions were also visualized with FloViz (a Schlumberger TM). As shown **in Figures 69** and **70**, the gas flooding process recovered 70% of initial oil in place. At 1800 days, the reservoir was 70% saturated with gas.

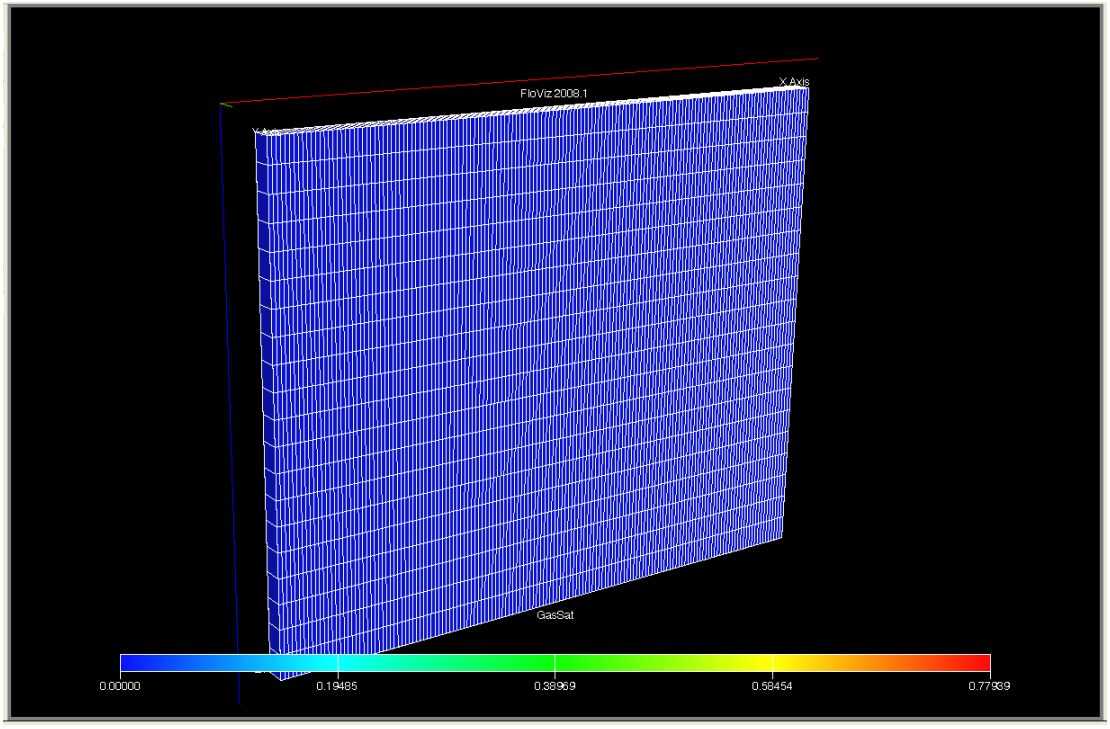

Figure 69: Initial gas saturation

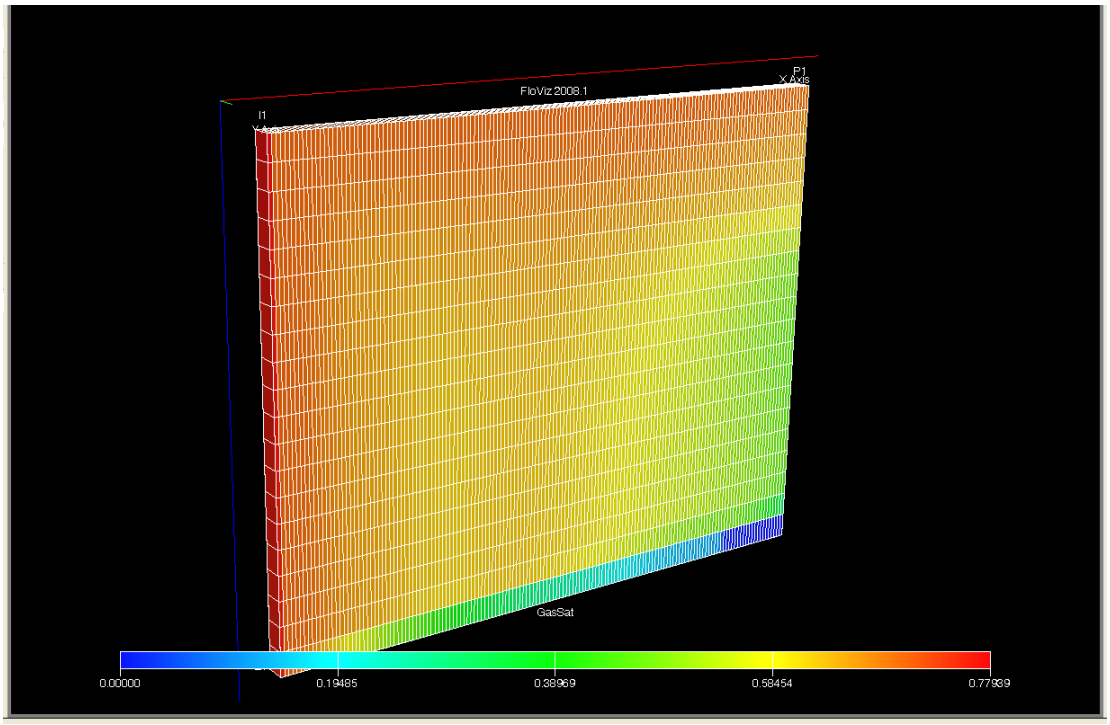

Figure 70: Gas saturation after 1800 days of gas injection

FloViz 3-D imagery provided a clear visualization of the extraction process of light hydrocarbons from oil. **Figures 71** through **80** illustrate the extraction of the different components at the gas front after 1800 days of injection.

Compositional grading of heavier components at the bottom and lighter components at the upper levels of the reservoir can be observed from these images.

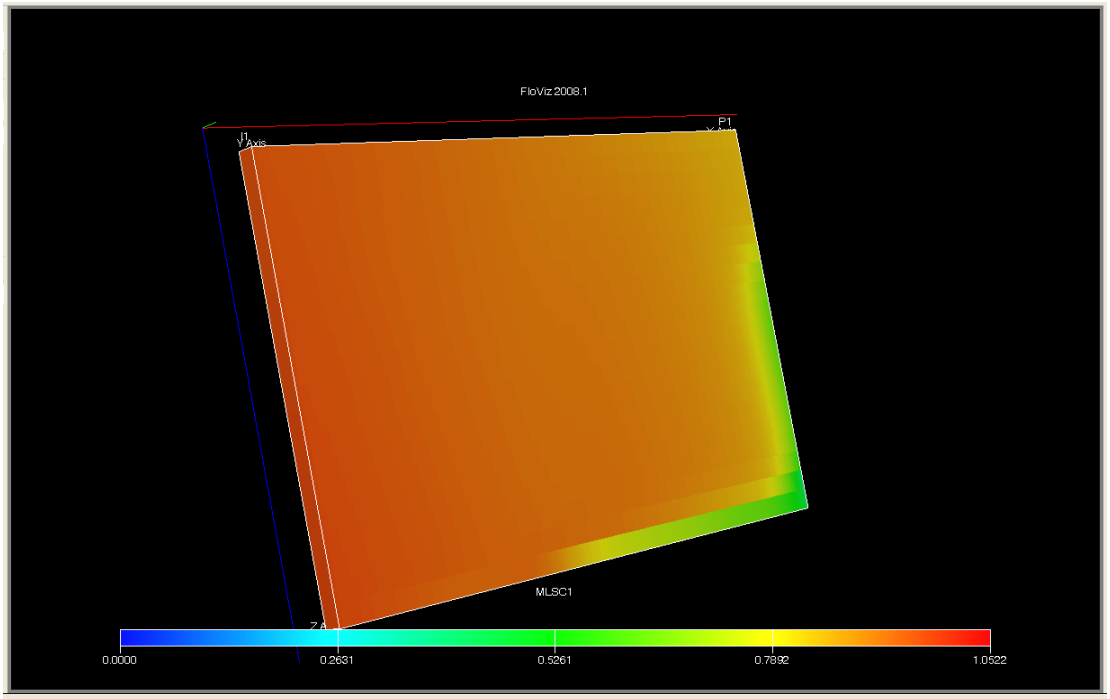

Figure 71: C_1 component distribution profile after 1800 days of gas injection

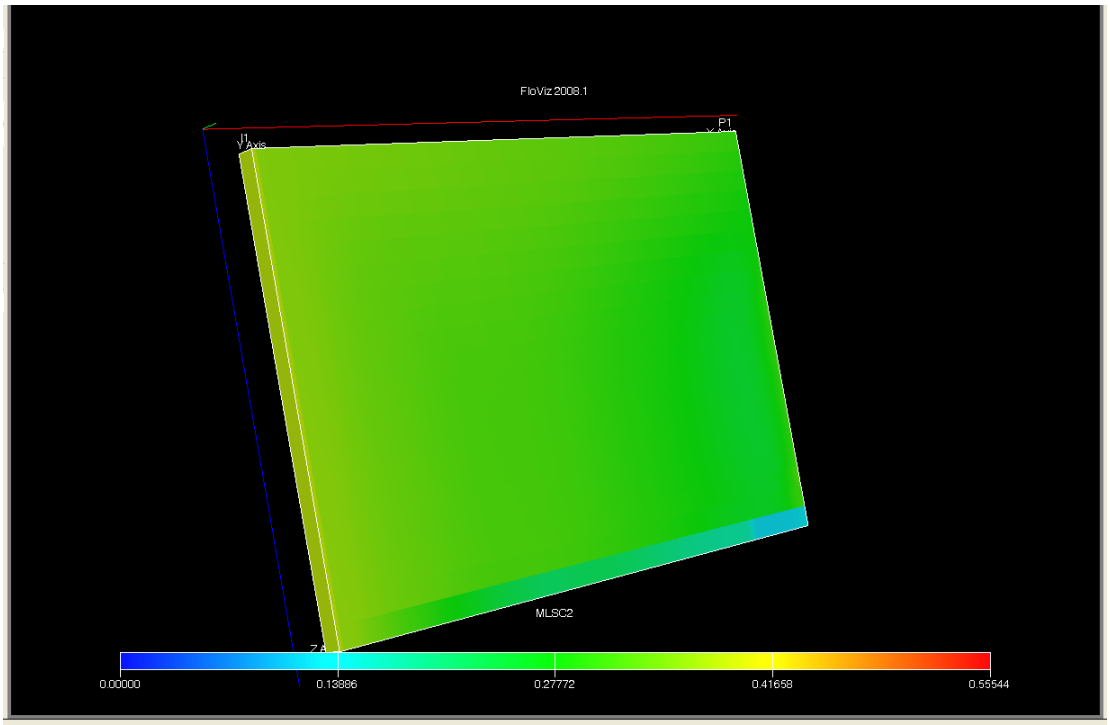

Figure 72: C_2 component distribution profile after 1800 days of gas injection

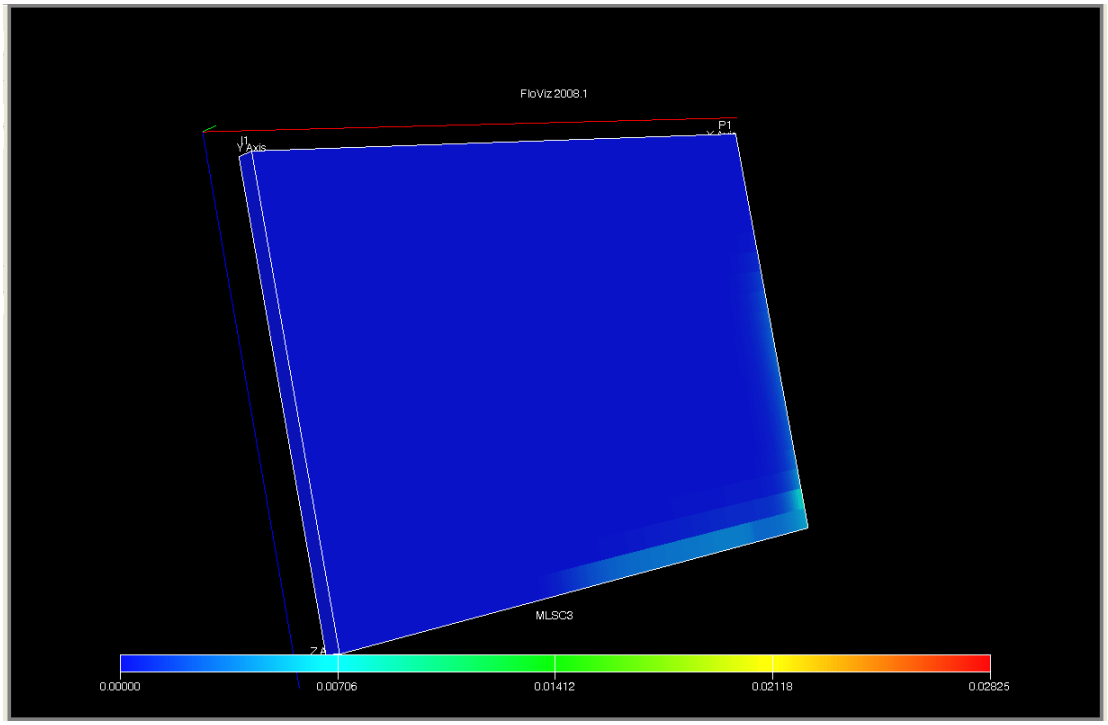

Figure 73: C_3 component distribution profile after 1800 days of gas injection

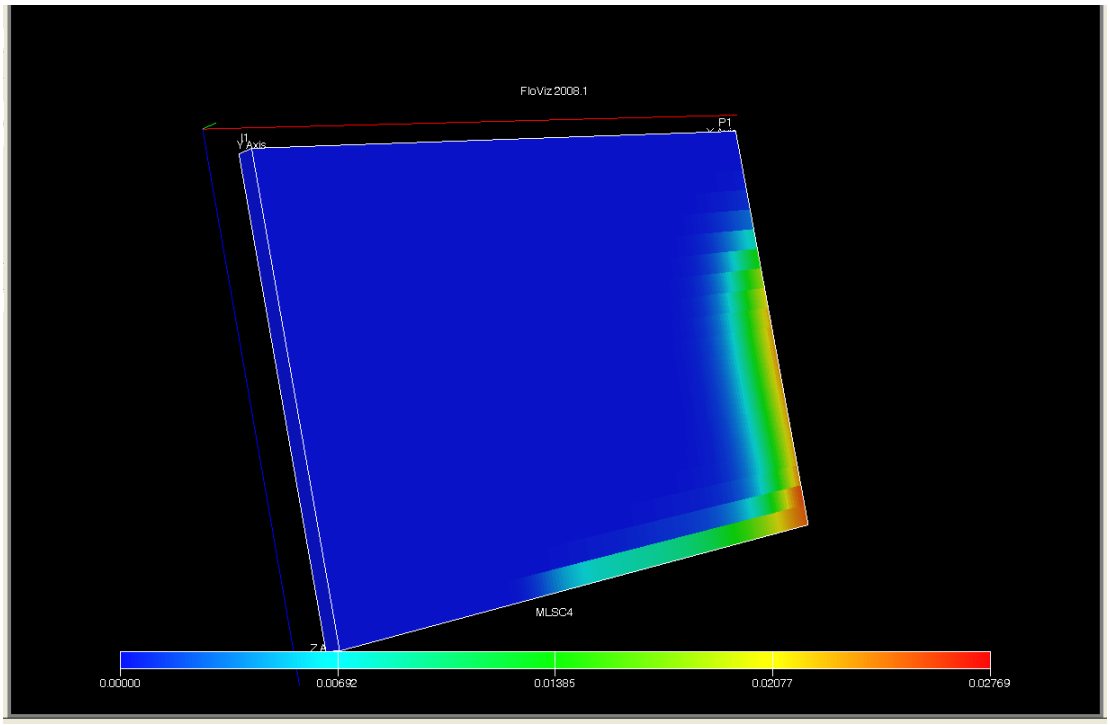

Figure 74: C_4 component distribution profile after 1800 days of gas injection

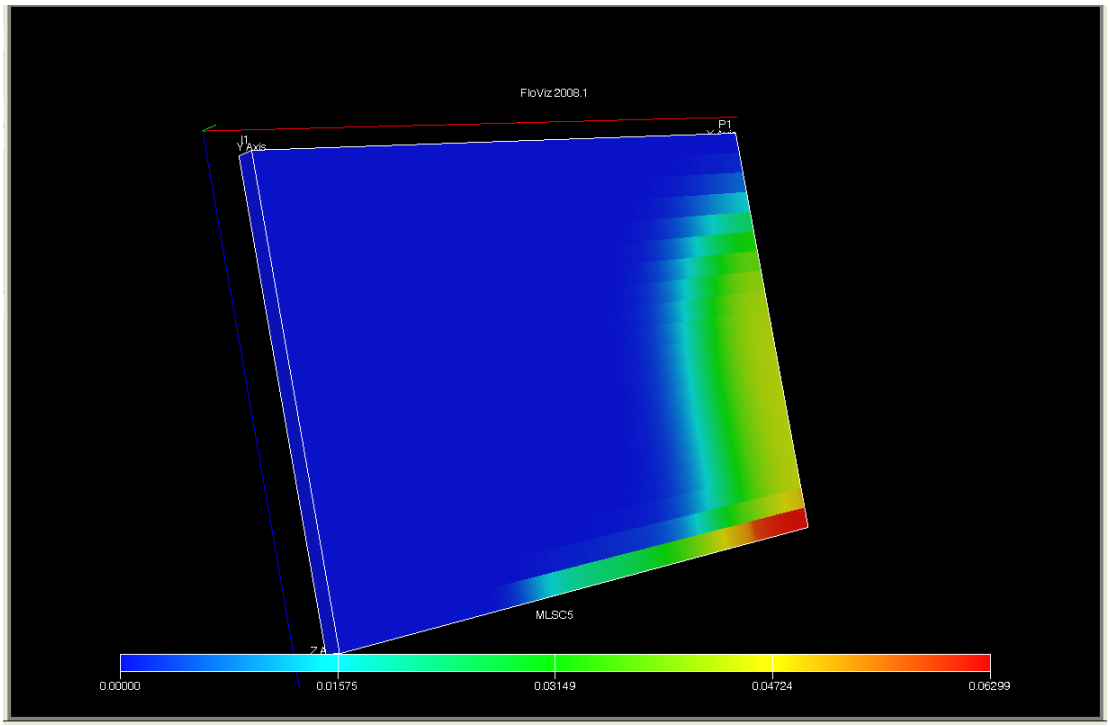

Figure 75: C_5 component distribution profile after 1800 days of gas injection

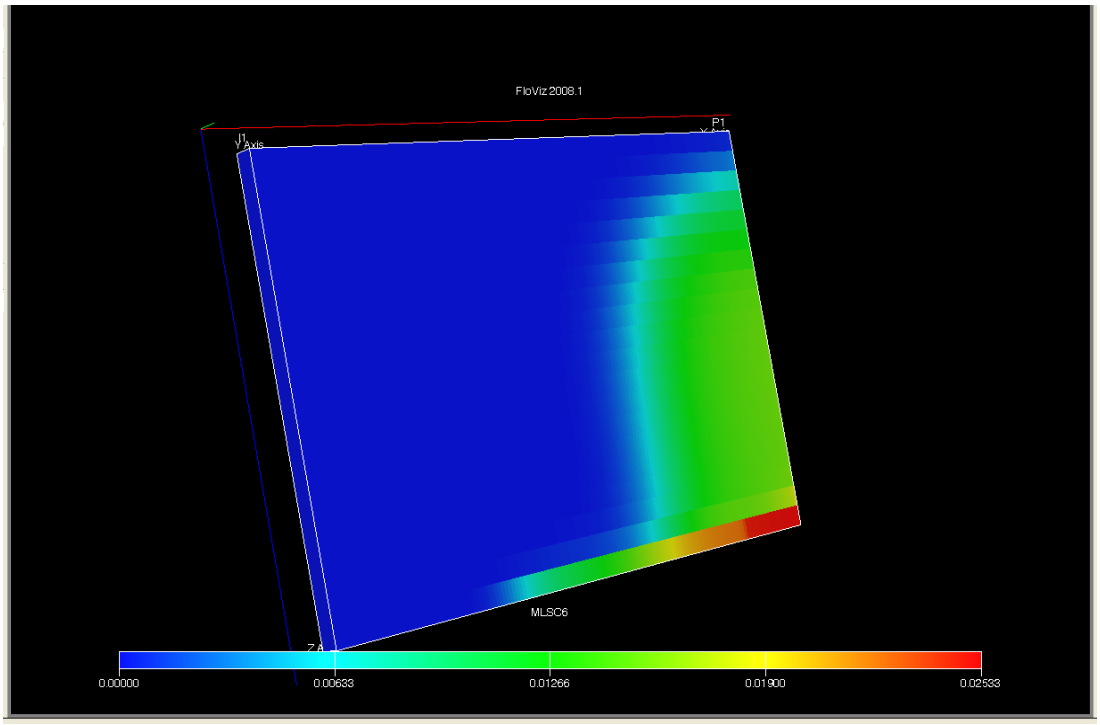

Figure 76: C_6 component distribution profile after 1800 days of gas injection

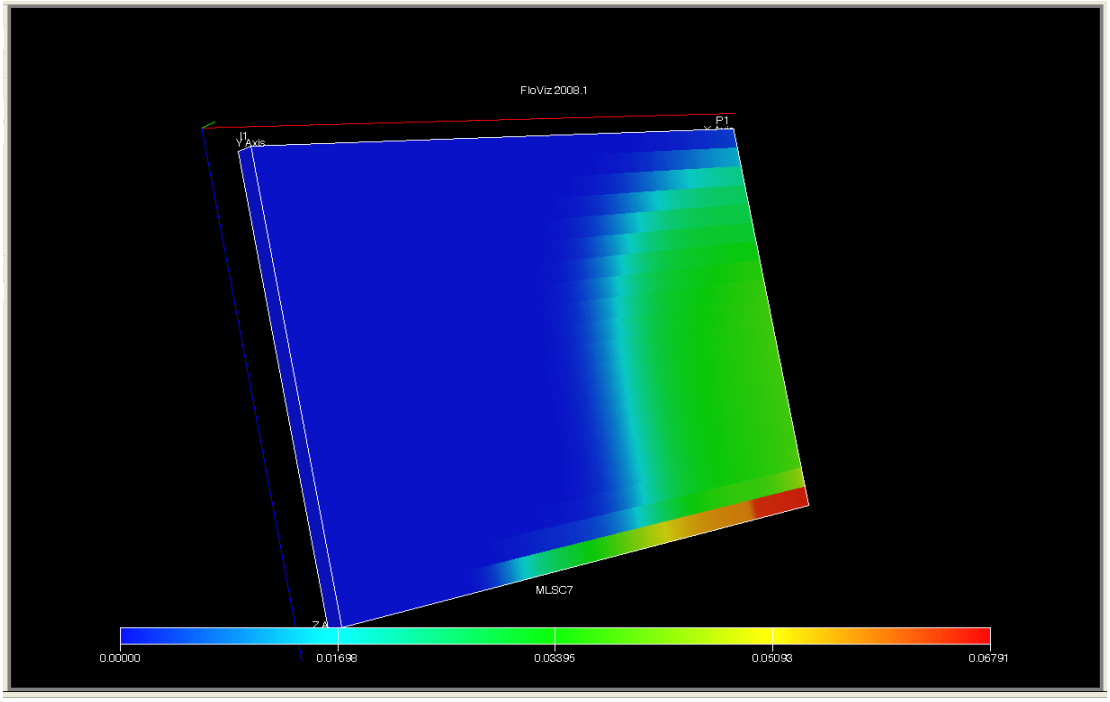

Figure 77: C_7 component distribution profile after 1800 days of gas injection

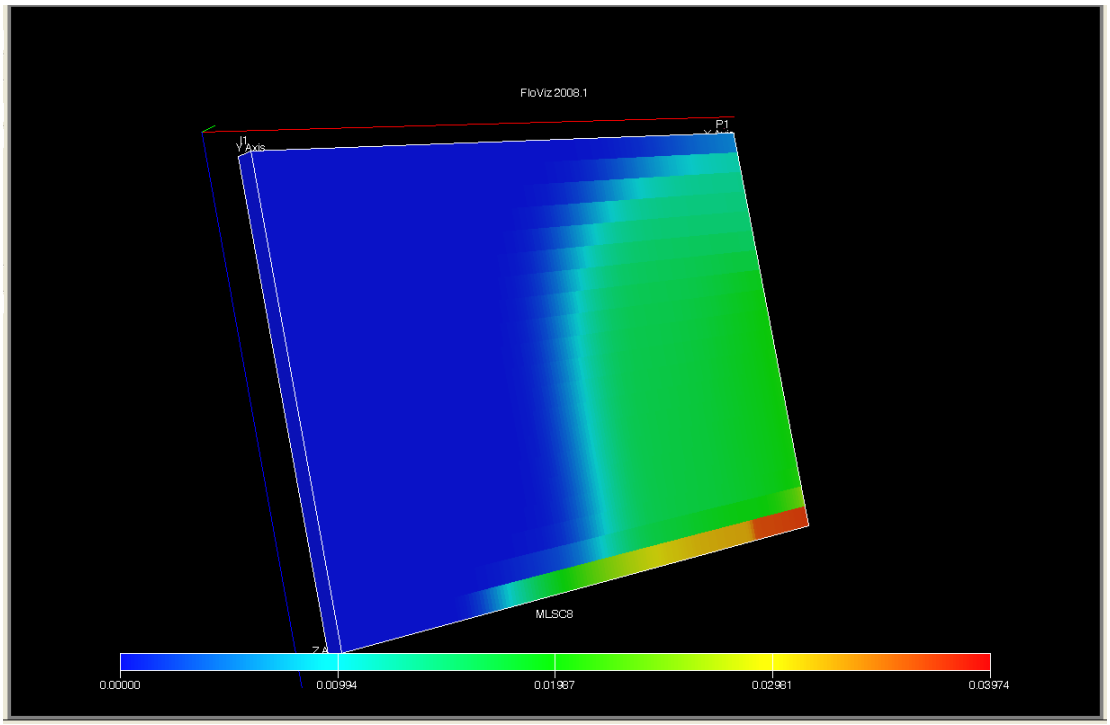

Figure 78: C_8 component distribution profile after 1800 days of gas injection

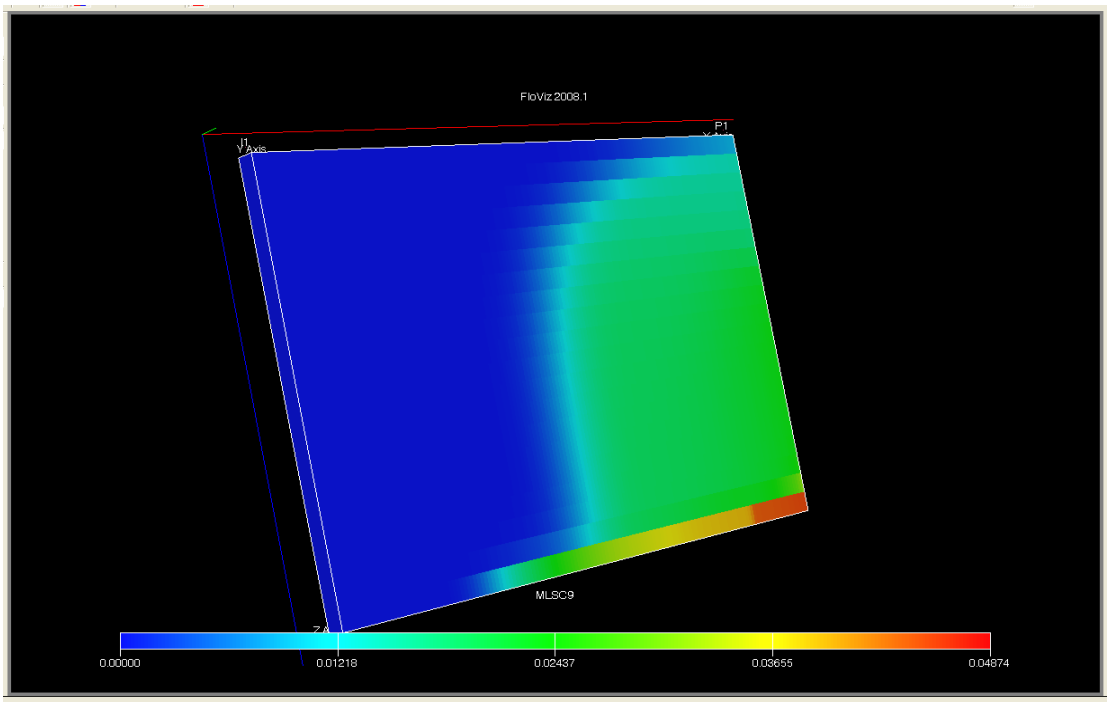

Figure 79: C_9 component distribution profile after 1800 days of gas injection

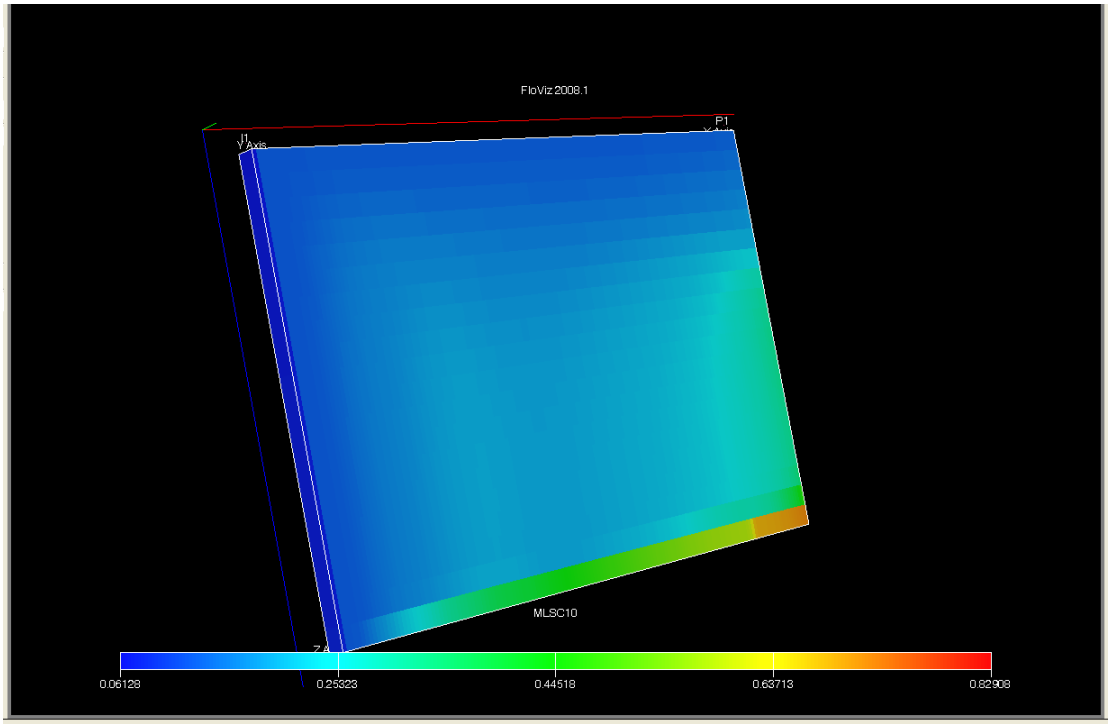

Figure 80: C_{10} component distribution profile after 1800 days of gas injection

The "cell-probe" feature in FloViz was used to retrieve data relevant to a particular cell. Data retrieved include:

- Reservoir pressure
- Saturation pressure
- Gas saturation
- Component molar fraction

CO_2 Sequestration

The gas injection process simulation yielded some produced gas at the production well. However, only 30% of the injected gas was produced. This produced gas, in field operations, would be treated and reinjected to recover more oil. The potential for CO_2 EOR as a sequestration method is vividly demonstrated by this simulation. **Figure 81** shows the cumulative gas injected compared to the cumulative gas produced over the entire simulation period, which is 1800 days.

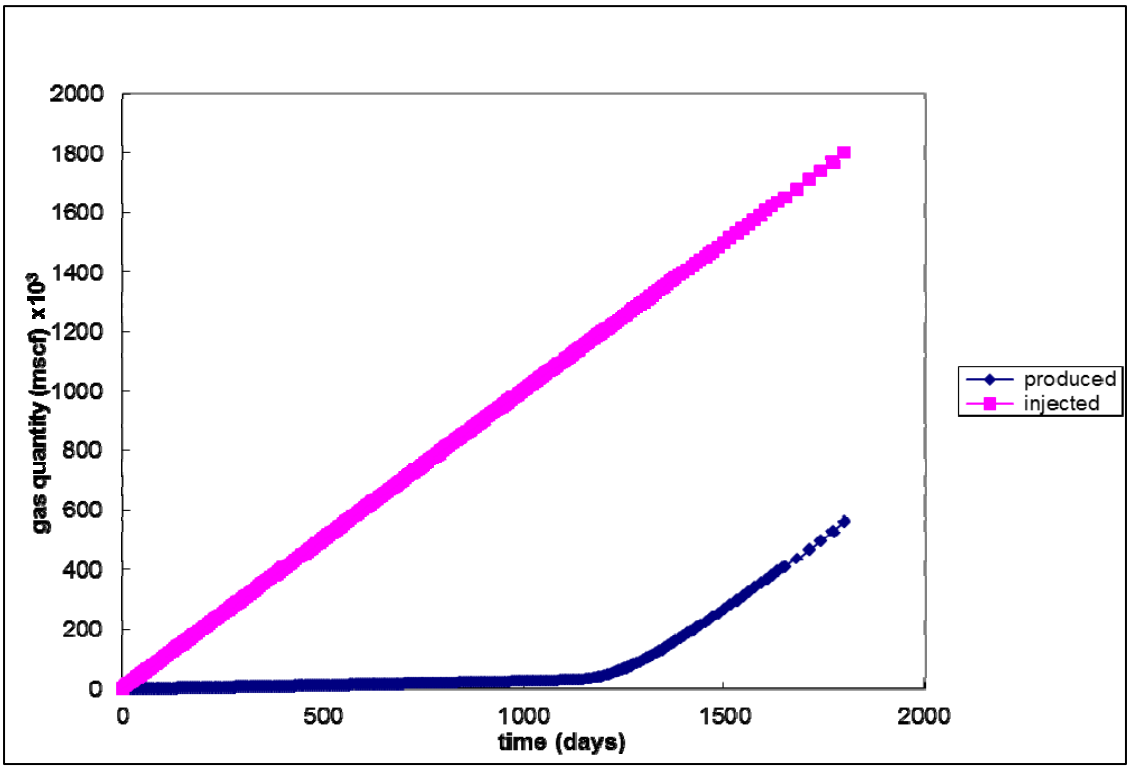

Figure 81: Cumulative gas injection and production

CO_2 EOR

This simulation study yielded a recovery of 77% of oil-initially-in-place (OIIP). The high oil recovery factor is indicative of a successful gas flooding operation. Data retrieved from the simulation results are plotted as shown in **Figure 82**.

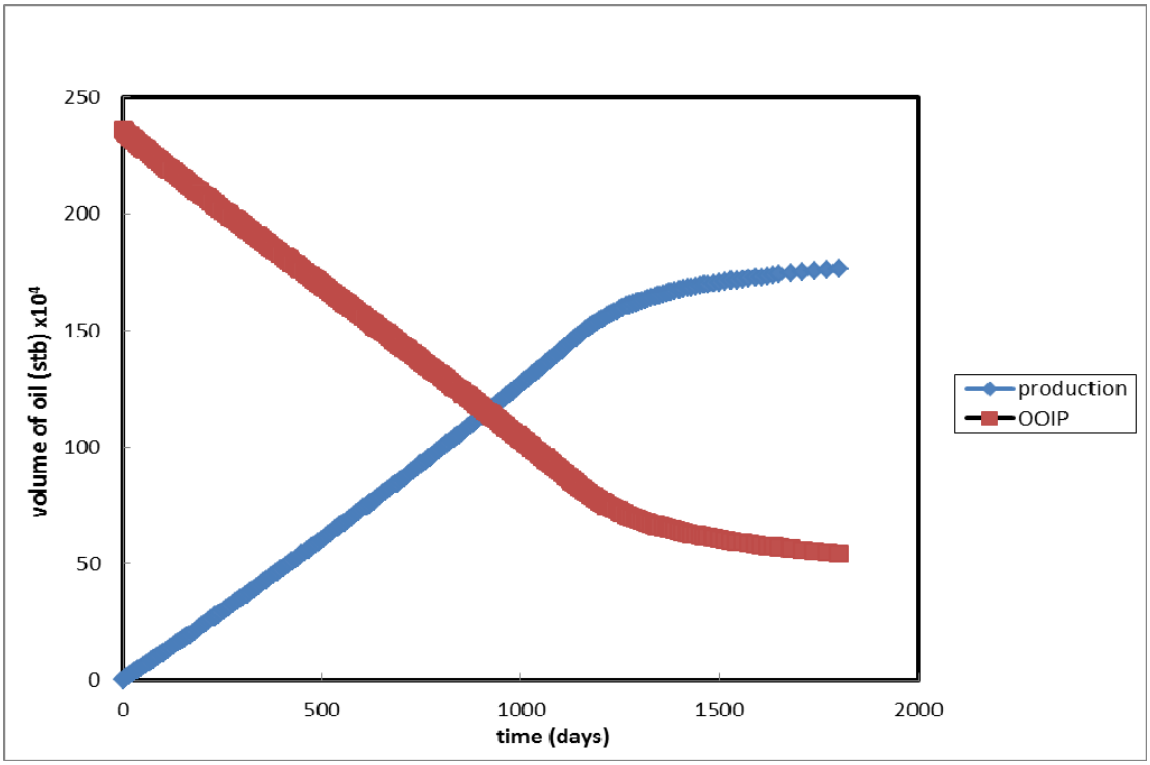

Figure 82: Oil recovery/depletion for simulation period

In addition, one of the critical aspects of visualizing the results of the CSEM model is the ability to display multiple reservoir silhouettes at once. Each reservoir is presented as a hemi-ellipsoid defined by the parameters: length, height, depth, α_1, and α_2. Length and height are the measurements given to the major and minor axis of the ellipse with these axes on 0 and 90 degrees. α_1 is the angle from the major axis to where the partial ellipsoid begins and α_2 is the angle from $\alpha 1$ to the where the ellipsoid ends.

Our goal is to provide an immersive visualization that will allow Dr. Stalnaker to interact and to visualize in immersive 3-D the multiple reservoirs. To that end, we started by developing an OpenGL algorithm that could draw an ellipsoid based on length, height, and depth. Once we had this algorithm working, it was modified to use α_1 and α_2, thus drawing partial ellipsoids. To accomplish the immersive visualization, we integrated the OpenGL visualization into the VR Juggler framework, which allowed us to present the visualization on a high-resolution stereoscopic tiled wall and use head and hand tracking for interaction.

This first prototype only showed one reservoir at a time, so our next step was to work closely with Dr. Stalnaker to define the strategy to show his complete dataset of reservoirs. Based on the CSEM model, each parameter of the partial ellipsoid has a related probability. Since these probabilities are all independent, we can easily calculate a joint probability and use that figure to group the reservoirs. This allows us to display groups of reservoirs at a time. The problem we faced was that no two reservoirs shared a joint probability. This meant that the data did not present a straightforward way to group the different kinds of reservoirs. In order to figure out a strategy to group the reservoirs without any ambiguity, we introduce a tolerance parameter to our grouping algorithm. By adjusting this parameter we can increase and decrease the number of groups created.

We decided to display each group as a ring and place each ring on a column. As we move up along the column, each ring's joint probability increases. Some work had to be done to adjust the diameter of each ring based on the number of reservoirs in the group and to calculate their spacing on the ring. We also added ring rotation, column translation, and an information pane to see the data for the selected reservoir. The two figures (**Figures 83** and **84**) below show the current state of the visualization.

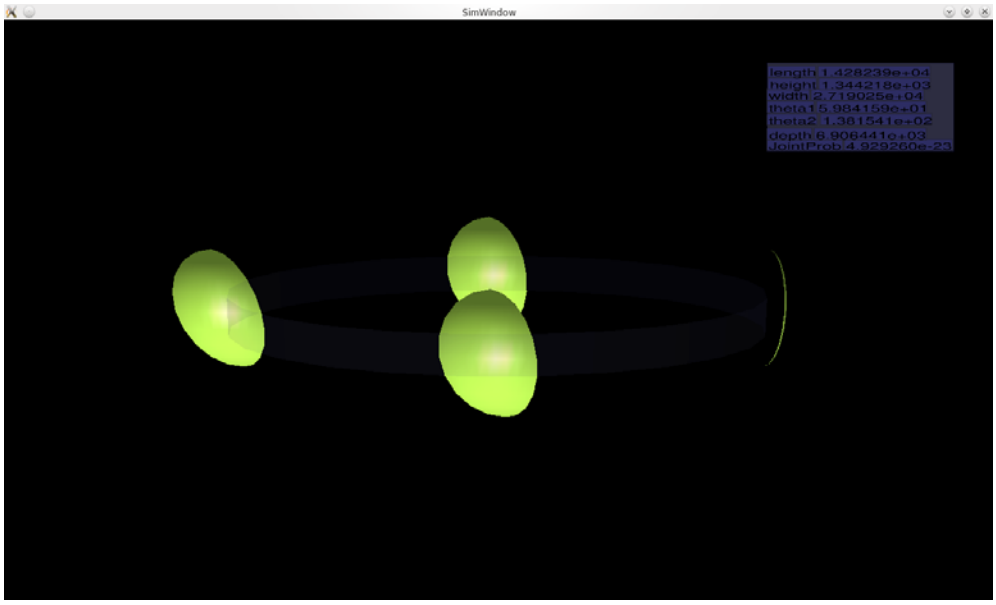

Figure 83: Current state of visualization (1)

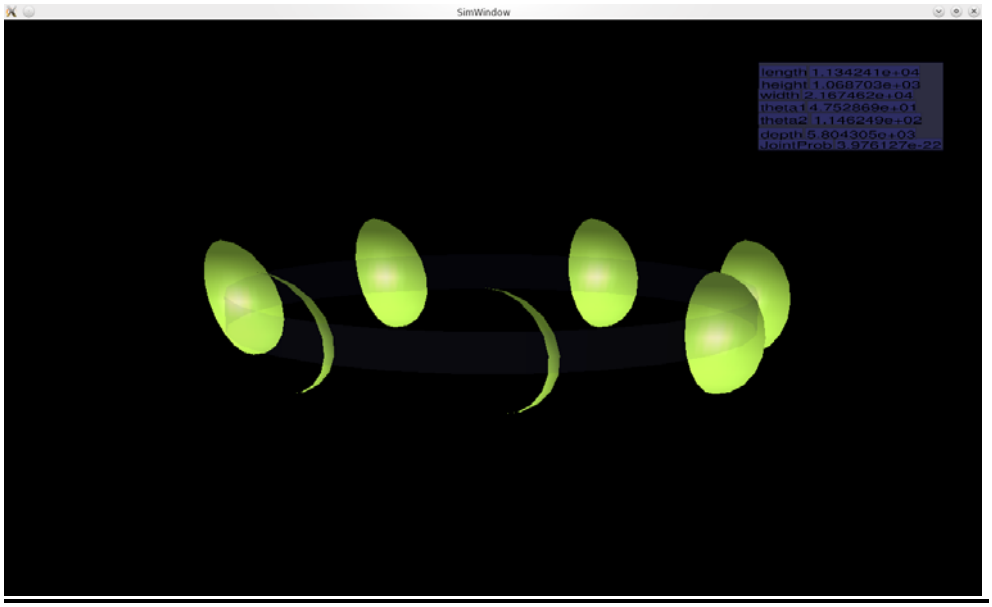

Figure 84: Current state of visualization (2)

Besides, we focused on the presentation of the available information and added more user control. While we are able to display multiple reservoir silhouettes at once (**Figure 85**), we were not conveying as much information to the user as possible. Through the use of color coding, we are able to quickly convey, to the user, the joint probabilities of all shown reservoirs. Furthermore, by color coding the ring and the background we are able to convey the resistivity of the reservoir and the host medium.

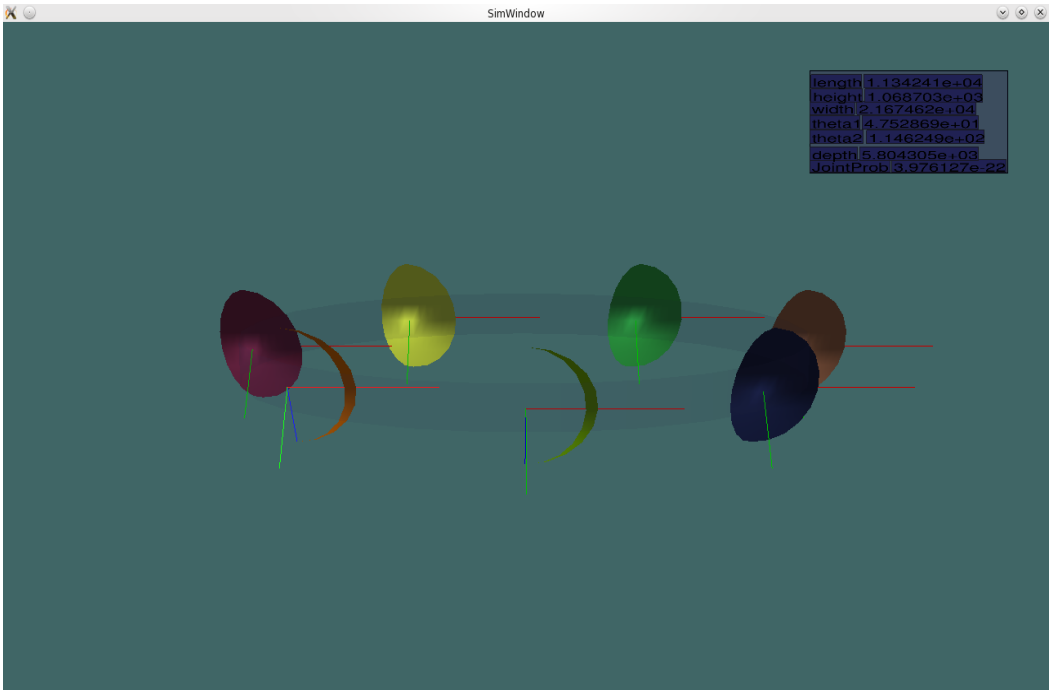

Figure 85: Current state of visualization (3)

CONCLUSIONS

Foam Study

New fluids have been designed to efficiently drill deepwater wells that cannot be cost-effectively drilled with current technologies. The new fluids are heavy-liquid foams that have low-density at shallow depth to avoid formation breakdown and high density at drilling depth to control formation pressure. We have provided the industry with formulations of new fluids in order to reduce casing programs and thus well construction cost in deepwater development.

Visualization was used in this part of the project. Visualization confirmed that significant end-effects existed at both ends of the sand packs. The end-affected length is about 3.5 cm in the 4.45 cm inner diameter tube. Visualization also indicated that gravity segregation effect in the horizontal flow experiments was not significant.

CO2 Study

Model building, testing, and validation was done using 2 common flue gases with the following compositions; 15% CO_2/85% N_2 and 30%CO_2/70% N_2, for selective South Louisiana oil samples with API gravity ranging between 31^o and 41^o at *in-situ* conditions ranging between 200 to 375 ºF and 2000 to 3200 psia. It was concluded that:

1. Comparing to Firoozabadi and Glasø correlations, this study's slim tube MMPs are more accurate.

2. Slim tube-generated MMPs underestimate MMPs; field scale-generated MMPs are recommended for South Louisiana EOR projects as they capture *in-situ* conditions and better portray production performance.

3. To model MMP for an EOR project, field-generated MMPs have to replace the industry's practice of using slim tube-generated MMPs. Failure to do so will most probably result in multi-contact miscibility and will hamper oil recovery.

Besides the development of new augmented MMP correlation that can be used to predict CO2 MMP, an artificial neural network has been developed for CO2 injection as an EOR reservoir management technique. The ANN model can be used to map recovery efficiencies for candidate light oil reservoirs in Louisiana with API gravities, reservoir temperatures, and reservoir pressures ranging from 31^o to 41^o, 200 to 375 ºF, and 2000 to 3200 psia, respectively.

Visualization was also used to better understand dominant EOR mechanism under miscible conditions and monitor frontal advance rate movement for the candidate Louisiana oil reservoirs. The visualization part confirmed an active vaporization mechanism.

Visualization also confirmed the fact that the potential for CO_2 EOR as a sequestration method is vividly demonstrated.

CSEM Study

The CSEM study team has compiled:

1. A statistical database of the electrical and geometric parameters of known hydrocarbon reservoirs occupying the first set of protractions off the coast of Louisiana in the Gulf of Mexico, where the geometric parameters are defined over a low dimensionality, common coordinate system dubbed the prototype hemi-ellipsoid model.

2. Statistically derived probability distributions of reservoir parameters computed using kernel density estimation.

3. A rejection sampling based algorithm useful for producing synthetic but realistic (as defined by known statistics) off-shore Louisiana Gulf of Mexico hydrocarbon reservoirs. The approach is easily extensible to any region for which a statistically significant number of geometric and electrical reservoir measurements exist. The technique should also be considered trainable or "learning", as additional information improves the statistically derived probability distributions.

4. A demonstrated, extensible, fully three-dimensional finite element modeling software package written in C++ and capable of producing the marine controlled source electromagnetic response of any arbitrary terrestrial or marine conductivity distribution.

5. A Monte Carlo derived understanding of the variation in off-shore Louisiana controlled-source electromagnetic responses.

6. An assessment of the utility of the widely used magnitude-versus-offset reconnaissance method in the Gulf of Mexico.

The CSEM group has also developed a simplified, approximate model of marine controlled source electromagnetic responses. The team has come up with a Standard and Bayesian inversion of MCSEM containing proven solutions to the common inversion problem of local minimum entrapment.

Visualization was also used to provide an immersive visualization that will allow Dr. Stalnaker to interact and to visualize in immersive 3-D the multiple reservoirs.

RECOMMENDATIONS

Foam Study

In the foam study, more foams can be tested under different conditions. A larger data bank can be generated in order to come up with an ANN model that can be used for mapping and predictive purposes.

CO2 Study

Understanding complex interactions between reservoir fluids and injection gas is important for flue gas and CO2 injection to be a competitive process in a given recovery project. Limited amount of data was used in this project and that is a drawback. Nevertheless, the developed correlations proved to be more accurate than the industry-standard published correlations. A larger data pool would have provided us with more data for training, testing, and validation purposes.

CSEM Study

It is recommended that as much additional statistical information regarding reservoir geometry and resistivity is obtained in order to improve the prior probability density functions. It is also recommended that additional regions be surveyed, and the prior and posterior probabilities in different regions—especially regions with contrasting geology be compared to the surveyed offshore Louisiana area.

In addition, two milestones of the original research were not met. One is relatively simple: assess the accuracy of our inversion method. A bound on the estimator variance exists, and can be computed: the Cramer-Rao lower bound. The second goal is more difficult, but very practical. We can use our model and our probability data to optimize MCSEM survey parameters without any specific a priori knowledge of a survey region. Both tasks have been completed for the UXO problem, and require only adaptation to the MCSEM task. However, in lieu of these missing milestones, we have produced the assessment of MVO performance, and we have produced a more successful accounting of GoM reservoirs than originally anticipated, including the surprisingly effective hemi-ellipsoid model of geometric parameters.

BIBLIOGRAPHY

Aliamiri, A., Stalnaker, J., & Miller, E. (2007). Statistical classification of buried unexploded ordnance using nonparametric prior models,. *IEEE Transactions on Geoscience and Remote Sensing , 45* (9), 2794-2806.

Anderson, T., & Darling, D. (1952). Asymptotic theory of certain "goodness-of-fit" criteria based on stochastic processes. *Annuals of Mathematical Statistics , 23*, 193-212.

Badea, E. (2001). Finite element analysis of controlled-source electromagnetic induction using Coloumb- gauged potentials. *Geophysics , 66* (3), 786-799.

Chave, A., & Cox, C. (1982). Controlled electromagnetic sources for measuring electrical conductivity beneath the oceans, 1, forward problem and model study,. *Journal of Geophysical Research , 87* (B7), 5327-5338.

Constable, S. (2006). Marine electromagnetic methods–A new tool for offshore exploration. *The Leading Edge , 25*, 438-444.

Constable, S. (2010). Ten years of marine CSEM for hydrocarbon exploration. *Geophysics , 75*, 75A67-75A81.

Constable, S., & Weiss, C. (2005). Mapping thin resistors (and hydrocarbons) with marine EM methods: Insights from 1D modeling. *Geophysics , 71*, G43-G51.

Duong, T. (2001). *An introduction to kernel density estimation*. Retrieved 2009, from http://www.maths.uwa.edu.au/~duongt/seminars/intro2kde/

Eidesmo, T., Ellingsrud, S. M., Constable, S., Sinha, S., Johnsen, S., Kong, F., et al. (2002). Sea Bed Logging (SBL), a new method for remote and direct identification of hydrocarbon filled layers in deep-water areas. *First Break , 20* (3), 144-152.

Flosadottir, A., & Constable, S. (1996). Marine controlled source electromagnetic sounding 1. Modeling and experimental design. *Journal of Geophysical Research , 101*, 5507-5517.

Gilks, W. R., Best, N., & Tan, K. (1995). Adaptive Rejection Metropolis Sampling within Gibbs Sampling. *Journal of the Royal Statistical Society. Series C (Applied Statistics) , 44* (4), 461-462.

Gueho, B. (2009). *A probabilistic description of offshore Louisiana reservoirs for marine controlled-source electromagnetic modeling.* Master's thesis, University of Louisiana at Lafayette.

Hou, Z., Rubin, Y., Hoverstein, M., Vasco, D., & Chen, J. (2006). Reservoir-parameter identification using minimum relative entropy-based Bayesian inversion of seismic AVA and marine CSEM data. *Geophysics , 71* (6), 77-88.

Hunt, J. L., & Burgess, G. (1995). Depositional styles from Miocene through Pleistocene in the North-Central Gulf of Mexico: An Historical Reconstruction. *Gulf Coast Association of Geological Societies Transactions , 45*, 275-284.

Hwang, J., Lay, S., & Lippman, A. (1994). Nonparametric multivariate density estimation: a comparative study. *IEEE Transactions on Signal Processing , 42* (10).

John, C. J., Jones, B., & Harder. (1996). Regional chronostratigraphic and depositional hydrocarbon trends in offshore Louisiana state waters. *Gulf Coast Association of Geological Societies Transactions , 46*, 193-202.

Key, K. (2009). 1D inversion of multicomponent, multifrequency marine CSEM data: Methodology and synthetic studies for resolving thin resistive layers. *Geophysics, , 74* (2), 9-20.

Lafayette and N. O. G. Societies. (1973). *Offshore Louisiana Oil and Gas Fields.* Lafayette and New Orleans Geological Societies.

Lillefors, H. (1967). On the Kolmogorov-Smirnov Test for Normality with Mean and Variance Unknown. *Journal of the American Statistical Association , 62* (318), 399-402.

MacGregor, L., & Tompkins, M. (2005). Imaging Hydrocarbon Reservoirs Using Marine Controlled-Source Electromagnetic Sounding. *OTC 17163.* Houston, TX: OTC 17163,

Offshore Technology Conference.
MacGregor, L., Andreis, D., Tomlinson, J., & Barker, N. (2006). Controlled-source electromagnetic imaging on the Nuggets-1 reservoir. *The Leading Edge , 25* (8), 985-992.
Mehta, K., & Oldenburg, D. (2005). Controlled Source Electromagnetic (CSEM) technique for detection and delineation of hydrocarbon reservoirs: an evaluation. *SEG Expanded Abstracts , 24*, 546.
Ostrander, J. W. (1984). Plane-wave reflection coefficients for gas sands at non-normal angles of incidence. *Geophysics , 49* (10), 1637-1648.
Salvador, A. (1987). Late Triassic-Jurassic paleogeography and origin of Gulf of Mexico Basin. *AAPG Bulletin , 71* (4), 419-451.
Scott, D. (1979). On optimal and data-based histograms. *Biometrika , 66* (3), 605-610.
Sivakumar, R. (1998). *A 3-D seismic interpretation of Ship Shoal 253 Field Offshore Louisiana: salt sediment interactions.* Master's thesis, University of Louisiana at Lafayette.
Stalnaker, J., & Miller, E. (2007). Particle swarm optimization as an inversion tool for a nonlinear UXO model. *Geosci. and Rem. Sens. Symposium, IGARSS 2007* , 432-435.
Stalnaker, J., Everett, M., Benevides, A., & Pierce, C. (2006). Mutual induction and the effect of host conductivity on the em induction response of buried plate targets using 3-d finite-element analysis. *IEEE Transactions on Geoscience and Remote Sensing , 44* (2), 251-259.
Tinley, M. (2010). *Stochastically constrained, simplified 3-dimensional electromagnetic modeling of offshore Louisiana oil and gas reservoirs.* Master's thesis, University of Louisiana at Lafayette.
Weimer, P. (1990). Sequence stratigraphy, facies geometries, and depositional history of Mississippi fan, Gulf of Mexico. *AAPG Bulletin , 74* (4), 425-453.
West, G., & Macnae, J. (1991). Physics of the electromagnetic induction exploration method. In M. Nabighian (Ed.), *Electromagnetic Methods in Applied Geophysics* (Vol. 2, pp. 5-45). Tulsa, Oklahoma: Society of Exploration Geophysicists.
Y., L., & Key, K. (2007). Two-dimensional marine controlled-source electromagnetic modeling, part 1: and adaptive finite element algorithm. *Geophysics , 72* (2), WA51–WA62.

APPENDIX – CO2 ANN MODEL DEVELOPMENT (MATLAB FILES)

ANN model

```
clear all
clc
neur=input('Input number of neurons -->');
nc=num2str(neur);
netf=['net_' nc]';
epf=['epoch_' nc '.res'];

%    LOADING TRAINING DATA
%    =====================
trainingdata;

%    DEFINING A VECTOR ASSOCATION PROBLEM
%    ====================================
%    p defines 3-element input vector (column vectors):
%    t defines 4-element output vector (column vectors):

p   =[data(:,2:5)];         %input data o
t   =[data(:,1)];           %desired output

%    DFINING MAX AND MIN VARIABLES
%    =============================
dw2_max      =max(p(:,1));     dw2_min  =min(p(:,1));
dw4_max     =max(p(:,2));      dw4_min  =min(p(:,2));
T1_max      =max(p(:,3));      T1_min   =min(p(:,3));
T2_max     =max(p(:,4));       T2_min   =min(p(:,4));
mpp_max     =max(t(:,1));     mpp_min   =min(t(:,1));

pmax    =[dw2_max dw4_max T1_max T2_max];
pmin    =[dw2_min dw4_min T1_min T2_min];
t_max   =[mpp_max];
t_min   =[mpp_min];

%    NORMALIZATION OF VARIABLES
%    ==========================
p1  =[p(:,1)/dw2_max p(:,2)/dw4_max p(:,3)/T1_max p(:,4)/T2_max];
t1  =[t(:,1)/mpp_max];

%    SAVING MAX AND MIN VECTORS
%    ==========================
data_max=[pmax t_max];
save data_max.dat data_max -ascii -double

data_min=[pmin t_min];
save data_min.dat data_min -ascii -double

%    PLOT TRAINING DATA
%    ==================
c=p1';
d=t1';
clf
subplot(211)
plot(c,d(1,:),'o')

subplot(212)
plot(c,d(1,:),'o')
```

```
%    SETTING NEURAL NETWORK PARAMETERS
%    ================================
pr  =[dw2_min/dw2_max   1       % min and max values
      dw4_min/dw4_max   1
      T1_min/T1_max     1
      T2_min/T2_max     1];

%Here NEWFF is used to create a two layer feed forward network.
%The network will have an input (ranging from min to max), followed
%by a layer of n1 TANSIG neurons, followed by a layer with n2
%PURELIN neuron.  TRAINLM backpropagation is used.  The network
%is also simulated.
n1  =neur;  %number of tansig neurons
n2  =1;     %number of linear neurons
a   =input('Do you want to reset your network Yes [0]/No [1] ->');
if a== 0
   net = newff(pr,[n1 n2],{'tansig', 'purelin'},'trainlm','learngdm','mse');
   y1 = sim(net,c);
   epoch =0;
else
   load(netf)
   epoch=load(epf);
end

% Here the network is trained for up to emax epochs to a error goal of
% mse, and then resimulated.

 net.trainParam.epochs = 2e3;
 net.trainParam.goal = 1e-6;
 net.trainParam.show = 100;
 net = train(net,c,d);
 w1 =net.iw{1,1};
 b1 =net.b{1};
 w2 =net.lw{2,1};
 b2 =net.b{2};

 w1f=['w1_' nc '.dat'];
 w2f=['w2_' nc '.dat'];
 b1f=['b1_' nc '.dat'];
 b2f=['b2_' nc '.dat'];

 save(w1f,'w1','-ascii','-double')
 save(b1f,'b1','-ascii','-double')
 save(w2f,'w2','-ascii','-double')
 save(b2f,'b2','-ascii','-double')

 save(netf,'net')
 epoch  = net.trainParam.epochs + epoch;
 save(epf,'epoch','-ascii')

 % Algorithm
 %
 %    TRAIN calls the function indicated by NET.trainFcn, using the
 %    adaption parameter values indicated by NET.trainParam.
 %
 %    Typically one epoch of training is defined as a single presentation
 %    of all input vectors to the network.  The network is then updated
 %    according to the results of all those presentations.
 %
 %    Training occurs until a maximum number of epochs occurs, the
```

```
 %    performance goal is met, or any other stopping condition of the
 %    function NET.trainFcn occurs.
 %
 %    Some training functions depart from this norm by presenting only
 %    one input vector (or sequence) each epoch. An input vector (or se-
quence)
 %    is chosen randomly each epoch from concurrent input vectors (or se-
quences).
 %    NEWC and NEWSOM return networks that use TRAINWB1, a training function
 %    that does this.
 %
 %  See also SIM, INIT, ADAPT

cont1   =sum(abs(w1(:,1)));
cont2   =sum(abs(w1(:,2)));
cont3   =sum(abs(w1(:,3)));
cont4   =sum(abs(w1(:,4)));

contsum =(cont1+cont2+cont3+cont4)/100;
cont1p  =cont1/contsum;
cont2p  =cont2/contsum;
cont3p  =cont3/contsum;
cont4p  =cont4/contsum;

fprintf('Contribution of W2= %2.2f [p.c.]\n',cont1p);
fprintf('Contribution of W4 = %2.2f [p.c.]\n',cont2p);
fprintf('Contribution of T1= %2.2f [p.c.]\n',cont3p);
fprintf('Contribution of T2= %2.2f [p.c.]\n',cont4p);

contf=['contrib_' nc '.res'];
fid =fopen(contf, 'w');
%MSE    =tr(1,length(tr))/length(data);
fprintf(fid, 'Number of Hidden Nodes     = %d\n',n1);
fprintf(fid, 'Total Number of Epochs     = %d\n\n',epoch);
%fprintf(fid, 'Mean Squarred Error        = %1.5e\n\n',mse);
fprintf(fid, 'Normalization rate: W2      = %1.5e\n',dw2_max);
fprintf(fid, 'Normalization rate: W4   = %1.5e\n',dw4_max);
fprintf(fid, 'Normalization rate: T1    = %1.5e\n',T1_max);
fprintf(fid, 'Normalization rate: T2  = %1.5e\n',T2_max);
fprintf(fid, 'Normalization rate: mpp  = %1.5e\n',mpp_max);
fprintf(fid, 'Contribution of W3= %2.2f [p.c.]\n',cont1p);
fprintf(fid, 'Contribution of W4 = %2.2f [p.c.]\n',cont2p);
fprintf(fid, 'Contribution of T1= %2.2f [p.c.]\n',cont3p);
fprintf(fid, 'Contribution of T2= %2.2f [p.c.]\n',cont4p);

fclose(fid);

warning off
disp('End of ANNBP')
```

Loop

```
clear sw so ka phi swc sor krw kro c0 c y2
mpp      =v(:,1);
dw2      =v(:,2);
dw4      =v(:,3);
T1     =v(:,4);
T2     =v(:,5);
```

```
n=length(mpp);

for k=1:n
    c0(k,:)=[dw2(k)/data_max(1) dw4(k)/data_max(2)...
             T1(k)/data_max(3) T2(k)/data_max(4)];
end

c   =c0';
y2 = sim(net,c);
mpp_ann=y2(1,:)'*data_max(5);
```

Test Function

```
load w1_5.dat;
load w2_5.dat;
load b1_5.dat;
load b2_5.dat;
w1=w1_5; w2=w2_5; b1=b1_5;  b2=b2_5;
load data_max.dat;
trainingdata;
nk=20;
p   =[data(nk,2:5)];        %input data o
t   =[data(nk,1)];           %desired output

p1  =[p(1,1)/data_max(1) p(1,2)/data_max(2)...
    p(1,3)/data_max(3) p(1,4)/data_max(4)];

q1=w1*p1'+b1;           %Input layer
n=q1';
q2=tansig(n);           %Tan Sigmoid function

q3=(w2*q2'+b2)*data_max(5);% Output layer

fprintf('MPP=%4.0f   MPP_ann=%4.0f\n',t,q3);

return
kk=29.9288
a1=2/(1+exp(-2*kk))-1
a2=tansig(kk)
```

Test Data

```
clear all
clc

fprintf('\n      ====================================\n');
fprintf('      = Program for ANN Model Validation =\n');
fprintf('      ====================================\n');
neur=input('\nInput number of neurons --> ');
nc=num2str(neur);
netf=['net_' nc]';
load(netf)
load data_max.dat;
trainingdata;

v   =data;
loop;
figure(1);
clf
```

```
plot(dw2,mpp,'ro',dw2,mpp_ann,'bd');
xlabel('W_{2}');
ylabel('MPP');
title('W2')

figure(2);
clf
plot(dw4,mpp,'ro',dw4,mpp_ann,'bd');
xlabel('W_{4}');
ylabel('MPP');
title('W4')

figure(3);
clf
plot(T1,mpp,'ro',T1,mpp_ann,'bd');
xlabel('T_{1}');
ylabel('MPP');
title('T1')

figure(4);
clf
plot(T2,mpp,'ro',T2,mpp_ann,'bd');
xlabel('T_{2}');
ylabel('MPP');
title('T2')
```

Training Data

```
data=[...
2200    0.22334115  0.986412    0.594469    0.192865    37.3
2440    0.21113925  1.071458    0.63679     0.177331    31.7
2030    0.22825842  0.953331    0.580283    0.197935    39.7
2300    0.21812263  1.032612    0.614312    0.183418    34.4
2540    0.19193796  1.11239     0.741185    0.172085    31.9
2550    0.19208606  1.114466    0.739734    0.171586    31.3
2025    0.22993754  0.932174    0.576584    0.199673    40.9
2100    0.22515752  0.982128    0.592603    0.189726    36
2490    0.19652994  1.152139    0.720142    0.182374    33.4
3150    0.22334115  0.986412    0.856035    0.277725    37.3
2870    0.21113925  1.071458    0.916977    0.255356    31.7
2625    0.22825842  0.953331    0.835608    0.285027    39.7
2745    0.21812263  1.032612    0.884609    0.264123    34.4
3120    0.19193796  1.11239     1.067307    0.247803    31.9
3010    0.19208606  1.114466    1.065217    0.247084    31.3
2840    0.22993754  0.932174    0.830281    0.287529    40.9
2680    0.22515752  0.982128    0.853348    0.273205    36
3080    0.19652994  1.152139    1.037004    0.262619    33.4
3300    0.22334115  0.986412    1.04032     0.337513    37.3
3265    0.21113925  1.071458    1.114382    0.310329    31.7
3220    0.22825842  0.953331    1.015496    0.346387    39.7
3220    0.21812263  1.032612    1.075046    0.320982    34.4
3310    0.19193796  1.11239     1.297074    0.301149    31.9
3310    0.19208606  1.114466    1.294534    0.300275    31.3
3220    0.22993754  0.932174    1.009022    0.349427    40.9
3230    0.22515752  0.982128    1.037055    0.33202     36
3305    0.19652994  1.152139    1.260248    0.319155    33.4];
```

ACKNOWLEDGMENT

This material is based upon work supported by the Department of Energy under Award Number **DE-NT0004651**.

National Energy Technology Laboratory

626 Cochrans Mill Road
P.O. Box 10940
Pittsburgh, PA 15236-0940

3610 Collins Ferry Road
P.O. Box 880
Morgantown, WV 26507-0880

One West Third Street, Suite 1400
Tulsa, OK 74103-3519

1450 Queen Avenue SW
Albany, OR 97321-2198

2175 University Ave. South
Suite 201
Fairbanks, AK 99709

Visit the NETL website at:
www.netl.doe.gov

Customer Service:
1-800-553-7681